PLASMA COLLECTION BY AN OBSTACLE

Thesis by
Hoanh Xuan Vu

In Partial Fulfillment of the Requirements
for the Degree of
Doctor of Philosophy

California Institute of Technology
Pasadena, California
1990

(Submitted May 17, 1990)

I would like to dedicate this thesis to my parents, without whom this work would have been impossible. I would also like to dedicate this thesis to my brothers for the regular midnight-escapades to the grocery stores in quest of junk foods. Dedication also goes to my eldest sister and her husband for without them, I would not have two adorably mischievous nieces.

ACKNOWLEDGEMENTS

I would like to thank my thesis advisor, Prof. Roy W. Gould, for his invaluable guidance during the course of this work, and for his frequent encouragement, without which this work would not have been possible.

I would like to thank Frank Cosso for his frequent help with the computers in times of despair, and for his help with the data acquisition system during the infancy of my career as a graduate student.

I would like to thank Dr. Paulette Liewer for teaching me to use the MFE CRAYs, which proved to be essential for the completion of this work.

I would like to thank the U.S. Department of Energy and the Magnetic Fusion Science Fellowship Program (administrated by the Oak Ridge Associated University) for supporting this work.

Last, but not least, I would like to thank my father and Dr. Michael Brown for their assistance with the proofreading of this manuscript.

ABSTRACT

The problem of plasma collection by an obstacle is investigated systematically to identify potentially important physical effects.

In the absence of an ambient toroidal plasma flow, plasma collection by a two-dimensional obstacle of half-width d extending to infinity in the y-direction (slab geometry) is studied in detail. The transport process is taken to be classical. The plasma is assumed to be strongly magnetized. The external magnetic field is assumed to be uniform, and is perpendicular to the obstacle's surface. Our numerical results suggest that both ion viscosity and ion viscous heating can be important in the regions where the ion velocity possesses sharp gradients, e.g., the region near the obstacle's tip.

A two-dimensional, semi-empirical, model is proposed to account for the effect of anomalous transport due to a low-frequency, microscopic, electrostatic fluctuation of the poloidal electric field. The obstacle has a half-width of d, and is assumed to extend to infinity in the y-direction. The plasma is assumed to be strongly magnetized. The external magnetic field is assumed to be uniform, and is perpendicular to the obstacle's surface. In general, our proposed model suggests the following:

1. Contrary to that which has been suggested in the literature, the cross-field ion viscosity coefficient (as well as the cross-field ion thermal conductivity) is not enhanced because the cross-field transport is dominated by the *fluctuation-induced* convection.
2. Viscous heating may have an important effect on the ion temperature when there exists a large velocity gradient. Furthermore, in the presence of anomalous transport, the physical mechanism by which viscous heating is generated is quite different from the case where the transport process is classical.

In the absence of an ambient toroidal plasma flow, our numerical results suggest that for realistic plasma parameters, the peaked ion temperature is up to 85% higher than the ambient ion temperature due to ion viscous heating.

A numerical code based on the above model is developed to deal with the case where the ambient toroidal plasma flow is finite. Such a situation arises in connection with experimental data obtained by the so-called *Janus* probe or *Mach* probe. Our numerical results indicate that near the obstacle's tip, the ions on the downstream side are hotter than those on the upstream side.

TABLE OF CONTENTS

LIST OF FIGURES

CHAPTER 1

Introduction

For the past several decades, tremendous efforts have been undertaken to study the physics of ionized gases, especially in association with controlled thermonuclear fusion. If thermonuclear fusion can be harnessed, it will provide an inexpensive, efficient method of producing virtually unlimited energy. Furthermore, controlled thermonuclear fusion is a relatively *clean* method of producing energy because there are very few dangerous radioactive byproducts associated with it. It is projected that scientific breakeven for controlled thermonuclear fusion will be achieved in the near future.

In order for nuclear fusion to occur under laboratory conditions, the ions have to be confined at high density and temperature for a sufficient amount of time to overcome the (ion-ion) Coulomb repulsion. The tokamaks (toroidal confinement devices) are the most promising confinement devices available today.

One of the major ongoing efforts is to improve the particle and the energy confinement time of the tokamak. Several suspects have been identified as being responsible for particle and energy losses. Two suspects are anomalous transport and high levels of impurity. Anomalous transport, transport that cannot be accounted for by classical transport theory, is believed to be the result of a randomly (turbulent) fluctuating electric field in the plasma. High levels of impurity are detrimental to the energy confinement time because the high Z impurity ions, usually heavy, have high radiation losses: they take energy from the plasma via collisions and other processes, and give it up in the form of radiation.

The efforts to reduce the impurity level in, as well as to characterize the state of, the plasma usually involves introducing foreign objects into the main body of the plasma. Consequently, it is essential that the physics underlying the plasma-object interactions be well understood. To demonstrate typical situations where foreign objects are introduced into the plasma, consider the following three examples.

1. In fusion tokamaks, in order to define the plasma edge and to reduce the level of ion impurity, limiters are used to collect energetic plasma particles escaping the core plasma before they bombard the containment wall. Consequently, *shadows*, the regions where the plasma density is partially depleted, are created by limiters, as illustrated in figure 1.1.
2. A common plasma diagnostic for density measurements consists of a single or an array of electrostatic Langmuir probes mounted in a probe housing.[1] The probe housing, in addition to its intended purpose as a protective housing, also collects plasma particles and, in most cases, even disturbs the plasma locally. In the extreme case where the probe housing is *large*, it essentially acts as a limiter[2] (see figure 1.1).
3. A typical *Mach* probe consists of two electrostatic Langmuir probes mounted on either side of an obstacle[3], as shown in figure 1.2. This probe is based on the concept of obstructing the plasma flow by means of a mechanical obstruction, and thereby seperating the upstream and downstream particle fluxes. It should be noted that is it desirable to position the obstacle such that it is normal to the ambient plasma flow. The electrostatic Langmuir probes on both sides of the obstacle are biased negatively to collect the upstream and downstream ion saturation currents. The collected ion saturation currents are assumed to be representative of the plasma flows in the upstream and downstream shadows of the obstacle. The objective is to use the measured upstream/downstream ion flux ratio to infer the magnitude of the ambient plasma flow. Currently, there are disagreements in the literature regarding the interpretation of Mach probe data.

Both computational and experimental aspects of plasma collection by an obstacle have been studied by many authors. Several experiments have been performed regarding the perturbing effects of large probes and limiters.[2,4-8] In addition to the experimental effort, extensive theoretical effort has also been focused on the modelling of, as well as the interpretation of data from, large probes.[9-13]

Despite the fact that so much effort has been expended in the subject of plasma collection by an obstacle, a number of fundamental issues have not been either addressed or satisfactorily resolved. This thesis is aimed at addressing a limited number of such issues. In particular, the fundamental physics of interest are:

1. Is it appropriate to neglect the parallel electron-ion collisional drag as is often done in the literature (without *a priori* or *a posteriori* justification)?
2. Can the ions be treated as an inviscid fluid, or should they be treated as a viscid fluid? If the ions should be treated as a viscid fluid, which component of the ion viscosity tensor is important for the transport of momentum?
3. What is the role of, and how important is, ion viscous heating?
4. Do the ions remain sufficiently isothermal while being accelerated toward the obstacle, so that one can neglect the ion energy equation?
5. How should the cross-field ion viscosity and ion thermal conductivity be modified to account for anomalous transport?
6. How should the experimental data from Mach probes be interpreted in order to infer the magnitude of the ambient plasma flow?

An *electrostatic sheath*, a thin layer of electron-depleted plasma whose thickness is of the order of the Debye shielding distance, is formed on the surface of an obstacle when immersed in a plasma. Upon entering this electrostatic sheath, the ions acquire a speed of at least c_s, the ion acoustic speed.[14-20] Consequently, an obstacle, when immersed in a plasma, acts as a particle collector. Often a qualitative argument based on particle balance[11] is used to show that such a particle collector will create a *shadow* (see figure 1.1), the region in which the plasma density is partially depleted, whose extent to either side of the obstacle is of the order $L_\parallel \sim c_s d^2/D_\perp$ (d is the dimension of the obstacle). If many obstacles are located sufficiently close to each other, their shadows can overlap, and probe measurements in such a plasma region will yield erroneous information regarding the unperturbed plasma parameters. Several models have been proposed to infer unperturbed plasma parameters from such probe measurements.[11–12] In these models, three basic assumptions are made: (1) the ions are isothermal, (2) the ions are inviscid, and (3) the parallel electron-ion collisional drag is neglected. However, as will be shown in chapter 3, the validity of these assumptions is questionable.

Because each particle collected at the obstacle's surface carries some momentum and energy, the surface is subject to a power flux that can heat up the obstacle. If the obstacle is brought to a sufficiently high temperature, it will release impurity ions into the main plasma. It is therefore desirable to construct a plausible model to predict power loading on obstacles under given operating conditions. There are transport codes available for this purpose.[21] However, such transport codes are far too complicated, and thus are not efficient. Furthermore, because of the complexity of these transport codes, it is difficult to identify the dominating physical mechanisms.

In the *scrape-off layer*, Mach probe measurements indicate that the ion saturation currents collected on the two sides of the obstacle are not equal,[3] suggesting the existence of an ambient plasma flow. Two contending models have been proposed to infer the magnitude of the ambient plasma flow from the upstream/downstream ion flux ratio.[9–10] In one model,[9] the ions are assumed to be isothermal and inviscid, i.e., the effects of ion viscosity and ion viscous heating are neglected altogether. As will be shown in chapter 5, the validity of this model is questionable. In the other model,[10] the ions are assumed to be isothermal and viscid. In fact, the cross-field ion viscosity coefficient is assumed to be *anomalous* due to turbulent transports. In particular, it was postulated that $\eta_\perp / nMD_{\perp t}$, the viscosity/diffusivity ratio, is of the order 1. As will be shown in chapter 5, the validity of this model is also questionable.

Thesis Outline

In chapter 2, the usual derivation of the two-fluid description of plasmas from the Boltzmann equation is modified to account for particle, momentum, and energy sources. The two-fluid description of plasma so obtained is then simplified to model a fully ionized, strongly magnetized plasma consisting of only two species: electrons and singly charged ions.

Chapter 3 begins with a simple model of plasma collection by an obstacle in the absence of an ambient plasma flow. In this model, the ions are assumed to be isothermal and inviscid. Five other models in which the ambient plasma flow is also assumed to be absent are then constructed, each taking into account a potentially important physical effect. The numerical results from these models are then compared with those from the first simple model where the ions are assumed to be isothermal and inviscid. Because each model isolates a different physical mechanism, the effects of different physical mechanisms are decoupled. Consequently, the dominating physical mechanisms can be easily identified. The potentially important physical effects considered in this chapter are: (1) the localization of the replacement particles, (2) the dependence of $D_\perp$ on the particle density $n(x,z)$, (3) the parallel electron-ion collisional drag, (4) ion viscosity, and (5) ion viscous heating. Throughout chapter 3, the electrons are assumed to be isothermal and inviscid, and the transport process is taken to be classical. Furthermore, the actual toroidal geometry shown in figure 1.1 is idealized to simplify tedious geometrical cosiderations. Figures 1.3a and 1.3b illustrate the idealized geometry employed in this chapter. A rectangular lattice of obstacles and its *unit cell* are shown in figure 1.3a. Because of symmetry, the actual domain of interest consists of only one quarter of the unit cell, as shown in figure 1.3b. The x and z directions correspond to the radial and toroidal directions, respectively. The y direction corresponds to the poloidal direction, and is assumed to be the ignorable direction. The (toroidal) magnetic field is assumed to be *strong* and uniform.

In chapter 4, a semi-empirical model is proposed to account for turbulent transport caused by a low-frequency, microscopic, electrostatic fluctuation of the poloidal electric field. In this chapter, the ambient plasma flow is taken to be zero. Numerical results are obtained for a set of plausible plasma parameters.

Chapter 5 is an extension of chapter 4 in an effort to account for the effect of a subsonic ambient plasma flow in the toroidal direction. Numerical results are obtained for three values of the ambient plasma flow. The results of this chapter have direct applications in the interpretation of Mach probe measurements.

Chapter 6 concludes the thesis with a brief summary of the primary numerical results regarding plasma collection by an obstacle.

Four appendices relevant to the work presented in chapters 2–5 are included in this thesis. Appendix A is a one-dimensional model of electrostatic sheaths with warm ions. Appendix B contains the coordinate transformations employed in chapters 2–5. Appendix C is a simple one-dimensional model of plasma collection by an obstacle. The primary purpose of Appendix C is to explain the origin and the nature of the singular behaviour found in the plasma response at the obstacle's surface. Appendix D contains the normalization procedure for a typical set of transport equations, and a listing of the computer code employed in section 3.7.

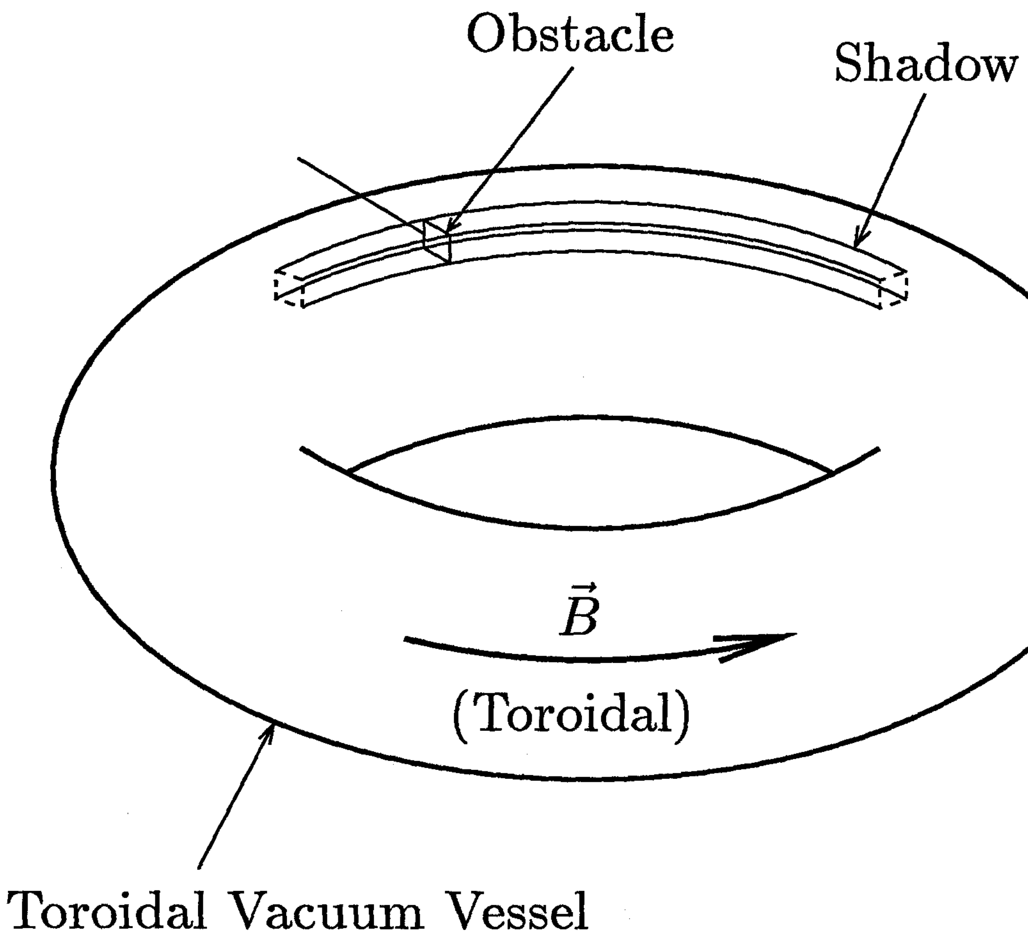

Figure 1.1: An obstacle and its shadow (region of reduced density) in a tokamak. The shadow is formed on both sides of the obstacle. Poloidal limiters or relatively large protective housings for diagnostic instruments will also have similar perturbing effects.

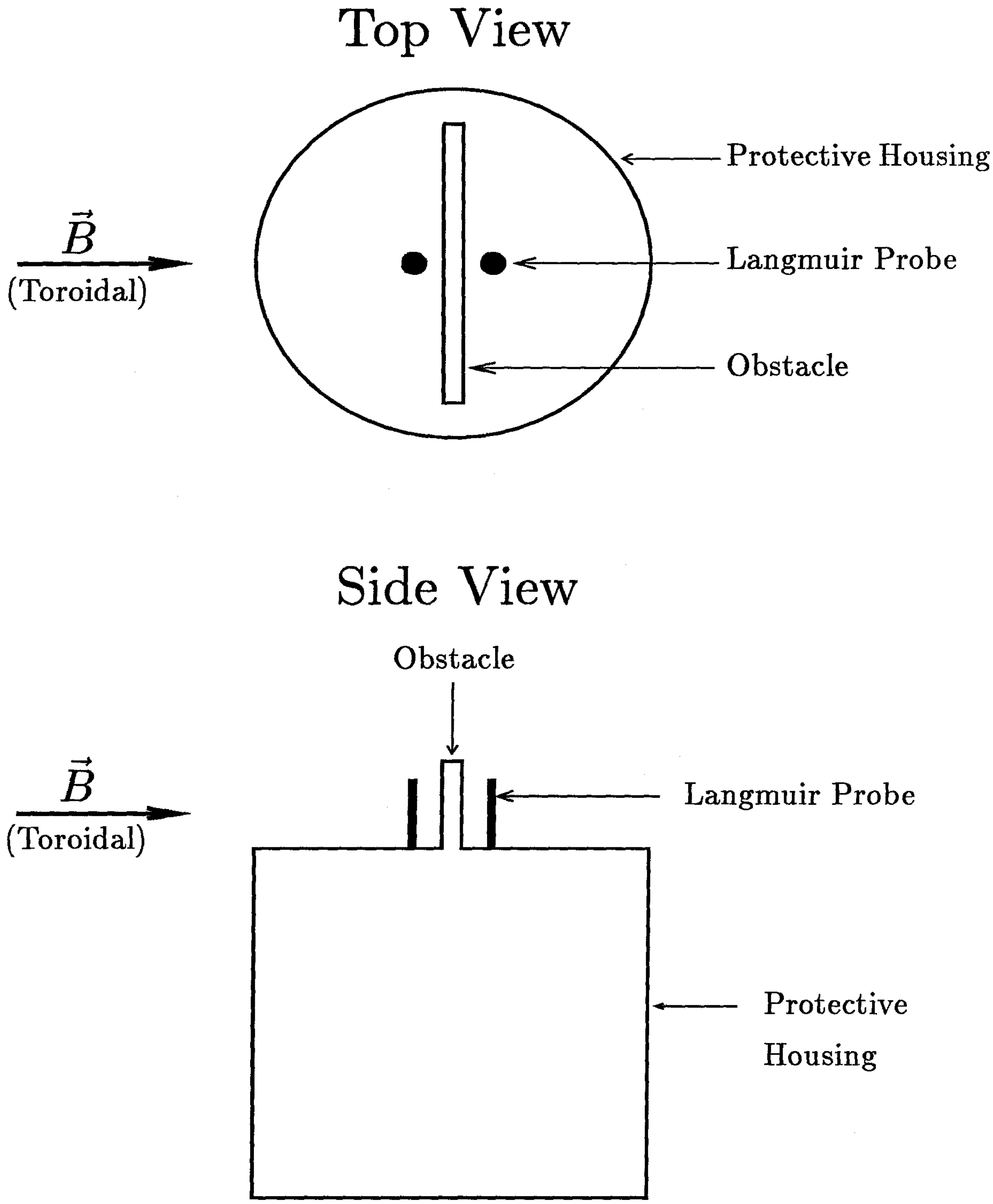

Figure 1.2: A Mach probe and its orientation with respect to the magnetic field. The upstream and downstream particle fluxes are separated by a mechanical obstruction. The probes on both sides of the obstacle are biased negatively so as to collect the ion saturation currents representative of the plasma flows in the shadows of the obstacle.

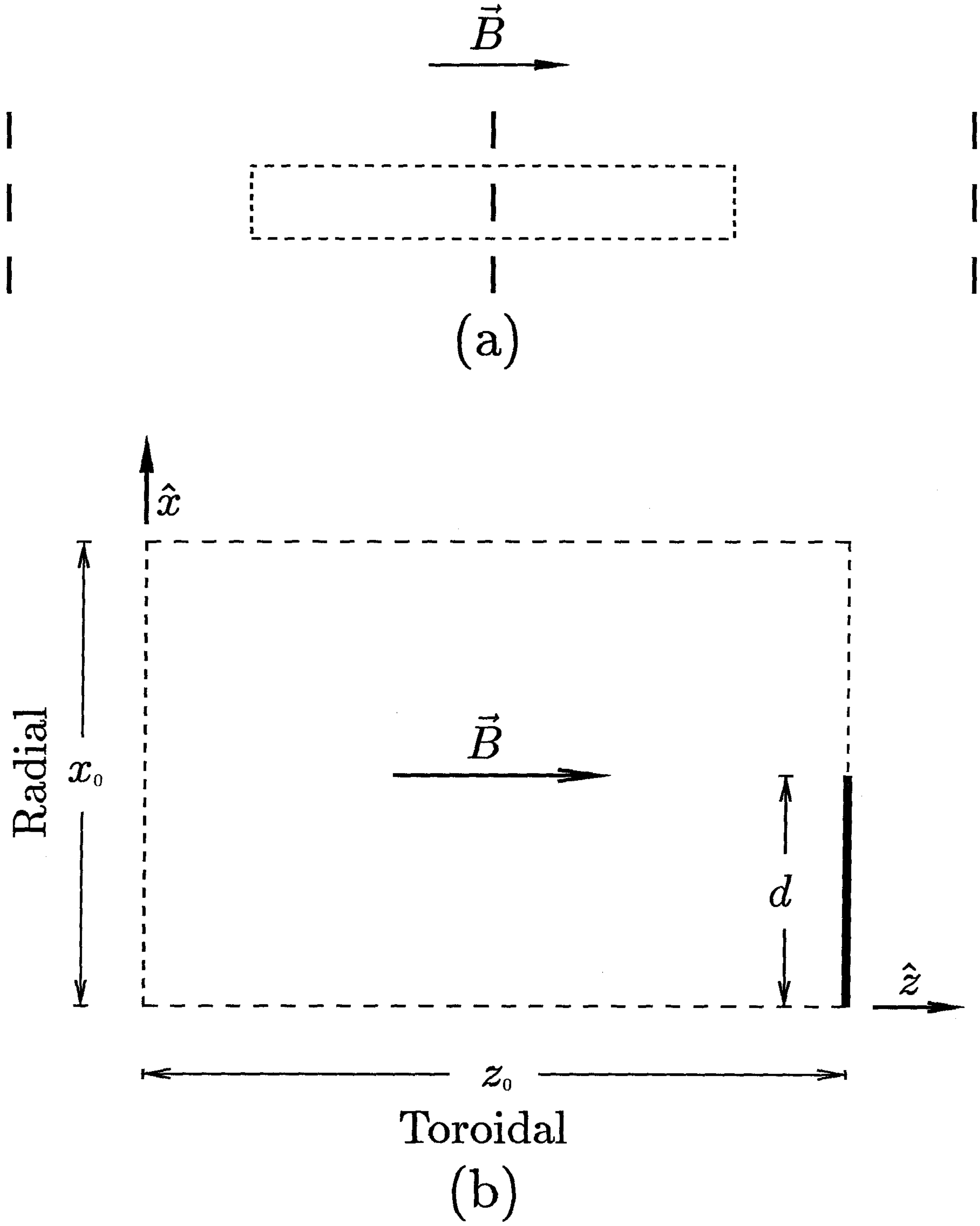

Figure 1.3: Idealized geometry consisting of a rectangular lattice of obstacles. The dashed box in (a) represents a unit cell of the lattice. Because of symmetry, the domain of interest is only one quarter of the unit cell, as shown in (b).

CHAPTER 2

A Derivation of the Two-Fluid Description of Plasmas with Particle, Momentum, and Energy Sources

In this chapter, we will first present the general two-fluid description of plasmas, which accounts for particle, momentum, and energy sources. We will then apply this two-fluid description to a *fully ionized*, *strongly magnetized* plasma consisting of only two species: electrons and singly charged ions.

2.1 Formulation

The derivation of the two-fluid description of plasmas from the Boltzmann equation has been given by many authors.[22-24] However, one of the main assumptions of this derivation is that there are no sources of particles, momentum, or energy. In order to appropriately account for particle, momentum, and energy sources, we shall modify the derivation of the macroscopic transport equations. Our effort is not an attempt to reiterate such a well-known derivation, but rather a modest attempt to incorporate particle, momentum, and energy sources into the transport equations.

The Boltzmann equation, which describes the motion of particles in phase space, can be written in the following form (see, for example, [22–24]):

$$\frac{\partial f_a}{\partial t} + \frac{\partial (v_\beta f_a)}{\partial x_\beta} + \frac{\partial}{\partial v_\beta}\left(\frac{F_{a\beta}}{m_a} f_a\right) = \left(\frac{\partial f_a}{\partial t}\right)_c \tag{2.1}$$

where m_a is the particle mass of species a. $f_a(\mathbf{r}, \mathbf{v}, t)$ is the distribution function of species a, i.e., $f_a(\mathbf{r}, \mathbf{v}, t)\, d^3\mathbf{r}\, d^3\mathbf{v}$ is the number of particles of species a in the volume element $d^3\mathbf{r}\, d^3\mathbf{v}$ located at the point $(\mathbf{r}, \mathbf{v})$ in phase space at time t. $\mathbf{F}_a$ is the net force exerted on a particle of species a at the position $(\mathbf{r}, \mathbf{v})$ in phase space. We shall limit our scope to the motion of charged particles in an electric field $\mathbf{E}$ and a magnetic field $\mathbf{B}$. If the particles of species a carry a charge e_a,

$$\mathbf{F}_a = e_a(\mathbf{E} + \mathbf{v}\times\mathbf{B}) \tag{2.2}$$

The R.H.S. of the Boltzmann equation represents the rate of change of the distribution function of species a due to collisions. In our model, we have chosen to write

$$\left(\frac{\partial f_a}{\partial t}\right)_c = C_{aa} + \sum_{b\neq a} C_{ab} + \gamma_a + \varepsilon_a \tag{2.3}$$

The first two terms of the R.H.S. of equation (2.3) represent collisions between charged particles. The first term, C_{aa}, is the self-collision term. It accounts for Coulomb collisions between charged particles of the same species. The quantity C_{ab} represents Coulomb collisions between charged particles of species a and those of species b. Thus, the second term, $\sum_{b\neq a} C_{ab}$, accounts for collisions between charged particles of species a with those of all other species. The Coulomb collisions represented by C_{aa} and $\sum_{b\neq a} C_{ab}$ are taken to be elastic collisions. We will assume that these Coulomb collisions do not convert particles of one species into another. Hence,

$$\int C_{ab}\, d^3\mathbf{v} = 0, \quad \forall \{a, b\} \tag{2.4}$$

Because the Coulomb collisions are assumed to be elastic, momentum and energy are conserved. As a result, the self-collision term C_{aa} will have the following properties:

$$\int m_a \mathbf{v} C_{aa}\, d^3\mathbf{v} = 0 \tag{2.5}$$

$$\int \frac{1}{2} m_a v^2 C_{aa}\, d^3\mathbf{v} = 0 \tag{2.6}$$

In any plasma, there is always a finite amount of background neutral gas. Although the kinetics of the neutral gas particles need not be taken into account if the neutral gas particles represent only a small fraction of the system, as is often the case with *fully ionized* tokamak fusion plasmas, we should account for their collisions with charged particles since these collisions do give rise to a finite rate of ionization. The term γ_a represents the rate of ionization due to such collisions. This term accounts for a source of particles. In general, this term also gives rise to a net input of momentum and energy since each particle introduced into the system carries with it some momentum and energy.

The term ε_a represents processes that introduce energy into the system without introducing significant amounts of particles and momentum to it, i.e.,

$$\int \varepsilon_a \, d^3\mathbf{v} = 0 \tag{2.7}$$

$$\int m_a \mathbf{v} \, \varepsilon_a \, d^3\mathbf{v} = 0 \tag{2.8}$$

Let us now define two convenient weighted-averages, namely,

$$\langle \psi \rangle_a = \frac{1}{n_a} \int \psi f_a \, d^3\mathbf{v}$$

$$\langle \psi \rangle_{Sa} = \frac{1}{S_{Pa}} \int \psi \gamma_a \, d^3\mathbf{v}$$

where

$$S_{Pa} = \int \gamma_a \, d^3\mathbf{v} \tag{2.9}$$

S_{Pa} is the net volumetric source of particles of species a since all other terms on the R.H.S. of equation (2.1) do not account for ionization, recombination, or dissociation. $\langle \psi \rangle_a$ and $\langle \psi \rangle_{Sa}$ are the weighted-average of the quantity ψ with respect to the particle distribution function f_a, and the source distribution function γ_a, respectively.

Our goal is to obtain the transport equations in terms of the macroscopic variables

$$n_a(\mathbf{r},t) = \int f_a(\mathbf{r},\mathbf{v},t) \, d^3\mathbf{v} \tag{2.10}$$

$$\mathbf{V}_a = \langle \mathbf{v} \rangle_a \tag{2.11}$$

$$T_a(\mathbf{r},t) = \left\langle \frac{1}{3} m_a |\mathbf{v} - \mathbf{V}_a|^2 \right\rangle_a \tag{2.12}$$

In general, for an arbitrary distribution function, one cannot close the set of macroscopic transport equations with a finite number of moments of the Bolztmann equation since the second term of the L.H.S. of equation (2.1) always introduces the $(n+1)^{st}$ moment into the equation for the n^{th} moment. The standard practice to circumvent this problem is to use only the first three moments of the Boltzmann equation, i.e., multiplying equation (2.1) by $\{1, m_a\mathbf{v}, \frac{1}{2}m_a v^2\}$ and integrating the resulting equations over velocity. Because of the second term of the L.H.S. of equation (2.1), the equation resulting from taking the second moment ($\left\langle \frac{1}{2}m_a v^2 \right\rangle_a$) contains the third moment ($\left\langle \frac{1}{2}m_a v^2\mathbf{v} \right\rangle_a$). In order to evaluate the third moment, it is assumed that each species is near thermodynamic equilibrium, i.e., its distribution function can only have small deviations from a Maxwellian distribution. The distribution function can then be expanded about a Maxwellian distribution, i.e.,

$$f_a(\mathbf{r},\mathbf{v},t) = n(\mathbf{r},t)\left(\frac{m_a}{2\pi T_a}\right)^{3/2} \exp\left(\frac{m_a|\mathbf{v}-\mathbf{V}_a|^2}{2T_a}\right)(1+\delta_a) \tag{2.13}$$

where δ_a is treated as a small perturbation ($\delta_a \ll 1$). The first order correction δ_a can be obtained explicitly by linearizing equation (2.1) using the above expression, given that the detail of the collision processes are known. The third moment can then be computed from the first-order corrected distribution function (see equation (2.13)) in terms of the first three moments. The set of transport equations can thus be closed with the first three moments of the Boltzmann equation. The reason we cannot properly close the set of transport equations with less than three moments is that it takes three moments to uniquely specify a Maxwellian distribution function: the zeroth moment specifies the distribution's volume in velocity space (particle density), the first moment specifies the distribution's mean value (mean drift velocity), and the third moment specifies the distribution's width (temperature). It should be kept in mind that this approach is no longer satisfactory if the species are not near thermodynamic equilibrium.

Taking the first three moments of the Boltzmann equation, using equations (2.3)–(2.12) and the fact that the distribution function vanishes sufficiently fast as

$|\mathbf{v}| \to \infty$, we obtain:

$$\frac{\partial n_a}{\partial t} + \boldsymbol{\nabla}\cdot (n_a \mathbf{V}_a) = S_{Pa} \tag{2.14}$$

$$\frac{\partial}{\partial t}(m_a n_a \mathbf{V}_a) + \boldsymbol{\nabla}\cdot (m_a n_a \langle \mathbf{v}\mathbf{v} \rangle_a) - e_a n_a(\mathbf{E} + \mathbf{V}_a \times \mathbf{B}) = S_{Pa} m_a \langle \mathbf{v} \rangle_{Sa} + \mathbf{R}_a \tag{2.15}$$

$$\frac{\partial}{\partial t}\left(\frac{1}{2} m_a n_a \left\langle v^2 \right\rangle_a\right) + \boldsymbol{\nabla}\cdot \left(\frac{1}{2} m_a n_a \left\langle v^2 \mathbf{v} \right\rangle_a\right) - e_a n_a \mathbf{E}\cdot \mathbf{V}_a = P_a \tag{2.16}$$

where

$$\mathbf{R}_a = \int m_a \mathbf{v} \sum_{b \neq a} C_{ab}\, d^3\mathbf{v}$$

$$P_a = \int \frac{1}{2} m_a v^2 \left(\sum_{b \neq a} C_{ab} + \gamma_a + \varepsilon_a \right) d^3\mathbf{v}$$

Equations (2.14)–(2.16) are termed the continuity, momentum, and energy equations, respectively.

It is convenient to write the velocity $\mathbf{v}$ as the sum of two components: $\mathbf{V}_a$, the mean drift velocity weighted with respect to the particle distribution function f_a, and $\mathbf{v}'$, the random velocity as seen by an observer moving with the mean drift velocity $\mathbf{V}_a$, i.e.,

$$\mathbf{v} = \mathbf{V}_a + \mathbf{v}'$$

It follows from the above equation that $\langle \mathbf{v}' \rangle_a = 0$. Hence,

$$\begin{aligned}
m_a n_a \langle \mathbf{v}\mathbf{v} \rangle_a &= m_a n_a \mathbf{V}_a \mathbf{V}_a + m_a n_a \langle \mathbf{v}'\mathbf{v}' \rangle_a \\
&= m_a n_a \mathbf{V}_a \mathbf{V}_a + n_a T_a \mathbf{I} + \boldsymbol{\pi}_a \\
\frac{1}{2} m_a n_a \left\langle v^2 \right\rangle_a &= \frac{1}{2} m_a n_a (V_a^2 + \left\langle v'^2 \right\rangle_a) \\
&= \frac{1}{2} m_a n_a V_a^2 + \frac{3}{2} n_a T_a \\
\frac{1}{2} m_a n_a \left\langle v^2 \mathbf{v} \right\rangle_a &= \frac{1}{2} m_a n_a (V_a^2 \mathbf{V}_a + \left\langle v'^2 \right\rangle_a \mathbf{V}_a + 2 \langle \mathbf{v}'\mathbf{v}' \rangle_a \cdot \mathbf{V}_a + \left\langle v'^2 \mathbf{v}' \right\rangle_a) \\
&= \left(\frac{1}{2} m_a n_a V_a^2 + \frac{5}{2} n_a T_a\right)\mathbf{V}_a + \mathbf{V}_a \cdot \boldsymbol{\pi}_a + \mathbf{q}_a
\end{aligned}$$

where

$$\boldsymbol{\pi}_a = m_a n_a \left\langle \mathbf{v}'\mathbf{v}' - \frac{1}{3}v'^2\mathbf{I} \right\rangle_a$$
$$= m_a n_a \langle \mathbf{v}'\mathbf{v}' \rangle_a - n_a T_a \mathbf{I}$$

$$\mathbf{q}_a = \frac{1}{2} m_a n_a \langle v'^2 \mathbf{v}' \rangle_a$$

Carrying out a similar transformation and making use of equation (2.4), one obtains:

$$\mathbf{R}_a = \int m_a \mathbf{v} \sum_{b\neq a} C_{ab}\, d^3\mathbf{v} = \int m_a \mathbf{v}' \sum_{b\neq a} C_{ab}\, d^3\mathbf{v}'$$

$$P_a = \int \frac{1}{2} m_a v^2 \Big(\sum_{b\neq a} C_{ab} + \gamma_a + \varepsilon_a \Big) d^3\mathbf{v}$$
$$= \mathbf{R}_a \cdot \mathbf{V}_a + \sum_{b\neq a} Q_{ab} + S_{Pa}\left[\frac{1}{2} m_a V_{Sa}^2 + \frac{3}{2} T_{Sa} \right] + S_{Ea}$$

where

$$\mathbf{V}_{Sa} = \langle \mathbf{v} \rangle_{Sa}$$
$$T_{Sa} = \left\langle \frac{1}{3} m_a |\mathbf{v} - \mathbf{V}_{Sa}|^2 \right\rangle_{Sa}$$
$$Q_{ab} = \int \frac{1}{2} m_a v'^2 C_{ab}\, d^3\mathbf{v}'$$
$$S_{Ea} = \int \frac{1}{2} m_a v^2 \varepsilon_a\, d^3\mathbf{v}$$

We need to relate the quantities $\sum_{b\neq a} Q_{ab}$, $\mathbf{q}_a$, $\boldsymbol{\pi}_a$, and $\mathbf{R}_a$ to the macroscopic variables n_a, $\mathbf{V}_a$, and T_a. These relations can be derived by the kinetic method previously outlined, i.e., by linearizing equation (2.1) using equation (2.13) and the fact that the self-collision term C_{aa} and the cross-collision term $\sum_{b\neq a} C_{ab}$ represent elastic Coulomb collisions. The distribution function f_a can then be corrected to first order. One can use the corrected distribution function to evaluate $\sum_{b\neq a} Q_{ab}$, $\mathbf{q}_a$, $\boldsymbol{\pi}_a$, and $\mathbf{R}_a$ (see, for example, [23]).

We will consider a simple system consisting of only two species of particles: electrons ($a = e$) and singly charged ions ($a = i$), i.e., $e_i = -e_e = e$; m and M will denote the electron and ion mass hereafter.

We will assume that our system is quasi-neutral, i.e., $n_e = n_i = n$. The reason is that any small deviation from quasi-neutrality will produce a very large electric field that tends to restore quasi-neutrality.

$\mathbf{R}_e$, the rate of change of the electron momentum due to electron-ion collisions, derived by kinetic methods,[23] can be written in the following form:

$$\mathbf{R}_e = mn\nu(\mathbf{V}_i - \mathbf{V}_e) \tag{2.17}$$

where ν is the electron-ion collision rate. The above result can be understood on the basis of elastic binary collisions. In an electron-ion collision, the momentum imparted on the ion has to be equal in magnitude and opposite in direction as that of the electron. However, because of mass disparity, the ion's velocity appears unchanged. A direct analogy to this situation is a ping-pong ball hitting a perfectly elastic brick wall. The momentum imparted on the electron is of the order of its initial momentum in the ion's inertial frame. The above equation gives the rate of change of the electron's momentum averaged over many such collisions. Of course, conservation of momentum demands that $\mathbf{R} = \mathbf{R}_i = -\mathbf{R}_e$. It is important to note that it is the electron-ion collision rate rather than the ion-ion or electron-electron collision rate that governs the rate of particle diffusion since collisions between two like-particles do not result in a displacement of the center of mass. τ_{ei}, the electron-ion collision time, has been computed by Braginskii[23]

$$\nu^{-1} = \tau_{ei} = \frac{3m^{1/2}T_e^{3/2}}{4(2\pi)^{1/2}\ln\Lambda e^4 Zn} \tag{2.18}$$

where $\ln\Lambda$ is the Coulomb logarithm,[22] the logarithm of the ratio of the maximum to minimum impact parameter. Z, the degree of ionization of the ions, is equal to 1 in our system.

The heat flux due to random motions $\mathbf{q}_a$, derived by kinetic methods,[23] can be written in the following form:

$$\mathbf{q}_a = -\kappa_{a\perp}\boldsymbol{\nabla}_\perp T_a - \kappa_{a_\parallel}\boldsymbol{\nabla}_\parallel T_a - \kappa_{a\wedge}\hat{z}\times\boldsymbol{\nabla}_\perp T_a \tag{2.19}$$

where $\hat{z}$ is the unit vector in the direction of $\mathbf{B}$. $\hat{z}$ shall retain the same meaning hereafter. Since the general expressions for the thermal conductivities are complicated, we shall focus our attention on *strongly magnetized* plasmas as this is often the case with tokamak fusion plasmas. A plasma is said to be strongly magnetized if $\omega_{ci}\tau_{ii} \gg 1$, where τ_{ii} and ω_{ci} are the ion-ion Coulomb collision time and the ion cyclotron frequency, respectively. τ_{ii} is related to τ_{ei} through the following relation:[23]

$$\frac{\tau_{ii}}{\tau_{ei}} \simeq \frac{1}{Z^2}\left(\frac{M}{m}\right)^{1/2}\left(\frac{T_i}{T_e}\right)^{3/2}$$

For a strongly magnetized plasma, the thermal conductivities are:[23]

$$\left.\begin{aligned}
\kappa_{e_\parallel} &= 3.16\frac{nT_e\tau_{ee}}{m}\\
\kappa_{e\perp} &= 4.66\frac{nT_e}{m\omega_{ce}^2\tau_{ee}}\\
\kappa_{e\wedge} &= \frac{5}{2}\frac{nT_e}{eB}\\
\kappa_{i_\parallel} &= 3.9\frac{nT_i\tau_{ii}}{M}\\
\kappa_{i\perp} &= 2\frac{nT_i}{M\omega_{ci}^2\tau_{ii}}\\
\kappa_{i\wedge} &= -\frac{5}{2}\frac{nT_i}{eB}
\end{aligned}\right\} \tag{2.20}$$

where $\tau_{ee} \sim \tau_{ei}$. The reason is that the relative velocity between an electron and an ion is of the same order as that between two electrons, and as a result, electron-electron collisions and electron-ion collisions occur at about the same rate.

Electron viscosity has a negligible contribution in the electron momentum equation because the electrons have a small mass. We will therefore neglect the contribution from electron viscosity.

Ion viscosity, derived by kinetic methods,[23] can be written in the following form:

$$\left.\begin{aligned}
\pi_{xx} &= -\frac{1}{2}\eta_0(W_{xx}+W_{yy}) - \frac{1}{2}\eta_1(W_{xx}-W_{yy}) - \eta_3 W_{xy}\\
\pi_{yy} &= -\frac{1}{2}\eta_0(W_{xx}+W_{yy}) + \frac{1}{2}\eta_1(W_{xx}-W_{yy}) + \eta_3 W_{xy}\\
\pi_{zz} &= -\eta_0 W_{zz}\\
\pi_{xy} &= -\eta_1 W_{xy} + \frac{1}{2}\eta_3(W_{xx}-W_{yy})\\
\pi_{xz} &= -\eta_2 W_{xz} - \eta_4 W_{yz}\\
\pi_{yz} &= -\eta_2 W_{yz} + \eta_4 W_{xz}\\
&\text{where}\\
W_{\alpha\beta} &= \frac{\partial V_{i\alpha}}{\partial x_\beta} + \frac{\partial V_{i\beta}}{\partial x_\alpha} - \frac{2}{3}\delta_{\alpha\beta}\nabla\cdot\mathbf{V}_i
\end{aligned}\right\}\qquad(2.21)$$

$\delta_{\alpha\beta}$ is the well-known Kronecker delta function. By definition (see equation (2.20)), $\boldsymbol{\pi}_a$ is a symmetric second rank tensor. The set of equations above, along with the appropriate set of coefficients ($\{\eta_k\}$, $k = 1, \ldots, 4$), completely defines ion viscosity. For a strongly magnetized plasma, the ion viscosity coefficients are:[23]

$$\left.\begin{aligned}
\eta_0 &= 0.96 n T_i \tau_{ii}\\
\eta_1 &= \frac{1}{4}\eta_2 = \frac{3}{10}\frac{nT_i}{\omega_{ci}^2\tau_{ii}}\\
\eta_3 &= \frac{1}{2}\eta_4 = \frac{1}{2}\frac{nT_i}{\omega_{ci}}
\end{aligned}\right\}\qquad(2.22)$$

Since the particle source S_{Pa} comes from ionization of neutral particles, electric charge balance requires that

$$S_{Pe} = Z S_{Pi} = S_P$$

with Z, the degree of ionization of the ions, being 1 in our physical system.

Q_{ie}, the amount of heat transferred from the electrons to the ions by collisions, is[23]

$$Q_{ie} = 3\frac{m}{M}\frac{n}{\tau_{ei}}(T_e - T_i) \qquad (2.23)$$

Q_{ie}, the amount of heat transferred from the ions to the electrons by collisions, is[23]

$$Q_{ei} = \mathbf{R}\cdot(\mathbf{V}_i - \mathbf{V}_e) - Q_{ie} \qquad (2.24)$$

Rewriting equations (2.14)–(2.16), we obtain:

$$\nabla\cdot\mathbf{J}=0 \tag{2.25}$$

$$\frac{\partial n}{\partial t}+\nabla\cdot(n\mathbf{V}_i)=S_P \tag{2.26}$$

$$\frac{\partial}{\partial t}(Mn\mathbf{V}_i)+\nabla\cdot(Mn\mathbf{V}_i\mathbf{V}_i)=en(\mathbf{E}+\mathbf{V}_i\times\mathbf{B})-\nabla(nT_i)-\nabla\cdot\boldsymbol{\pi}_i+S_PM\mathbf{V}_{Si}+\mathbf{R} \tag{2.27}$$

$$\frac{\partial}{\partial t}(mn\mathbf{V}_e)+\nabla\cdot(mn\mathbf{V}_e\mathbf{V}_e)=-en(\mathbf{E}+\mathbf{V}_e\times\mathbf{B})-\nabla(nT_e)+S_Pm\mathbf{V}_{Se}-\mathbf{R} \tag{2.28}$$

$$\begin{aligned}\frac{\partial}{\partial t}\left[\frac{1}{2}MnV_i^2+\frac{3}{2}nT_i\right]+\nabla\cdot\left[(\frac{1}{2}MnV_i^2+\frac{5}{2}nT_i)\mathbf{V}_i\right]&=-\nabla\cdot(\mathbf{V}_i\cdot\boldsymbol{\pi}_i)+(en\mathbf{E}+\mathbf{R})\cdot\mathbf{V}_i\\&\quad-\nabla\cdot\mathbf{q}_i+S_P\left[\frac{1}{2}MV_{Si}^2+\frac{3}{2}T_{Si}\right]\\&\quad+S_{Ei}+Q_{ie}\end{aligned} \tag{2.29}$$

$$\begin{aligned}\frac{\partial}{\partial t}\left[\frac{1}{2}mnV_e^2+\frac{3}{2}nT_e\right]+\nabla\cdot\left[(\frac{1}{2}mnV_e^2+\frac{5}{2}nT_e)\mathbf{V}_e\right]&=-(en\mathbf{E}+\mathbf{R})\cdot\mathbf{V}_e-\nabla\cdot\mathbf{q}_e\\&\quad+S_P\left[\frac{1}{2}mV_{Se}^2+\frac{3}{2}T_{Se}\right]+S_{Ee}\\&\quad+Q_{ei}\end{aligned} \tag{2.30}$$

where $\mathbf{R}$, $\boldsymbol{\pi}_i$, $\mathbf{q}_i$, $\mathbf{q}_e$, Q_{ie}, and Q_{ei} are given by equations (2.17)-(2.24). Equations (2.25)–(2.30) form a closed set of valid transport equations, provided that the assumptions we made are satisfied by the physical system. These equations are, however, not geometry-specific.

2.2 Application of Transport Equations to Steady-Flow Problems

We would like to use the transport equations in the context of a two-dimensional model. Figure 2.1 illustrates the geometry of our system. The external magnetic field is in the $\hat{z}$ direction. x_0 and z_0 are the physical extents of the plasma column. The obstacle is modeled as a two-dimensional strip of width $2d$, extending to infinity in the y direction, i.e., y is the ignorable coordinate. We would like to study the behaviour of the macroscopic quantities such as the plasma density, velocity field, and temperature in the presence of one or more such obstacles.

An electrostatic sheath, a thin layer of non-neutral, electron-depleted plasma whose thickness is of the order of the Debye shielding distance λ_D, is formed on the surface of an obstacle when immersed in a plasma. The ions are accelerated to a speed of at least c_s, the ion acoustic speed, upon entering the electrostatic sheath. This is the Bohm sheath criterion, first shown by Bohm for cold ions.[14] Extensions of this work by others[15–20] show that this condition is also valid for warm ions. A simple physical explanation for this effect can be stated as follows. Consider a hypothetical situation where an obstacle is introduced into a plasma that is in equilibrium and has no mean flow. The electrons, being lighter and faster, arrive at the obstacle faster and in greater numbers than the ions. Since there is a finite probability for the electrons to be captured by the obstacle, some of the electrons that arrive at the obstacle will stick on the surface. As a result, the obstacle, initially neutral, is negatively charged and therefore accelerates ions toward it. The electrons, however, are repelled by the obstacle. Only those electrons with a kinetic energy greater than the height of the obstacle's electrostatic potential energy barrier can impinge on its surface. In fact, since the electrons impinge on the surface of the obstacle at such a high rate, only a small fraction of the electrons can be allowed to reach the obstacle if a steady-state is to be reached. In steady-state, the obstacle's potential barrier adjusts itself in such a manner that the electrons and ions arrive at the obstacle at equal rates, i.e., no net current is collected at the wall. An ion accelerated through such an electrostatic potential will obtain a speed of at least c_s upon entering the sheath. Appendix A is a simple one-dimensional model of electrostatic sheaths with warm ions. This model is a variation of the one-dimensional model of electrostatic sheaths with cold ions proposed by Chen.[17] Although more rigorous models have been presented in the literature,[15–20] our simple model is much easier to understand, and contains the essential physics of sheath formations.

It was shown by Self[16] that the transition from a quasineutral plasma to a non-neutral sheath is a smooth transition. The division between the sheath and the main plasma is therefore an artificial one. However, when the Debye shielding distance is small, the electrostatic potential possesses two markedly different scale lengths. The plasma can then be well approximated by two regions: one where the plasma is quasineutral, and one whose thickness is of the order of the Debye shielding distance λ_D where the plasma is electron-depleted. It is in this limit that the concept of an electrostatic sheath is a useful one.

We will assume that the Debye shielding distance is small in our physical system. This is often a good assumption in most tokamak fusion plasmas. In principle, our transport equations, used in conjunction with Poisson's equation, are adequate for modelling the plasma including the sheath region. However, since the sheath has a very small scale length, we have to solve an elliptic PDE (Poisson's equation) on an extremely fine grid at every iteration. This is computationally difficult and unnecessary. We will therefore assume that the plasma is quasineutral and exclude the sheath region from our domain of interest. Since the sheath is assumed to be thin in our physical system, we will define the sheath edge to be the location where the ions acquire a speed equal to the local ion acoustic speed (the ion's velocity component parallel to the external magnetic field $\mathbf{B}$ is taken to be the ion acoustic speed at the obstacle).

As particles are being removed at the obstacle, momentum and energy are also being removed since each particle carries with it some momentum and energy. The particle, momentum, and energy fluxes removed at the obstacle are replenished by their respective volumetric sources in the macroscopic transport equations. A steady state is achieved when there is an exact balance of particle, momentum, and energy. It is this steady-state collection of particles, momentum, and energy that we would like to investigate.

In steady-state, the electric field can be expressed as the gradient of an electrostatic potential, i.e.,

$$\mathbf{E} = -\boldsymbol{\nabla}\phi \tag{2.31}$$

The externally applied magnetic field $\mathbf{B}$ is assumed to be static and uniform. $\delta\mathbf{B}$, the magnetic field generated by the plasma current, is assumed to be negligible compared to $\mathbf{B}$. This is a good approximation in most tokamak fusion plasmas.

Due to the lack of knowledge of details of the ionization process, $\mathbf{V}_{Si}$ and T_{Si} are unknown quantities. However, assuming that the exact treatment of these quantities will not affect the solution significantly, we will therefore assume that the source ions are born with the mean velocity and temperature of the bulk ions, i.e.,

$$\mathbf{V}_{Si} = \mathbf{V}_i \tag{2.32}$$

$$T_{Si} = T_i \tag{2.33}$$

Because the ratio of electron to ion mass is small, several simplifications can be made to the transport equations. First of all, we can assume that the electrons are isothermal because of their high thermal conductivities in the direction parallel to $\mathbf{B}$. Only a small parallel gradient of T_e is necessary to cause a finite amount of heat flux required for energy balance. Second, both the L.H.S. (electron inertia) and the third term of the R.H.S. of equation (2.28) (electron momentum source) can be neglected.

In summary, the transport equations (2.25)-(2.30), when applied to our steady-flow problems, can be reduced to the following form:

$$\boldsymbol{\nabla}\cdot\mathbf{J} = 0 \tag{2.34}$$

$$\boldsymbol{\nabla}\cdot(n\mathbf{V}_i) = S_P \tag{2.35}$$

$$\boldsymbol{\nabla}\cdot(Mn\mathbf{V}_i\mathbf{V}_i) = en(-\boldsymbol{\nabla}\phi + \mathbf{V}_i\times\mathbf{B}) - \boldsymbol{\nabla}(nT_i) - \boldsymbol{\nabla}\cdot\boldsymbol{\pi}_i + S_P M\mathbf{V}_i + \mathbf{R} \tag{2.36}$$

$$0 = -en(-\boldsymbol{\nabla}\phi + \mathbf{V}_e\times\mathbf{B}) - T_{e0}\boldsymbol{\nabla}n - \mathbf{R} \tag{2.37}$$

$$\begin{aligned}\boldsymbol{\nabla}\cdot\left[(\frac{1}{2}MnV_i^2 + \frac{5}{2}nT_i)\mathbf{V}_i\right] &= -\boldsymbol{\nabla}\cdot(\mathbf{V}_i\cdot\boldsymbol{\pi}_i) + (en\mathbf{E} + \mathbf{R})\cdot\mathbf{V}_i - \boldsymbol{\nabla}\cdot\mathbf{q}_i \\ &\quad + S_P\left[\frac{1}{2}MV_i^2 + \frac{3}{2}T_i\right] + S_{Ei} + Q_{ie}\end{aligned} \tag{2.38}$$

Equations (2.34)-(2.38) are the transport equations in the conservative form. Equation (2.37) is often called the generalized Ohm's law. As a reminder, the above set of transport equations can be closed with equations (2.17)-(2.24).

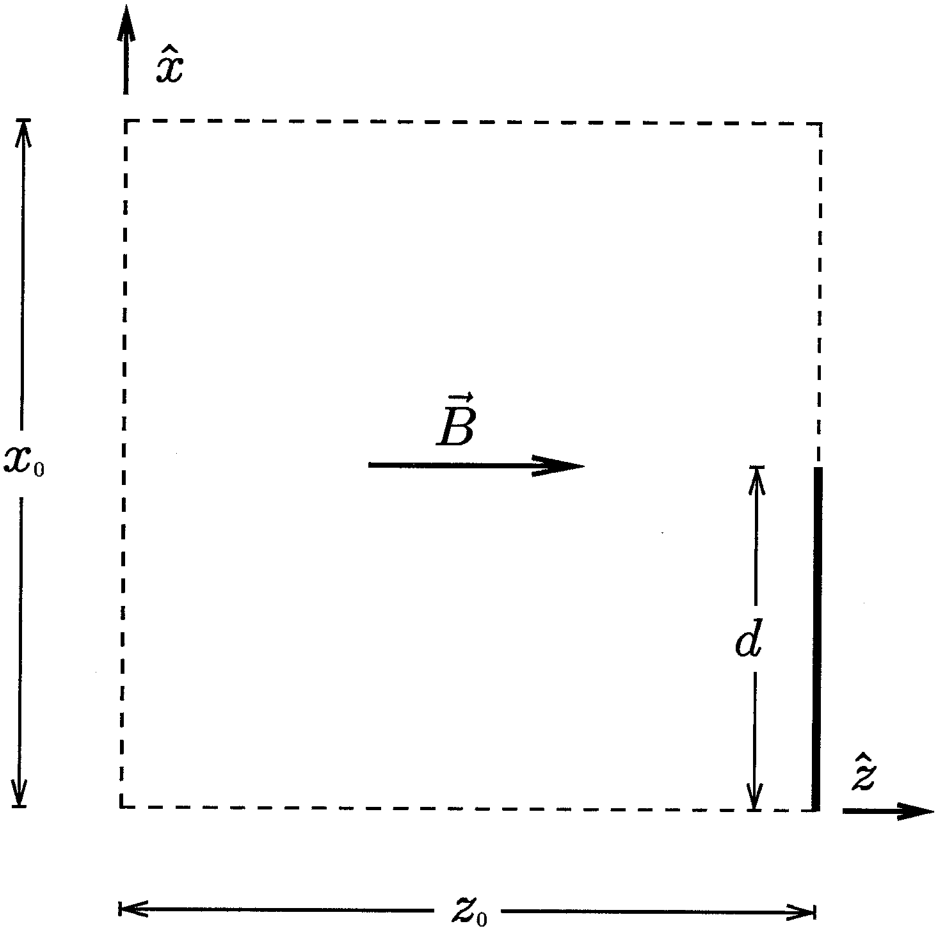

Figure 2.1: Geometry of physical system in the absence of an ambient flow. The dashed lines represent the periodic boundary. The thick solid line represents the obstacle. The magnetic field **B** is assumed to be uniform, and is in the z-direction. The two-dimensional obstacle extends to infinity in the y-direction, and has a width of $2d$.

CHAPTER 3

Plasma Collection by an Obstacle with No Ambient Plasma Flow in the Absence of Anomalous Transport

In this chapter, we will perform a detailed numerical study of plasma collection by a two-dimensional insulating obstacle in the absence of an ambient plasma flow, using the *classical* transport equations derived in chapter 2. Our goal is to construct the simplest model possible that contains the essential physics. The physical effects to be investigated in this chapter are: (1) parallel electron-ion collisional drag, (2) ion viscosity, (3) ion viscous heating near the limiter, (4) localization of particle sources, and (5) density-dependent particle transport coefficient. We will study each effect separately to assess its relative importance. Slab geometry is studied since the obstacle is assumed to be a two-dimensional strip. The results for slab geometry should provide the correct qualitative behaviour of the macroscopic variables. Extension of this model to cylindrical geometry is straightforward.

3.1 Typical Tokamak Plasma Parameters

In this section, we will present typical plasma parameters found in the edge region of *large tokamaks.* The edge region of the tokamak is often referred to as the *scrape-off layer* (SOL). The plasma in this region is generally cooler and more tenuous than the core plasma. Because the plasma in the SOL is relatively cool, probes and material objects can be inserted without releasing large amounts of impurity ions which, in practice, can disrupt the plasma. Consequently, the plasma-probe interaction is modeled only in the SOL.

3.1.1 Basic Plasma Parameters

$$T_e \sim T_i \sim 30\,\mathrm{eV}$$

$$n_e \simeq n_i \sim 10^{13}\,\mathrm{cm}^{-3}$$

$$B \sim 5\,\mathrm{T}$$

For a hydrogen plasma (electrons and protons), we have:

$$v_{th,i} = \sqrt{T_i/M} \sim 5\times10^6\,\mathrm{cm/s}$$

$$v_{th,e} = \sqrt{T_e/m} \sim 2\times10^8\,\mathrm{cm/s}$$

$$c_s = \sqrt{\frac{T_e+T_i}{M}} \sim 8\times10^6\,\mathrm{cm/s}$$

$$\omega_{ci} = eB/M \sim 5\times10^8\,\mathrm{sec}^{-1}$$

$$\omega_{ce} = eB/m \sim 10^{12}\,\mathrm{sec}^{-1}$$

$$\rho_i = v_{th,i}/\omega_{ci} \sim 1\times10^{-2}\,\mathrm{cm}$$

$$\rho_e = v_{th,e}/\omega_{ce} \sim 2\times10^{-4}\,\mathrm{cm}$$

$$\lambda_D = \sqrt{\frac{T_e}{4\pi n e^2}} \sim 1\times10^{-3}\,\mathrm{cm}$$

For a wide range of plasma temperature and plasma density, $\ln\Lambda$ (the Coulomb logarithm) is approximately 10. The collision times and the collision mean-free-paths can be computed from the above plasma parameters:

$$\tau_{ii} = \frac{3M^{1/2}T_i^{3/2}}{4(2\pi)^{1/2}\ln\Lambda e^4 Z^3 n} \sim 3\times10^{-5}\,\mathrm{sec}$$

$$\tau_{ei} = \frac{3m^{1/2}T_e^{3/2}}{4(2\pi)^{1/2}\ln\Lambda e^4 Z n} \sim 8\times10^{-7}\,\mathrm{sec}$$

$$\tau_{ee} \sim \tau_{ei} \sim 8\times10^{-7}\,\mathrm{sec}$$

$$\lambda_{ei} = v_{th,e}\tau_{ei} \sim 2\times10^2\,\mathrm{cm}$$

$$\lambda_{ii} = v_{th,i}\tau_{ii} \sim 2\times10^2\,\mathrm{cm}$$

$$\lambda_{ee} = v_{th,e}\tau_{ee} \sim 2\times10^2\,\mathrm{cm}$$

$$\omega_{ci}\tau_{ii} \sim 2\times10^4$$

$$\omega_{ce}\tau_{ee} \sim 8\times10^5$$

3.1.2 Classical Transport Coefficients

$$\begin{aligned}
D_\perp &= \frac{c_s^2}{\omega_{ce}\omega_{ci}\tau_{ei}} \sim \frac{\rho_e^2}{\tau_{ei}} \sim 0.2\,\mathrm{cm}^2/\mathrm{s} \\
\frac{\eta_{\parallel i}}{nMD_\perp} &= \frac{\kappa_{\parallel i}}{nD_\perp} = \left(\frac{T_i}{T_e+T_i}\right)(\omega_{ce}\tau_{ei})(\omega_{ci}\tau_{ii}) \sim 8\times 10^9 \\
\frac{\eta_{\perp i}}{nMD_\perp} &= \frac{\kappa_{\perp i}}{nD_\perp} = \left(\frac{T_i}{T_e+T_i}\right)\left(\frac{\omega_{ce}\tau_{ei}}{\omega_{ci}\tau_{ii}}\right) \sim 20 \\
\frac{\eta_{\parallel e}}{\eta_{\parallel i}} &= \frac{T_e}{T_i}\frac{\tau_{ee}}{\tau_{ii}} \sim 2\times 10^{-2} \\
\frac{\eta_{\perp e}}{\eta_{\perp i}} &= \frac{T_e}{T_i}\frac{\tau_{ee}}{\tau_{ii}}\left(\frac{\omega_{ci}\tau_{ii}}{\omega_{ce}\tau_{ee}}\right) \sim 10^{-5} \\
\frac{\kappa_{\parallel e}}{\kappa_{\parallel i}} &= \frac{M}{m}\frac{T_e}{T_i}\frac{\tau_{ee}}{\tau_{ii}} \sim 40 \\
\frac{\kappa_{\perp e}}{\kappa_{\perp i}} &= \frac{M}{m}\frac{T_e}{T_i}\frac{\tau_{ee}}{\tau_{ii}}\left(\frac{\omega_{ci}\tau_{ii}}{\omega_{ce}\tau_{ee}}\right)^2 \sim 2\times 10^{-2}
\end{aligned}$$

3.2 Isothermal, Inviscid Model

In this section, we will study particle collection by a single insulating obstacle, using the simplest model. Figure 3.1 illustrates the geometry of our model. The obstacle is assumed to be a two-dimensional strip of width $2d$, extending to infinity in the y direction, i.e., y is the ignorable coordinate. Our domain of interest is $0 \le x \le x_0$ and $0 \le z \le z_0$.

3.2.1 Basic Assumptions and Formulation

Physically, the ions are expected to cool as they approach the obstacle, except for the region where viscous heating is important (see section 3.7). However, for simplicity, we will neglect the ion energy equation and assume that the ions are isothermal. The validity of this assumption will be discussed in more detail in a later section.

Ion viscosity represents the diffusion of ion momentum from one region of the plasma to another. It is caused by deviations of the ion distribution function from a Maxwellian distribution. If the ions are in perfect thermodynamic equilibrium, i.e., the ion distribution function is exactly Maxwellian, ion viscosity will vanish. In this simple model, we will assume that the ions are in thermodynamic equilibrium and neglect ion viscosity.

In a magnetized plasma, individual charged particles (electrons and ions) gyrate about fixed magnetic field lines. In the absence of interspecies collisions, charged particles cannot diffuse across the field lines. The perpendicular electron-ion collisional drag $\mathbf{R}_\perp$ is the only mechanism causing particle diffusion across the field lines. Without collisions, the electrons and ions simply drift in the y direction (y is the ignorable coordinate), causing no particle diffusion across the field lines. The drift velocity in this case is the sum of the $\mathbf{E}\times\mathbf{B}$ and the diamagnetic drifts. Since particle diffusion across the field lines is caused by electron-ion collisions, these collisions actually enhance the perpendicular ion motion.

The parallel electron-ion collisional drag $\mathbf{R}_\parallel$ does not have the same role in the parallel ion motion as $\mathbf{R}_\perp$ does in the cross-field ion motion. The basic difference is that the ion motion across the field lines is diffusive, whereas the ion motion along the field lines is a free-streaming motion. Since the parallel ion motion is a free-streaming motion, the electron-ion collisional drag along the field lines hinders the motion. Conceptually, the term $\mathbf{R}_\parallel$ is not very important since its only effect is to compete against the electric field and the ion pressure gradient, which are the principal driving forces in the parallel direction. Therefore, we will neglect it in this simple model. A more elaborate discussion of this term will be offered in a later section.

Detailed balance requires particles to be replenished as they are removed at the obstacle. Otherwise, all particles in the plasma column will be removed after some time, resulting in a trivial steady state where the plasma density is zero everywhere. Assuming that the exact treatment of the particle source will not affect the solution significantly (this assumption will be justified a posteriori), we will take S_P to be spatially uniform.

The electron-ion collision rate ν (see equation (2.18)) is proportional to the particle density n. However, we will take ν to be independent of n in this model. Although this model might not be quantitatively correct, it should provide us with the correct qualitative features of the macroscopic variables.

With the assumptions made in this simple model, equations (2.34)–(2.38) can be reduced to the following form:

$$\nabla\cdot\mathbf{J}=0 \tag{3.1}$$

$$\nabla\cdot(n\mathbf{V}_i)=S_0 \tag{3.2}$$

$$\nabla\cdot(Mn\mathbf{V}_i\mathbf{V}_i)=en(-\nabla\phi+\mathbf{V}_i\times\mathbf{B})-T_{i0}\nabla n+S_0M\mathbf{V}_i+mn\nu_0(\mathbf{V}_e-\mathbf{V}_i)_\perp \tag{3.3}$$

$$0=-en(-\nabla\phi+\mathbf{V}_e\times\mathbf{B})-T_{e0}\nabla n-mn\nu_0(\mathbf{V}_e-\mathbf{V}_i)_\perp \tag{3.4}$$

We would like to extract the physical quantities n (plasma density) and $\mathbf{V}_i$ (ion fluid velocity) from the above equations. This can be achieved by manipulating the generalized Ohm's law (equation (3.4)) to obtain both the electrostatic potential ϕ and the electron fluid velocity $\mathbf{V}_e$ in terms of n and $\mathbf{V}_i$. These expressions for ϕ and $\mathbf{V}_e$ can be substituted into equation (3.3). The resulting equation and the continuity equation (3.2) then form a closed set of transport equations for our model.

Integrating the z-component of equation (3.4) with respect to z, and then differentiating the resulting equation with respect to x, one obtains:

$$e\frac{\partial\phi}{\partial x}-\frac{T_{e0}}{n}\frac{\partial n}{\partial x}=e\frac{d\phi_0}{dx}-\frac{T_{e0}}{n_0}\frac{dn_0}{dx}=f(x) \tag{3.5}$$

where $\phi_0(x)=\phi(x,0)$ and $n_0(x)=n(x,0)$.

The perpendicular component of the generalized Ohm's law can be rewritten in the following form:

$$0=-en(-\nabla_\perp\phi+\mathbf{V}_{i\perp}\times\mathbf{B})+\mathbf{J}_\perp\times\mathbf{B}-T_{e0}\nabla_\perp n+\frac{m\nu_0}{e}\mathbf{J}_\perp$$

Solving for $\mathbf{J}_\perp$ from the above expression, using equation (3.5) and the fact that y is the ignorable coordinate, one obtains:

$$\mathbf{J}_\perp = \frac{ne}{1+\alpha^2}(\mathbf{V}_{i\perp} + \alpha\mathbf{V}_{i\perp}\times\hat{z}) - \frac{n}{B(1+\alpha^2)}f(x)(\alpha\hat{x}+\hat{y}) \tag{3.6}$$

where $\alpha = m\nu_0/eB$.

Because the obstacle in this model is assumed to be an insulating one, the local current density collected on the surface of the obstacle can be taken to be identically zero. From symmetry, the component of the current density normal to all other boundaries is required to vanish. As a result, J_x must satisfy the following constraint for all values of x:

$$\int_0^{z_0} J_x(x,z)dz = 0$$

Substituting the x-component of equation (3.6) into the expression above, one obtains:

$$f(x) = \frac{eB}{\alpha}\int_0^{z_0} n(V_{ix} + \alpha V_{iy})dz \Big/ \int_0^{z_0} ndz \tag{3.7}$$

Since we would like to investigate the problem of plasma collection by a single obstacle, the quantities x_0 and z_0 will be chosen sufficiently large that the region far from the obstacle is unperturbed. For such large values of z_0, $f(x)$ is negligible, i.e., equation (3.6) reduces to:

$$\mathbf{J}_\perp = \frac{ne}{1+\alpha^2}(\mathbf{V}_{i\perp} + \alpha\mathbf{V}_{i\perp}\times\hat{z})$$

Since we have eliminated the electron fluid velocity from the transport equations, we can now let $\mathbf{v}$ denote the ion fluid velocity without causing any confusion. With this new notation, the transport equations for our model become:

$$\nabla\cdot(n\mathbf{v}) = S_0 \tag{3.8}$$

$$\nabla\cdot(Mn\mathbf{v}\mathbf{v}) = \frac{neB}{1+\alpha^2}(\mathbf{v}_\perp\times\hat{z} - \alpha\mathbf{v}_\perp) - (T_{i0}+T_{e0})\nabla n + S_0 M\mathbf{v} \tag{3.9}$$

where $\alpha = m\nu_0/eB$.

In general, the macroscopic transport equations are appropriate for describing the fluid motion of the plasma when the ion Larmor radius is small compared to the width of the obstacle, i.e., $c_s/\omega_{ci} \ll d$. Otherwise, the individual particle orbits have to be separately accounted for, and the approach of averaging over particle orbits is no longer appropriate.

The tip of the obstacle, i.e., the point $(x = d, z = z_0)$, proves to be a problem for the following reason. From symmetry, v_z, the ion's velocity component parallel to the magnetic field $\mathbf{B}$, is required to be zero above the tip $(d < x \le x_0,\ z = z_0)$. v_z, on the other hand, is taken to be $\pm c_s$ below the tip $(0 \le x < d,\ z = z_0)$ according to the Bohm sheath criterion. The behaviour of v_z in the neigbourhood of the tip is not well understood. At this time, we do not have a satisfactory remedy for this problem. Instead, in order to assess the importance of the exact treatment of the tip, we will study two cases where (1) v_z is taken to be uniform below the tip, i.e.,

$$v_z = \pm c_s, \quad 0 \le x < d,\ z = z_0$$

and (2) v_z is taken to have a sharp, but continuous, profile below the tip, e.g.,

$$v_z = \pm c_s \left[1 - \left(\frac{x}{d}\right)^{16}\right], \quad 0 \le x < d,\ z = z_0$$

In both cases, v_z is taken to be zero on and above the tip $(0 \le x \le d,\ z = z_0)$.

3.2.2 Analytical Results

Three essential features of the model can be extracted analytically from the transport equations (3.8)–(3.9).

From symmetry, the normal component of the ion fluid velocity and that of the density gradient on the bottom boundary (the line $x = 0$) are zero. The z-component of the ion momentum equation (equation (3.9)) on this boundary becomes:

$$Mnv_z\frac{\partial v_z}{\partial z} = -(T_{i0} + T_{e0})\frac{\partial n}{\partial z}$$

Integrating the above equation with respect to z, using the fact that v_z vanishes on the left boundary (the line $z = 0$) due to symmetry, one obtains:

$$n(x=0,z) = n(0,0)\exp\left(-\frac{1}{2}\frac{v_z^2}{c_s^2} \right)$$

where $c_s = \sqrt{(T_{i0} + T_{e0})/M}$. Since v_z is taken to be c_s on the surface of the obstacle (Bohm's sheath criterion), we have:

$$n(0,z_0) = n(0,0)e^{-1/2} \simeq 0.61n(0,0) \tag{3.10}$$

Thus, one important feature of the solution to the transport equations is that the plasma density on the obstacle is always about 40% lower than the unperturbed plasma density, independent of ν_0, S_0, B, T_{i0}, or T_{e0}. This result is also valid independent of the exact treatment of the particle source term, e.g., it is valid even if the particle source is proportional to n instead of being spatially uniform.

Particle balance demands that the rate of particle production be equal to the rate at which particles are removed at the obstacle. Thus, using the assumption that the particle source is spatially uniform, one obtains:

$$S_0 x_0 z_0 = \int_0^d n(x,z_0)v_z(x,z_0)dx$$

Using equation (3.10) and the Bohm's sheath criterion, the above equation yields:

$$n_\infty \simeq n(0,0) \simeq e^{1/2}\frac{S_0 x_0 z_0}{c_s d} \tag{3.11}$$

The above equation shows how the unperturbed plasma density is related to the rate of particle production. Furthermore, it can be easily shown, by scaling the transport equations (3.8)–(3.9) with S_0, that the plasma density profile $n(x,z)$ scales linearly with S_0, whereas the ion fluid velocity $\mathbf{v}$ is independent of S_0. As a result, it is not important which value one uses for S_0 as long as $S_0 > 0$.

An obstacle inserted into a magnetized plasma will cast a *shadow* along the magnetic field lines. The particle collection length of such an obstacle is a measure of the length of its shadow. Often a qualitative argument based on particle balance[25] is used to show that a floating obstacle inserted into a magnetized plasma will have a particle collection length of the order $L_{\parallel} \sim d^2 c_s / D_{\perp}$. This result is obtained by equating the perpendicular particle flux diffusing into the shadow which, presumably, extends into the plasma by a distance $L_{\parallel}$ from the obstacle, to the rate at which particles are removed at the obstacle. We can show, from the transport equations (3.8)–(3.9), that this is in fact valid, provided that the particle source is spatially uniform. Let us assume that the perpendicular convective term $Mn(\mathbf{v} \cdot \boldsymbol{\nabla})\mathbf{v}_{\perp}$ is small, and can be neglected. The conditions under which this assumption is valid will be presented a posteriori. With this assumption, the perpendicular component of the ion momentum equation (equation (3.9)) becomes:

$$0 = \frac{neB}{1+\alpha^2}(\mathbf{v}_{\perp} \times \hat{z} - \alpha \mathbf{v}_{\perp}) - (T_{i0} + T_{e0}) \boldsymbol{\nabla}_{\perp} n$$

Solving for the cross-field particle flux $n\mathbf{v}_{\perp}$ from the above equation, one obtains:

$$\begin{aligned} n\mathbf{v}_{\perp} &= \frac{c_s^2}{\omega_{ci}}(-\alpha \boldsymbol{\nabla}_{\perp} n + \hat{z} \times \boldsymbol{\nabla}_{\perp} n) \\ &= -D_{\perp} \boldsymbol{\nabla}_{\perp} n + \frac{c_s^2}{\omega_{ci}} \hat{z} \times \boldsymbol{\nabla}_{\perp} n \end{aligned} \tag{3.12}$$

where

$$D_{\perp} = \frac{c_s^2 \alpha}{\omega_{ci}} = \frac{c_s^2 \nu_0}{\omega_{ce} \omega_{ci}} \tag{3.13}$$

Equation (3.12) states that the ion fluid motion is the superposition of a cross-field diffusion and a diamagnetic drift. Substituting the above expression for $n\mathbf{v}_{\perp}$ into the continuity equation (equation (3.10)), and using the fact that y is the ignorable coordinate, one obtains:

$$-D_{\perp} \frac{\partial^2 n}{\partial x^2} + \frac{\partial}{\partial z}(n v_z) = S_0$$

The above equation can be written in the following form:

$$-\frac{\partial^2 n}{\partial \tilde{x}^2} + \frac{\partial}{\partial \tilde{z}}(n \tilde{v}_z) = \tilde{S}_0$$

where $\tilde{x} = x/d$, $\tilde{z} = D_{\perp} z / c_s d^2$, $\tilde{v}_z = v_z / c_s$, and $\tilde{S}_0 = d^2 S_P / D_{\perp}$. Thus, for a given value of $\tilde{S}_0$, the density profile $n(\tilde{x}, \tilde{z})$ has a unique solution. As a result, the particle collection length must have the following form:

$$L_{\parallel} \propto \frac{c_s d^2}{D_{\perp}} \tag{3.14}$$

This is consistent with the argument based on particle balance.

From equation (3.12), it is clear that the convective term $Mn(\mathbf{v}\cdot\boldsymbol{\nabla})\mathbf{v}_\perp$ can be neglected only if $D_\perp/c_s d \ll 1$ and $c_s/\omega_{ci}d \ll 1$. For a typical obstacle with a width of 2 cm, the plasma parameters given in section (3.1) yield $D_\perp/c_s d \sim 3\times10^{-8}$ and $c_s/\omega_{ci}d \sim 0.02$. It is readily seen that the requirements $D_\perp/c_s d \ll 1$ and $c_s/\omega_{ci}d \ll 1$ are easily satisfied in the SOL of a large tokamak.

To understand the physical meaning of the definition of $D_\perp$ (equation (3.13)), let us recall that in an electron-ion collision, the center of mass is displaced by a distance of the order of ρ_e, the electron Larmor radius. Following the usual random-walk argument, the cross-field particle transport coefficient is given by

$$\begin{aligned} D_\perp &\sim \rho_e^2\nu_0 \\ &\sim \frac{T_e/m}{(eB/m)^2}\nu_0 \\ &\sim \frac{T_e/M}{(eB/M)}\frac{m\nu_0}{eB} \\ &\sim \frac{c_s^2\alpha}{\omega_{ci}^2} \end{aligned}$$

This is also consistent with equation (3.13).

3.2.3 Numerical Method

We have chosen to solve the transport equations in the non-conservative form. The transport equations (3.8)–(3.9) can be written in the non-conservative form as follows:

$$n\boldsymbol{\nabla}\cdot\mathbf{v} + \mathbf{v}\cdot\boldsymbol{\nabla}n = S_0 \tag{3.15}$$

$$(\mathbf{v}\cdot\boldsymbol{\nabla})\mathbf{v} = \frac{\omega_{ci}}{1+\alpha^2}(\mathbf{v}_\perp\times\hat{z} - \alpha\mathbf{v}_\perp) - \frac{c_s^2}{n}\boldsymbol{\nabla}n \tag{3.16}$$

Equations (3.15)–(3.16) are solved using three different numerical schemes. We are confident of the numerical solutions of the transport equations since all three different numerical schemes yield, within numerical accuracy, the same result.

Initial-Value Method

In this method, equations (3.15)–(3.16) will not be solved directly. Instead, we will solve the following time-dependent equations:

$$\frac{\partial n}{\partial t} + n\boldsymbol{\nabla}\cdot\mathbf{v} + \mathbf{v}\cdot\boldsymbol{\nabla}n = S_0 \tag{3.17}$$

$$\frac{\partial \mathbf{v}}{\partial t} + (\mathbf{v}\cdot\boldsymbol{\nabla})\mathbf{v} = \frac{\omega_{ci}}{1+\alpha^2}(\mathbf{v}_\perp \times \hat{z} - \alpha\mathbf{v}_\perp) - \frac{c_s^2}{n}\boldsymbol{\nabla}n \tag{3.18}$$

The steady-state solution of the above equations is also the solution of the transport equations (3.15)–(3.16).

For the numerical solution of equations (3.17)–(3.18) we use the corresponding difference equations on a non-uniform rectangular grid of 49×49 (see Appendix B for the details of the coordinate transformations). In order to obtain the solution to equations (3.15)–(3.16), equations (3.17)–(3.18) are advanced in time until a steady-state solution is reached. The equations are advanced in time using a two-step method as follows:

$$\begin{aligned}\boldsymbol{\psi}^{k+1/2} &= \boldsymbol{\psi}^{k} + \frac{\delta t}{2}\mathbf{F}(\boldsymbol{\psi}^{k})\\ \boldsymbol{\psi}^{k+1} &= \boldsymbol{\psi}^{k} + \delta t\mathbf{F}(\boldsymbol{\psi}^{k+1/2})\end{aligned}$$

where

$$\boldsymbol{\psi} = \begin{bmatrix}\mathbf{v}\\ n\end{bmatrix}$$

$$\mathbf{F} = \frac{\partial \boldsymbol{\psi}}{\partial t}$$

The superscript denotes time, i.e., $t = k\delta t$. All spatial derivatives are evaluated using central differences (see Appendix B), making our numerical scheme accurate to second order in space.

The principal advantage of this numerical scheme is that it is easy to implement, and does not require a large amount of core memory. A major drawback of this method is that the Courant condition imposes an upper bound on the time step δt. For a relatively fine grid, this restriction on δt becomes so severe that it takes up to one week on an IBM-PS2/Model 80 (an IBM personal computer based on the Intel

80386 CPU) to complete one run. This is our main motivation for exploring other available numerical schemes.

Pseudo Newton-Raphson Method

With some algebraic manipulation, equations (3.15)–(3.16) can be rewritten as follows:

$$n\boldsymbol{\nabla}\cdot\mathbf{v}+\mathbf{v}\cdot\boldsymbol{\nabla}n=S_0 \tag{3.19}$$

$$\mathbf{v}_\perp=-\frac{D_\perp}{c_s^2}\left[(\mathbf{v}\cdot\boldsymbol{\nabla})\mathbf{v}+\frac{c_s^2}{n}\boldsymbol{\nabla}n\right]+\frac{1}{\omega_{ci}}\hat{z}\times\left[(\mathbf{v}\cdot\boldsymbol{\nabla})\mathbf{v}+\frac{c_s^2}{n}\boldsymbol{\nabla}n\right] \tag{3.20}$$

Because the above PDEs are obtained from equations (3.15)–(3.16) by pure algebraic manipulations, the finite-difference solutions of the two sets of PDEs are identical. In this numerical scheme, equations (3.19)–(3.20) are solved directly by linearization. We first set up the problem in exactly the same manner as the standard Newton-Raphson method for solving a set of non-linear algebraic equations (see, for example, [26–28]). $\mathbf{v}$ and n can be written as follows:

$$\left.\begin{aligned}\mathbf{v}&=\mathbf{v}_0+\boldsymbol{\xi}\\ n&=n_0+n_1\end{aligned}\right\} \tag{3.21}$$

In essence, $\mathbf{v}_0$ and n_0 are the trial solution, and have to be known a priori. $\boldsymbol{\xi}$ and n_1 are the difference between the exact solution and the trial solution. Our goal is to solve for $\boldsymbol{\xi}$ and n_1 in terms of $\mathbf{v}_0$ and n_0. Linearizing equations (3.19)–(3.20) using (3.21), one obtains:

$$n_0\boldsymbol{\nabla}\cdot\boldsymbol{\xi}+n_1\boldsymbol{\nabla}\cdot\mathbf{v}_0+\mathbf{v}_0\cdot\boldsymbol{\nabla}n_1+\boldsymbol{\xi}\cdot\boldsymbol{\nabla}n_0=S_0-n_0\boldsymbol{\nabla}\cdot\mathbf{v}_0-\mathbf{v}_0\cdot\boldsymbol{\nabla}n_0 \tag{3.22}$$

$$\left.\begin{aligned}&\boldsymbol{\xi}_\perp+\frac{D_\perp}{c_s^2}\Bigg[(\mathbf{v}_0\cdot\boldsymbol{\nabla})\boldsymbol{\xi}+(\boldsymbol{\xi}\cdot\boldsymbol{\nabla})\mathbf{v}_0\\ &\qquad\qquad+\frac{c_s^2}{n_0}\boldsymbol{\nabla}n_1-n_1\frac{c_s^2}{n_0^2}\boldsymbol{\nabla}n_0\Bigg]\\ &-\frac{1}{\omega_{ci}}\hat{z}\times\Bigg[(\mathbf{v}_0\cdot\boldsymbol{\nabla})\boldsymbol{\xi}+(\boldsymbol{\xi}\cdot\boldsymbol{\nabla})\mathbf{v}_0\\ &\qquad\qquad+\frac{c_s^2}{n_0}\boldsymbol{\nabla}n_1-n_1\frac{c_s^2}{n_0^2}\boldsymbol{\nabla}n_0\Bigg]\end{aligned}\right\}=\left\{\begin{aligned}&-\mathbf{v}_{0\perp}-\frac{D_\perp}{c_s^2}\Bigg[(\mathbf{v}_0\cdot\boldsymbol{\nabla})\mathbf{v}_0\\ &\qquad\qquad+\frac{c_s^2}{n_0}\boldsymbol{\nabla}n_0\Bigg]\\ &+\frac{1}{\omega_{ci}}\hat{z}\times\Bigg[(\mathbf{v}_0\cdot\boldsymbol{\nabla})\mathbf{v}_0\\ &\qquad\qquad+\frac{c_s^2}{n_0}\boldsymbol{\nabla}n_0\Bigg]\end{aligned}\right. \tag{3.23}$$

In our scheme, equation (3.22) is used to determine n_1. The x, y, and z components of equation (3.23) are used to determine ξ_x, ξ_y, and ξ_z, respectively. Figure 3.1 illustrates our indexing convention. i $(1 \leq i \leq i_m)$ and j $(1 \leq j \leq j_m)$ are the indices for the x and z direction, respectively. The finite-difference approximation of equations (3.22)–(3.23) can be written in the following matrix form:

$$\begin{pmatrix} \mathbf{B}_1 & \mathbf{C}_1 & & & \\ \mathbf{A}_2 & \mathbf{B}_2 & \mathbf{C}_2 & & \\ & \mathbf{A}_3 & \mathbf{B}_3 & \mathbf{C}_3 & \\ & & \ddots & \ddots & \ddots \\ & & & \mathbf{A}_{i_m} & \mathbf{B}_{i_m} \end{pmatrix} \begin{pmatrix} \varsigma_1 \\ \varsigma_2 \\ \varsigma_3 \\ \vdots \\ \varsigma_{i_m} \end{pmatrix} = \begin{pmatrix} \mathbf{r}_1 \\ \mathbf{r}_2 \\ \mathbf{r}_3 \\ \vdots \\ \mathbf{r}_{i_m} \end{pmatrix} \tag{3.24}$$

where ς_i is the column vector containing all unknowns on the i^{th} row, i.e.,

$$\varsigma_i = \begin{pmatrix} \boldsymbol{\xi}^{i1} \\ n_1^{i1} \\ \boldsymbol{\xi}^{i2} \\ n_1^{i2} \\ \vdots \\ \boldsymbol{\xi}^{ij_m} \\ n_1^{ij_m} \end{pmatrix}$$

Since $\boldsymbol{\xi}$ is a three-component vector, the column vector ς_i has $4j_m$ elements. $\mathbf{r}_i$ is the residual vector of the i^{th} row. $\mathbf{A}_i$, $\mathbf{B}_i$, and $\mathbf{C}_i$ are square matrices of rank $4j_m$. Furthermore, these square matrices have relatively simple band structures.

The remaining task is to solve equation (3.24) for $\boldsymbol{\xi}$ and n_1, and use them to correct the initial trial solution $\mathbf{v}_0$ and n_0. This process is repeated until the desired accuracy is achieved.

Standard iterative methods for solving linear systems of algebraic equations are generally applicable only to systems with diagonally dominant matrices. Unfortunately, equation (3.24) does not fall within this category since it is a finite-difference approximation of a set of hyperbolic PDEs. Thus, in order to be able to utilize iterative techniques, we will modify equation (3.24) in such a manner as to make the block-tridiagonal matrix diagonally dominant. The easiest way to do so is to add $\beta\mathbf{I}$ to each diagonal element of the block-tridiagonal matrix of equation (3.24), where

β is a parameter one can adjust. $\mathbf{I}$ is the identity matrix of rank $4j_m$. The resulting equation is written as follows:

$$\begin{pmatrix} \tilde{\mathbf{B}}_1 & \mathbf{C}_1 & & & \\ \mathbf{A}_2 & \tilde{\mathbf{B}}_2 & \mathbf{C}_2 & & \\ & \mathbf{A}_3 & \tilde{\mathbf{B}}_3 & \mathbf{C}_3 & \\ & & \ddots & \ddots & \ddots \\ & & & \mathbf{A}_{i_m} & \tilde{\mathbf{B}}_{i_m} \end{pmatrix} \begin{pmatrix} \varsigma_1 \\ \varsigma_2 \\ \varsigma_3 \\ \vdots \\ \varsigma_{i_m} \end{pmatrix} = \begin{pmatrix} \mathbf{r}_1 \\ \mathbf{r}_2 \\ \mathbf{r}_3 \\ \vdots \\ \mathbf{r}_{i_m} \end{pmatrix} \tag{3.25}$$

where $\tilde{\mathbf{B}}_i = \mathbf{B}_i + \beta\mathbf{I}$. For lack of better words, we have chosen to call equation (3.25) the *Pseudo Newton-Raphson* method. The reason is that although equation (3.25) is a variation of the Newton-Raphson method, it does not have the quadratic-convergent property.

Equation (3.25) is solved by the block Gauss-Seidel iterative technique,[27] i.e., treating the x-direction explicitly and the z-direction implicitly. In effect, we are solving the following equation:

$$\begin{pmatrix} \tilde{\mathbf{B}}_1 & & & \\ & \tilde{\mathbf{B}}_2 & & \\ & & \ddots & \\ & & & \tilde{\mathbf{B}}_{i_m} \end{pmatrix} \begin{pmatrix} \varsigma_1^{\ k+1} \\ \varsigma_2^{\ k+1} \\ \vdots \\ \varsigma_{i_m}^{\ k+1} \end{pmatrix} = - \begin{pmatrix} 0 & C_1 & & \\ A_2 & 0 & C_2 & \\ & \ddots & \ddots & \ddots \\ & & A_{i_m} & 0 \end{pmatrix} \begin{pmatrix} \varsigma_1^{\ k} \\ \varsigma_2^{\ k} \\ \vdots \\ \varsigma_{i_m}^{\ k} \end{pmatrix} + \begin{pmatrix} \mathbf{r}_1 \\ \mathbf{r}_2 \\ \vdots \\ \mathbf{r}_{i_m} \end{pmatrix} \tag{3.26}$$

When the above matrix equation converges to the desired accuracy (inner iteration loop), the trial solution $\mathbf{v}_0$ and n_0 can be corrected. The whole process is repeated until $\mathbf{v}_0$ and n_0 converge to the desired accuracy (outer iteration loop). Since there are two iteration loops, it is really an art to choose a *good* value for β. If β is too large, the inner iteration loop (equation (3.26)) converges very fast. However, the rate of convergence of the outer iteration loop is slow. On the other hand, if β is too small, the inner iteration loop converges very slowly, or not at all. The trick is to choose β in such a way that both the inner and outer iteration loops converge sufficiently fast.

The inner iteration loop (equation (3.26)) can be solved quite efficiently since $\tilde{\mathbf{B}}_i$ has a simple band structure. In general, for a system of four first-order hyperbolic PDEs, $\tilde{\mathbf{B}}_i$ contains at most seven bands on either side of the principle diagonal. In our particular case, $\tilde{\mathbf{B}}_i$ has only five bands to either side of the principle diagonal.

The principle advantage of the Pseudo Newton-Raphson method is that it does not require a large amount of core memory. Also, it is fairly efficient since algebraic equations involving band matrices are easy to solve. The only drawback is that it is not easy to implement. We find that the pseudo Newton-Raphson method is about a 65% improvement in computer time over the time-dependent method described previously.

Newton-Raphson Method

The only difference between this method and the Pseudo Newton-Raphson method is that in this method, equation (3.24) is solved directly by Gaussian elimination without modification. The Pseudo Newton-Raphson has to solve a modified version of equation (3.24) iteratively. The principle of the Newton-Raphson method has already been outlined in the previous section.

The main advantage of this method is that it converges quadratically. Normally, convergence to within the accuracy of the double precision number is obtained in only five or six iterations. Of course, as a matter of practicality, we only need to obtain a convergence to within the order of the truncation error. We find that this method is about a 70% improvement in computer time over the pseudo Newton-Raphson method described previously. The major drawback of this numerical scheme is that it requires a tremendous amount of core memory not available on small mainframe computers. Fortunately, this problem can be overcome with careful memory management and with the aid of a mass storage device. The reason is that equation (3.24) is a block-tridiagonal system. At any time, it is sufficient to keep only five square matrices of dimension $4j_m$ in core memory for manipulation. After each elimination process, matrices are written onto the mass storage device for the backward substitution process. This entire problem with a moderately fine grid (49×49) was done on a personal computer equipped with 4 megabytes of core memory and 20 megabytes of mass storage capacity. Another drawback is that this numerical scheme is very tedious to implement. However, despite all of the technical difficulties associated with the implementation, we prefer this method over both the pseudo Newton-Raphson and the time-dependent method. For our particular transport equations, we are fairly satisfied with the efficiency of this method.

3.2.4 Boundary Conditions

It is convenient to distinguish two types of boundaries: a physical boundary (the obstacle's surface, drawn as a solid line in figure 2.1), and a periodic boundary (drawn as dashed lines in figure 2.1).

Periodic boundary conditions are to be applied on the periodic boundary. In particular, v_x and v_y are odd functions about the top and bottom boundaries. v_z and n are even functions about these same boundaries. v_x, v_y, and n are even functions about the left and right periodic boundaries. v_z is an odd function about these same boundaries. These particular boundary conditions imply that there is no particle, momentum, or energy flux crossing the periodic boundary. With these periodic boundary conditions, the transport equations (3.8)–(3.9) are automatically satisfied on the periodic boundary.

The boundary conditions to be applied on the obstacle's surface are more subtle. The perpendicular and parallel components of the ion momentum equation (equation (3.9)) determine the perpendicular and parallel component of the ion fluid velocity, respectively. The continuity equation (equation (3.8)) determines the particle density. In order to utilize the perpendicular component of the ion momentum equation to determine $\mathbf{v}_\perp$, we need to know $\partial \mathbf{v}_\perp / \partial z$. Since such a boundary condition is not available, we will approximate $\partial \mathbf{v}_\perp / \partial z$ by a one-sided finite difference. Our justification for doing so is that as the grid gets finer, this approximation becomes more accurate. In order to utilize the continuity equation and the parallel component of the ion momentum equation, we need to know $\partial n/\partial z$ and $\partial v_z/\partial z$. Again, such explicit boundary conditions are not available. However, we do know that on the obstacle's suface, v_z is taken to be c_s by the virtue of the Bohm's sheath criterion. The question is whether one should use the Bohm's sheath criterion in conjunction with the parallel component of the ion momentum equation or the Bohm's sheath criterion, discarding the parallel component of the ion momentum equation. In either case, we still need to know $\partial n/\partial z$. As before, we will approximate it by a one-sided finite difference. If we choose to utilize the parallel component of the ion momentum equation instead of discarding it, we can use it in conjunction with the one-sided finite difference approximation of $\partial n/\partial z$ to determine $\partial v_z/\partial z$, i.e., we need not specify $\partial v_z/\partial z$ explicitly. This seems to be the correct choice since specifying both v_z and $\partial v_z/\partial z$ on the same boundary would be overspecifying boundary conditions. On the other hand, if we use the Bohm's sheath criterion and discard the parallel component of the ion momentum equation, we would need to approximate $\partial v_z/\partial z$ by a one-sided finite difference. This method appears to be wrong since we are specifying both v_z and $\partial v_z/\partial z$ on the same boundary. The subtlety is that it is actually the correct choice to use the Bohm's sheath criterion and discard the parallel component of the ion momentum equation. The reason is that v_z and n are singular at the obstacle's surface. Appendix C is an extensive discussion of this important point.

3.2.5 Numerical Results

The plasma response was obtained for various magnetic field strengths (characterized by the size of the ion orbit) and diffusion coefficients. Figures 3.2a and 3.2b are a three-dimensional plot and a contour plot of the particle density. For this particular case, $D_\perp/c_s d = 1/256$, $c_s/\omega_{ci} d = 10^{-2}$, $x_0/d = 2$, and $z_0/d = 640$. The parallel ion fluid velocity v_z is taken to be c_s identically across the obstacle's surface. x_0 and z_0 are chosen in such a manner that the particle density on both the left and the top boundaries is approximately uniform.

Figure 3.2a shows that there exists a small region near the obstacle where the density is partially depleted. This region is often referred to as the obstacle's *shadow*. We define the particle collection length as the distance (along the bottom boundary) from the obstacle's surface where the particle density is $0.6n_\infty$ (n_∞ is the particle density far from the obstacle) to the point where the particle density is $0.8n_\infty$. Figure 3.3 is a plot of the particle collection length versus the inverse of the cross-field diffusion coefficient for two values of the magnetic field strength. In both cases, the particle collection length appears to be inversely proportional to the diffusion coefficient and linearly proportional to both the ion acoustic speed (c_s) and the square of the obstacle's half-width. For $c_s/\omega_{ci}d = 10^{-2}$, the particle collection can be approximated as follows:

$$L_\parallel \simeq 0.23\frac{c_s d^2}{D_\perp} \qquad\qquad \text{if} \;\; D_\perp/c_s d \ll 1$$

Thus, if the transport of particles in the SOL of a tokamak is classical, the length of the shadow is about 10^7 cm for $d \sim 1$ cm. However, if the transport process is anomalous as is often the case with tokamak plasmas, the length of the shadow will be significantly reduced. The effect of anomalous transport will be discussed in more detail in chapter 4.

Our numerical results also show that the particle density (along the bottom periodic boundary) at the obstacle's surface is about $0.6n_\infty$.

In summary, we find that the numerical results exhibit the same qualitative features found in the analytical analysis (see section 3.2.2).

A potential problem with the above results is that by assumption, the parallel ion fluid velocity v_z is discontinuous at the tip of the obstacle. v_z is taken to be c_s identically across the obstacle's surface (Bohm's sheath criterion), whereas it is taken to be 0 along the right boundary above the obstacle due to symmetry, resulting in a discontinuity at the tip of the obstacle. We would like to assess the sensitivity of the plasma response with respect to the treatment of v_z in the neighbourhood of the obstacle's tip. This is achieved by assuming that v_z has a sharp, but continuous profile, e.g.,

$$v_z = \begin{cases} c_s \left[1 - (x/d)^{16} \right] & \text{if } x \leq d \\ 0 & \text{if } x \geq d \end{cases}$$

Figures 3.4a and 3.4b are a three-dimensional plot and a contour plot of the particle density. For this particular case, $D_\perp / c_s d = 1/256$, $c_s/\omega_{ci}d = 10^{-2}$, $x_0/d = 2$, and $z_0/d = 640$. Figures 3.4 and 3.2 correspond to the same set of physical parameters. The only difference between the two solutions is the difference in boundary condition on the obstacle's surface. Let $n(x, z)$ and $n^*(x, z)$ be the particle densities presented in figures 3.4 (countinous boundary condition) and 3.2 (discontinuous boundary condition), respectively. We define $\delta n(x, z)$ as follows:

$$\delta n = \frac{n - n^*}{n^*_\infty}$$

Figure 3.5 is a three-dimensional plot of δn as a function of spatial position. It shows that the two solutions differ the most in the neighbourhood of the tip of the obstacle. However, the overall difference is not significant.

Figure 3.6 is a plot of the particle collection length versus the inverse of the diffusion coefficient for the two different treatments of the boundary condition on the obstacle. In both cases, $c_s/\omega_{ci}d = 10^{-2}$. Figure 3.6 also shows that the difference between the two solutions is not significant.

It is our conclusion that the exact treatment of the obstacle's tip is not important in this simple model since the solution of the transport equations (3.8)–(3.9) is not sensitive to the discontinuity there. As a result, we will take the parallel ion fluid v_z to be c_s across the obstacle's surface hereafter, e.g.,

$$v_z = \begin{cases} c_s & \text{if } x < d \\ 0 & \text{if } x \geq d \end{cases} \tag{3.27}$$

3.3 Localization of Particle Source

In section 3.2, we assumed that there is no particle, momentum, or energy flux crossing the boundary, except at the obstacle where they are removed. The compensating particles came entirely from within the plasma column. The volumetric rate of particle production was assumed to be spatially uniform.

In this section, unlike section 3.2, we will assume the other extreme limit where the volumetric rate of particle production within the plasma column is zero. The compensating particles come entirely from the top boundary. The plasma collection process is still assumed to be isothermal and inviscid. Thus, the transport equations (3.8)–(3.9) with $S_0 = 0$ are applicable to this study.

In a real system, it is actually a mixture of the two extreme limits. The compensating particles come partially from the *exterior* region, and partially from the *interior* region. Our purpose is to study the qualitative difference, if any, between the two extreme limits and to examine how sensitive the particle density is to the localization of the particle source.

In section 3.2, the particles removed at the obstacle come partly from within (volumetric source S_0) and partly from outside (cross-field particle diffusion) the obstacle's shadow. When the volumetric particle source is assumed to be zero, the particles removed at the obstacle come entirely from outside the shadow region via cross-field diffusion. In this case, an average particle traverses a longer path before being removed. Therefore, the obstacle's shadow is expected to extend farther into the plasma.

3.3.1 Boundary Conditions

The boundary conditions are the same as those described in section 3.2.4 except at the top boundary. There, the cross-field particle flux is taken to be uniform, e.g.,

$$n(x_0, z)v_x(x_0, z) = \Gamma_0 \tag{3.28}$$

where Γ_0 is constant (not a function of z).

n_∞ can be related to Γ_0 through detailed balance, i.e.,

$$\Gamma_0 z_0 = c_s \int_0^d n(x, z_0) dx$$

Since we have shown in section 3.2.2 that $n(0, z_0) = e^{-1/2} n_\infty$, the above equation reduces to:

$$n_\infty \simeq e^{1/2} \frac{\Gamma_0 z_0}{c_s d} \tag{3.29}$$

It can be shown from the above equation and the transport equations (3.8)–(3.9) with $S_0 = 0$ that the particle density n scales linearly with Γ_0 and that the ion fluid velocity $\mathbf{v}$ is independent of Γ_0.

Along the top boundary, we also need to know $\partial v_y/\partial x$, $\partial v_z/\partial x$, and $\partial n/\partial x$ in addition to equation (3.28). $\partial v_z/\partial x$ is taken to be zero along the top boundary. The two remaining cross-field gradients are approximated by one-sided finite differences.

3.3.2 Numerical Results

We have obtained the plasma response of the transport equations ($S_0 = 0$) for various values of the cross-field diffusion coefficient. The magnetic field strength for these cases was chosen so that $c_s/\omega_{ci} d = 10^{-2}$. Figures 3.7a and 3.7b are a three-dimensional plot and a contour plot of the particle density. For this particular case, $D_\perp / c_s d = 1/256$, $c_s/\omega_{ci} d = 10^{-2}$, $x_0/d = 2$, and $z_0/d = 640$.

The cases presented in figures 3.2 and 3.7 correspond to the same set of physical parameters. The only difference between them is the origin of the source particles. One noticeable difference is that unlike figure 3.2a, figure 3.7a indicates that the particle density on the top boundary has a non-vanishing cross-field gradient. This is expected since a non-vanishing density gradient is required to support a cross-field particle diffusion which, in turn, is required for detailed balance. Comparing figure 3.7b to figure 3.2b (contour plots of the particle density) reveals that the obstacle's shadow extends farther into the plasma. This effect of lengthening the obstacle's shadow can also be observed by noticing that in figure 3.7a, the particle density is not quite uniform on the left boundary. In fact, the obstacle's shadow is expected to extend farther into the plasma by the qualitative argument presented in section 3.2.

Figure 3.8 is a plot of the particle collection length versus the inverse of the cross-field diffusion coefficient. The upper curve results when the replacement particles come entirely from the top boundary of the plasma column. In this case, the volumetric particle source S_0 is assumed to be zero. For the purpose of comparison, we have also included the lower curve, which results when the replacement particles come entirely from within the plasma column via a uniform volumetric particle source S_0 (see section 3.2.5). In this case, the particle flux crossing the top boundary of the plasma column is assumed to be zero. Figure 3.8 shows that the particle collection length of an obstacle is indeed lengthened when the replacement particles come from outside the plasma column via particle diffusion across the top boundary.

In summary, the plasma response obtained exhibits the same qualitative features one expects from a simple argument. We have studied the two extreme limits where (1) the replacement particles come entirely from within the plasma column via a uniform volumetric source (section 3.1), and (2) the replacement particles come entirely from outside the plasma column via cross-field particle diffusion across the top boundary. In a realistic physical system, it is actually a mixture of the two extreme limits. Usually, we do not know what fraction of the replacement particles come from the exterior or interior region. The purpose of this study is to determine the uncertainty due to the lack of knowledge regarding the localization of the replacement particles. For the purpose of studying the qualitative features of the plasma response, we think that it is not important to determine the exact localization of the replacement particles. Thus, we will assume hereafter that the replacement particles come entirely from within the plasma column via a spatially uniform volumetric particle source. The cross-field particle flux at the top boundary is assumed to be zero.

3.4 Non-Uniform Cross-Field Diffusion Coefficient

The cross-field diffusion coefficient can be written as follows (see equation (3.13)):

$$D_\perp = \frac{c_s^2 \nu_0}{\omega_{ce}\omega_{ci}}$$

where ν_0, the electron-ion collision rate, is given by the following expression (see equation (2.18)):

$$\nu_0 = \frac{4(2\pi)^{1/2} \ln \Lambda e^4 Z n}{3m^{1/2} T_e^{3/2}} \propto n$$

Using the above expressions, the cross-field diffusion coefficient is rewritten as follows:

$$D_\perp = D_{\perp\infty} \frac{n}{n_\infty} \tag{3.30}$$

In section 3.2, we assumed that the cross-field diffusion coefficient is spatially uniform. From the above equation, we see that this assumption is not correct.

In this section, we will take the cross-field diffusion coefficient to be proportional to the particle density n. $D_{\perp\infty}$, the cross-field diffusion coefficient far from the obstacle, is a specified coefficient in this model. The plasma collection process is still assumed to be isothermal and inviscid. The transport equations (3.8)–(3.9), with $D_\perp$ given by equation (3.30), are still applicable in this model.

In the obstacle's shadow region where the particle density is partially depleted, the rate of cross-field particle diffusion is lower when the diffusion coefficient is taken to be proportional to the particle density than when the diffusion coefficient is assumed to be spatially uniform. Thus, in order to transport enough particles into the shadow region for removal, cross-field particle diffusion must occur over a longer scale length, i.e., the particle collection length of the obstacle must extend farther into the plasma. This is the only conceivable effect on the plasma response by assuming that the cross-field diffusion coefficient is proportional to the particle density n.

The boundary conditions for this model are exactly the same as those described in section 3.2.4. Equation (3.30) is linearized as follows:

$$D_{\perp} = D_{\perp\infty}\left[\frac{n_0}{n_{0\infty}} + \frac{n_1}{n_{0\infty}} - \frac{n_0 n_{1\infty}}{n_{0\infty}^2}\right]$$

Equations (3.22)–(3.23) (linearized forms of the transport equations (3.8)–(3.9)), used in conjunction with the above equation, are solved using the Newton-Raphson method described in section 3.2.3.

Numerical Results

The plasma response was obtained for various values of the cross-field diffusion coefficient $D_{\perp\infty}$. For these cases, the magnetic field strength was chosen so that $c_s/\omega_{ci}d = 10^{-1}$. Figures 3.9a and 3.9b are a three-dimensional plot and a contour plot of the particle density. For this particular case, $D_{\perp\infty} = 1/256$, $c_s/\omega_{ci}d = 10^{-2}$, $x_0/d = 2$, and $z_0/d = 640$.

The cases presented in figures 3.2 and 3.9 correspond to the same set of physical parameters. The only difference between them is that in figure 3.2, the cross-field diffusion coefficient is assumed to be spatially uniform, whereas it is taken to be proportional to the particle density n in figure 3.9. Let $n(x,z)$ and $n^*(x,z)$ be the particle densities presented in figures 3.9 ($D_{\perp}$ proportional to n) and 3.2 (spatially uniform $D_{\perp}$), respectively. We define $\delta n(x,z)$ as follows:

$$\delta n = \frac{n - n^*}{n^*_{\infty}}$$

Figure 3.10 is a three-dimensional plot of δn as a function of spatial position. It shows that the two solutions differ the most in the shadow region where the particle density is relatively low. Far from the obstacle, i.e., outside the shadow region, the two solutions differ very little. The overall difference it not significant.

Figure 3.11 is a plot of the particle collection length versus the inverse of the cross-field diffusion coefficient for $c_s/\omega_{ci}d = 10^{-2}$. The upper curve results when the diffusion coefficient is taken to be proportional to the particle density n. For the purpose of comparison, we have also included the lower curve, which results when the diffusion coefficient is assumed to be spatially uniform (see section 3.2.5). Figure 3.11 shows that the particle collection length is lengthened by only about 15%. It should be noted that the effect of lengthening the particle collection length has been anticipated by the simple argument given in section 3.4.

In summary, we see that the plasma response changes very little when the cross-field diffusion coefficient is taken to be proportional to the particle density n. The particle collection length increases by only about 15%. It is our conclusion that the assumption that the cross-field diffusion coefficient is spatially uniform is a rather good assumption. The additional complexity due to the exact treatment of the spatial variation of the diffusion coefficient is not justified because the overall correction is not significant.

3.5 Parallel Electron-Ion Collisional Drag

In all of the previous sections, the parallel electron-ion collisional drag $\mathbf{R}_{\parallel}$ was neglected. However, we did not give a justification for doing so. In this section, we will show by dimensional analysis that it appears necessary to account for this term because its magnitude is of the order of the parallel electron pressure gradient. The plasma collection process is still assumed to be isothermal and inviscid.

3.5.1 Dimensional Analysis

The purpose of this section is to estimate the magnitude of the parallel electron-ion collisional drag. This is achieved by first assuming that it can be neglected. An approximate plasma response can then be obtained. The magnitude of the parallel electron-ion collisional drag is evaluated a posteriori using the approximate plasma response.

When the parallel electron-ion collisional drag is neglected, $\mathbf{J}_{\perp}$ is given as follows:

$$\mathbf{J}_\perp = \frac{ne}{1+\alpha^2}(\mathbf{v}_\perp + \alpha \mathbf{v}_\perp \times \hat{z}) \tag{3.31}$$

where $\alpha = \nu_0/\omega_{ce} = D_\perp \omega_{ci}/c_s^2$, provided that z_0 is sufficiently large compared to the particle collection (see section 3.2.1).

With the above expression, the isothermal, inviscid transport equations can be written as follows:

$$\boldsymbol{\nabla}\cdot \mathbf{J} = 0 \tag{3.32}$$

$$\boldsymbol{\nabla}\cdot (n\mathbf{v}) = S_0 \tag{3.33}$$

$$\boldsymbol{\nabla}\cdot (n\mathbf{v}\mathbf{v}) = \frac{\omega_{ci}}{1+\alpha^2} n(\mathbf{v}_\perp \times \hat{z} - \alpha \mathbf{v}_\perp) - c_s^2 \boldsymbol{\nabla} n + S_0 \mathbf{v} \tag{3.34}$$

Solving for the cross-field ion fluid velocity using equation (3.33) and the perpendicular component of equation (3.34), one obtains:

$$\mathbf{v}_\perp = -\frac{D_\perp}{c_s^2}\left[(\mathbf{v}\cdot\boldsymbol{\nabla})\mathbf{v}_\perp + \frac{c_s^2}{n}\boldsymbol{\nabla}_\perp n\right] + \frac{1}{\omega_{ci}}\hat{z}\times\left[(\mathbf{v}\cdot\boldsymbol{\nabla})\mathbf{v}_\perp + \frac{c_s^2}{n}\boldsymbol{\nabla}_\perp n\right]$$

Assuming that the cross-field convective term $(\mathbf{v}\cdot\boldsymbol{\nabla})\mathbf{v}_\perp$ is small, $\mathbf{v}_\perp$ can be approximated by two successive approximations, e.g.,

$$\mathbf{v}_{0\perp} = \frac{1}{n}\left(-D_\perp \boldsymbol{\nabla}_\perp n + \frac{c_s^2}{\omega_{ci}}\hat{z}\times\boldsymbol{\nabla}_\perp n\right)$$

$$\begin{aligned}\mathbf{v}_\perp = \mathbf{v}_{0\perp} &- \frac{D_\perp}{c_s^2}\left[(\mathbf{v}_\parallel\cdot\boldsymbol{\nabla})\mathbf{v}_{0\perp} + (\mathbf{v}_{0\perp}\cdot\boldsymbol{\nabla})\mathbf{v}_{0\perp}\right]\\ &+ \frac{1}{\omega_{ci}}\hat{z}\times\left[(\mathbf{v}_\parallel\cdot\boldsymbol{\nabla})\mathbf{v}_{0\perp} + (\mathbf{v}_{0\perp}\cdot\boldsymbol{\nabla})\mathbf{v}_{0\perp}\right]\end{aligned}$$

Using the two equations above and equation (3.31), the perpendicular current density $\mathbf{J}_\perp$ can be written as follows:

$$\mathbf{J}_\perp = \frac{ne}{\omega_{ci}}\hat{z}\times\left[c_s^2\frac{\boldsymbol{\nabla}_\perp n}{n} + (\mathbf{v}_\parallel\cdot\boldsymbol{\nabla})\mathbf{v}_{0\perp} + (\mathbf{v}_{0\perp}\cdot\boldsymbol{\nabla})\mathbf{v}_{0\perp}\right] \tag{3.35}$$

In the obstacle's shadow, the parallel ion fluid velocity is of the order of the ion acoustic speed, i.e., $v_\parallel \sim O(c_s)$. Furthermore, the perpendicular and the parallel scale lengths are expected to be d and $L_\parallel$, respectively, i.e.,

$$\boldsymbol{\nabla}_\perp \sim O(1/d)\hat{x}$$

$$\boldsymbol{\nabla}_\parallel \sim O(1/L_\parallel)\hat{z}$$

A simple relation between $L_{\parallel}$ and d has also been found in section 3.2.2, namely

$$L_{\parallel} \sim O(c_s d^2/D_\perp)$$

Substituting the above expressions into equations (3.32) and (3.35), using the fact that y is the ignorable coordinate, one obtains:

$$\begin{aligned} J_z &\sim O[(c_s d/D_\perp)J_x] \\ J_x &\sim O[(D_\perp c_s/\omega_{ci}^2 d^3)\, enc_s] \end{aligned}$$

From the above expressions, one obtains:

$$J_z \sim O\left[\left(\frac{c_s}{\omega_{ci} d}\right)^2 enc_s\right]$$

The ratio of the parallel electron-ion collisional drag to the parallel electron pressure gradient is estimated as follows:

$$\begin{aligned} \frac{R_{\parallel}}{T_e \partial n/\partial z} &= \frac{m\nu_0 J_z}{eT_e \partial n/\partial z} \\ &\sim O\left[m\nu_0 \left(\frac{c_s}{\omega_{ci} d}\right)^2 enc_s \frac{L_{\parallel}}{neT_e}\right] \\ &\sim O(1 + T_e/T_i) \end{aligned}$$

where $\nu_0 = D_\perp \omega_{ce}\omega_{ci}/c_s^2$ (see equation (3.13)). The above expression states that the parallel electron-ion collisional drag might not small compared to the parallel electron pressure gradient. Therefore, it appears necessary to account for it in the transport equations.

3.5.2 Formulation

For an isothermal, inviscid plasma with a spatially uniform rate of particle production, the transport equations (2.34)–(2.38) are reduced as follows:

$$\nabla \cdot \mathbf{J} = 0 \tag{3.36}$$

$$\nabla \cdot (n\mathbf{v}) = S_0 \tag{3.37}$$

$$\nabla\cdot(Mn\mathbf{v}\mathbf{v}) = en(-\nabla\phi + \mathbf{v}\times\mathbf{B}) - T_{i0}\nabla n + S_0 M\mathbf{v} - \frac{m\nu_0}{e}\mathbf{J} \tag{3.38}$$

$$0 = -en(-\nabla\phi + \mathbf{v}\times\mathbf{B}) + \mathbf{J}\times\mathbf{B} - T_{e0}\nabla n + \frac{m\nu_0}{e}\mathbf{J} \tag{3.39}$$

where $\mathbf{J}$ is the net current density. ν_0, rate of electron-ion collision, is taken to be spatially uniform. If the parallel electron-ion collisional drag were neglected as in section 3.2, equations (3.37)–(3.39) would form a closed set of transport equations, and it would have been unnecessary to include equation (3.36). However, since the parallel electron-ion collisional drag is included, we have introduced an additional unknown, namely, $\mathbf{J}_{\parallel}$. In this case, equations (3.37)–(3.39) no longer form a closed set of equations since we have more unknowns than equations. Therefore, it is necessary to include equation (3.36) to close the set of transport equations. By integrating the z-component of the generalized Ohm's law (equation (3.39)), and then differentiating it with respect to x, one obtains:

$$e\frac{\partial\phi}{\partial x} - \frac{T_{e0}}{n}\frac{\partial n}{\partial x} = e\frac{d\phi_0}{dx} - \frac{T_{e0}}{n_0}\frac{dn_0}{dx} - \frac{m\nu_0}{e}\frac{\partial}{\partial x}\int_0^z \frac{J_z(x,z')}{n(x,z')}\,dz'$$

where $\phi_0(x) = \phi(x,0)$ and $n_0(x) = n(x,0)$. The last term of the R.H.S. of the above equation is the additional effect due to the parallel electron-ion collisional drag. Were it not for this term, the particle density n would be related to the electrostatic potential ϕ by the usual Boltzmann factor, i.e.,

$$n(x,z) = n_0(x)\exp\left[\frac{e\phi(x,z) - e\phi_0(x)}{T_{e0}}\right]$$

Solving for $\mathbf{J}_{\perp}$ from the perpendicular components of the generalized Ohm's law, one obtains:

$$J_x = \frac{n}{1+\alpha^2}\left[n(v_x + \alpha v_y) + \alpha^2\frac{\partial}{\partial x}\int_0^z \frac{J_z(x,z')}{n(x,z')}\,dz' - \frac{\alpha}{B}f_0(x)\right]$$
$$J_y = \frac{J_x - nev_x}{\alpha}$$

where

$$\alpha = \nu_0/\omega_{ce}$$
$$f_0(x) = e\frac{d\phi_0}{dx} - \frac{T_{e0}}{n}\frac{dn_0}{dx}$$

Dividing both sides of the equation above for J_x by n, differentiating the result with respect to z, one obtains:

$$(1+\alpha^2)\frac{\partial}{\partial z}\left(\frac{J_x}{n}\right) - \alpha^2\frac{\partial}{\partial x}\left(\frac{J_z}{n}\right) = e\frac{\partial}{\partial z}(v_x + \alpha v_y) \tag{3.40}$$

Since the current density $\mathbf{J}$ is divergenceless, it can be easily formulated in terms of a *stream function* Ψ, i.e.,

$$\left.\begin{aligned} J_x &= e\frac{\partial \Psi}{\partial z} \\ J_z &= -e\frac{\partial \Psi}{\partial x} \end{aligned}\right\} \tag{3.41}$$

With the above definition, equation (3.36) is automatically satisfied. Substituting the definition for Ψ into equation (3.40), one obtains a Poisson-like equation for Ψ as follows:

$$(1+\alpha^2)\frac{\partial}{\partial z}\left(\frac{1}{n}\frac{\partial \Psi}{\partial z}\right) + \alpha^2\frac{\partial}{\partial x}\left(\frac{1}{n}\frac{\partial \Psi}{\partial x}\right) = \frac{\partial}{\partial z}(v_x + \alpha v_y) \tag{3.42}$$

Using the generalized Ohm's law and the definition for Ψ, one can eliminate both the current density $\mathbf{J}$ and the electric field $\nabla\phi$ from the ion momentum equation (equation (3.38)). The result is as follows:

$$\nabla\cdot(n\mathbf{v}\mathbf{v}) = \omega_{ci}\left[\hat{x}\frac{1}{\alpha}\left(\frac{\partial \Psi}{\partial z} - nv_x\right) - \hat{y}\frac{\partial \Psi}{\partial z}\right] - c_s^2\nabla n + S_0\mathbf{v} \tag{3.43}$$

In summary, as a result of the parallel electron-ion collisional drag, the electrons no longer obey the simple Boltzmann relation. Because the current density $\mathbf{J}$ is divergenceless, it can be defined in terms of a stream function Ψ. The general Ohm's law is then used to obtain a Poisson-like equation for the stream function Ψ. The electric field is eliminated from the ion momentum equation by using the generalized Ohm's law. With both the current density $\mathbf{J}$ and the electrostatic potential ϕ eliminated, our primitive variables consist of only three variables: the ion fluid velocity $\mathbf{v}$, the particle density n, and the stream function Ψ. In this case, equations (3.37) and (3.42)–(3.43) form a closed set of isothermal, inviscid transport equations that account for the parallel electron-ion collisional drag.

3.5.3 Numerical Method

For reasons regarding numerical stability, we will not obtain the plasma response directly from equations (3.37) and (3.42)–(3.43). We will, however, obtain the plasma response from a mathematically equivalent set of equations. The transformation begins with the following choice for rewriting the stream function Ψ:

$$\begin{aligned} \Psi &= \psi + \Phi \\ \Phi(x,z) &= \int_0^z \frac{n(v_x + \alpha v_y)}{1+\alpha^2}\, dz' \end{aligned} \tag{3.44}$$

With a fair amount of tedious manipulation, equations (3.37) and (3.42)–(3.43) can be written in the following form:

$$n\nabla\cdot \mathbf{v} + \mathbf{v}\cdot\nabla n = S_0 \tag{3.45}$$

$$\mathbf{v}_\perp = -\frac{D_\perp}{c_s^2}\left[(\mathbf{v}\cdot\nabla)\mathbf{v} + \frac{c_s^2}{n}\nabla n\right] + \frac{1}{\omega_{ci}}\hat{z}\times\left[(\mathbf{v}\cdot\nabla)\mathbf{v} + \frac{c_s^2}{n}\nabla n\right] - \left(\frac{1+\alpha^2}{\alpha}\right)\frac{1}{n}\frac{\partial\psi}{\partial z}\hat{y} \tag{3.46}$$

$$(1+\alpha^2)\frac{\partial}{\partial z}\left(\frac{1}{n}\frac{\partial\psi}{\partial z}\right) + \alpha^2\frac{\partial}{\partial x}\left(\frac{1}{n}\frac{\partial\psi}{\partial x}\right) + \alpha^2\frac{\partial}{\partial x}\left(\frac{1}{n}\frac{\partial\Phi}{\partial x}\right) = 0 \tag{3.47}$$

The new set of primitive variables are: the ion fluid velocity $\mathbf{v}$, the particle density n, ψ, and Φ. Our choice of splitting the stream function Ψ into two parts is not arbitrary, and has a clear physical meaning. Φ is that part of the stream function that is independent of the parallel electron-ion collisional drag. ψ, on the other hand, is that part of the stream function that is exclusively due to the parallel electron-ion collision drag. In fact, if ψ were neglected, we would recover the same set of transport equations obtained by neglecting the parallel electron-ion collisional drag.

The plasma response is obtained from equations (3.44)–(3.47). This set of equations is solved by the Newton-Raphson method (linearization) described in section 3.2.3. In addition, the linearized form of equation (3.44) is integrated using Simpson's rule. Equations (3.45)–(3.47) are discretized using second-order central differences (see Appendix B).

3.5.4 Boundary Conditions

Periodic boundary conditions are used on the domain's boundary except at the obstacle. v_x and v_y are odd functions about the top and bottom boundaries. v_z and n are even functions about these same boundaries. v_x, v_y, and n are even about the left and right boundaries except at the obstacle. v_z is an odd function about these same boundaries. On the obstacle's surface, v_z is taken to be the ion acoustic speed c_s (Bohm's sheath criterion). ψ is equal to zero on the top, bottom, and left boundary. On the right boundary, $\psi = -\Phi$. Since Φ is a definite integral, it does not need any boundary condition.

3.5.5 Numerical Results

The plasma response was obtained for various values of the cross-field diffusion coefficient. For these cases, the magnetic field strength was chosen so that $c_s/\omega_{ci}d = 10^{-2}$. Figure 3.12a and 3.12b are a three-dimensional plot and a contour plot of the particle density. For this particular case, $D_\perp/c_sd = 1/256$, $c_s/\omega_{ci}d = 10^{-2}$, $x_0/d = 2$, and $z_0/d = 640$. For the purpose of comparison, we define a relative deviation $\delta n(x,z)$ as follows:

$$\delta n = \frac{n - n^*}{n^*_\infty}$$

where n and n^* are the particle densities presented in figures 3.12 (parallel electron-ion collisional drag accounted for) and 3.2 (no parallel electron-ion collisional drag). Figure 3.13 is a three-dimensional plot of δn as a function of spatial position. It shows that there is no discernable difference between the two plasma responses in this case. Figure 3.14 is a plot of the parallel collection length versus the inverse of the cross-field diffusion coefficient. For the purpose of comparison, a similar curve for the case where the parallel electron-ion collisional drag was neglected has also been included. This figure also shows that there is no discernable difference between the plasma responses for various values of the diffusion coefficient.

In summary, it is our conclusion that although a dimensional analysis shows that the parallel electron-ion collisional drag may be an important physical effect, its inclusion does not change the plasma response appreciably. This is both a peculiarity and a disappointment. However, this rather extensive investigation is not a total loss. Without this study, one could not justify neglecting the parallel electron-ion collisional drag a priori.

3.6 Isothermal, Viscid Model

In previous sections, we have neglected ion viscosity. However, a simple analysis will show that the ion viscosity tensor has two important terms that cannot be neglected: the cross-field transport of y-directed and z-directed momenta. In this model, we will take these terms into account. The plasma collection process is assumed to be isothermal.

3.6.1 Formulation

Unlike particle diffusion, which is due to electron-ion collision, ion viscosity is due to ion-ion collisions. It represents the diffusion of ion fluid momentum in configuration space. In the absence of anomalous transport, the viscosity coefficients computed from classical transport theory for a strongly magnetized plasma can be written as follows (see equation (2.22)):

$$\left.\begin{aligned} \eta_0 &\sim nT_i\tau_{ii} \\ \eta_1 \sim \eta_2 &\sim \frac{\eta_0}{(\omega_{ci}\tau_{ii})^2} \\ \eta_3 \sim \eta_4 &\sim \frac{\eta_0}{\omega_{ci}\tau_{ii}} \end{aligned}\right\} \tag{3.48}$$

where τ_{ii} is the ion-ion collision time. Since the ions are much heavier than the electrons, the ion-ion collision time is longer than the electron-ion collision time. In particular, $\tau_{ei}/\tau_{ii} \sim \sqrt{m/M}$ provided that $T_e \sim T_i$ (see section 2.1). Using the fact that $D_\perp = c_s^2/\omega_{ce}\omega_{ci}\tau_{ei}$, the cross-field ion viscosity coefficient can be related to the cross-field particle diffusion coefficient as follows:

$$\frac{\eta_1}{nMD_\perp} \sim \frac{\eta_2}{nMD_\perp} \sim \sqrt{M/m} \tag{3.49}$$

The above expression states that the ion momentum can diffuse across the magnetic field much easier than particles can. While momentum is carried by particles, the rates at which momentum and particles diffuse across the magnetic field are different. At first, this seems to be a counter-intuitive result. However, a simple qualitative argument will show that the rate of ion momentum diffusion is in fact greater than that of particle diffusion by a factor of $\sqrt{M/m}$. The subtlety is that particle and momentum diffusion are governed by two different collision processes, i.e., electron-ion and ion-ion collisions, respectively. The step size of the random walk process for ion-ion collision is of the order of the ion Larmor radius, whereas it is only of the order of the electron Larmor radius for electron-ion collision. Following the usual qualitative argument, the cross-field particle diffusion coefficient and the cross-field ion viscosity coefficient can be estimated as follows:

$$D_\perp \sim \rho_e^2/\tau_{ei}$$

$$\eta_\perp \sim \eta_1 \sim \eta_2 \sim nM\rho_i^2/\tau_{ii}$$

Taking the ratio of the above expressions, one obtains:

$$\frac{\eta_\perp}{nMD_\perp} \sim \sqrt{M/m}$$

This result is consistent with equation (3.49).

The cross-field ion viscosity coefficient $\eta_\perp$ is reduced by a factor of $(\omega_{ci}\tau_{ii})^2$ compared with the parallel viscosity coefficient η_0. This is a manifestation of the fact that in an ion-ion collision, the momentum is transported across the magnetic field by a distance of the order of the ion Larmor radius, whereas it is transported along the field by a distance of the order of the ion-ion mean-free-path.

In a two-dimensional flow with y being the ignorable coordinate, the ion viscosity tensor given by equation (2.21) yields:

$$\boldsymbol{\nabla}\cdot\boldsymbol{\pi} = \left(\frac{\partial\pi_{xx}}{\partial x} + \frac{\partial\pi_{zx}}{\partial z}\right)\hat{x} + \left(\frac{\partial\pi_{xy}}{\partial x} + \frac{\partial\pi_{zy}}{\partial z}\right)\hat{y} + \left(\frac{\partial\pi_{xz}}{\partial x} + \frac{\partial\pi_{zz}}{\partial z}\right)\hat{z}$$

where

$$\left.\begin{aligned}
\pi_{xx} &= -\frac{1}{3}\eta_0\left(\frac{\partial v_x}{\partial x} - 2\frac{\partial v_z}{\partial z}\right) - \eta_1\frac{\partial v_x}{\partial x} - \eta_3\frac{\partial v_y}{\partial z} \\
\pi_{xy} &= \pi_{yx} = -\eta_1\frac{\partial v_y}{\partial x} + \eta_3\frac{\partial v_x}{\partial x} \\
\pi_{xz} &= \pi_{zx} = -\eta_2\left(\frac{\partial v_x}{\partial z} + \frac{\partial v_z}{\partial x}\right) - \eta_4\frac{\partial v_y}{\partial z} \\
\pi_{zy} &= -\eta_2\frac{\partial v_y}{\partial z} + \eta_4\left(\frac{\partial v_x}{\partial z} + \frac{\partial v_z}{\partial x}\right) \\
\pi_{zz} &= -\frac{2}{3}\eta_0\left(2\frac{\partial v_z}{\partial z} - \frac{\partial v_x}{\partial x}\right)
\end{aligned}\right\}$$

Following the same qualitative argument presented in section 3.5.1 (dimensional analysis), we can show that the expression above for ion viscosity can be approximated by the following expression:

$$\boldsymbol{\nabla}\cdot\boldsymbol{\pi} \sim -\frac{\partial}{\partial x}\left(\eta_\perp\frac{\partial v_y}{\partial x}\right)\hat{y} - \frac{\partial}{\partial x}\left(\eta_\perp\frac{\partial v_z}{\partial x}\right)\hat{z} \tag{3.50}$$

The first term of the R.H.S. of the above expression represents the transport of the y-directed momentum across the magnetic field. The second term of the R.H.S. represents the cross-field transport of parallel momentum.

Because the addition of ion viscosity does not affect the generalized Ohm's law, the expression for $\mathbf{J}_\perp$ derived from it (see section 3.2.1) is still valid in this model, i.e.,

$$\mathbf{J}_\perp = \frac{ne}{1+\alpha^2}(\mathbf{v}_\perp + \alpha\mathbf{v}_\perp\times\hat{z})$$

Using equations (3.49)–(3.50) and the above expression for $\mathbf{J}_\perp$, the 2-D transport equations can be written as follows:

$$\boldsymbol{\nabla}\cdot(n\mathbf{v}) = S_0 \tag{3.51}$$

$$\boldsymbol{\nabla}\cdot(Mn\mathbf{v}\mathbf{v}) = \frac{neB}{1+\alpha^2}(\mathbf{v}_\perp\times\hat{z} - \alpha\mathbf{v}_\perp) - (T_{i0} + T_{e0})\boldsymbol{\nabla}n - \boldsymbol{\nabla}\cdot\boldsymbol{\pi} + S_0M\mathbf{v} \tag{3.52}$$

where

$$\begin{aligned}
\boldsymbol{\nabla}\cdot\boldsymbol{\pi} &= -\frac{\partial}{\partial x}\left(\eta_\perp\frac{\partial v_y}{\partial x}\right)\hat{y} - \frac{\partial}{\partial x}\left(\eta_\perp\frac{\partial v_z}{\partial x}\right)\hat{z} \\
\frac{\eta_\perp}{nMD_\perp} &= \sqrt{M/m}
\end{aligned}$$

Equations (3.51)–(3.52) are the two-dimensional isothermal, viscid transport equations describing ion fluid motion in the absence of anomalous transport.

3.6.2 Numerical Method and Boundary Conditions

With some manipulation, equations (3.51)–(3.52) can be written as follows:

$$n\boldsymbol{\nabla}\cdot\mathbf{v}+\mathbf{v}\cdot\boldsymbol{\nabla}n=S_0 \tag{3.53}$$

$$\mathbf{v}_\perp=-\frac{D_\perp}{c_s^2}\left[(\mathbf{v}\cdot\boldsymbol{\nabla})\mathbf{v}+\frac{c_s^2}{n}\boldsymbol{\nabla}n+\boldsymbol{\nabla}\cdot\boldsymbol{\pi}\right]+\frac{1}{\omega_{ci}}\hat{z}\times\left[(\mathbf{v}\cdot\boldsymbol{\nabla})\mathbf{v}+\frac{c_s^2}{n}\boldsymbol{\nabla}n+\boldsymbol{\nabla}\cdot\boldsymbol{\pi}\right] \tag{3.54}$$

The plasma response is obtained from equations (3.53)–(3.54) using the Newton-Raphson method (linearization) described in section 3.2.3.

Periodic boundary conditions requiring that no particle and momentum fluxes can be transported into the domain of interest are applied on the boundary except for the surface of the obstacle. There, the Bohm sheath criterion is utilized.

3.6.3 Numerical Results and Discussion

The plasma response was obtained for various values of the cross-field diffusion coefficient. The magnetic field was chosen so that $c_s/\omega_{ci}d=10^{-2}$. Figure 3.15 is a three-dimensional plot of the particle density. For this particular case, $D_\perp/c_sd=1/256$, $c_s/\omega_{ci}d=10^{-2}$, $x_0/d=2$, and $z_0/d=40$. The only difference between the case presented here and the case presented in figure 3.2 is the inclusion of ion viscosity. A comparison between the two cases reveals several interesting qualitative differences.

First, for a hydrogen plasma where $\sqrt{M/m}\sim 43$, the inclusion of ion viscosity reduces the scale length in the parallel direction by roughly an order of magnitude. Second, the ratio of the particle density at the obstacle to the undisturbed particle density is no longer $e^{-1/2}$ as in sections 3.2-3.5 where ion viscosity was neglected. Last, the particle density near the tip of the obstacle is *higher* than that far away from the obstacle. This is a very counter-intuitive result since one expects the particle density far away from the obstacle to be highest. However, the following *intuitive* qualitative argument will show that this behaviour is to be expected. At a given parallel distance away from the obstacle, the particles at the bottom boundary are accelerated toward the obstacle at a faster rate than those elsewhere. In fact, the parallel ion fluid velocity v_z monotonically decreases away from the bottom boundary. Thus, at any given point, parallel momentum is transported across the magnetic field from the bottom boundary to the top boundary. Since the cross-field flux of parallel momentum is zero on both the top and bottom boundaries, parallel momentum is simply being transported from one part of the plasma column to another. The motion toward the obstacle of the ion fluid elements near the bottom boundary, especially those on the bottom boundary, is retarded because they have to drag the slower fluid elements from above with them. Because of this retarding force (ion viscosity), the rate at which particles arrive at the obstacle is reduced, resulting in a lower particle density at the obstacle. The particle collection (scale length in the parallel direction) is therefore reduced accordingly. Near the top boundary, the parallel motion of the ion fluid elements is enhanced since they are being dragged from below by the faster fluid elements. As a result, they pile up on the right boundary above the obstacle and form a *density bump*.

Another explanation, though less intuitive, can be offered to explain the observed behaviour of the plasma response. Because the parallel ion fluid velocity v_z monotonically decreases away from the bottom boundary, the x-directed flux of parallel ion momentum always points away from the shadow region (in the direction from the bottom boundary to the top boundary) except at the top and bottom boundaries. There, the x-directed flux of parallel momentum is zero. Since parallel momentum is being deposited into the region near the top boundary and has no place to go, a density gradient is necessary to balance the additional viscous force, resulting in a *density bump*. The parallel momentum deposited into the region near the top boundary actually comes from the region near the bottom boundary. There, since the parallel momentum is being removed without replacement, an additional density gradient is necessary to balance the viscous force, resulting in further lowering of the particle density on the obstacle's surface.

Figure 3.16 is a plot of the particle collection length versus the inverse of the cross-field particle diffusion coefficient for a hydrogen plasma. The magnetic field was chosen so that $c_s/\omega_{ci}d = 10^{-2}$. For the purpose of comparison, a similar plot for the case where ion viscosity was neglected (see section 3.2) has been included. The lower curve results when ion viscosity is included, whereas the upper curve results when ion viscosity is neglected. Figure 3.16 shows that when ion viscosity is included, the particle collection is reduced roughly by an order of magnitude.

In summary, it is our conclusion that ion viscosity can be an important effect in classical transport theory. Its inclusion changes the qualitative behaviour of the plasma response, e.g., the formation of a *density bump*. For a hydrogen plasma, the scale length in the parallel direction is also reduced by about an order of magnitude when ion viscosity is included.

3.7 Non-Isothermal, Viscid Model

In previous models (see sections 3.2–3.6), the ions and the electrons are assumed to be isothermal and the energy equations are not used. This approach is justified when both species of particles (ions and electrons) can conduct heat along and across the magnetic field at a sufficiently fast rate. In this section, we would like to examine the validity of this assumption.

3.7.1 Basic Assumptions and Formulation

On the obstacle's surface, both the ions and the electrons are assumed to have a parallel sonic flow at the obstacle's surface (Bohm's sheath criterion). Immediately above the obstacle, the flow along the magnetic field for both the ions and the electrons vanish due to symmetry. Therefore, there exists a large perpendicular shear of parallel flow in the neighbourhood of the obstacle's tip. If the perpendicular viscosity coefficient is sufficiently large, the heat generated by viscosity due to this perpendicular shear of parallel flow can make an important contribution to the plasma response. In a strongly magnetized plasma, the heat generated by electron viscosity is small because the electrons have a small perpendicular viscosity coefficient. The heat generated by ion viscosity is, on the contrary, significant because the ions have a much higher perpendicular viscosity coefficient.

The electrons have a high thermal conductivity along the magnetic field because of their light mass. As a result, only a small parallel gradient of T_e is required to conduct heat to a local heat sink, or away from a local heat source. Since the electrons have no significant heat sink or heat source, they remain nearly isothermal. Thus, we conclude that the assumption that the electrons are isothermal is a plausible assumption in this model.

Because the ions are much heavier than the electrons, they have a smaller thermal conductivity coefficient along the magnetic field, and as a result, they cannot conduct heat along the magnetic field sufficiently fast to be isothermal, especially when there exists a significant heat sink or heat source. In this particular study, the heat generated by ion viscosity in the neighbourhood of the obstacle's tip is rather significant. Therefore, the assumption that the ions are isothermal is not a valid assumption. As a result, we will need to use the ion energy equation to describe the ions' energy transport.

With the assumption that the electrons are isothermal, the transport equations can be written as follows (see section 2.2):

$$\boldsymbol{\nabla}\cdot(n\mathbf{v}) = S_0 \tag{3.55}$$

$$\boldsymbol{\nabla}\cdot(Mn\mathbf{v}\mathbf{v}) = ne(\mathbf{E}+\mathbf{v}\times\mathbf{B}) - \boldsymbol{\nabla}(nT_i) - \boldsymbol{\nabla}\cdot\boldsymbol{\pi} + S_0M\mathbf{v} + \mathbf{R} \tag{3.56}$$

$$\begin{aligned}\boldsymbol{\nabla}\cdot\left[\left(\frac{1}{2}Mv^2+\frac{5}{2}T_i\right)n\mathbf{v}\right] &= (ne\mathbf{E}+\mathbf{R}-\boldsymbol{\nabla}\cdot\boldsymbol{\pi})\cdot\mathbf{v} - \pi_{\alpha\beta}\frac{\partial v_\alpha}{\partial\beta} + Q_{ie}\\ &\quad - \boldsymbol{\nabla}\cdot\mathbf{q} + S_E + S_0\left(\frac{1}{2}Mv^2+\frac{3}{2}T_i\right)\end{aligned} \tag{3.57}$$

$$0 = -ne(\mathbf{E}+\mathbf{v}\times\mathbf{B}) + \mathbf{J}\times\mathbf{B} - T_{e0}\boldsymbol{\nabla}n - \mathbf{R} \tag{3.58}$$

where

$$\mathbf{E} = -\nabla\phi$$

$$\mathbf{R} = -\frac{m\nu_0}{e}\mathbf{J}$$

When $T_e \sim T_i$, the electron-ion energy equilibration time is much longer than either the electron-electron or the ion-ion energy equilibration time. We are interested in the short time scale in which the ions and the electrons have reached their respective equilibria without establishing an equilibrium among each other. Q_{ie}, the heat transferred from the electrons to the ions by collisions, is therefore neglected because it occurs over a long time scale in which we are not interested.

A simple dimensional analysis similar to that presented in section 3.5.1 shows that the contribution of ion viscosity in the ion momentum equation can be approximated as follows:

$$\nabla\cdot\boldsymbol{\pi} \sim -\frac{\partial}{\partial x}\left(\eta_\perp\frac{\partial v_y}{\partial x}\right)\hat{y} - \frac{\partial}{\partial x}\left(\eta_\perp\frac{\partial v_z}{\partial x}\right)\hat{z}$$

where

$$\left.\begin{aligned} \eta_\perp &\sim \frac{nT_i}{\omega_{ci}^2\tau_{ii}} \\ &= \sqrt{\frac{M}{m}}\, nMD_{\perp\infty}\frac{r^{3/2}}{1+r}\left(\frac{T_i}{T_{i\infty}}\right)^{-1/2} \\ r &= \frac{T_{e0}}{T_{i\infty}} \\ D_{\perp\infty} &= \frac{c_{s\infty}^2}{\omega_{ce}\omega_{ci}\tau_{ei}} \\ c_{s\infty} &= \sqrt{\frac{T_{e0}+T_{i\infty}}{M}} \end{aligned}\right\} \tag{3.59}$$

τ_{ii} and τ_{ei} are the ion-ion Coulomb collision time and the electron-ion Coulomb collision time, respectively.

$-\pi_{\alpha\beta}\partial v_\alpha/\partial\beta$ is the energy dissipation term due to ion viscosity. It is often referred to as the *heat generated by viscosity.* It represents the conversion of kinetic energy into thermal energy due to ion-ion collisions. A simple dimensional analysis similar to that presented in section 3.5.1 shows that this energy dissipation term can be approximated as follows:

$$Q_{vis} = -\pi_{\alpha\beta}\frac{\partial v_\alpha}{\partial \beta} \sim \eta_\perp\left[\left(\frac{\partial v_y}{\partial x}\right)^2 + \left(\frac{\partial v_z}{\partial x}\right)^2\right]$$

The contribution of the ion heat flux can be written as follows:

$$\nabla\cdot \mathbf{q} = -\frac{\partial}{\partial x}\left(\kappa_\perp\frac{\partial T_i}{\partial x}\right) - \frac{\partial}{\partial z}\left(\kappa_\parallel\frac{\partial T_i}{\partial z}\right)$$

where

$$\left.\begin{aligned}\kappa_\parallel &\sim \frac{nT_i\tau_{ii}}{M}\\ &\sim \frac{1}{D_{\perp\infty}}\left(\frac{c_{s\infty}^2}{\omega_{ci}}\right)^2\sqrt{\frac{m}{M}}\frac{1}{r^{3/2}(1+r)}n\left(\frac{T_i}{T_{i\infty}}\right)^{5/2}\\ \kappa_\perp &\sim \frac{\kappa_\parallel}{(\omega_{ci}\tau_{ii})^2}\\ &\sim \sqrt{\frac{M}{m}}nD_{\perp\infty}\frac{r^{3/2}}{1+r}\left(\frac{T_i}{T_{i\infty}}\right)^{-1/2}\end{aligned}\right\} \tag{3.60}$$

We also need to know the detail (spatial variation) of S_E, the volumetric source of energy. However, since we are interested in the qualitative behaviour of the plasma response, any reasonable choice for S_E will probably suffice. In this particular model, we will take S_E to be spatially uniform, i.e., $S_E = S_{E0}$. It can be readily shown from the transport equations (3.55)–(3.58) that $S_{E0} = S_0 T_{i\infty}$.

The numerical results of section 3.5 suggest that $\mathbf{R}_\parallel$, the parallel electron-ion collisional drag, does not make an important contribution to the generalized Ohm's law. As a result, we will neglect the contribution of $\mathbf{R}_\parallel$ in the transport equations (3.55)–(3.58).

Following the same approach presented in section 3.2, the electric field and the perpendicular current density can be deduced from the generalized Ohm's laws, e.g.,

$$ne\mathbf{E} = -T_{e0}\nabla n$$

$$\mathbf{J}_\perp = \frac{ne}{1+\alpha^2}(\mathbf{v}_\perp + \alpha\mathbf{v}_\perp\times\hat{z})$$

where $\alpha = 1/\tau_{ei}\omega_{ce}$.

Using the above expressions for $\mathbf{E}$ and $\mathbf{J}_\perp$, equations (3.55)–(3.58) can be reduced to the following form:

$$\nabla\cdot(n\mathbf{v}) = S_0 \tag{3.61}$$

$$\begin{aligned}\nabla\cdot(Mn\mathbf{v}\mathbf{v}) =& \frac{neB}{1+\alpha^2}(\mathbf{v}_\perp \times \hat{z} - \alpha\mathbf{v}_\perp) - \nabla[n(T_{e0}+T_i)] \\ &+ \frac{\partial}{\partial x}\left(\eta_\perp \frac{\partial v_y}{\partial x}\right)\hat{y} + \frac{\partial}{\partial x}\left(\eta_\perp \frac{\partial v_z}{\partial x}\right)\hat{z} + S_0 M\mathbf{v}\end{aligned} \tag{3.62}$$

$$\begin{aligned}\frac{3}{2}n\mathbf{v}\cdot\nabla T_i =& -nT_i\nabla\cdot\mathbf{v} + \frac{\partial}{\partial x}\left(\kappa_\perp \frac{\partial T_i}{\partial x}\right) + \frac{\partial}{\partial z}\left(\kappa_\parallel \frac{\partial T_i}{\partial z}\right) \\ &+ \eta_\perp\left[\left(\frac{\partial v_y}{\partial x}\right)^2 + \left(\frac{\partial v_z}{\partial x}\right)^2\right] + S_0 T_{i\infty}\end{aligned} \tag{3.63}$$

where the transports coefficients are given by equations (3.59)–(3.60). Equations (3.61)–(3.63) form a set of self-consistent transport equations appropriate to this model.

The plasma response is obtained by solving the transport equations (3.61)–(3.63) using the standard linearization technique (Newton-Raphson). Appendix D contains a detailed description of the normalization of physical variables as well as a complete listing of the computer code.

3.7.2 Boundary Conditions

The usual periodic boundary conditions are applied on the boundary of the domain except at the obstacle. There, the ions are assumed to have a local sonic flow by virtue of the Bohm's sheath criterion. Above the obstacle, the ions cannot have any parallel flow due to symmetry. As a result, a large perpendicular shear of parallel flow exists at the obstacle's tip, causing heat to be generated (at the expense of the ions' kinetic energy) via ion-ion collisions. The amount of heat generated by ion viscosity depends on the magnitude of the perpendicular shear of parallel flow. Up to the present time, only one-dimensional models of electrostatic sheaths (infinite collecting walls) have been proposed.[14–20] Therefore, the exact transition from local sonic flow to zero parallel flow in the neighbourhood of the obstacle's tip is not known.

We propose the following qualitative argument to estimate the perpendicular shear of parallel flow at the tip of the obstacle. In one-dimensional models of electrostatic sheaths, the ions are assumed to be collisionless and unmagnetized. In the SOL (scrape-off layer) of most fusion tokamaks, the Debye length is much smaller than both the ion-ion mean-free-path and the ion Larmor radius (see section 3.1). Therefore, the ions are more or less collisionless and unmagnetized within the sheath region. Furthermore, since the Debye length is much smaller than the size of a typical obstacle, the sheath region can be treated as being one-dimensional, and the Bohm's sheath criterion can be used. However, within an ion Larmor radius from the tip of the obstacle, the ions with zero mean flow can enter the sheath region via either ion-ion collisions or gyration. Consequently, the one-dimensional Bohm's sheath criterion cannot be applied to the region within a distance of the order of an ion Larmor radius from the obstacle's tip. It is therefore physically plausible to assume that the transition from local sonic flow to zero parallel flow occurs within a distance of the order of an ion Larmor radius, i.e.,

$$\left.\frac{\partial v_z}{\partial x}\right|_{tip} \sim -\left.\frac{c_s}{\rho_i}\right|_{tip}$$

The above expression can be used in conjunction with the Bohm's sheath criterion to obtain the plasma response. Because of the inherent uncertainty associated with the treatment of the obstacle's tip, the plasma response obtained can only provide us with the qualitative behaviour of the actual plasma response.

3.7.3 Numerical Results and Discussion

The plasma response was obtained for various values of the cross-field diffusion coefficient. In this particular study, the plasma is assumed to consist of only electrons and protons, i.e., $\sqrt{M/m} \sim 43$. The magnetic field was chosen so that

$c_{s\infty}/\omega_{ci}d = 10^{-2}$. Figures 3.17–3.20 are three-dimensional plots of the parallel flow, the ion temperature, the particle density, and the ion pressure, respectively. For this particular case, $D_{\perp\infty}/c_{s\infty}d = 1/256$, $c_{s\infty}/\omega_{ci}d = 10^{-2}$, $T_{e0}/T_{i\infty} = 1$, $x_0/d = 2$, and $z_0/d = 40$. The viscosity coefficient and the thermal conductivities are related to the cross-field diffusion coefficient by equations (3.59)–(3.60).

Figure 3.17 shows that the parallel flow (v_z) is nearly uniform across the surface of the obstacle, and that a large perpendicular shear of parallel flow exists only within a small region away from the obstacle's tip. Thus, the effect of ion heating due to viscosity is localized to a small region near the tip of the obstacle.

Figure 3.18 shows that the ion temperature is strongly enhanced in the neighbourhood of the obtacle's tip. Furthermore, $\partial T_i/\partial x$ is discontinuous at the obstacle's tip. The reason is that the heat generated by ion viscosity due to the perpendicular shear of parallel flow at the obstacle's tip is treated as a *point source* of energy. In order to thermally conduct heat away from such a point source, the perpendicular derivative of the ion temperature must be discontinuous. There is an apparent paradox regarding how the ions can sustain such a large perpendicular shear of parallel flow, and thereby converts kinetic energy into thermal energy by means of viscous heating. How is it possible that the ions can heat themselves up indefinitely? The explanation is that the ions can sustain such a large perpendicular shear of parallel flow by accelerating through the presheath's potential. The ions' kinetic energy is then converted into thermal energy via ion-ion collisions (viscosity). Another question is, of course, how the sheath's potential can accelerate ions indefinitely without collapsing. The following hypothetical situation will help to demonstrate this question.

Imagine a collection of k electrons tightly bounded on a finite-sized object, e.g., the obstacle in our particular study. Suppose further that the object on which the electrons are bounded is a metallic sphere of radius r_0. Consequently, the electrostatic potential due to this metallic sphere is

$$\phi = -\frac{ke}{r}$$

where $r \geq r_0$. A singly charged ion starting from rest at infinity will be accelerated toward the object according to

$$\frac{1}{2}Mv^2 + e\phi = 0$$

Upon arrival at the metallic sphere, the ion obtains a speed of

$$v_0 = \sqrt{-\frac{2e\phi_0}{M}} = \sqrt{\frac{2ke^2}{Mr_0}}$$

After the arrival to the ion, the electrostatic potential due to the metallic sphere is

$$\phi = -\frac{(k-1)e}{r}$$

where $r \geq r_0$. It is evident that the ion derives its kinetic energy from the electrostatic potential. The initial electrostatic field has enough energy to collect only k singly charged ions. After collecting k singly charged ions, the metallic sphere is neutralized, and the initial electrostatic potential energy is completely converted into kinetic energy.

By the same token, we can argue that the electrostatic sheath cannot accelerate ions indefinitely. Yet, the Bohm's sheath criterion insists that the sheath accelerates the ions to the local ion acoustic speed indefinitely. How is this possible?

This apparent paradox can be resolved by noting that the sheath's electrostatic potential is set up in such a manner that the electrons and the ions arrive at the sheath in equal numbers. Therefore, for every ion that enters the sheath, there is an accompanying electron. Consequently, the sheath's electrostatic potential is unchanged, i.e., it is sustained indefinitely. Of course, the collected electrons and ions will have to be replenished. The thermal energy of the source electrons is the source of energy from which the electrostatic sheath derives its energy. The electrostatic energy of the sheath is in turn the source of energy from which the accelerating ions derive their kinetic energy. The ions' kinetic energy is in turn converted into thermal energy by means of ion-ion collisions. We see that the transfer of thermal energy from the electrons to the ions is rather subtle.

Figure 3.19 shows that the particle density builds up above the obstacle, and that it decreases sharply in a small region near the tip of the obstacle. The build-up of particles is an effect due to ion viscosity (see section 3.5). Near the obstacle where the ions are heated up significantly, the particle density is sharply reduced in order to keep the ion pressure from being too high. Otherwise, the force balance equation (ion momentum equation) cannot be satisfied. Figure 3.20 shows that the ion pressure is indeed not too strongly enhanced in the region near the obstacle where the ion temperature is significantly enhanced.

Comparing figures 3.18 and 3.19 shows that the plasma response possesses two markedly different scale lengths: a long scale length over which particles diffuse into the obstacle's shadow for collection, and a short scale length over which the ions are heated up significantly due to ion viscous heating. The two scale lengths can be related by the following qualitative argument. As shown in section 3.2.2, the particle collection length $L_{\|}$ is found by equating the contributions of the perpendicular and parallel particle fluxes, resulting in the following expression

$$L_{\|} \sim \frac{c_s d^2}{D_\perp} \tag{3.64}$$

Similarly, L_T, the scale length for the ion temperature, can be found by equating the contributions of the perpendicular and parallel thermal fluxes, i.e.,

$$-\kappa_\perp \frac{\partial T_i}{\partial x} L_T \sim n c_s T_i d$$

A simple estimate of the above expression shows that

$$L_T \sim \frac{n c_s d^2}{\kappa_\perp} \tag{3.65}$$

Using equation (3.60), equations (3.64)–(3.65) can be manipulated to yield:

$$\frac{L_T}{L_{\|}} \sim \sqrt{\frac{m}{M}} \ll 1 \tag{3.66}$$

As a result of equation (3.66), the plasma response possesses a *boundary layer.* This is the reason why we needed a rather large number of grid points in the parallel direction.

In summary, it is our conclusion that the effect of ion heating due to ion viscosity can be important in the region near the obstacle's tip where there exists a large velocity gradient. Furthermore, the introduction of the ion energy equation introduces a boundary layer into the plasma response. Our numerical results suggest that the assumption that the ions are isothermal is a rather poor assumption. Furthermore, the ions cannot be treated as being adiabatic since the ion thermal flux is not negligible.

3.8 Summary

Three major models of plasma collection by an insulating, floating obstacle were proposed in this chapter: (1) the inviscid, isothermal model, (2) the viscid, isothermal model, and (3) the viscid, non-isothermal model. In the absence of anomalous transport, we find that the first two models are not adequate for describing the plasma collection process. The reason is that the cross-field ion viscosity coefficient is much larger than the cross-field particle diffusion coefficient, and as a result, the effect of momentum transport across the magnetic field cannot be neglected. Furthermore, because of a large perpendicular shear of parallel flow in the region near the obstacle's tip, the heat generated by ion viscosity (the conversion of kinetic energy into thermal energy via ion-ion collisions) cannot be neglected. The ions cannot be considered isothermal because they do not thermally conduct heat away from the obstacle's tip fast enough. Although the third model is far more complicated than the first two models, it contains the important physics needed to properly describe the plasma collection process.

According to the viscid, non-isothermal model, the plasma response possesses two highly disparate scale lengths. The particle collection length $L_\parallel$ is the long scale length. L_T, the scale length for the ion temperature, is the short scale length.

The two scale lengths can be related as follows:

$$\left.\begin{aligned} L_{\parallel} &\sim \frac{c_s d^2}{D_\perp} \\ \frac{L_T}{L_{\parallel}} &\sim \sqrt{\frac{m}{M}} \ll 1 \end{aligned}\right\} \tag{3.67}$$

Furthermore, this model predicts that the ion temperature is strongly enhanced in the region near the obstacle's tip where there is a large perpendicular shear of parallel flow. As a result, the tip of the obstacle has to withstand a greater incoming flux of energy. Except near the obstacle's tip, our numerical results indicate that the ions cool slightly as they approach the surface of the obstacle.

Another interesting observation suggested by our numerical results is that one-dimensional models of the plasma collection process do not provide a qualitatively correct plasma response because the edge-effect is not accounted for properly; it is the edge-effect that causes the ion to be heated up.

The particle density is predicted to rise in the region above the obstacle due to the effect of ion viscosity, and to decrease sharply within a layer of thickness L_T due to the heating of ions.

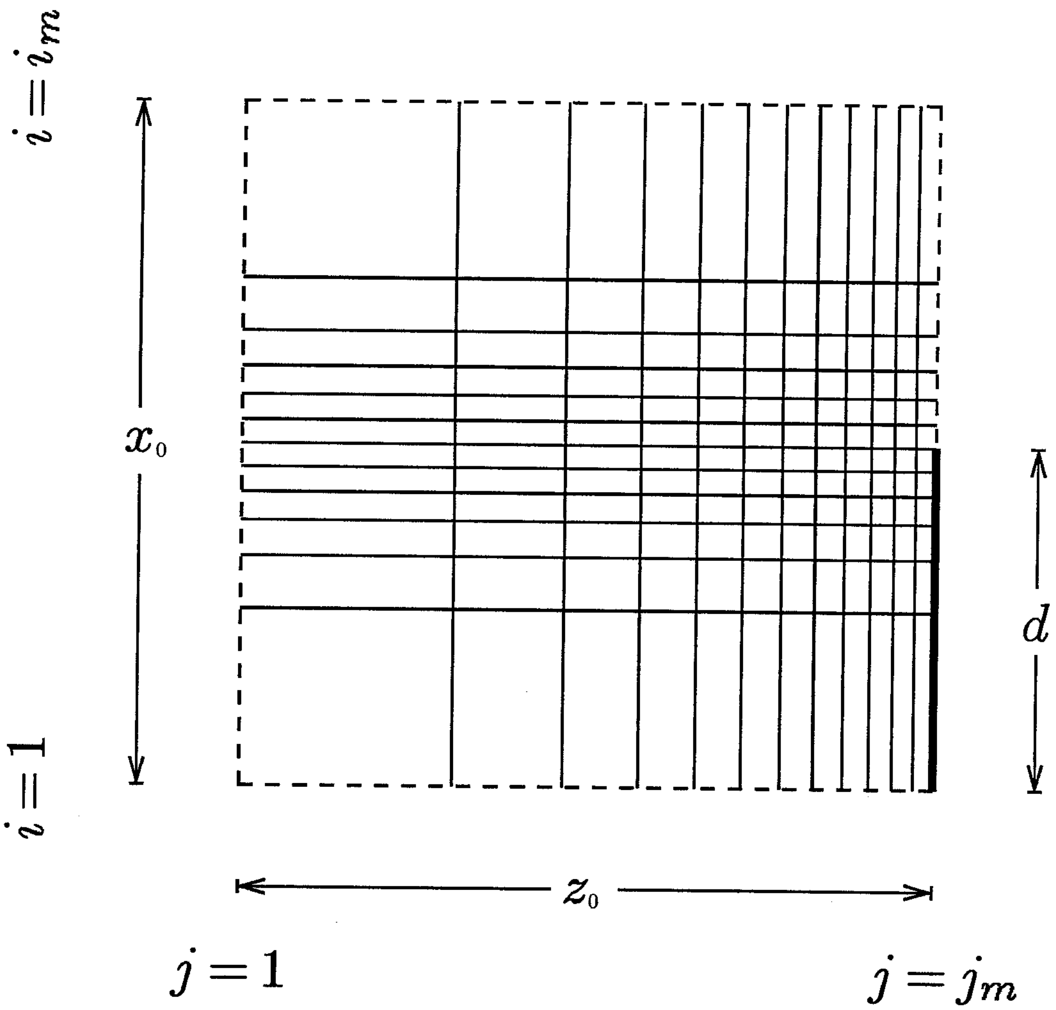

Figure 3.1: Computational grid and indexing convention. A non-uniform, rectangular computational grid is constructed such that the grid is finest at the obstacle's tip where the gradients are expected to be steepest. The indices i and j correspond to the x and z coordinates, respectively.

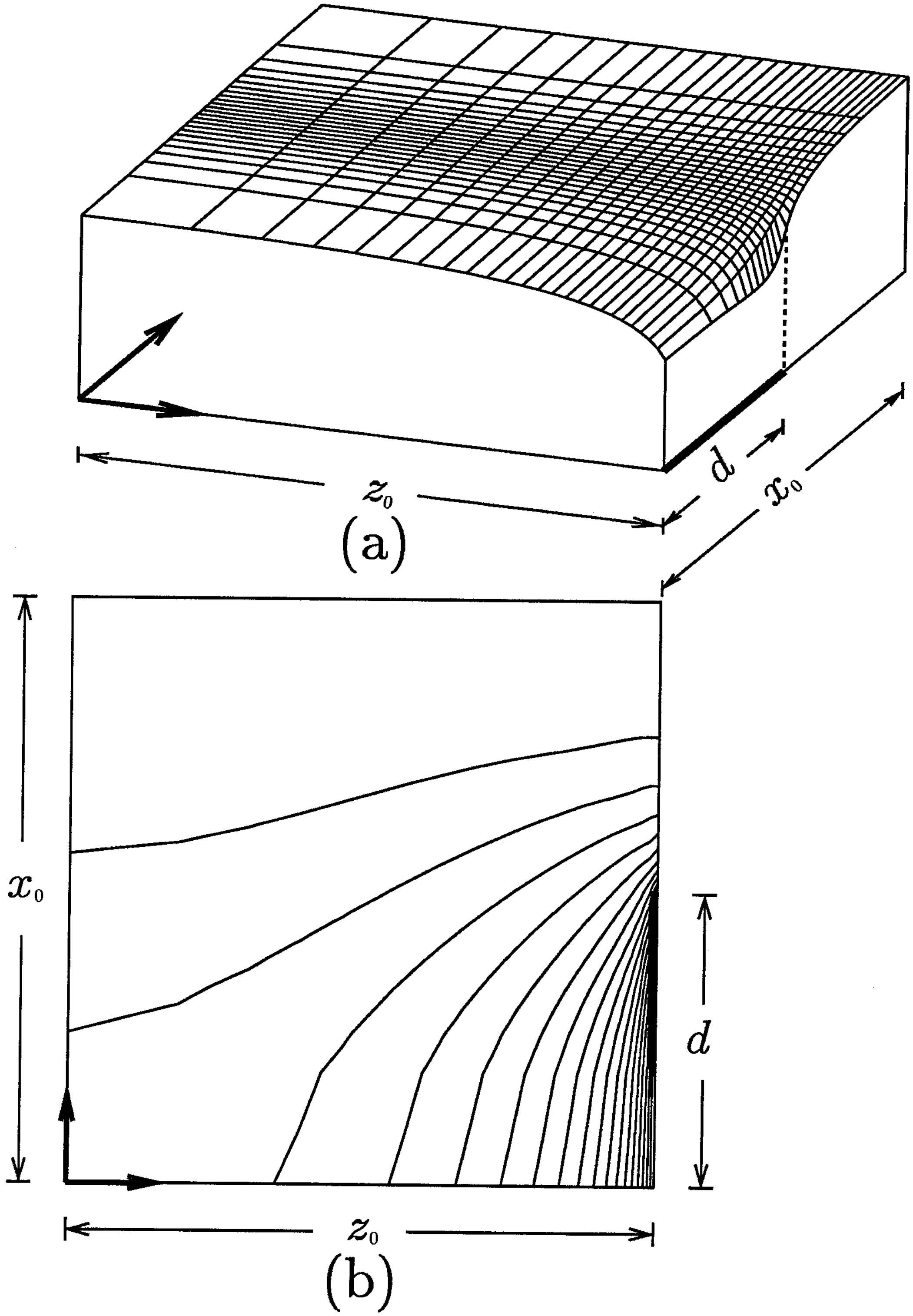

Figure 3.2: $n(x, z)$ obtained from isothermal, inviscid classical transport equations with: $\mathbf{R}_{\parallel}$ neglected, $v_z(x, z)$ discontinuous at obstacle's tip, volumetric particle generation. $D_{\perp}/c_s d = 1/256$, $c_s/\omega_{ci} d = 10^{-2}$, $x_0/d = 2$, and $z_0/d = 640$.

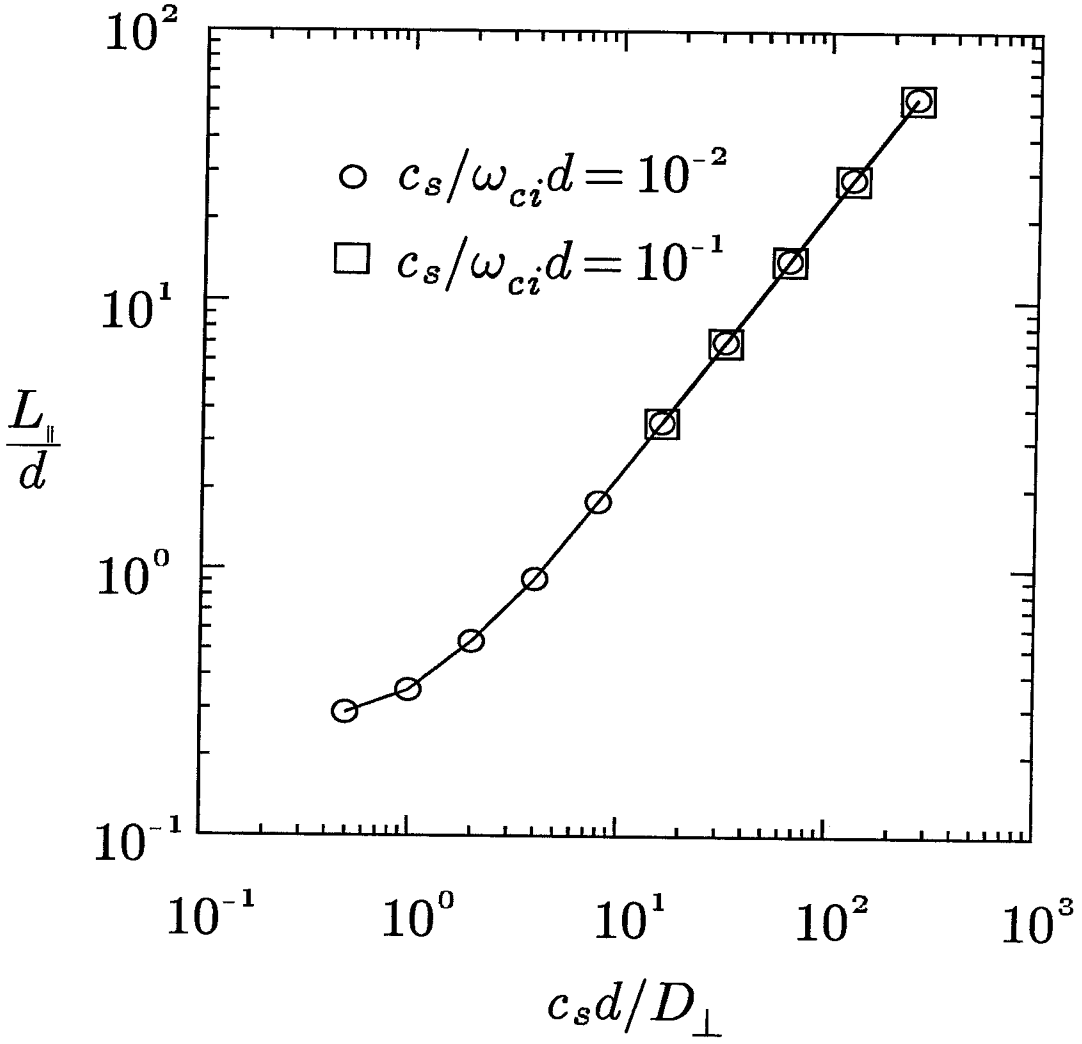

Figure 3.3: $L_\parallel/d$ vs. $c_s d/D_\perp$ for isothermal, inviscid transport equations with: $\mathbf{R}_\parallel$ neglected, $v_z(x,z)$ discontinuous at obstacle's tip, volumetric particle generation. The curves are obtained with $c_s/\omega_{ci}d = 10^{-1}$, 10^{-2}.

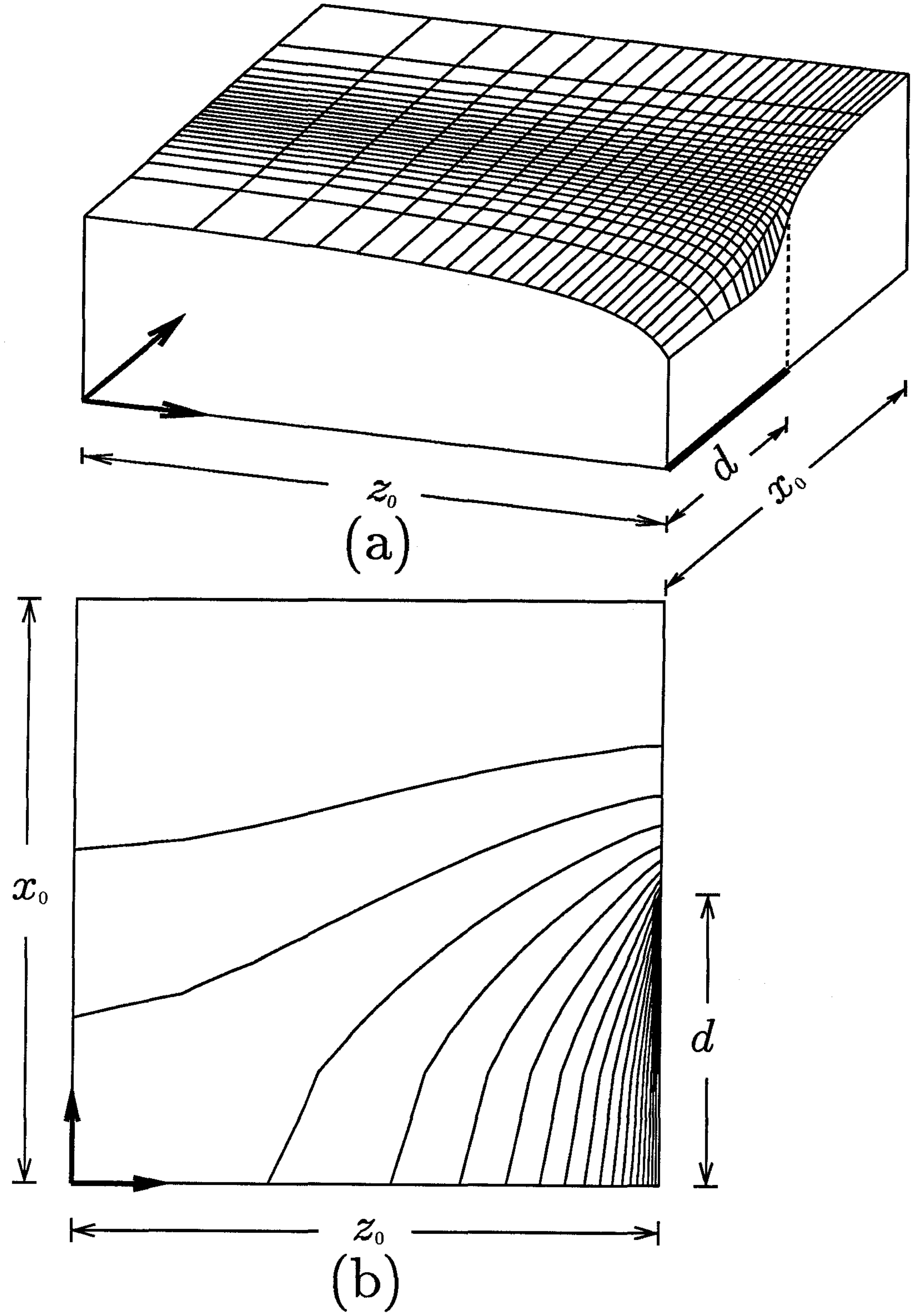

Figure 3.4: $n(x,z)$ obtained from isothermal, inviscid classical transport equations with: $\mathbf{R}_{\|}$ neglected, $v_z(x,z)$ continuous at obstacle's tip, volumetric particle generation. $D_\perp/c_s d = 1/256$, $c_s/\omega_{ci} d = 10^{-2}$, $x_0/d = 2$, and $z_0/d = 640$.

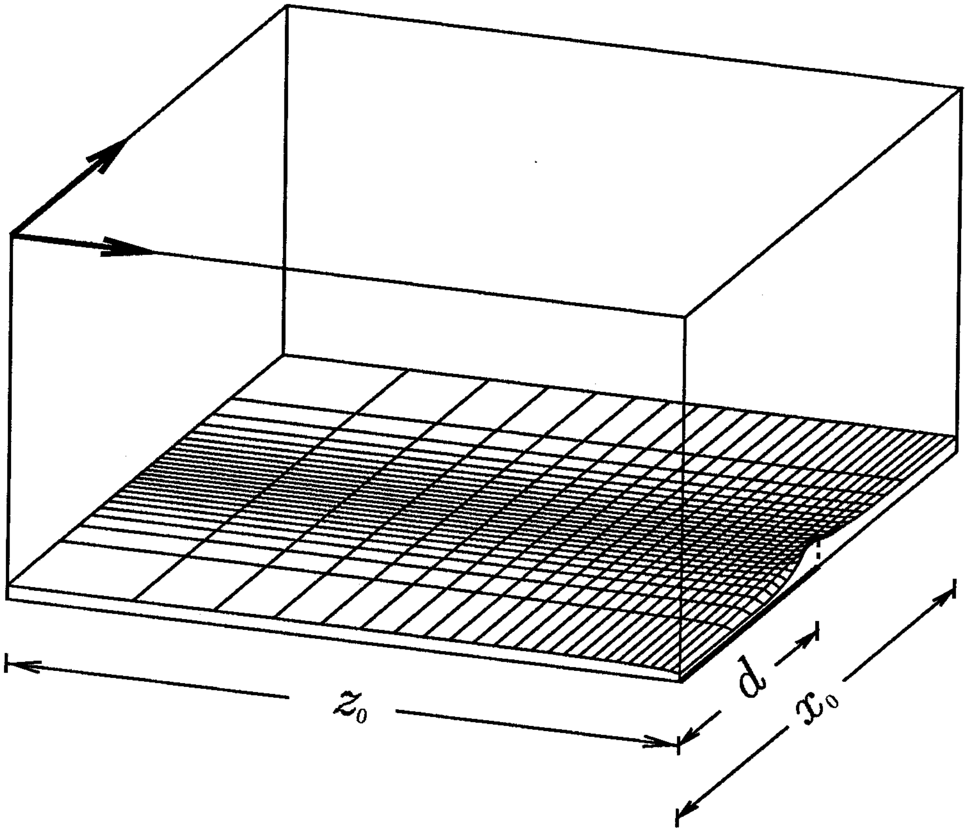

Figure 3.5: 3-D plot of $\delta n(x,z)$ showing the percentage discrepancy between $n(x,z)$ obtained by assuming: (a) $v_z(x,z)$ discontinuous at obstacle's tip (figure 3.4a), and (b) $v_z(x,z)$ continuous at obstacle's tip (figure 3.2a). The rectangular box shown above has a height of 1.

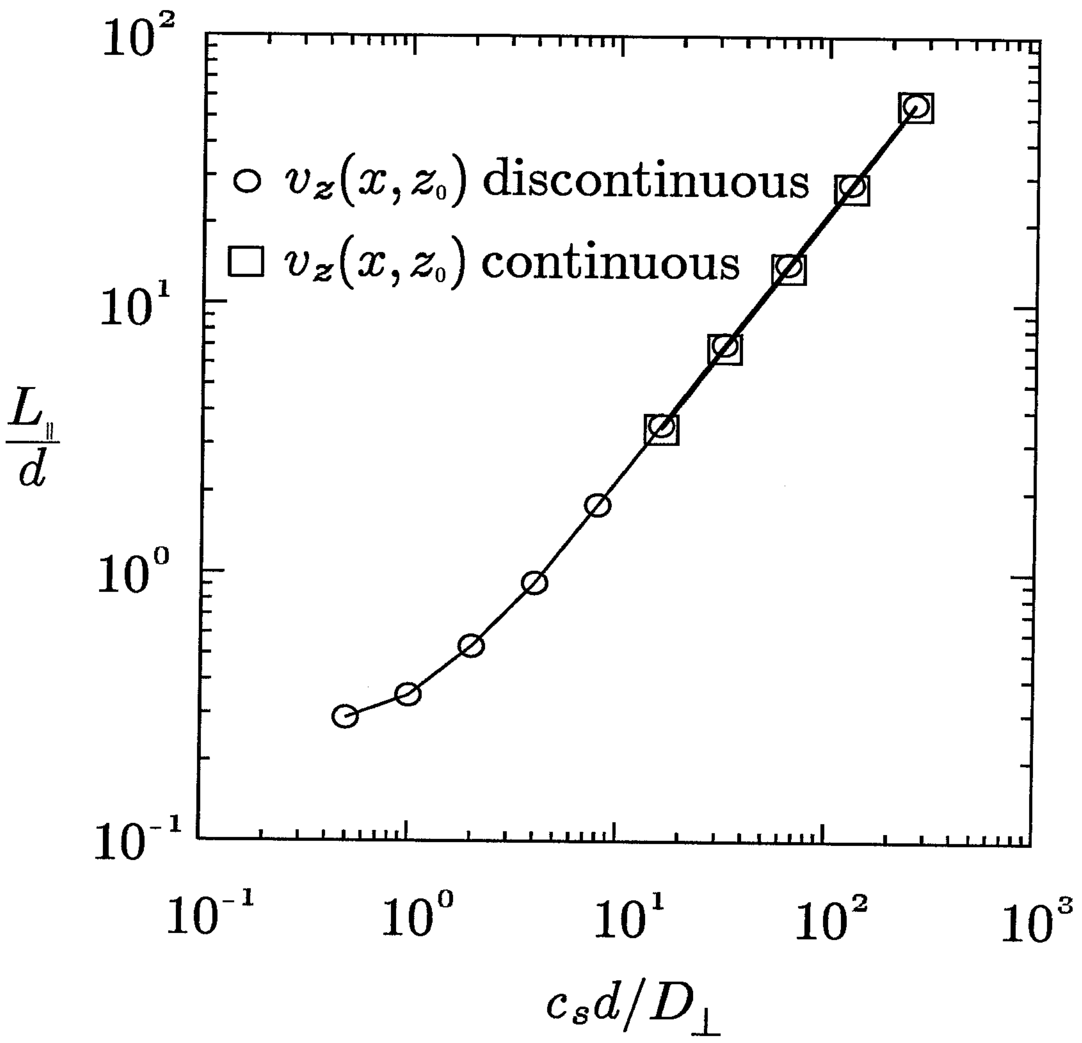

Figure 3.6: $L_\parallel/d$ vs. $c_s d/D_\perp$ for isothermal, inviscid transport equations with: $\mathbf{R}_\parallel$ neglected, $v_z(x,z)$ continuous at obstacle's tip, volumetric particle generation. For comparison, a similar curve obtained by assuming that $v_z(x,z)$ is discontinuous at the obstacle's tip (figure 3.3) is also included. $c_s/\omega_{ci}d = 10^{-2}$ for both curves.

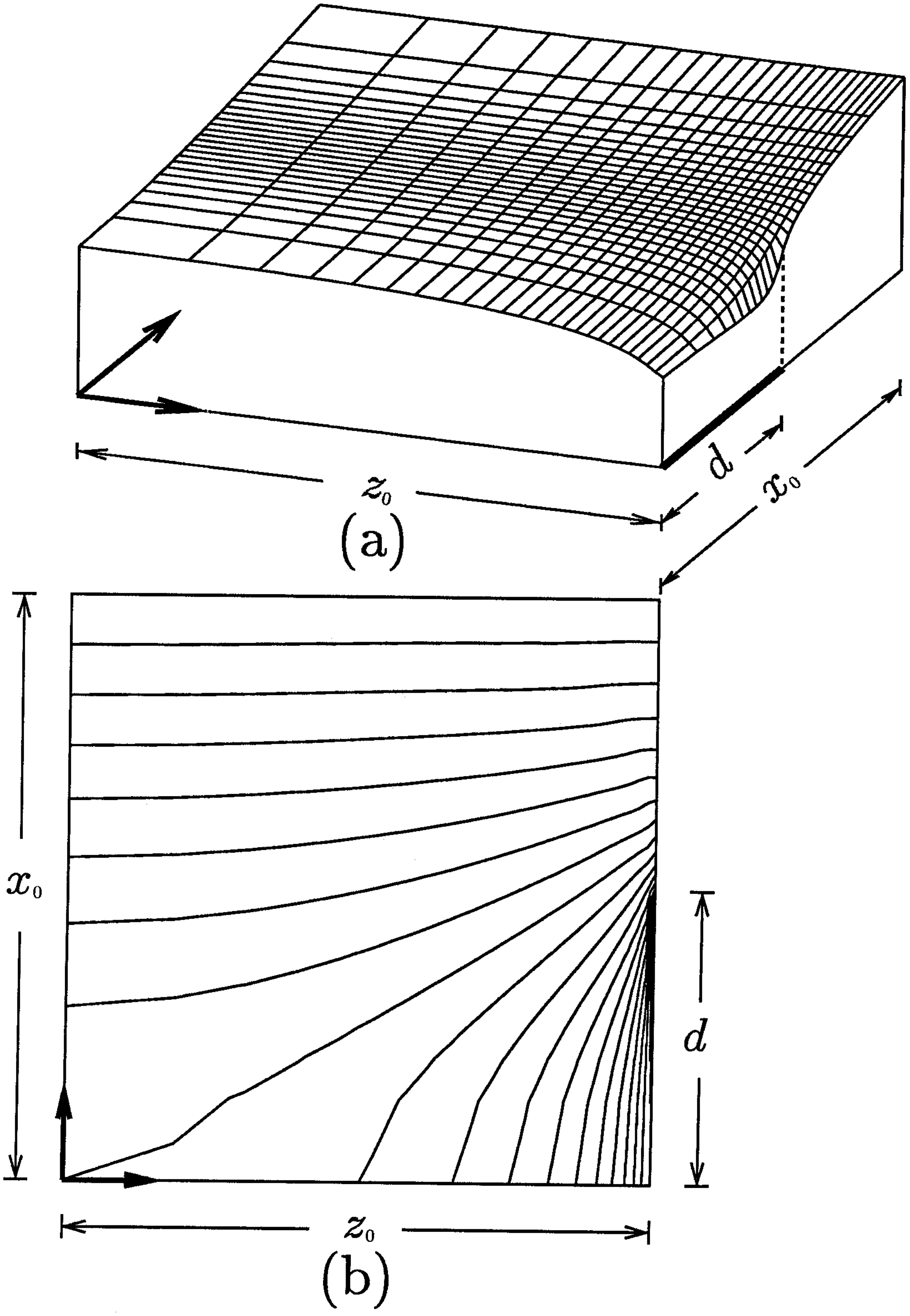

Figure 3.7: $n(x, z)$ obtained from isothermal, inviscid classical transport equations with: $\mathbf{R}_{\|}$ neglected, $v_z(x, z)$ discontinuous at obstacle's tip, replacement particles coming from top boundary. $D_{\perp}/c_s d = 1/256$, $c_s/\omega_{ci} d = 10^{-2}$, $x_0/d = 2$, $z_0/d = 640$.

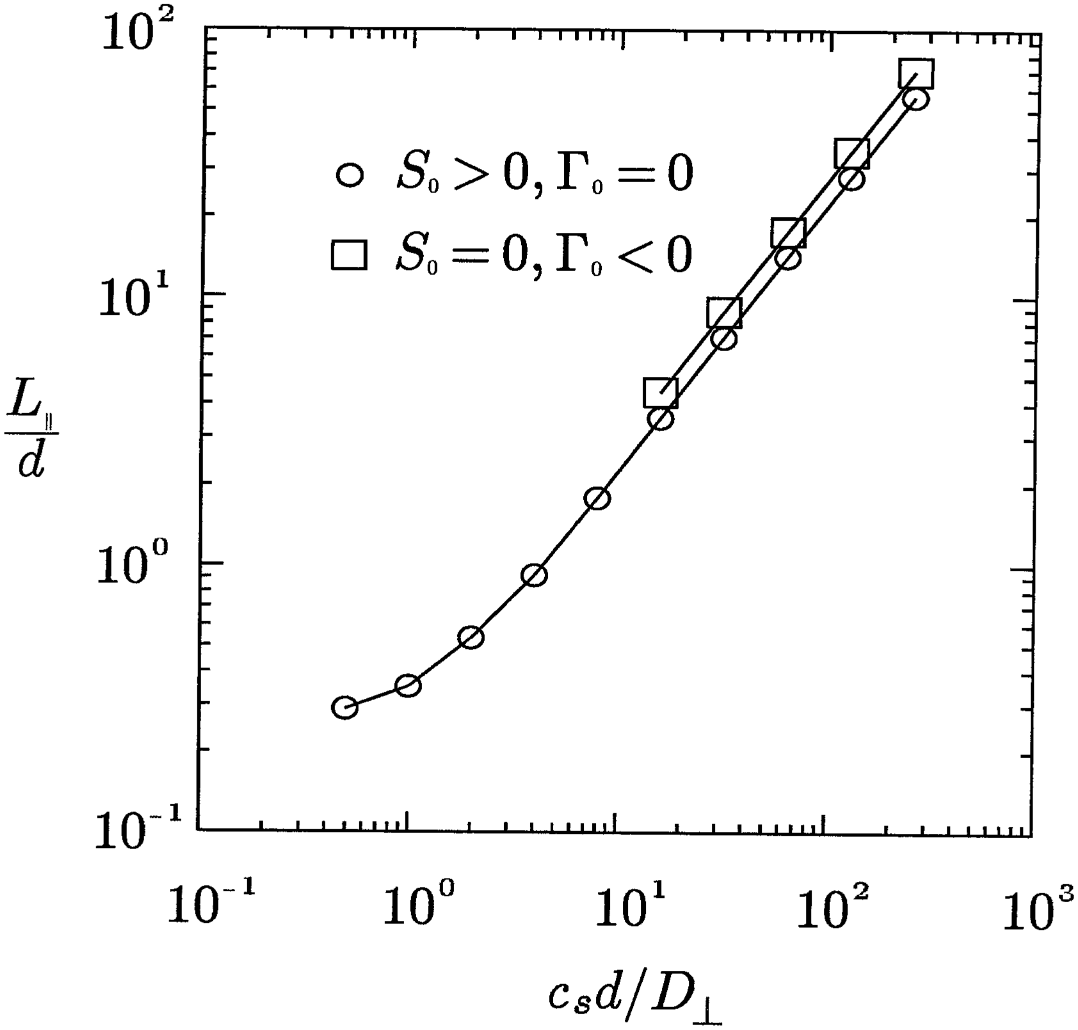

Figure 3.8: $L_\parallel/d$ vs. $c_s d/D_\perp$ for isothermal, inviscid transport equations with: $\mathbf{R}_\parallel$ neglected, $v_z(x,z)$ continuous at obstacle's tip, replacement particles coming from top boundary (no volumetric particle generation). For comparison, a similar curve obtained by assuming that the replacement particles are generated throughout the volume (figure 3.6) is also included. $c_s/\omega_{ci}d = 10^{-2}$ for both curves.

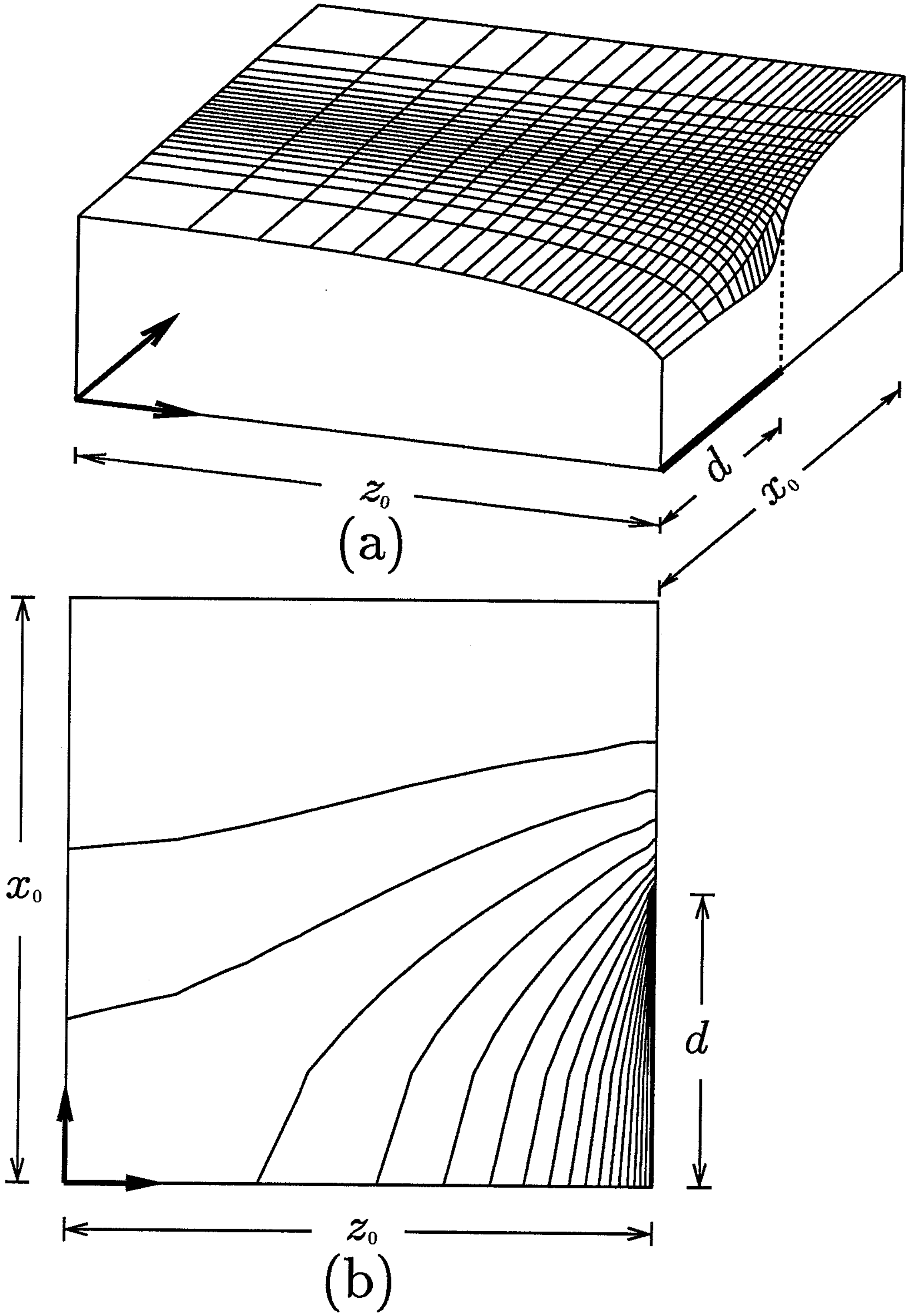

Figure 3.9: $n(x,z)$ obtained from isothermal, inviscid classical transport equations with: $\mathbf{R}_{\parallel}$ neglected, $v_z(x,z)$ continuous at obstacle's tip, volumetric particle generation, $D_{\perp} = D_{\perp\infty}(n/n_{\infty})$. $D_{\perp\infty}/c_s d = 1/256$, $c_s/\omega_{ci} d = 10^{-2}$, $x_0/d = 2$, $z_0/d = 640$.

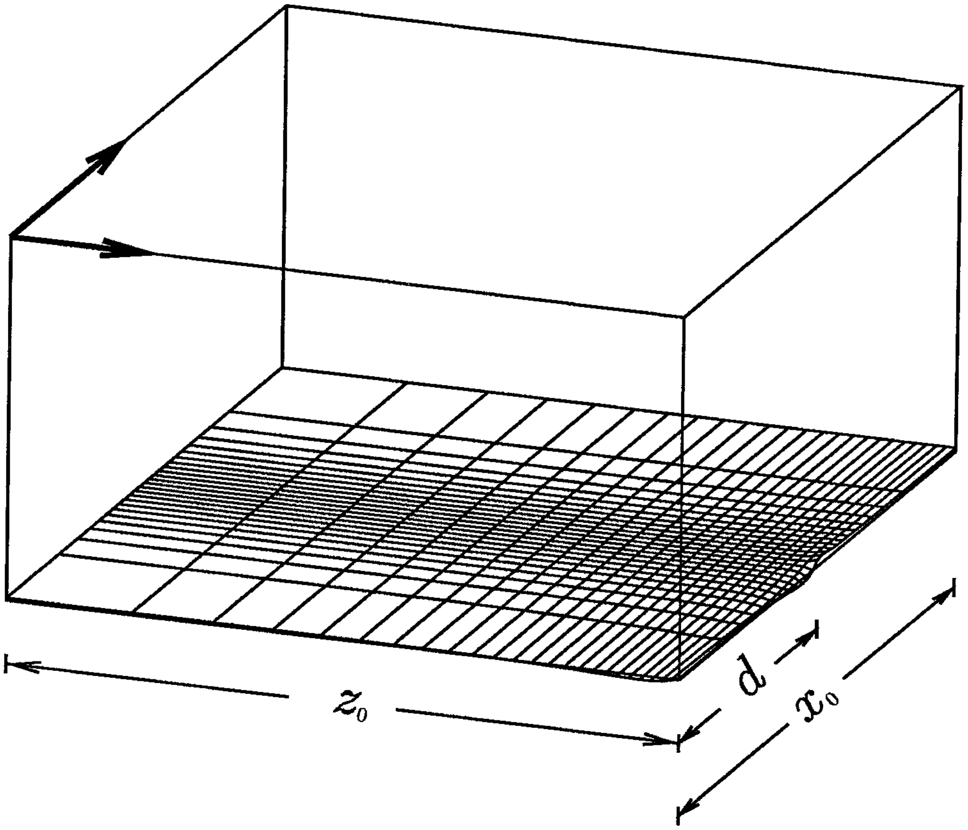

Figure 3.10: 3-D plot of $\delta n(x,z)$ showing the percentage discrepancy between $n(x,z)$ obtained by assuming: (a) $D_\perp = D_{\perp\infty}(n/n_\infty)$ (figure 3.9a), and (b) $D_\perp$ = constant (figure 3.2a). $D_{\perp\infty}/c_s d = 1/256$, $c_s/\omega_{ci} d = 10^{-2}$, $x_0/d = 2$, and $z_0/d = 640$. The rectangular box shown above has a height of 1.

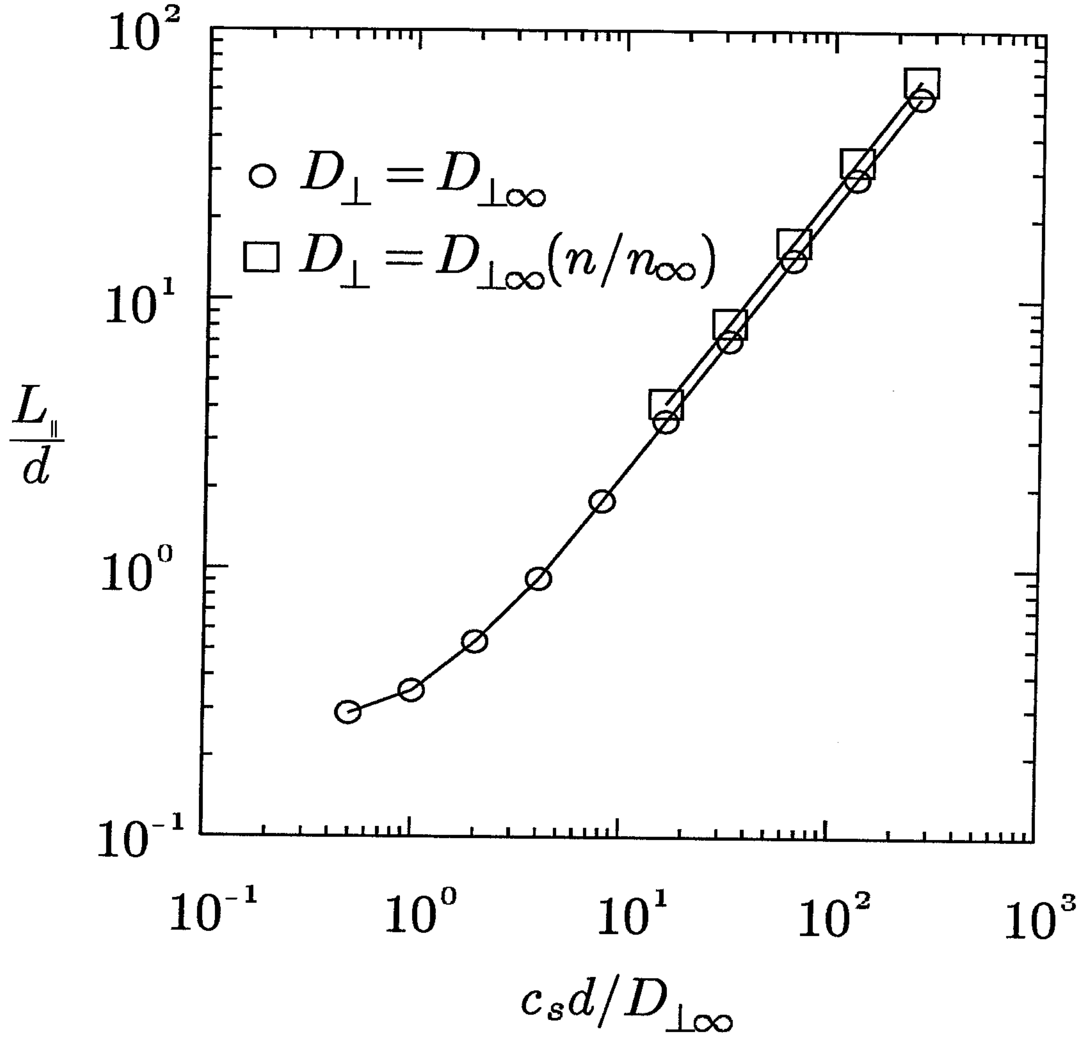

Figure 3.11: $L_\parallel/d$ vs. $c_s d/D_\perp$ for isothermal, inviscid transport equations with: $\mathbf{R}_\parallel$ neglected, $v_z(x,z)$ continuous at obstacle's tip, volumetric particle generation, $D_\perp = D_{\perp\infty}(n/n_\infty)$. For comparison, a similar curve obtained by assuming that $D_\perp =$ constant (figure 3.8) is also included. $c_s/\omega_{ci}d = 10^{-2}$ for both curves.

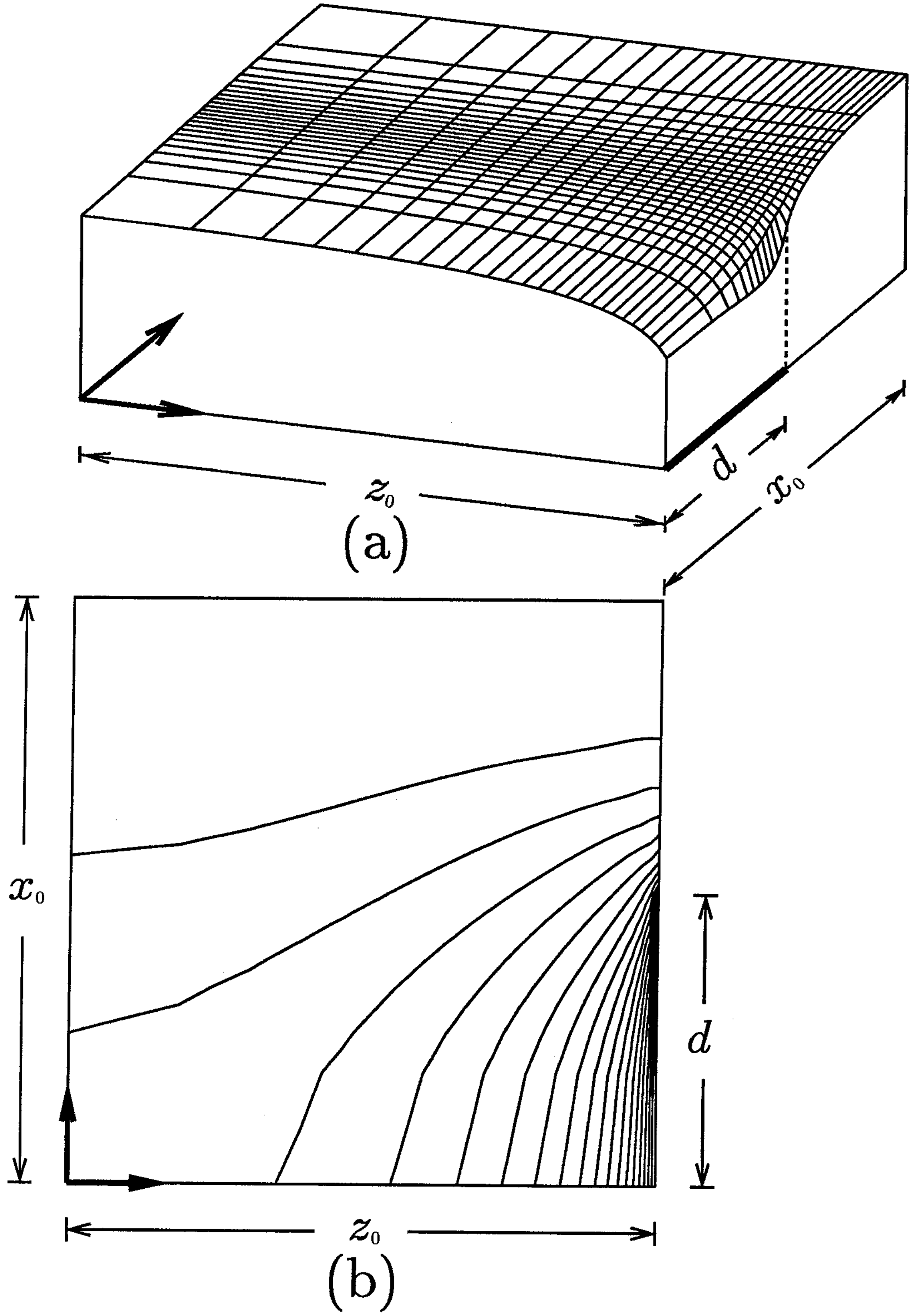

Figure 3.12: $n(x, z)$ obtained from isothermal, inviscid classical transport equations with: $\mathbf{R}_{\parallel}$ included, $v_z(x, z)$ discontinuous at obstacle's tip, volumetric particle generation. $D_{\perp}/c_s d = 1/256$, $c_s/\omega_{ci} d = 10^{-2}$, $x_0/d = 2$, and $z_0/d = 640$.

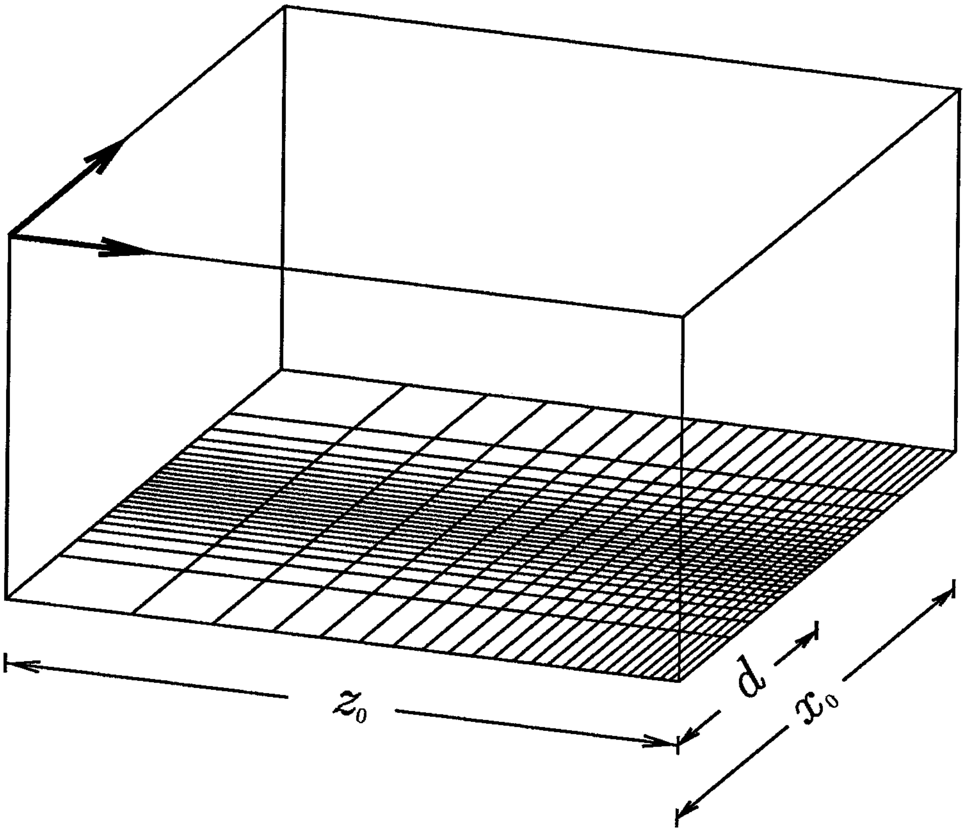

Figure 3.13: 3-D plot of $\delta n(x,z)$ showing the percentage discrepancy between $n(x,z)$ obtained from isothermal, inviscid classical transport equations with: (a) $\mathbf{R}_{\|}$ included (figure 3.12a), and (b) $\mathbf{R}_{\|}$ neglected (figure 3.2a). The rectangular box shown above has a height of 1.

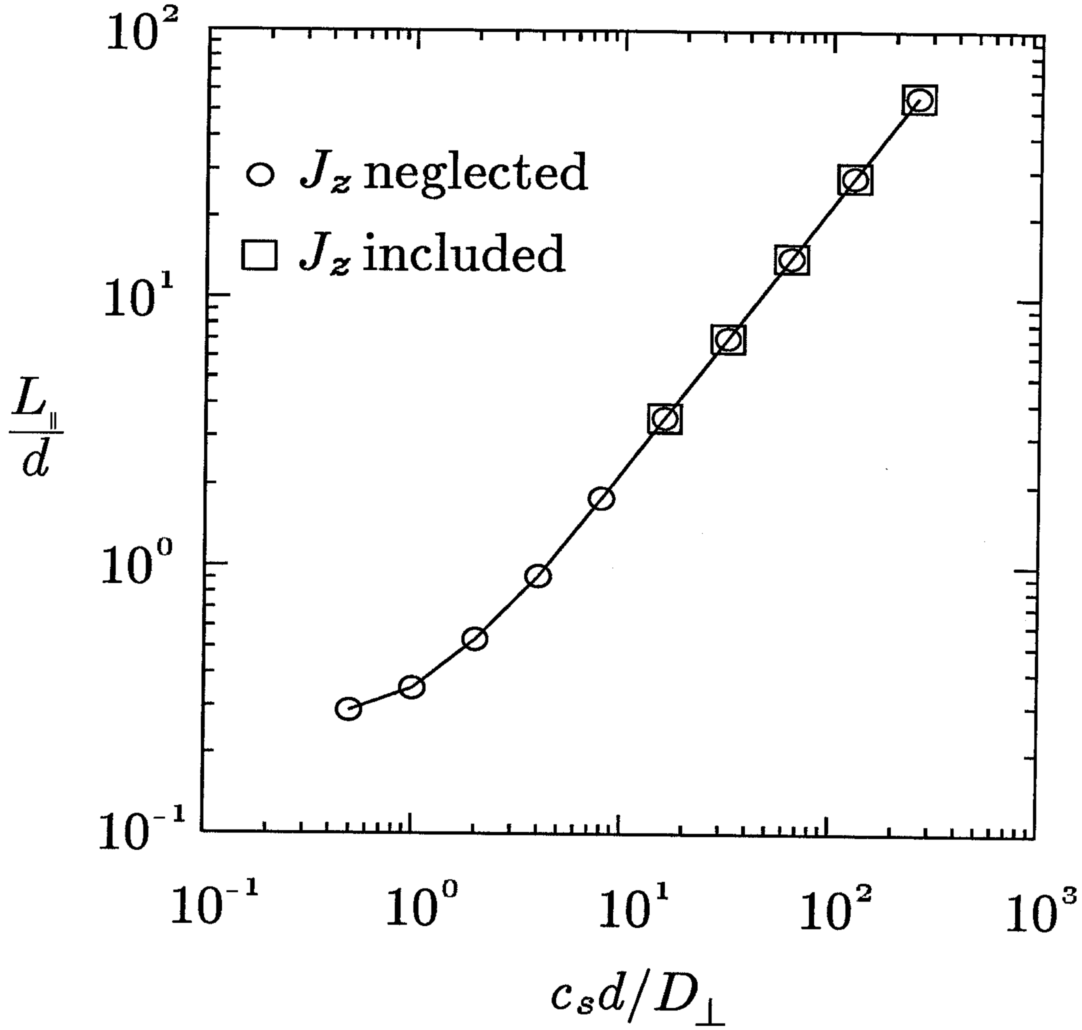

Figure 3.14: $L_\parallel/d$ vs. $c_s d/D_\perp$ for isothermal, inviscid transport equations with: $\mathbf{R}_\parallel$ included, $v_z(x,z)$ discontinuous at obstacle's tip, volumetric particle generation. For comparison, a similar curve obtained with $\mathbf{R}_\parallel$ neglected (figure 3.3) is also included. $c_s/\omega_{ci}d = 10^{-2}$ for both curves. Note that $\mathbf{R}_\parallel$ and $\mathbf{J}_\parallel$ are related by a multiplicative constant.

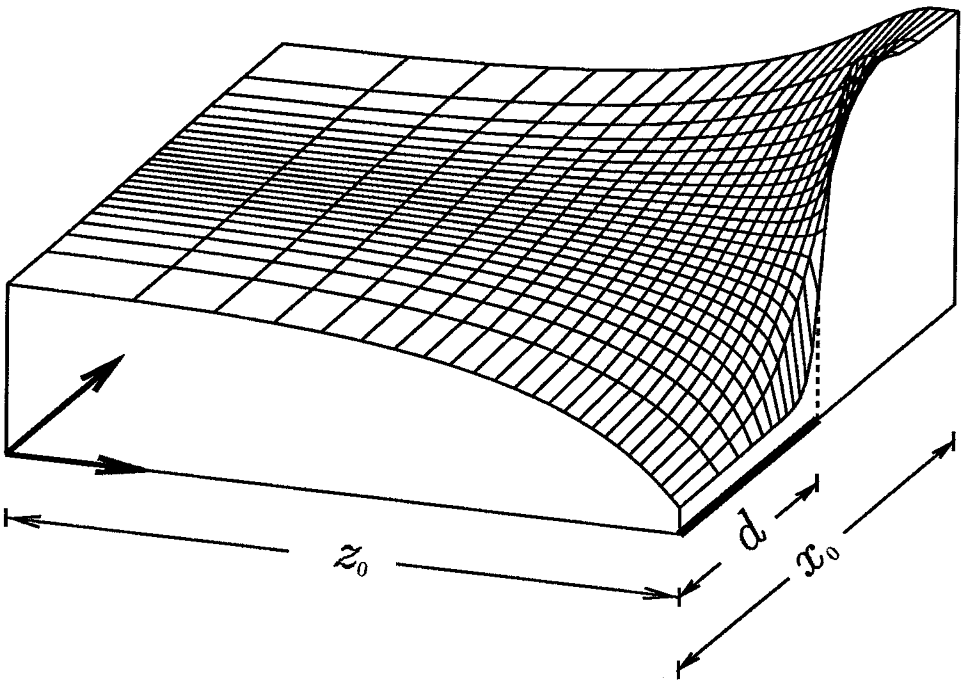

Figure 3.15: 3-D plot of $n(x, z)$ obtained from isothermal, viscid classical transport equations with: $\mathbf{R}_{\|}$ neglected, $v_z(x, z)$ discontinuous at obstacle's tip, volumetric particle generation. $D_\perp / c_s d = 1/256$, $c_s/\omega_{ci} d = 10^{-2}$, $x_0/d = 2$, $z_0/d = 640$. Note that a *density bump* is formed above the obstacle.

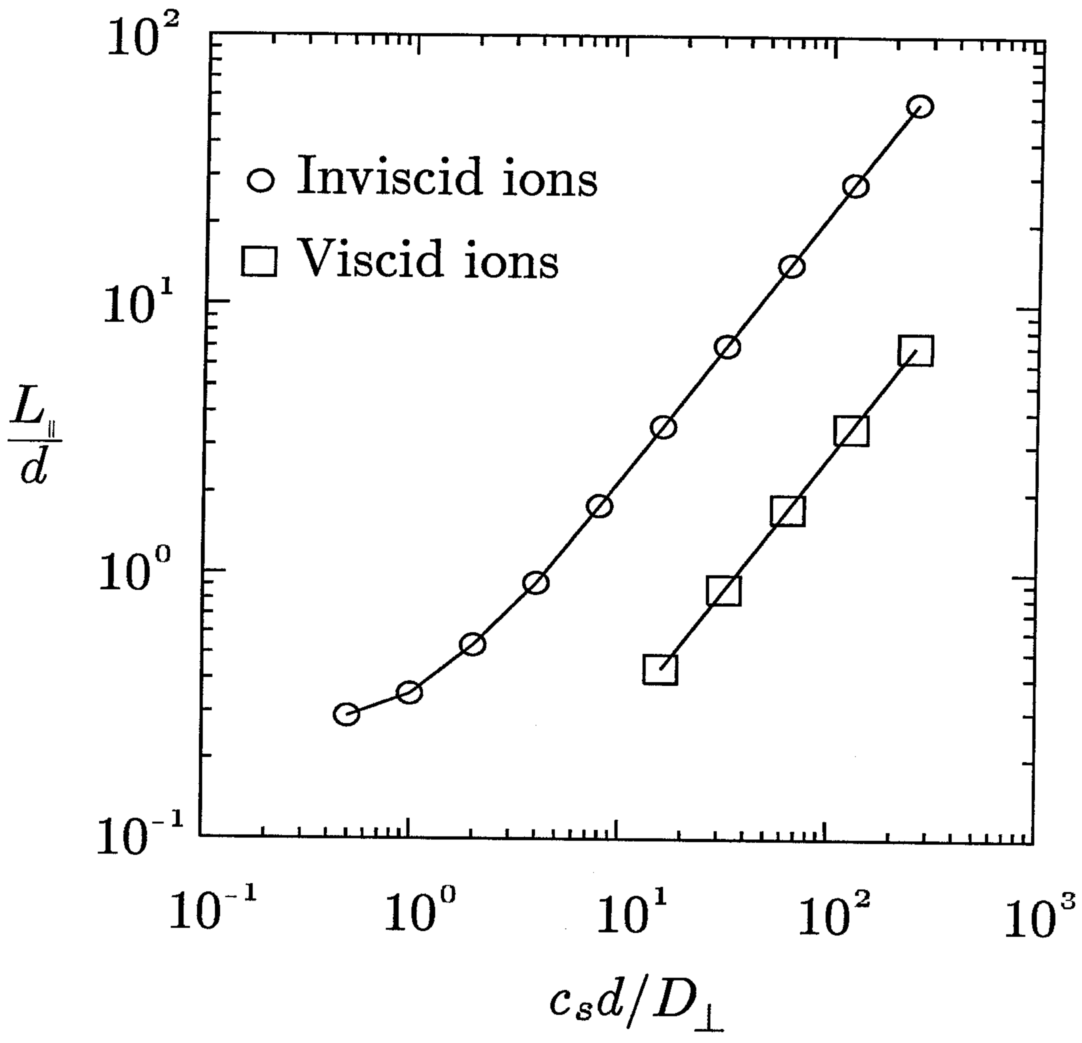

Figure 3.16: $L_\parallel/d$ vs. $c_s d/D_\perp$ for isothermal, viscid transport equations with: $\mathbf{R}_\parallel$ neglected, $v_z(x,z)$ discontinuous at obstacle's tip, volumetric particle generation. For comparison, a similar curve obtained by assuming that the ions are inviscid is also included (figure 3.3). $c_s/\omega_{ci}d = 10^{-2}$ for both curves. The plasma is taken to be a hydrogen plasma, i.e., $\sqrt{M/m} \sim 43$. Note that the inclusion of ion viscosity reduces the parallel scale length by about an order of magnitude.

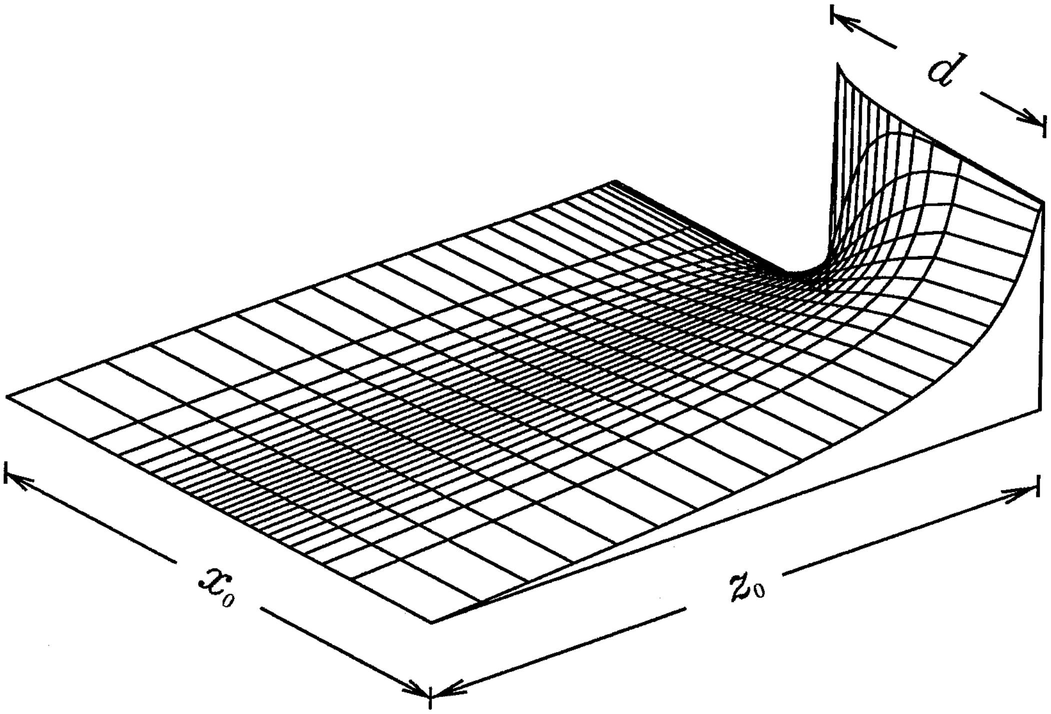

Figure 3.17: 3-D plot of $v_z(x,z)$ obtained from non-isothermal, viscid classical transport equations with: $\mathbf{R}_{\|}$ neglected, $v_z(x,z)$ discontinuous at obstacle's tip, volumetric particle generation. $D_{\perp\infty}/c_{s\infty}d = 1/256$, $T_{e0}/T_{i\infty} = 1$, $M/m \sim 1837$, $c_{s\infty}/\omega_{ci}d = 10^{-2}$, $x_0/d = 2$, and $z_0/d = 40$. The transport coefficients are taken to be the Braginskii transport coefficients. The numerical results were obtained for a grid of 49×193. However, a grid of only 25×25 is shown for clarity.

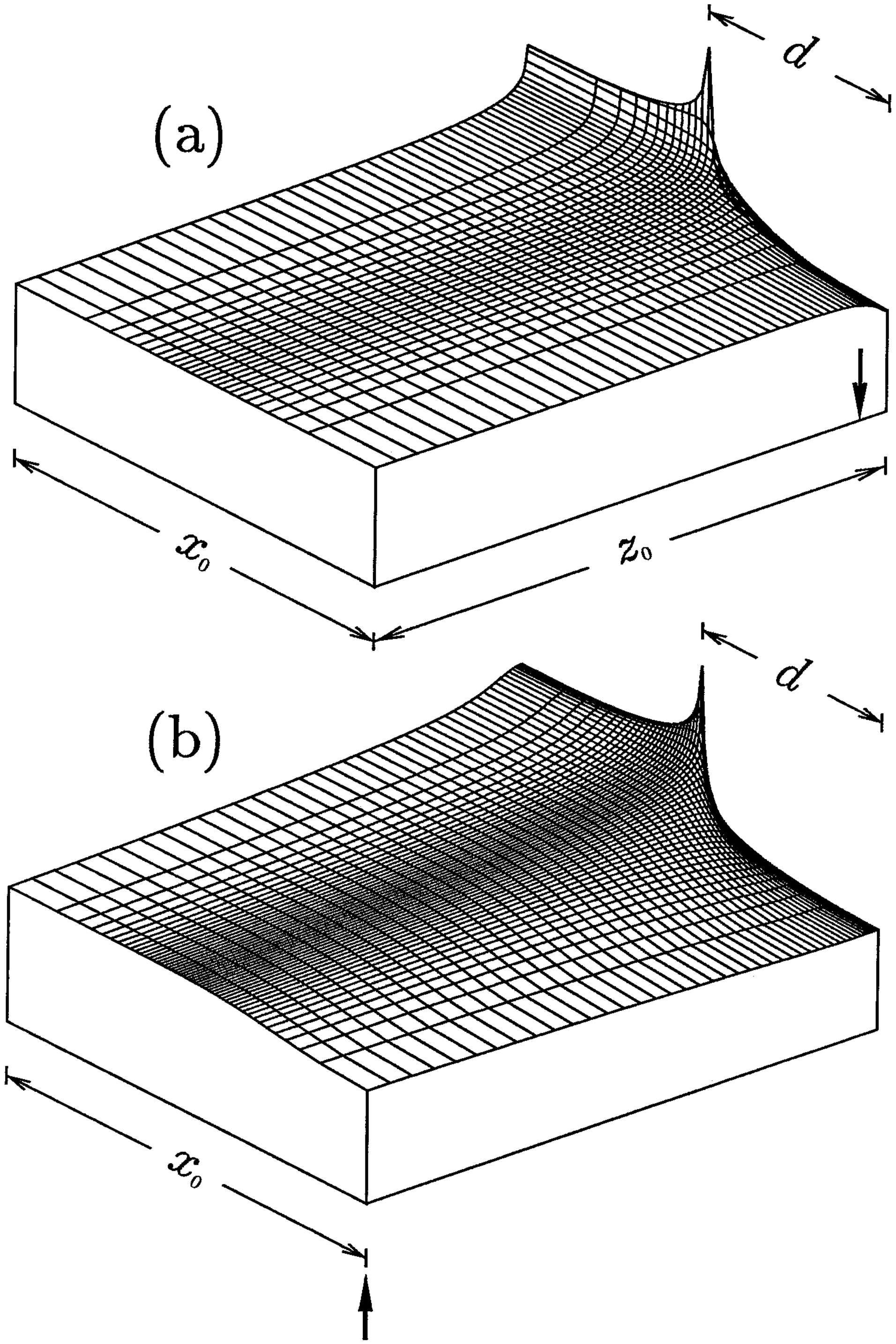

Figure 3.18: $T_i(x,z)$ obtained from non-isothermal, viscid classical transport equations with: $\mathbf{R}_\parallel$ neglected, $v_z(x,z)$ discontinuous at obstacle's tip, volumetric particle generation. $D_{\perp\infty}/c_{s\infty}d = 1/256$, $T_{e0}/T_{i\infty} = 1$, $M/m \sim 1837$, $c_{s\infty}/\omega_{ci}d = 10^{-2}$, x_0/d=2, z_0/d=40. The transport coefficients are taken to be the Braginskii transport coefficients. The dark arrows in (a) and (b) refer to the same physical location.

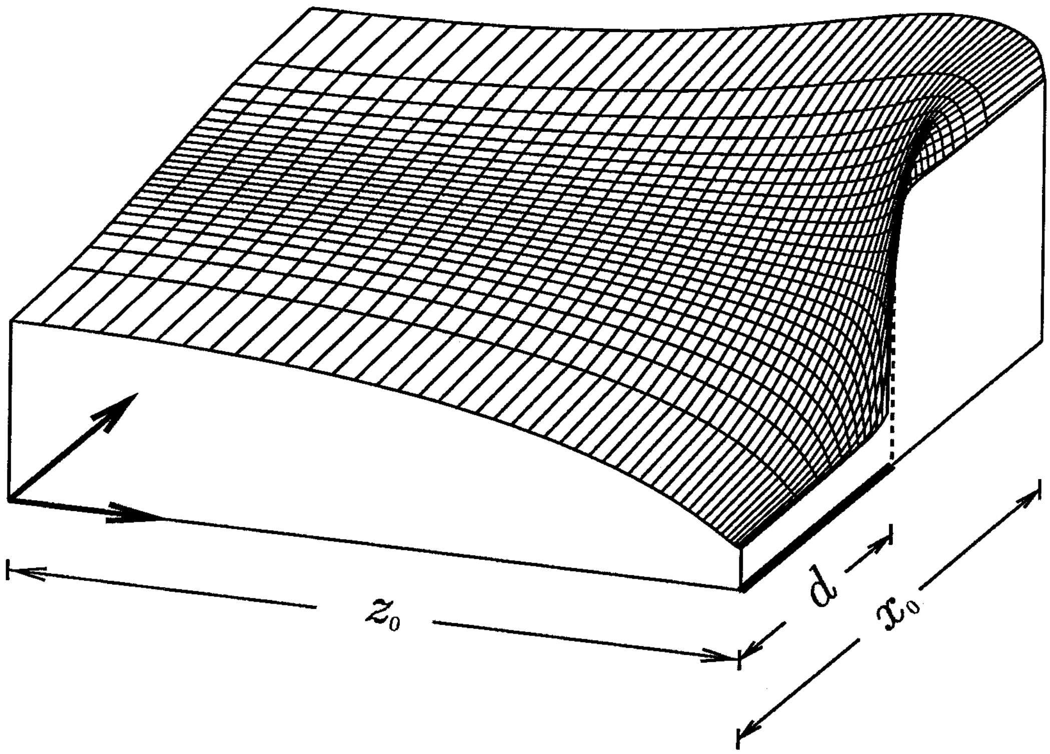

Figure 3.19: $n(x,z)$ obtained from non-isothermal, viscid classical transport equations with: $\mathbf{R}_{\|}$ neglected, $v_z(x,z)$ discontinuous at obstacle's tip, volumetric particle generation. $D_{\perp\infty}/c_{s\infty}d = 1/256$, $T_{e0}/T_{i\infty} = 1$, $M/m \sim 1837$, $c_{s\infty}/\omega_{ci}d = 10^{-2}$, $x_0/d = 2$, and $z_0/d = 40$. The transport coefficients are taken to be the Braginskii transport coefficients. The numerical results were obtained for a grid of 49×193. However, a grid of only 25×49 is shown for clarity.

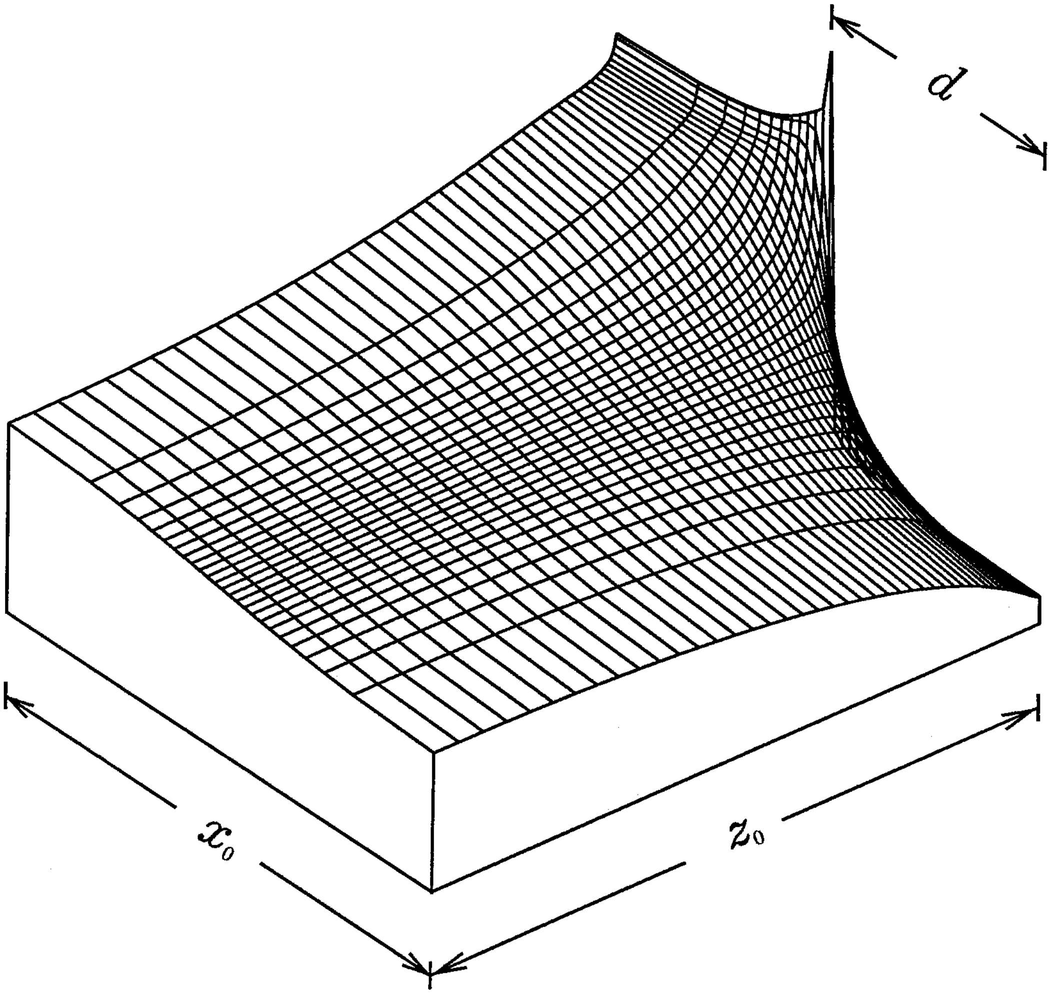

Figure 3.20: 3-D plot of ion pressure obtained from non-isothermal, viscid classical transport equations with: $\mathbf{R}_{\|}$ neglected, $v_z(x,z)$ discontinuous at obstacle's tip, volumetric particle generation. $D_{\perp\infty}/c_{s\infty}d = 1/256$, $T_{e0}/T_{i\infty} = 1$, $M/m \sim 1837$, $c_{s\infty}/\omega_{ci}d = 10^{-2}$, $x_0/d = 2$, and $z_0/d = 40$. The transport coefficients are taken to be the Braginskii transport coefficients. The numerical results were obtained for a grid of 49×193. However, a grid of only 25×49 is shown for clarity.

CHAPTER 4

Plasma Collection by an Obstacle with No Ambient Plasma Flow in the Presence of Anomalous Transport

Plasma turbulence is a subject of such complexity that there is not a *unified* approach of modelling a realistic plasma system. Many different theoretical approaches have been developed to study various aspects of plasma turbulence.[29] Much effort has also been focused on measuring fluctuation levels of various macroscopic variables to assess (1) the characteristics of plasma turbulence in a given experiment, and (2) the correlation between different fluctuating quantities. An extensive summary of theoretical and experimental studies of plasma turbulence in connection with anomalous transport is given in Ref. [30].

Due to the complexity of plasma turbulence, we will not attempt to derive the various *anomalous* transport coefficients from the theories of turbulence. Instead, we will take a more rudimentary approach of expressing *anomalous fluxes* in terms of correlation of respective fluctuating macroscopic variables. Our goal is to identify, under restrictive assumptions, the correlations necessary to *characterize* the effects of the underlying microscopic turbulence on the transport of particle, momentum, and energy. Measurements of fluctuation levels of a limited number of macroscopic variables have been given in the literature (see, for example, [31]). Typical experimentally determined correlations can be used in our model as *given.* The fluctuations of macroscopic variables are not treated in a self-consistent manner in our approach. It should be noted that we do not pretend to understand the basic nature of plasma turbulence. Our study is only an effort to describe the effects of plasma turbulence in a purely phenomenological manner.

4.1 Basic Assumptions

Our model still assumes the usual two-dimensional geometry with y being the ignorable coordinate (see figure 2.1). In our model, plasma turbulence is assumed to be caused by a low frequency ($\omega \ll \omega_{ci}$), microscopic ($\rho_i \ll \lambda \ll d$, where λ is a typical wavelength), electrostatic ($\tilde{\mathbf{B}} = 0$) fluctuation of the electric field in the perpendicular direction, i.e.,

$$\mathbf{E}(x,z,t) = -\boldsymbol{\nabla}\phi(x,z) + \tilde{\mathbf{E}}_{\perp}(x,z,t)$$

As a result, various macroscopic variables also fluctuate on a similar time scale. Since the fluctuations occur on a time scale much slower than the electron response time, the electrons remain nearly isothermal. The electrons are also taken to be inviscid because of their light mass. As suggested in section 3.5, the parallel electron-ion collisional drag is taken to be small, and will be neglected. As a result, the electrons obey the usual Boltzmann relation in both the parallel and the perpendicular directions (see section 3.2). The ions are assumed to be born with the temperature and mean velocity of the bulk ions.

Following the same formulation presented in chapter 3 and assuming that both the perpendicular ion inertia and viscous force are small compared with the perpendicular pressure gradient, we can show that the transport equations can be written as follows:

$$\frac{\partial n}{\partial t} + \boldsymbol{\nabla}\cdot(n\mathbf{v}) = S_0 \tag{4.1}$$

$$\frac{\partial}{\partial t}(Mn\mathbf{v}_{\parallel}) + \boldsymbol{\nabla}\cdot(Mn\mathbf{v}\mathbf{v}_{\parallel}) = \mathbf{J}\times\mathbf{B} - \boldsymbol{\nabla}[n(T_{e0}+T_i)] - (\boldsymbol{\nabla}\cdot\boldsymbol{\pi})_{\parallel} + S_0 M\mathbf{v}_{\parallel} \tag{4.2}$$

$$\frac{3}{2}n\left(\frac{\partial T_i}{\partial t} + \mathbf{v}\cdot\boldsymbol{\nabla}T_i\right) = -nT_i\boldsymbol{\nabla}\cdot\mathbf{v} - \boldsymbol{\nabla}\cdot\mathbf{q} - \pi_{\alpha\beta}\frac{\partial v_\alpha}{\partial\beta} + S_0 T_{i\infty} \tag{4.3}$$

where

$$\left.\begin{aligned}
\mathbf{J}_\perp &= \frac{ne}{1+\alpha^2}\Big(\mathbf{v}_\perp - \mathbf{v}_{D\perp} + \alpha(\mathbf{v}_\perp - \mathbf{v}_{D\perp})\times\hat{z}\Big)\\
\mathbf{v}_{D\perp} &= \frac{\tilde{\mathbf{E}}_\perp\times\mathbf{B}}{B^2}\\
\nabla\cdot\mathbf{q} &= -\frac{\partial}{\partial x}\left(\kappa_\perp\frac{\partial T_i}{\partial x}\right) - \frac{\partial}{\partial z}\left(\kappa_\parallel\frac{\partial T_i}{\partial z}\right)\\
\alpha &= \frac{D_{\perp\infty}}{c_{s\infty}^2\omega_{ci}}\\
r &= T_{e0}/T_{i\infty}\\
\kappa_\parallel &\sim \frac{1}{D_{\perp\infty}}\left(\frac{c_{s\infty}^2}{\omega_{ci}}\right)^2\sqrt{\frac{m}{M}}\frac{1}{r^{3/2}(1+r)}\,n\left(\frac{T_i}{T_{i\infty}}\right)^{5/2}\\
\kappa_\perp &\sim \frac{\kappa_\parallel}{(\omega_{ci}\tau_{ii})^2} \sim \sqrt{\frac{M}{m}}D_{\perp\infty}\frac{r^{3/2}}{1+r}\,n\left(\frac{T_i}{T_{i\infty}}\right)^{-1/2}
\end{aligned}\right\}\tag{4.4}$$

The ion viscosity tensor is the same as that given in section (3.6). The particle density $n(x,z,t)$ can be written as follows:

$$n(x,z,t) = \overline{n}(x,z) + \tilde{n}(x,z,t) \tag{4.5}$$

where $\overline{n}$ is the time-averaged density. $\tilde{n}$ represents a density fluctuation with zero mean, i.e., $\overline{\tilde{n}} = 0$. It should be noted that the time-scale over which time-averaging is performed must satisfy two requirements: (a) it must be long compared to the characteristic time of the fluctuations, and (b) it must be short compared to any macroscopic time scale of the plasma system. Since we are interested in a *steady-state* plasma response in which the ion-electron energy equilibration process is neglected, the second requirement will be satisfied if the electron-ion energy equilibration time is sufficiently long. Similar definitions can be written for T_i, T_e, and $\mathbf{v}$. In our model, only second-order correlations are retained. Correlations of third-order or higher are assumed to be negligible. Furthermore, the transport coefficients and plasma parameters far from the obstacle are assumed to be non-fluctuating, i.e.,

$$\left.\begin{aligned}
c_{s\infty} &= \sqrt{\frac{\overline{T}_{e0}+\overline{T}_{i\infty}}{M}} \\
\kappa_{\parallel\infty} &= \frac{\overline{n}_{\infty}}{D_{\perp\infty}}\left(\frac{c_{s\infty}^{2}}{\omega_{ci}}\right)^{2}\sqrt{\frac{m}{M}}\,\frac{1}{r^{3/2}(1+r)} \\
\kappa_{\perp\infty} &= \sqrt{\frac{M}{m}}\,\overline{n}_{\infty}D_{\perp\infty}\frac{r^{3/2}}{1+r} \\
\eta_{\parallel\infty} &= M\kappa_{\parallel\infty} \\
\eta_{\perp\infty} &= M\kappa_{\perp\infty} \\
\eta_{\wedge\infty} &= \frac{\overline{n}_{\infty}\overline{T}_{i\infty}}{\omega_{ci}}
\end{aligned}\right\} \tag{4.6}$$

where $r=\overline{T}_{e0}/\overline{T}_{i\infty}$. The functional forms of the viscosity coefficients and thermal conductivities are given bellow:

$$\left.\begin{aligned}
\kappa_{\parallel} &= \kappa_{\parallel\infty}\left(\frac{n}{\overline{n}_{\infty}}\right)\left(\frac{T_i}{\overline{T}_{i\infty}}\right)^{5/2} \\
\kappa_{\perp} &= \kappa_{\perp\infty}\left(\frac{n}{\overline{n}_{\infty}}\right)\left(\frac{T_i}{\overline{T}_{i\infty}}\right)^{-1/2} \\
\eta_{\parallel} &= \eta_{\parallel\infty}\left(\frac{n}{\overline{n}_{\infty}}\right)\left(\frac{T_i}{\overline{T}_{i\infty}}\right)^{5/2} \\
\eta_{\perp} &= \eta_{\perp\infty}\left(\frac{n}{\overline{n}_{\infty}}\right)\left(\frac{T_i}{\overline{T}_{i\infty}}\right)^{-1/2} \\
\eta_{\wedge} &= \eta_{\wedge\infty}\left(\frac{n}{\overline{n}_{\infty}}\right)\left(\frac{T_i}{\overline{T}_{i\infty}}\right)
\end{aligned}\right\}$$

4.1.1 Time-Averaged Continuity Equation

Because the parallel electric field, one of the principal driving forces in the parallel direction, is assumed to be non-fluctuating, the parallel component of the ion velocity will also be taken to be non-fluctuating, i.e., $\mathbf{v}_{\parallel}=\overline{\mathbf{v}_{\parallel}}$. Time-averaging equation (4.1) (in steady-state), one obtains:

$$\boldsymbol{\nabla}\cdot\left(\overline{n}\,\overline{\mathbf{v}}+\boldsymbol{\Gamma}_{t\perp}\right)=S_0 \tag{4.7}$$

where $\mathbf{\Gamma}_{t\perp} = \overline{\tilde{n}\tilde{\mathbf{v}}_\perp}$ is often referred to as the *fluctuation-induced* particle flux.

4.1.2 Time-Averaged Momentum Equation

Time-averaging the parallel component of equation (4.2) (in steady-state), one obtains:

$$\nabla\cdot(M\overline{n\mathbf{v}\mathbf{v}_{\parallel}}) = -\nabla_{\parallel}[\overline{n(T_{e0}+T_i)}] - (\nabla\cdot\overline{\boldsymbol{\pi}})_{\parallel} + S_0 M\overline{\mathbf{v}}_{\parallel} \tag{4.8}$$

We will now evaluate the equation above term by term. First, the time-averaged parallel flux of momentum can be written as follows:

$$M\overline{n\mathbf{v}\mathbf{v}_{\parallel}} = M(\overline{n}\,\overline{\mathbf{v}} + \mathbf{\Gamma}_{t\perp})\overline{\mathbf{v}}_{\parallel} \tag{4.9}$$

Equation (4.8) states that an anomalous flux of particles will also result in an anomalous flux of momentum by means of convection.

The time-averaged total pressure can be written as follows:

$$\overline{n(T_{e0}+T_i)} = \overline{n}(\overline{T}_{e0}+\overline{T}_i) + \overline{\tilde{n}\tilde{T}_{e0}} + \overline{\tilde{n}\tilde{T}_i} \tag{4.10}$$

The time-averaged ion viscosity tensor can be written as follows:

$$\overline{\boldsymbol{\pi}} = \boldsymbol{\pi}_c + \boldsymbol{\pi}_t \tag{4.11}$$

where $\boldsymbol{\pi}_c$ is the classical ion viscosity tensor. $\boldsymbol{\pi}_t$ is the *anomalous* ion viscosity tensor. The classical viscosity tensor can be written in the following form (see equation (2.21)):

$$\left.\begin{aligned}
\pi_{c,xx} &= -\frac{1}{2}\eta_{\parallel c}(\overline{W}_{xx}+\overline{W}_{yy}) - \frac{1}{2}\eta_{\perp c}(\overline{W}_{xx}-\overline{W}_{yy}) - \eta_{\wedge c}\overline{W}_{xy}\\
\pi_{c,yy} &= -\frac{1}{2}\eta_{\parallel c}(\overline{W}_{xx}+\overline{W}_{yy}) + \frac{1}{2}\eta_{\perp c}(\overline{W}_{xx}-\overline{W}_{yy}) + \eta_{\wedge c}\overline{W}_{xy}\\
\pi_{c,zz} &= -\frac{1}{2}\eta_{\parallel c}\overline{W}_{zz}\\
\pi_{c,xy} &= -\eta_{\perp c}\overline{W}_{xy} + \frac{1}{2}\eta_{\wedge c}(\overline{W}_{xx}-\overline{W}_{yy})\\
\pi_{c,xz} &= -\eta_{\perp c}\overline{W}_{xz} - \eta_{\wedge c}\overline{W}_{yz}\\
\pi_{c,yz} &= -\eta_{\perp c}\overline{W}_{yz} + \eta_{\wedge c}\overline{W}_{xz}
\end{aligned}\right\} \tag{4.12}$$

where

$$\left.\begin{aligned}
\overline{W}_{\alpha\beta} &= \frac{\partial \overline{v}_\alpha}{\partial x_\beta} + \frac{\partial \overline{v}_\beta}{\partial x_\alpha} - \frac{2}{3}\delta_{\alpha\beta}\boldsymbol{\nabla}\cdot\overline{\mathbf{v}} \\
\eta_{\parallel c} &= \eta_{\parallel\infty}\left(\frac{\overline{n}}{\overline{n}_\infty}\right)\left(\frac{\overline{T}_i}{\overline{T}_{i\infty}}\right)^{5/2} \\
\eta_{\perp c} &= \eta_{\perp\infty}\left(\frac{\overline{n}}{\overline{n}_\infty}\right)\left(\frac{\overline{T}_i}{\overline{T}_{i\infty}}\right)^{-1/2} \\
\eta_{\wedge c} &= \eta_{\wedge\infty}\left(\frac{\overline{n}}{\overline{n}_\infty}\right)\left(\frac{\overline{T}_i}{\overline{T}_{i\infty}}\right)
\end{aligned}\right\} \tag{4.13}$$

The anomalous viscosity tensor can be written in the following form:

$$\left.\begin{aligned}
\pi_{t,xx} = &- \frac{1}{2}(\overline{\eta}_\parallel - \eta_{\parallel c})(\overline{W}_{xx} + \overline{W}_{yy}) - \frac{1}{2}(\overline{\eta}_\perp - \eta_{\perp c})(\overline{W}_{xx} - \overline{W}_{yy}) \\
&- (\overline{\eta}_\wedge - \eta_{\wedge c})\overline{W}_{xy} \\
&- \frac{1}{2}\eta_{\parallel c}\left(\frac{\overline{\tilde{n}\tilde{W}_{xx}} + \overline{\tilde{n}\tilde{W}_{yy}}}{\overline{n}} + \frac{5}{2}\frac{\overline{\tilde{T}_i\tilde{W}_{xx}} + \overline{\tilde{T}_i\tilde{W}_{yy}}}{\overline{T}_i}\right) \\
&- \frac{1}{2}\eta_{\perp c}\left(\frac{\overline{\tilde{n}\tilde{W}_{xx}} - \overline{\tilde{n}\tilde{W}_{yy}}}{\overline{n}} - \frac{1}{2}\frac{\overline{\tilde{T}_i\tilde{W}_{xx}} - \overline{\tilde{T}_i\tilde{W}_{yy}}}{\overline{T}_i}\right) \\
&- \eta_{\wedge c}\left(\frac{\overline{\tilde{n}\tilde{W}_{xy}}}{\overline{n}} + \frac{\overline{\tilde{T}_i\tilde{W}_{xy}}}{\overline{T}_i}\right)
\end{aligned}\right\} \tag{4.14}$$

$$\left.\begin{aligned}
\pi_{t,yy} = &- \frac{1}{2}(\overline{\eta}_\parallel - \eta_{\parallel c})(\overline{W}_{xx} + \overline{W}_{yy}) + \frac{1}{2}(\overline{\eta}_\perp - \eta_{\perp c})(\overline{W}_{xx} - \overline{W}_{yy}) \\
&+ (\overline{\eta}_\wedge - \eta_{\wedge c})\overline{W}_{xy} \\
&- \frac{1}{2}\eta_{\parallel c}\left(\frac{\overline{\tilde{n}\tilde{W}_{xx}} + \overline{\tilde{n}\tilde{W}_{yy}}}{\overline{n}} + \frac{5}{2}\frac{\overline{\tilde{T}_i\tilde{W}_{xx}} + \overline{\tilde{T}_i\tilde{W}_{yy}}}{\overline{T}_i}\right) \\
&+ \frac{1}{2}\eta_{\perp c}\left(\frac{\overline{\tilde{n}\tilde{W}_{xx}} - \overline{\tilde{n}\tilde{W}_{yy}}}{\overline{n}} - \frac{1}{2}\frac{\overline{\tilde{T}_i\tilde{W}_{xx}} - \overline{\tilde{T}_i\tilde{W}_{yy}}}{\overline{T}_i}\right) \\
&+ \eta_{\wedge c}\left(\frac{\overline{\tilde{n}\tilde{W}_{xy}}}{\overline{n}} + \frac{\overline{\tilde{T}_i\tilde{W}_{xy}}}{\overline{T}_i}\right)
\end{aligned}\right\} \tag{4.15}$$

$$\pi_{t,zz} = -\frac{1}{2}(\overline{\eta}_\parallel - \eta_{\parallel c})\overline{W}_{zz} - \frac{1}{2}\eta_{\parallel c}\left(\frac{\overline{\tilde{n}\tilde{W}_{zz}}}{\overline{n}} + \frac{5}{2}\frac{\overline{\tilde{T}_i\tilde{W}_{xx}}}{\overline{T}_i}\right) \tag{4.16}$$

$$\left.\begin{aligned}\pi_{t,xy} = &-(\overline{\eta}_\perp - \eta_{\perp c})\overline{W}_{xy} + \frac{1}{2}(\overline{\eta}_\wedge - \eta_{\wedge c})(\overline{W}_{xx} - \overline{W}_{yy}) \\ &- \eta_{\perp c}\left(\frac{\overline{\tilde{n}\tilde{W}_{xy}}}{\overline{n}} - \frac{1}{2}\frac{\overline{\tilde{T}_i\tilde{W}_{xy}}}{\overline{T}_i}\right) \\ &+ \frac{1}{2}\eta_{\wedge c}\left(\frac{\overline{\tilde{n}\tilde{W}_{xx}} - \overline{\tilde{n}\tilde{W}_{yy}}}{\overline{n}} + \frac{\overline{\tilde{T}_i\tilde{W}_{xx}} - \overline{\tilde{T}_i\tilde{W}_{yy}}}{\overline{T}_i}\right)\end{aligned}\right\} \tag{4.17}$$

$$\left.\begin{aligned}\pi_{t,xz} = &-(\overline{\eta}_\perp - \eta_{\perp c})\overline{W}_{xz} - (\overline{\eta}_\wedge - \eta_{\wedge c})\overline{W}_{yz} \\ &- \eta_{\perp c}\left(\frac{\overline{\tilde{n}\tilde{W}_{xz}}}{\overline{n}} - \frac{1}{2}\frac{\overline{\tilde{T}_i\tilde{W}_{xz}}}{\overline{T}_i}\right) - \eta_{\wedge c}\left(\frac{\overline{\tilde{n}\tilde{W}_{yz}}}{\overline{n}} + \frac{\overline{\tilde{T}_i\tilde{W}_{yz}}}{\overline{T}_i}\right)\end{aligned}\right\} \tag{4.18}$$

$$\left.\begin{aligned}\pi_{t,yz} = &-(\overline{\eta}_\perp - \eta_{\perp c})\overline{W}_{yz} + (\overline{\eta}_\wedge - \eta_{\wedge c})\overline{W}_{xz} \\ &- \eta_{\perp c}\left(\frac{\overline{\tilde{n}\tilde{W}_{yz}}}{\overline{n}} - \frac{1}{2}\frac{\overline{\tilde{T}_i\tilde{W}_{yz}}}{\overline{T}_i}\right) + \eta_{\wedge c}\left(\frac{\overline{\tilde{n}\tilde{W}_{xz}}}{\overline{n}} + \frac{\overline{\tilde{T}_i\tilde{W}_{xz}}}{\overline{T}_i}\right)\end{aligned}\right\} \tag{4.19}$$

where

$$\left.\begin{aligned}\tilde{W}_{\alpha\beta} &= \frac{\partial\tilde{v}_\alpha}{\partial x_\beta} + \frac{\partial\tilde{v}_\beta}{\partial x_\alpha} - \frac{2}{3}\delta_{\alpha\beta}\boldsymbol{\nabla}\cdot\tilde{\mathbf{v}} \\ \frac{\overline{\eta}_\wedge - \eta_{\wedge c}}{\eta_{\wedge c}} &= \frac{\overline{\tilde{n}\tilde{T}_i}}{\overline{n}\,\overline{T}_i} \\ \frac{\overline{\eta}_\parallel - \eta_{\parallel c}}{\eta_{\parallel c}} &= \frac{5}{2}\frac{\overline{\eta}_\wedge - \eta_{\wedge c}}{\eta_{\wedge c}} \\ \frac{\overline{\eta}_\perp - \eta_{\perp c}}{\eta_{\wedge c}} &= -\frac{1}{2}\frac{\overline{\eta}_\wedge - \eta_{\wedge c}}{\eta_{\wedge c}}\end{aligned}\right\} \tag{4.20}$$

4.1.3 Time-Averaged Energy Equation

Time-averaging equation (4.3) (in steady-state), one obtains:

$$\frac{3}{2}\overline{n\mathbf{v}\cdot\boldsymbol{\nabla}T_i} = -\overline{nT_i\boldsymbol{\nabla}\cdot\mathbf{v}} - \boldsymbol{\nabla}\cdot\overline{\mathbf{q}} - \overline{\pi_{\alpha\beta}\frac{\partial v_\alpha}{\partial\beta}} + S_0\overline{T}_{i\infty} \tag{4.21}$$

We will now evaluate the equation above term by term.

$$\overline{n\mathbf{v}\cdot\boldsymbol{\nabla}T_i} = (\overline{n}\,\overline{\mathbf{v}} + \boldsymbol{\Gamma}_{t\perp})\cdot\boldsymbol{\nabla}\overline{T}_i + \overline{n}\,\overline{\tilde{\mathbf{v}}_\perp\cdot\boldsymbol{\nabla}\tilde{T}_i} + \overline{\mathbf{v}}\cdot\overline{\tilde{n}\boldsymbol{\nabla}\tilde{T}_i} \tag{4.22}$$

$$\overline{nT_i\boldsymbol{\nabla}\cdot\mathbf{v}} = (\overline{n}\,\overline{T}_i + \overline{\tilde{n}\tilde{T}_i})\,\boldsymbol{\nabla}\cdot\overline{\mathbf{v}} + \overline{n}\,\overline{\tilde{T}_i\boldsymbol{\nabla}\cdot\tilde{\mathbf{v}}_\perp} + \overline{T}_i\,\overline{\tilde{n}\boldsymbol{\nabla}\cdot\tilde{\mathbf{v}}_\perp} \tag{4.23}$$

The time-averaged heat flux $\overline{\mathbf{q}}$ can be written as follows:

$$\overline{\mathbf{q}} = \mathbf{q}_c + \mathbf{q}_t \tag{4.24}$$

where $\mathbf{q}_c$ is the classical heat flux. $\mathbf{q}_t$ is the *anomalous heat flux.* The classical heat flux is:

$$\mathbf{q}_c = -\kappa_{\perp c}\frac{\partial \overline{T}_i}{\partial x}\hat{x} - \kappa_{\parallel c}\frac{\partial \overline{T}_i}{\partial z}\hat{z} \tag{4.25}$$

where

$$\left.\begin{aligned} \kappa_{\perp c} &= \kappa_{\perp\infty}\left(\frac{\overline{n}}{\overline{n}_\infty}\right)\left(\frac{\overline{T}_i}{\overline{T}_{i\infty}}\right)^{-1/2} \\ \kappa_{\parallel c} &= \kappa_{\parallel c}\left(\frac{\overline{n}}{\overline{n}_\infty}\right)\left(\frac{\overline{T}_i}{\overline{T}_{i\infty}}\right)^{5/2} \end{aligned}\right\} \tag{4.26}$$

The anomalous heat flux is:

$$\left.\begin{aligned} \mathbf{q}_t = &-\left((\overline{\kappa}_\perp - \kappa_{\perp c})\frac{\partial \overline{T}_i}{\partial x} + \kappa_{\perp c}\left[\overline{\frac{\tilde{n}}{\overline{n}}\frac{\partial \tilde{T}_i}{\partial x}} - \frac{1}{4}\frac{1}{\overline{T}_i}\frac{\partial}{\partial x}(\overline{\tilde{T}_i\tilde{T}_i})\right]\right)\hat{x} \\ &-\left((\overline{\kappa}_\parallel - \kappa_{\parallel c})\frac{\partial \overline{T}_i}{\partial z} + \kappa_{\parallel c}\left[\overline{\frac{\tilde{n}}{\overline{n}}\frac{\partial \tilde{T}_i}{\partial z}} + \frac{5}{4}\frac{1}{\overline{T}_i}\frac{\partial}{\partial z}(\overline{\tilde{T}_i\tilde{T}_i})\right]\right)\hat{z} \end{aligned}\right\} \tag{4.27}$$

where

$$\left.\begin{aligned} \frac{\overline{\kappa}_\perp - \kappa_{\perp c}}{\kappa_{\perp c}} &= \frac{\overline{\eta}_\perp - \eta_{\perp c}}{\eta_{\perp c}} \\ \frac{\overline{\kappa}_\parallel - \kappa_{\parallel c}}{\kappa_{\parallel c}} &= \frac{\overline{\eta}_\parallel - \eta_{\parallel c}}{\eta_{\parallel c}} \end{aligned}\right\} \tag{4.28}$$

The heat generated by viscosity (dissipation) can be written as follows:

$$\overline{-\pi_{\alpha\beta}\frac{\partial v_\alpha}{\partial \beta}} = -(\pi_{c,\alpha\beta} + \pi_{t,\alpha\beta})\frac{\partial \overline{v}_\alpha}{\partial \beta} - \overline{\tilde{\pi}_{\alpha\beta}\frac{\partial \tilde{v}_\alpha}{\partial \beta}} \tag{4.29}$$

The fluctuation $\tilde{\pi}_{\alpha\beta}$ can be computed in terms of various correlations, but is too lengthy to be included. It should be noted that only second-order correlations are retained. Correlations of higher orders are assumed to be negligible.

4.2 Estimates of Correlations

It is evident that turbulent transport is an extremely complex process. Different *modes* of plasma turbulence lead to different transport properties (see, for example, [29]). It is a rather formidable task, if at all possible, to study turbulent transport of a plasma system with arbitrary perturbations. It is our goal to study the time-averaged steady-state plasma response in the presence of a low-frequency, microscopic, electrostatic fluctuation of the electric field in the y direction. This corresponds to a fluctuation of the poloidal electric field in toroidal geometry. Even under these restrictive assumptions, only a limited set of fluctuating macroscopic quantities have been measured. Consequently, we do not have as much information as necessary to characterize the plasma turbulence process. Our goal is to utilize as much of the information available in the literature as possible. The correlations that have not been measured will not be treated.

Because the electric field fluctuates on a time-scale slower than the ion response time, it causes a slowly fluctuating $\mathbf{E}\times\mathbf{B}$ drift, i.e., $\mathbf{v}_{D\perp} = \tilde{\mathbf{E}}\times\mathbf{B}/B^2$. It has been observed in the edge plasmas of several tokamaks that low-frequency, electrostatic fluctuations are similar in characteristic independent of the size of the tokamaks. In particular, typical fluctuation levels in the edge plasma of the Caltech Research Tokamak have been observed to be: [1,32]

$$\begin{aligned}
\frac{\sqrt{\overline{\tilde{T}_e^2}}}{\overline{T}_e} &\sim 15\% \\
\frac{\sqrt{\overline{\tilde{n}^2}}}{\overline{n}} &\sim 30\% - 50\% \\
\left|\overline{\tilde{n}\tilde{\mathbf{v}}_\perp}\right| = \left|\frac{\overline{\tilde{n}\tilde{\mathbf{E}}_\perp\times\mathbf{B}}}{B^2}\right| &\sim 1 - 2\times10^{17}\,\mathrm{cm}^{-2}\mathrm{sec}^{-1} \\
\frac{\partial\overline{n}}{\partial x} &\sim 5\times10^{11}\,\mathrm{cm}^{-4}
\end{aligned}$$

$$\begin{aligned}
\left(|\tilde{T}_e|/\overline{T}_e\right)_{max} &\sim 0.3 \\
\left(|\tilde{n}|/\overline{n}\right)_{max} &\sim 0.8
\end{aligned}$$

We will make the usual conjecture that the anomalous particle flux is proportional to the mean density gradient, i.e.,

$$\mathbf{\Gamma}_{t\perp} \equiv \overline{\tilde{n}\tilde{\mathbf{v}}_\perp} = -D_{\perp t}\nabla_\perp \overline{n} \tag{4.30}$$

It should be noted that the conjecture above has not been verified experimentally. The anomalous cross-field particle diffusion coefficient can then be estimated as follows:

$$D_{\perp t} = -\frac{\overline{\tilde{n}\tilde{E}}/B}{\partial\overline{n}/\partial x} \sim \frac{1-2\times10^{17}\,\mathrm{cm}^{-2}\mathrm{sec}^{-1}}{5\times10^{11}\,\mathrm{cm}^{-4}} \sim 2-4\times10^5\,\mathrm{cm}^2/\mathrm{s} \tag{4.31}$$

In the edge of the Caltech Research Tokamak, the classical particle diffusion coefficient $D_{\perp\infty}$ is about 0.2 cm^2/s, which is much less than the observed anomalous diffusion coefficient $D_{\perp t}$. As a result, the following approximation is taken to be valid:

$$\overline{n}\,\overline{\mathbf{v}}_\perp + \mathbf{\Gamma}_{t\perp} \simeq \mathbf{\Gamma}_{t\perp} = -D_{\perp t}\nabla_\perp\overline{n}$$

Recent measurements suggested that although $\tilde{T}_e$ and $\tilde{n}$ are not small, they do not tend to be well-correlated. For instance, for $\tilde{T}_e$ and $\tilde{n}$ comparable to those presented in Ref. [32] , Lin *et al.*[33] found that $\overline{\tilde{n}\tilde{T}_e}/\overline{n}\,\overline{T}_e = 0.017$. Therefore, we will neglect the correlation $\overline{\tilde{n}\tilde{T}_e}$ in our model.

Unlike $\tilde{T}_e$, $\tilde{T}_i$ has not been measured since the usual Langmuir probe measurements do not contain information regarding the ion temperature. Because of this lack of knowledge, we are forced to neglect correlations containing $\tilde{T}_i$, e.g., $\overline{\tilde{n}\tilde{T}_i}$. As a result, the anomalous viscosity tensor can be estimated as follows:

$$\left.\begin{aligned}
\pi_{t,xx} &\sim -\left(\frac{\eta_{\parallel c}}{2\overline{n}}\right)\overline{\tilde{n}\tilde{W}}_{xx} \\
\pi_{t,yy} &\sim \pi_{t,xx} \\
\pi_{t,zz} &\sim 0 \\
\pi_{t,xy} &\sim -\left(\frac{\eta_{\wedge c}}{\eta_{\parallel c}}\right)\pi_{t,xx} \\
\pi_{t,xz} &\sim -\left(\frac{\eta_{\perp c}}{\overline{n}}\right)\overline{\tilde{n}\tilde{W}}_{xz} \\
\pi_{t,yz} &\sim -\left(\frac{\eta_{\wedge c}}{\eta_{\perp c}}\right)\pi_{t,xz}
\end{aligned}\right\} \tag{4.32}$$

where

$$\left.\begin{aligned} \overline{\tilde{n}\tilde{W}_{xx}} &= \frac{4}{3}\overline{\tilde{n}\frac{\partial \tilde{v}_x}{\partial x}} \sim O\left(\overline{n}\,\frac{\partial}{\partial x}(\overline{\tilde{n}\tilde{v}_x}/\,\overline{n}\,)\right) \sim O\left(\overline{n}\,\frac{\partial}{\partial x}(\Gamma_{\perp t}/\overline{n}\,)\right) \\ \overline{\tilde{n}\tilde{W}_{xz}} &= \overline{\tilde{n}\frac{\partial \tilde{v}_x}{\partial z}} \sim O\left(\overline{n}\,\frac{\partial}{\partial z}(\overline{\tilde{n}\tilde{v}_x}/\,\overline{n}\,)\right) \sim O\left(\overline{n}\,\frac{\partial}{\partial z}(\Gamma_{\perp t}/\,\overline{n}\,)\right) \end{aligned}\right\} \tag{4.33}$$

Finally, the last term of the R.H.S. of equation (4.30) can be written in the following form:

$$\left.\begin{aligned} \overline{\tilde{\pi}_{\alpha\beta}\frac{\partial \tilde{v}_\alpha}{\partial \beta}} &= \overline{\tilde{\pi}_{xx}\frac{\partial \tilde{v}_x}{\partial x}} + \overline{\tilde{\pi}_{xz}\frac{\partial \tilde{v}_x}{\partial z}} \\ \overline{\tilde{\pi}_{xx}\frac{\partial \tilde{v}_x}{\partial x}} &\sim -\frac{1}{2}\eta_{\parallel c}\left(\overline{\tilde{n}\frac{\partial \tilde{v}_x}{\partial x}} \left(\frac{\overline{W}_{xx} + \overline{W}_{yy}}{\overline{n}}\right) + \overline{\tilde{W}_{xx}\frac{\partial \tilde{v}_x}{\partial x}}\right) \\ \overline{\tilde{\pi}_{xz}\frac{\partial \tilde{v}_x}{\partial z}} &\sim -\left(\frac{\eta_{\perp c}\overline{W}_{xz} + \eta_{\wedge c}\overline{W}_{yz}}{\overline{n}}\right)\overline{\tilde{n}\frac{\partial \tilde{v}_x}{\partial z}} - \eta_{\perp c}\,\overline{\tilde{W}_{xz}\frac{\partial \tilde{v}_x}{\partial z}} \end{aligned}\right\} \tag{4.34}$$

where

$$\left.\begin{aligned} \overline{\tilde{W}_{xx}\frac{\partial \tilde{v}_x}{\partial x}} &\geq \frac{1}{|\,\tilde{n}\,|^2_{max}}\overline{\left(\tilde{n}\frac{\partial \tilde{v}_x}{\partial x}\right)^2} \geq O\left(\frac{\partial}{\partial x}(\Gamma_{\perp t}/\,\overline{n}\,)\right)^2 \\ \overline{\tilde{W}_{xz}\frac{\partial \tilde{v}_x}{\partial z}} &\geq \frac{1}{|\,\tilde{n}\,|^2_{max}}\overline{\left(\tilde{n}\frac{\partial \tilde{v}_x}{\partial z}\right)^2} \geq O\left(\frac{\partial}{\partial z}(\Gamma_{\perp t}/\,\overline{n}\,)\right)^2 \end{aligned}\right\} \tag{4.35}$$

4.3 Model Equations

Using the estimates of various correlations presented in section (4.2), the time-averaged continuity, momentum, and energy equations can be written as follows:

$$\mathbf{\nabla}_{\parallel}\cdot(\,\overline{n}\,\overline{\mathbf{v}}_{\parallel}) - D_{\perp t}\nabla^2_{\perp}\,\overline{n} = S_0 \tag{4.36}$$

$$M(\,\overline{n}\,\overline{\mathbf{v}}_{\parallel} - D_{\perp t}\mathbf{\nabla}_{\perp}\overline{n}\,)\cdot\mathbf{\nabla}\,\overline{\mathbf{v}}_{\parallel} = -\mathbf{\nabla}_{\parallel}[\,\overline{n}\,(\,\overline{T}_{e0} + \overline{T}_i)] + \mathbf{\nabla}\cdot\left(\eta_{\parallel c}\mathbf{\nabla}_{\parallel}\,\overline{\mathbf{v}}_{\parallel} + \eta_{\perp c}\mathbf{\nabla}_{\perp}\,\overline{\mathbf{v}}_{\parallel}\right) \tag{4.37}$$

$$\left.\begin{aligned} \frac{3}{2}(\,\overline{n}\,\overline{\mathbf{v}}_{\parallel} - D_{\perp t}\mathbf{\nabla}_{\perp}\overline{n}\,)\cdot\mathbf{\nabla}\,\overline{T}_i = &-\overline{n}\,\overline{T}_i\,\mathbf{\nabla}\cdot\left(\overline{\mathbf{v}}_{\parallel} - \frac{D_{\perp t}}{\overline{n}}\mathbf{\nabla}_{\perp}\overline{n}\right) \\ &+ \mathbf{\nabla}\cdot\left(\kappa_{\perp c}\mathbf{\nabla}_{\perp}\overline{T}_i + \kappa_{\parallel c}\mathbf{\nabla}_{\parallel}\overline{T}_i\right) \\ &+ \eta_{\perp c}\left(\frac{\partial \overline{v}_{\parallel}}{\partial x}\right)^2 + \eta_{\parallel c}\left[\frac{\partial}{\partial x}\left(\frac{D_{\perp t}}{\overline{n}}\frac{\partial \overline{n}}{\partial x}\right)\right]^2 \\ &+ S_0\overline{T}_{i\infty} \end{aligned}\right\} \tag{4.38}$$

It should be noted that a dimensional analysis has also been performed, and only the most significant contributions from $(\nabla \cdot \boldsymbol{\pi})_{\parallel}$ and $\overline{\pi_{\alpha\beta}\partial v_{\alpha\beta}/\partial\beta}$ are retained. Equations (4.36)–(4.38) were derived under a number of restrictive assumptions, and can be solved to obtain the time-averaged plasma response in the presence of a low-frequency, microscopic, electrostatic fluctuation of the electric field in the y direction. Although the time-averaged plasma response so obtained may not be quantitatively correct, it should provide useful information regarding the qualitative behaviour of the *actual* time-averaged plasma response.

4.4 Numerical Results

The plasma response is obtained from the transport equations (4.36)–(4.38). The transport equations are solved using the usual Newton-Raphson method on a grid of 193×41. For the cases to be presented in this chapter, realistic plasma parameters are used, i.e.,

$$\frac{D_{\perp t}}{D_{\perp c}} \sim 2\times10^{4}$$

$$\frac{M}{m} \sim 1837$$

$$\frac{c_{s\infty}}{\omega_{ci} d} \sim 10^{-2}$$

The physical extents of the system are chosen sufficiently large to ensure that far from the obstacle, the density $n(x, z)$ and the ion temperature $T_i(x, z)$ are unperturbed. For the cases to be presented in this chapter, $x_0/d = 2$ and $z_0/L = 2$ with $L \equiv c_{s\infty}d^2/D_{\perp t}$.

The plasma response for two particular cases for which $T_{e0}/T_{i\infty} = 1$ and $T_{e0}/T_{i\infty} = 1.5$ have been obtained numerically.

Figures 4.1a and 4.1b are a three dimensional plot and a contour plot of the density $n(x, z)$ with $T_{e0}/T_{i\infty} = 1$. Our numerical results indicate that the parallel particle collection length of the obstacle is of the order of L. Comparing figures 4.1a and 4.1b (anomalous transport) with figures 3.2a and 3.2b (classical transport with inviscid, isothermal ions), we see that the density $n(x, z)$ is qualitatively similar for the two models except for the difference in the parallel collection length. In particular, $L_{\parallel t}/L_{\parallel c} \sim D_{\perp c}/D_{\perp t} = 5\times10^{-5}$.

Figure 4.2 is a three dimensional plot of the ion temperature $T_i(x,z)$ with $T_{e0}/T_{i\infty} = 1$. Figure 4.2 shows that the ions remain nearly isothermal in the entire domain except for a small region around the tip of the obstacle. There, the ions are heated up significantly due to viscous heating. For this particular case, the ion temperature is peaked slightly below the obstacle's tip, and is about 80% higher than the ambient ion temperature. Comparing figure 4.2 with figure 3.19 (classical transport with viscid, non-isothermal ions) shows that the qualitative behaviours of the ion temperature for the two models are quite different. In figure 3.19, the ions near the obstacle's tip are heated by a *point source* of energy (perpendicular shear of parallel velocity), resulting in a cusp at the obstacle's tip. In figure 4.2, the ions near the obstacle's tip are heated predominantly by viscous heating caused by the perpendicular shear of perpendicular velocity. Because the perpendicular velocity is continuous at the obstacle's tip, no cusp is formed. Therefore, although the ions are heated up near the tip of the obstacle by means of viscous heating in both models, the mechanisms by which viscous heating is generated are very different.

Figures 4.3a and 4.3b are a three dimensional plot and a contour plot of the density $n(x,z)$ with $T_{e0}/T_{i\infty} = 1.5$. Comparing figures 4.3a and 4.3b with figures 4.1a and 4.1b ($T_{e0}/T_{i\infty} = 1$) shows that the density $n(x,z)$ is somewhat insensitive to the exact value of $T_{e0}/T_{i\infty}$.

Figure 4.4 is a three dimensional plot of the ion temperature $T_i(x,z)$ with $T_{e0}/T_{i\infty} = 1.5$. Comparing figure 4.4 with figure 4.2 ($T_{e0}/T_{i\infty} = 1$) shows that the peaked ion temperature is a fairly sensitive function of the ratio $T_{e0}/T_{i\infty}$. In this particular case where $T_{e0}/T_{i\infty} = 1.5$, the peaked ion temperature is about 25% higher than the ambient ion temperature.

In summary, our numerical results suggest that in the presence of anomalous transport caused by low-frequency, microscopic, electrostatic fluctuations, the particle density $n(x,z)$ has a scalelength of the order of $L \equiv c_{s\infty}d^2/D_{\perp t}$. Furthermore,

$n(x, z)$ can be found, within reasonable accuracy, by solving a simpler model describing the motion of inviscid, isothermal ions with an effective perpendicular diffusion coefficient $D_{\perp t}$. Our results also suggest that the ions are significantly heated in a small region near the tip of the obstacle by means of viscous heating. The ratio of the peaked ion temperature to the ambient ion temperature is a sensitive function of the ratio $T_{e0}/T_{i\infty}$. Because the ion temperature is high near the tip of the obstacle, the obstacle's tip has to withstand a significantly higher heat flux than elsewhere.

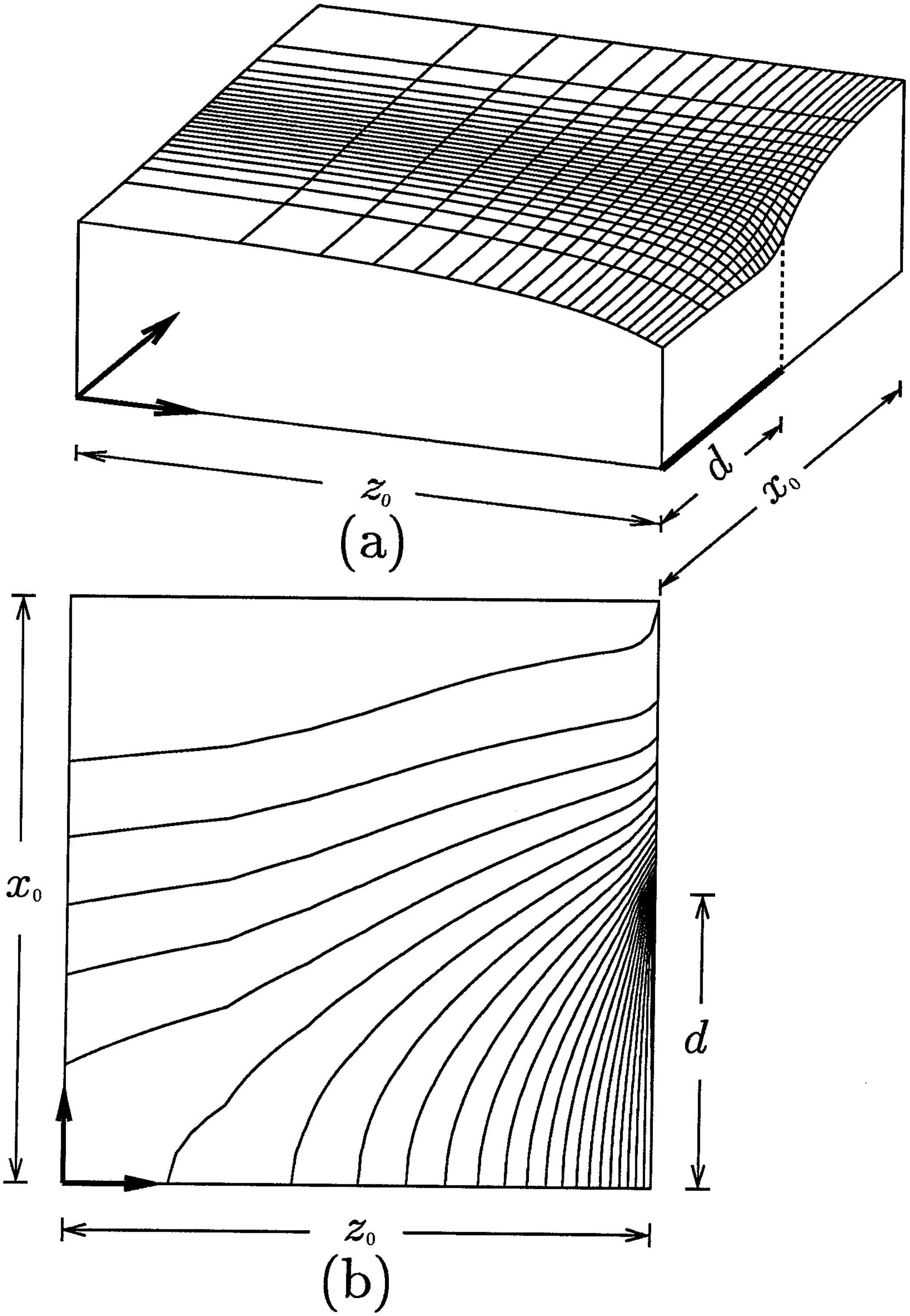

Figure 4.1: $n(x,z)$ obtained from semi-empirical transport equations accounting for anomalous transport and viscous effects with no ambient flow. $D_{\perp t}/D_{\perp c}=2\times10^4$, $T_{e0}/T_{i\infty}=1$, $M/m=1837$, $c_{s\infty}/\omega_{ci}d=10^{-2}$, $x_0/d=2$, $z_0/L=2$ $(L\equiv c_{s\infty}d^2/D_{\perp t})$.

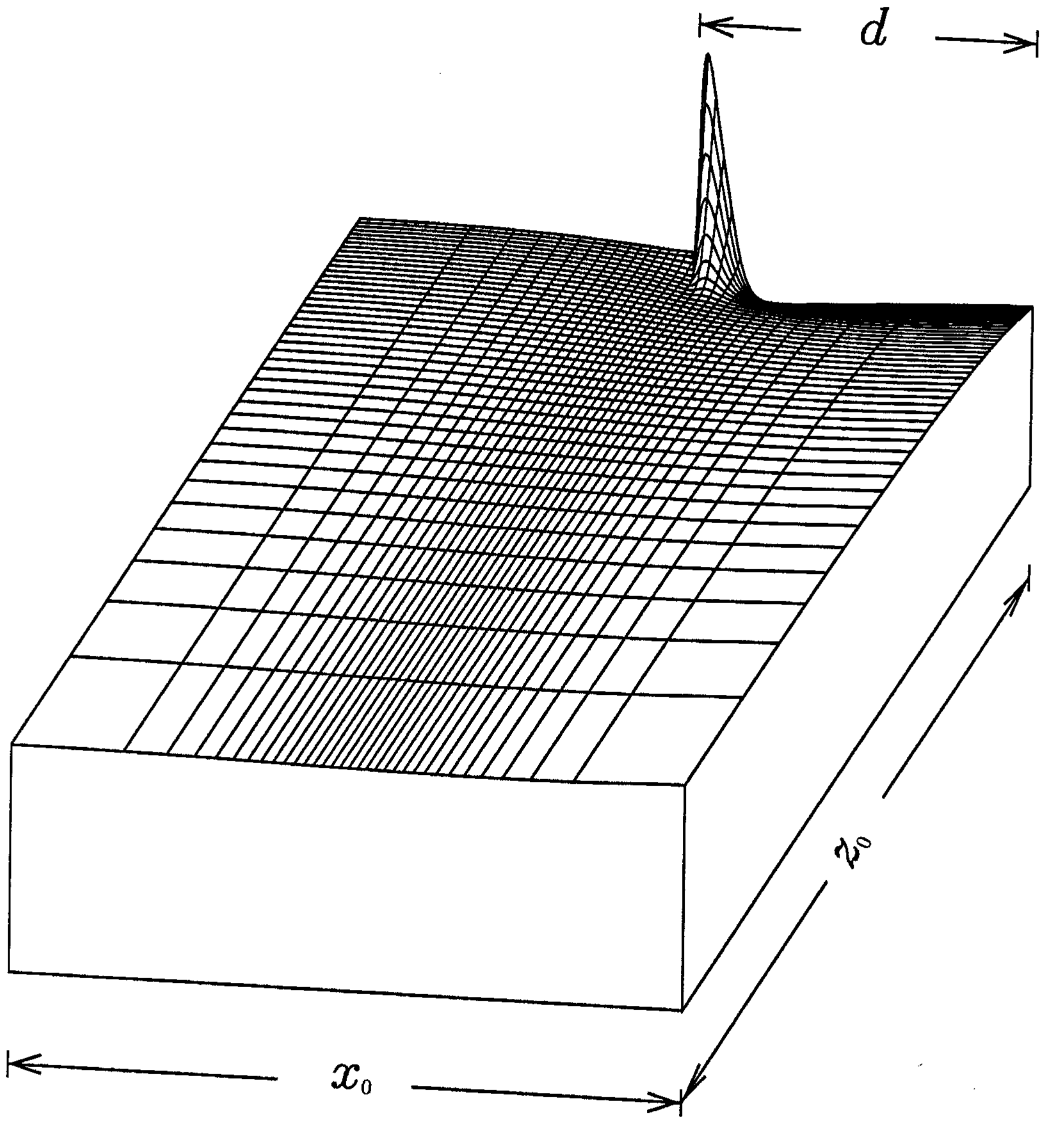

Figure 4.2: 3-D plot of $T_i(x, z)$ obtained from semi-empirical transport equations accounting for anomalous particle transport, ion viscosity, and ion viscous heating in the absence of an ambient plasma flow. $D_{\perp t}/D_{\perp c} = 2\times10^4$, $T_{e0}/T_{i\infty} = 1$, $M/m \sim 1837$, $c_{s\infty}/\omega_{ci}d = 10^{-2}$, $x_0/d = 2$, and $z_0/L = 2$ $(L \equiv c_{s\infty}d^2/D_{\perp t})$. Anomalous particle transport is assumed to be caused by a randomly fluctuating poloidal electric field.

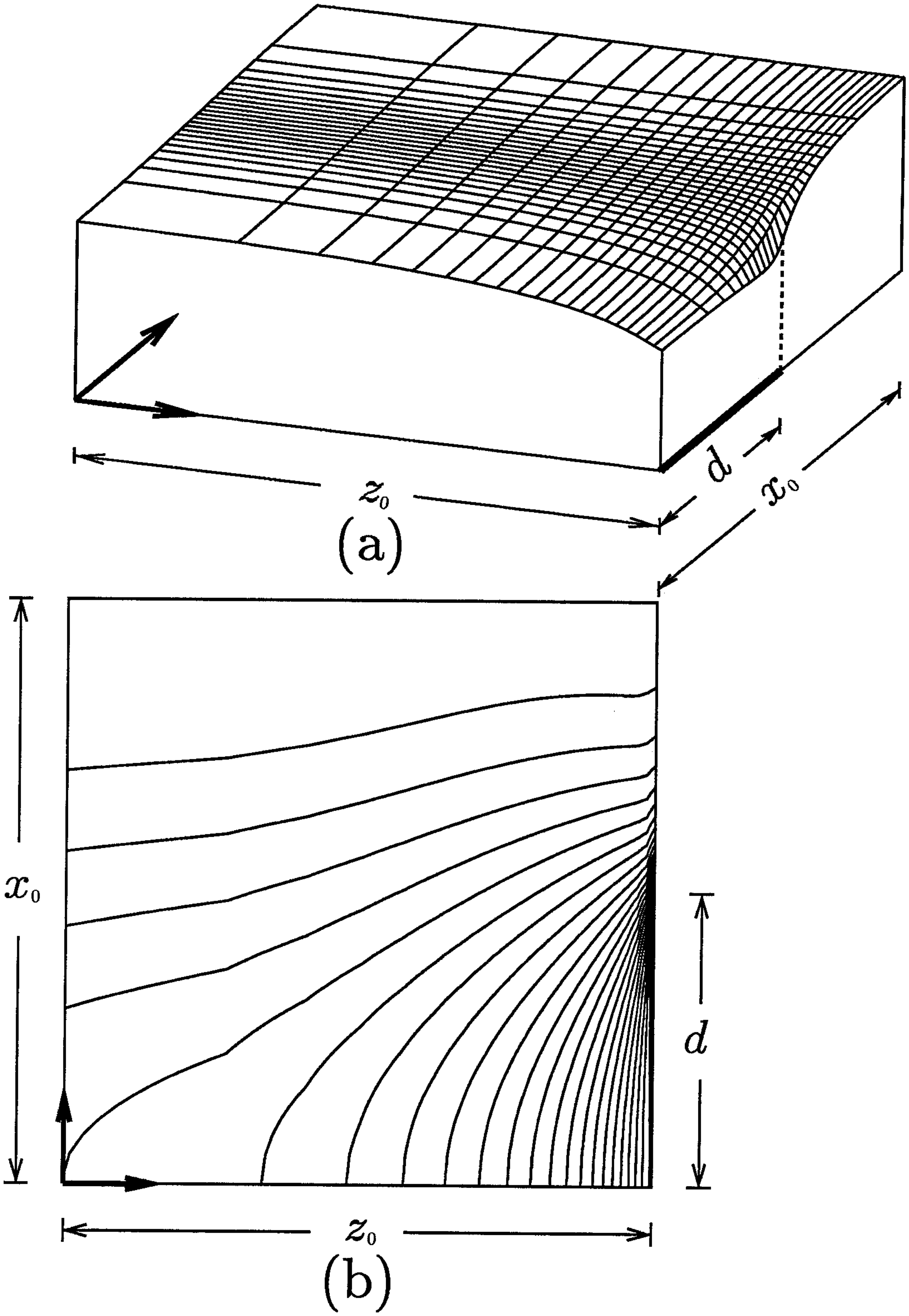

Figure 4.3: $n(x,z)$ obtained from semi-empirical transport equations accounting for anomalous transport and viscous effects with no ambient flow. $D_{\perp t}/D_{\perp c}=2\times10^4$, $T_{e0}/T_{i\infty}=3/2$, $M/m=1837$, $c_{s\infty}/\omega_{ci}d=10^{-2}$, $x_0/d=2$, $z_0/L=2$ ($L\equiv c_{s\infty}d^2/D_{\perp t}$).

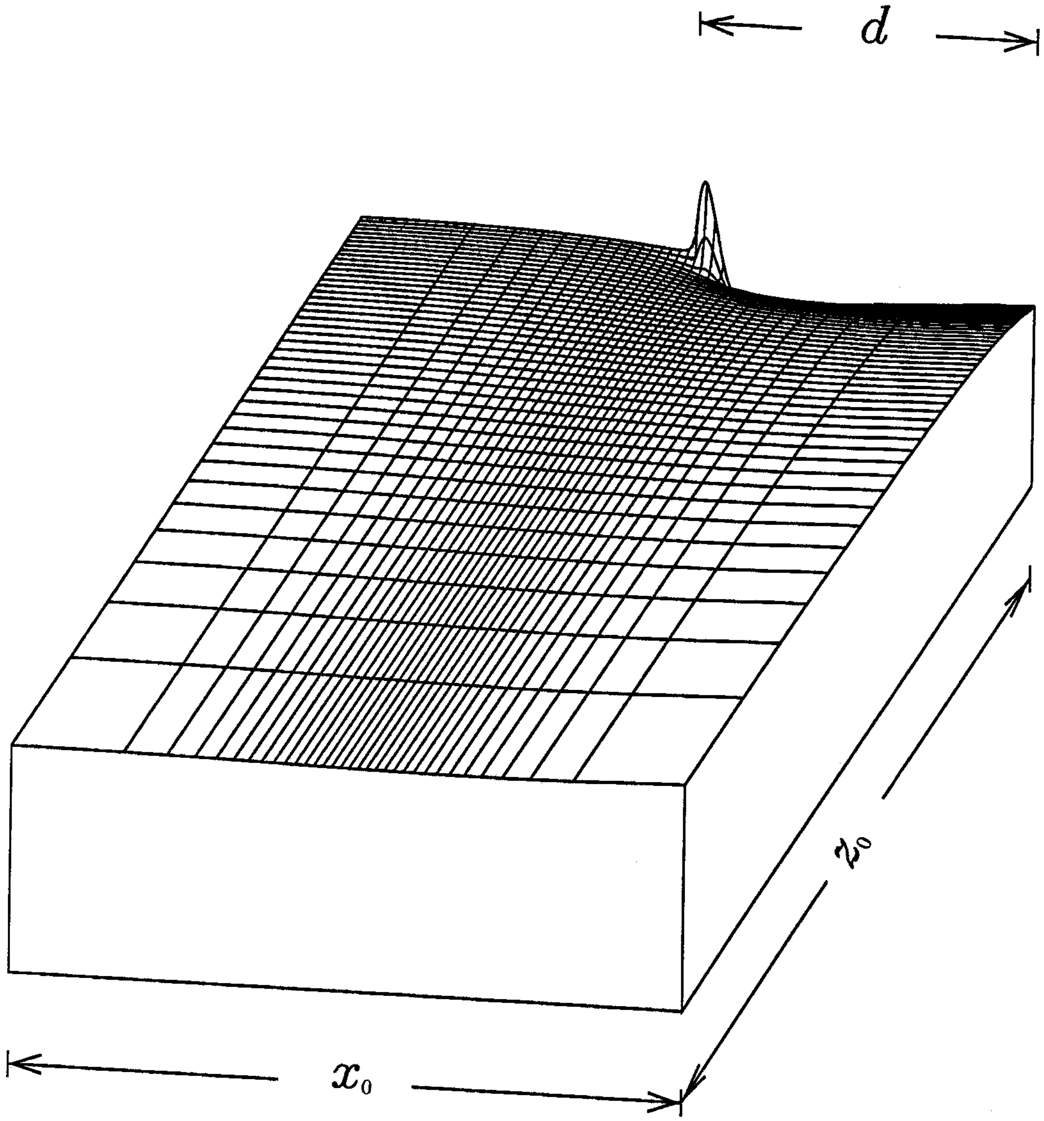

Figure 4.4: 3-D plot of $T_i(x,z)$ obtained from semi-empirical transport equations accounting for anomalous particle transport, ion viscosity, and ion viscous heating in the absence of an ambient plasma flow. $D_{\perp t}/D_{\perp c} = 2\times10^4$, $T_{e0}/T_{i\infty} = 3/2$, $M/m \sim 1837$, $c_{s\infty}/\omega_{ci}d = 10^{-2}$, $x_0/d = 2$, and $z_0/L = 2$ ($L \equiv c_{s\infty}d^2/D_{\perp t}$). Anomalous particle transport is assumed to be caused by a randomly fluctuating poloidal electric field.

CHAPTER 5

Plasma Collection by an Obstacle with a Subsonic Ambient Plasma Flow in the Presence of Anomalous Transport

A problem of interest is one in which two electrostatic Langmuir probes mounted on either side of an unbiased (floating at the plasma potential) obstacle are used to measure the *upstream* and *downstream* ion fluxes. Such a plasma diagnostic is the so-called *Mach* probe or *Janus* probe.[3] In the absence of an ambient plasma flow, aside from various asymmetries of the experimental apparatus, the measured upstream and downstream ion fluxes would be roughly equal. In the presence of an ambient plasma flow, the measured upstream and downstream ion fluxes are no longer equal. Several models have been proposed to interpret experimental data from the Janus probes.[9–10, 34] The main objective of these models is to infer the ambient plasma flow from the upstream/downstream ion flux ratio.

Stangeby[9] proposed a one-dimensional fluid model in which the ions are taken to be inviscid and isothermal. Hutchinson,[10] on the other hand, proposed a model in which the ions are taken to be isothermal and the cross-field ion viscosity coefficient is postulated to be *anomalous*, i.e., $\eta_\perp \sim nMD_{\perp t}$. Because of the difference in the treatment of ion viscosity, Hutchinson's model predicts an ambient plasma flow much smaller than that predicted by Stangeby's model for any given upstream/downstream ion flux ratio.

There have been strong disagreements in the literature regarding the importance of ion viscosity in connection with the interpretation of Janus probe data.[35–36] In Ref. [35], it was pointed out that although the ratio $\eta_\perp/nMD_{\perp t}$ is not known, the choice $\eta_\perp / nMD_{\perp t} \sim 1$ "is an arbitrary one and assumes much stronger viscosity than previously considered in the literature." In reply to this comment, it was conceded in Ref. [36] that although the choice $\eta_\perp / nMD_{\perp t} \sim 1$ is an arbitrary one, it is "plainly less 'arbitrary' than choosing $\eta_\perp = 0$," and that all theories that assume $\eta_\perp = 0$ are "fatally flawed."

In this chapter, we propose a two-fluid model describing plasma collection by an obstacle with a subsonic ambient plasma flow in the presence of anomalous transport. In our model, anomalous transport is assumed to be caused by a low frequency, microscopic, electrostatic fluctuation of the poloidal electric field (see chapter 4). Our goal is to predict the upstream/downstream ion flux ratio given that the ambient plasma flow is known. The physical mechanisms included in our model are different from those in Refs. [9–10].

5.1 Model and Discussion

The geometry of our model is shown in figure 5.1. The thick solid line represents the obstacle with half-width d. The obstacle is located at $z = 0$. The ambient plasma flow is taken to be $\mathbf{M}_\infty$ on both the left and right boundaries ($z = \pm z_0$). The external magnetic field is in the z-direction, and is taken to be uniform. The top and bottom boundaries ($x = 0, x_0$) are periodic boundaries, i.e., the particle density $n(x, z)$, the parallel ion fluid velocity $v_\parallel(x, z)$, and the ion temperature $T_i(x, z)$ are symmetrical about these boundaries.

In our model, anomalous transport is assumed to be caused by a low-frequency, microscopic, electrostatic fluctuation of the poloidal electric field (the y direction in our two-dimensional geometry corresponds to the poloidal direction in toroidal geometry). Using the model proposed in chapter 4, the transport equations are written as follows (see equations (4.36)–(4.38)):

$$\boldsymbol{\nabla}_\parallel \cdot (\overline{n}\,\overline{\mathbf{v}}_\parallel) - D_{\perp t} \nabla_\perp^2 \overline{n} = S_0 \tag{5.1}$$

$$M(\overline{n}\,\overline{\mathbf{v}}_\parallel - D_{\perp t} \boldsymbol{\nabla}_\perp \overline{n}) \cdot \boldsymbol{\nabla}\, \overline{\mathbf{v}}_\parallel = -\boldsymbol{\nabla}_\parallel [\overline{n}(\overline{T}_{e0} + \overline{T}_i)] + \boldsymbol{\nabla} \cdot \left(\eta_{\parallel c} \boldsymbol{\nabla}_\parallel \overline{\mathbf{v}}_\parallel + \eta_{\perp c} \boldsymbol{\nabla}_\perp \overline{\mathbf{v}}_\parallel \right) \tag{5.2}$$

$$\left.\begin{aligned}\frac{3}{2}(\overline{n}\overline{\mathbf{v}}_{\parallel} - D_{\perp t}\boldsymbol{\nabla}_{\perp}\overline{n})\cdot\boldsymbol{\nabla}\overline{T}_i = &-\overline{n}\,\overline{T}_i\,\boldsymbol{\nabla}\cdot\left(\overline{\mathbf{v}}_{\parallel} - \frac{D_{\perp t}}{\overline{n}}\boldsymbol{\nabla}_{\perp}\overline{n}\right)\\ &+\boldsymbol{\nabla}\cdot\left(\kappa_{\perp c}\boldsymbol{\nabla}_{\perp}\overline{T}_i + \kappa_{\parallel c}\boldsymbol{\nabla}_{\parallel}\overline{T}_i\right)\\ &+\eta_{\perp c}\left(\frac{\partial\overline{v}_{\parallel}}{\partial x}\right)^2 + \eta_{\parallel c}\left[\frac{\partial}{\partial x}\left(\frac{D_{\perp t}}{\overline{n}}\frac{\partial\overline{n}}{\partial x}\right)\right]^2\\ &+S_0\overline{T}_{i\infty}\end{aligned}\right\} \tag{5.3}$$

where

$$\left.\begin{aligned}\kappa_{\perp c} &= \kappa_{\perp\infty}\left(\frac{\overline{n}}{\overline{n}_{\infty}}\right)\left(\frac{\overline{T}_i}{\overline{T}_{i\infty}}\right)^{-1/2}\\ \kappa_{\parallel c} &= \kappa_{\parallel\infty}\left(\frac{\overline{n}}{\overline{n}_{\infty}}\right)\left(\frac{\overline{T}_i}{\overline{T}_{i\infty}}\right)^{5/2}\\ \eta_{\perp c} &= \eta_{\perp\infty}\left(\frac{\overline{n}}{\overline{n}_{\infty}}\right)\left(\frac{\overline{T}_i}{\overline{T}_{i\infty}}\right)^{-1/2}\\ \eta_{\parallel c} &= \eta_{\parallel\infty}\left(\frac{\overline{n}}{\overline{n}_{\infty}}\right)\left(\frac{\overline{T}_i}{\overline{T}_{i\infty}}\right)^{5/2}\end{aligned}\right\} \tag{5.4}$$

A discussion about the difference between our proposed model and previous models[9-10, 35-36] is in order.

First and foremost, our previous numerical results (see chapters 3 and 4) have consistently indicated that viscous heating can be an important effect near the obstacle's tip. Consequently, unlike previous models that either assume that the ions are isothermal or do not take into account the effect of viscous heating, our model allows for the possibility of ion heating by viscous dissipation (see equation (5.3)).

Our model, based on a number of plausible assumptions, indicates that although the cross-field particle diffusion coefficient is enhanced because of turbulent transport, the viscosity coefficients and thermal conductivities are not enhanced. The subtlety is that because of anomalous particle transport, the cross-field transport of momentum and energy associated with convection is indeed enhanced. However, the cross-field transport of momentum and energy associated with the random motion of particles (viscosity and thermal conduction) is not enhanced. As a result, it will be shown in the forthcoming discussion that our model neither agrees nor disagrees entirely with those presented in Refs. [9–10, 35–36].

According to our model, $\eta_\perp / nMD_{\perp t} = D_{\perp c}/D_{\perp t} \sim 10^{-4}$. Consequently, we agree with Stangeby [35] in that the choice of $\eta_\perp / nMD_{\perp t} \sim 1$ overestimates the effect of cross-field viscosity. However, we disagree with Stangeby [10] because he neglected the effect of ion viscosity altogether. In fact, the plasma response obtained with the effect of ion viscosity entirely neglected is not physically plausible. To illustrate this point, equation (5.2) on the bottom boundary ($x = 0$) is written as follows:

$$v_\parallel \frac{\partial v_\parallel}{\partial z} = -\frac{c_{s\infty}^2}{n}\frac{\partial n}{\partial z}$$

where ion viscosity has been entirely neglected. For simplicity, the ions are also taken to be isothermal. Integrating the equation above with respect to z and applying the proper boundary conditions, one obtains:

$$n(0,z) = \begin{cases} n(0,-z_0)\exp\left(-\frac{1}{2}\frac{v_\parallel^2(0,z) - M_\infty^2}{c_{s\infty}^2}\right) & -z0 < z < 0^- \\ n(0,z_0)\exp\left(-\frac{1}{2}\frac{v_\parallel^2(0,z) - M_\infty^2}{c_{s\infty}^2}\right) & 0^+ < z < z_0 \end{cases}$$

Of course, z_0 is chosen sufficiently large that $n(0, z_0) = n(0, -z_0) = n_\infty$. Applying the Bohm sheath criterion, one obtains:

$$n(0,0^-) = n(0,0^+) = n_\infty \exp\left(\frac{1}{2}\frac{M_\infty^2 - c_{s\infty}^2}{c_{s\infty}^2}\right)$$

The equation above states that independent of the ambient plasma flow, the upstream density and the downstream density are always equal. Physically, one expects the upstream density to be higher than the downstream density because on the upstream side, in addition to cross-field diffusion, particles are constantly streaming into the shadow region by virtue of the ambient plasma flow. Consequently, neglecting ion viscosity entirely leads to an unphysical plasma repsonse.

Hutchinson [10,36] recognized that viscosity can be an important effect. In this respect, we agree with him that if a plausible model is to be constructed, the effect of ion viscosity should be included. However, we strongly disagree with him that 'unity remains arguably the most plausible order of magnitude for the viscosity/diffusivity ratio.'[36] In fact, in our model, the parallel transport of parallel momentum, rather than the perpendicular transport of parallel momentum, is the dominant viscous force.

5.2 Numerical Results

The plasma response is obtained from the transport equations (5.1)–(5.4). The transport equations are solved using the usual Newton-Raphson method on a non-uniform grid of 49×97. For the cases to be presented in this chapter, the basic plasma parameters are taken as follows:

$$\frac{D_{\perp t}}{D_{\perp c}} \sim 10^4$$

$$\frac{M}{m} \sim 1837$$

$$\frac{c_{s\infty}}{\omega_{ci} d} \sim 10^{-2}$$

$$\frac{T_{e0}}{T_{i\infty}} \sim 1$$

Figure 5.2 is a three-dimensional plot of the particle density $n(x, z)$ with $M_\infty = 0.20$, where M_∞ is defined as the ratio of the ambient plasma flow to the ambient ion acoustic speed. For clarity, the upstream and downstream density profiles have been plotted separately. It should be noted that the z coordinate has been scaled by the characteristic length $L \equiv c_{s\infty} d^2 / D_{\perp t}$. For realistic plasma parameters, $L \sim 10^3$ cm. Figure 5.3 is a plot of the density along the *boundary* that partitions the upstream and downstream sides ($z = 0$). Figures 5.2 and 5.3 suggest three interesting features.

First, the shadow extends longer into the downstream side of the obstacle than it does on the upstream side. This effect can be explained by the following qualitative argument. On the upstream side of the obstacle, in addition to the diffusion process through which particles are displaced into the shadow region for collection, plasma particles are also being swept into the shadow region by means of the ambient plasma flow. Consequently, fewer particles need to be displaced into the shadow region for collection, resulting in a shorter parallel scale length on the upstream side. On the downstream side, because of the ambient plasma flow, particles being displaced into the shadow region for collection by means of diffusion are initially moving away from the obstacle. These particles have to be decelerated to a complete halt, turned around, and accelerated in the opposite direction in order to be collected on the downstream surface of the obstacle, resulting in a longer parallel scale length on the downstream side.

Second, the density on the upstream surface is higher than that on the downstream surface. This effect can also be explained by the qualitative argument given above. It should be noted that this is a rather important effect. The reason is that in a realistic situation where only the upstream/downstream ion flux ratio is known (Mach probe data), we would like to be able to infer the ambient plasma flow from this ratio. For this particular case, the upstream/downstream ion flux ratio is about 1.20.

Third, the density on the downstream surface of the obstacle is lowest near the obstacle's tip, not at the point $(x, z) = (0, 0^+)$ where one expects the density to be lowest. The reason is that near the tip where ion viscous heating is most significant, the ion temperature is highest, resulting in a higher rate of particle collection and a lower local particle density than elsewhere.

Figure 5.4 is a three-dimensional plot of the ion temperature $T_i(x, z)$ with $M_\infty = 0.20$. For clarity, the upstream and downstream density profiles have been plotted separately. For comparison, a plot of the ion temperature on both the upstream and downstream surfaces of the obstacle is shown in figure 5.5. Figures 5.4 and 5.5 indicate that the ions on the upstream surface of the obstacles are somewhat hotter than those on the downstream surface, except near the obstacle's tip. There, the ions on the downstream surface of the obstacles are significantly hotter than those on the upstream surface. The reason is that the perpendicular shear of perpendicular velocity associated with diffusion is much larger on the downstream surface than on the upstream surface, resulting in a greater amount of viscous heating on the downstream surface near the obstacle's tip. Figure 5.4 indicates that except for a small region near the obstacle's tip where viscous heating is significant, the ions remain relatively isothermal.

Figure 5.6 is a plot of typical streamlines with $M_\infty = 0.20$. One may think of these streamlines as the trajectories of *tagged* ion fluid elements. Figure 5.6 shows that there are three distinct types of flow separated by two separatices. Those streamlines below the lower separatrix represent particles accelerating toward the upstream surface of obstacle. Those streamlines between the two separatrices represent particles accelerating from the upstream side into the downstream side where they are eventually decelerated to a complete halt, turned around, and accelerated in the opposite direction toward the downstream surface of the obstacle. Those streamlines above the upper separatrix represent particles flowing past the obstacle. These particles are not collected on either surface of the obstacle.

Numerical results have also been obtained for the cases in which $M_\infty = 0.10$ and $M_\infty = 0.15$. For these cases, the upstream/downstream ion flux ratio is about 1.10 and 1.15, respectively. The density, ion temperature, and streamlines for these particular cases are qualitatively similar to the case in which $M_\infty = 0.20$.

In summary, our numerical results suggest that the parallel scale length on the downstream side is longer than that on the upstream side. The ion flux on the upstream surface is found to be higher than that on the downstream surface. For the cases presented in this chapter in which $M_\infty = 0.10,\ 0.15,\ 0.20$, the upstream/downstream ion flux ratio is about 1.10, 1.15, and 1.20, respectively. It was also found that near the tip of the obstacle, the ions on the downstream surface are significantly hotter than those on the upstream surface. An examination of the plasma flow pattern suggested that there are three distinct types of flow separated by two separatrices.

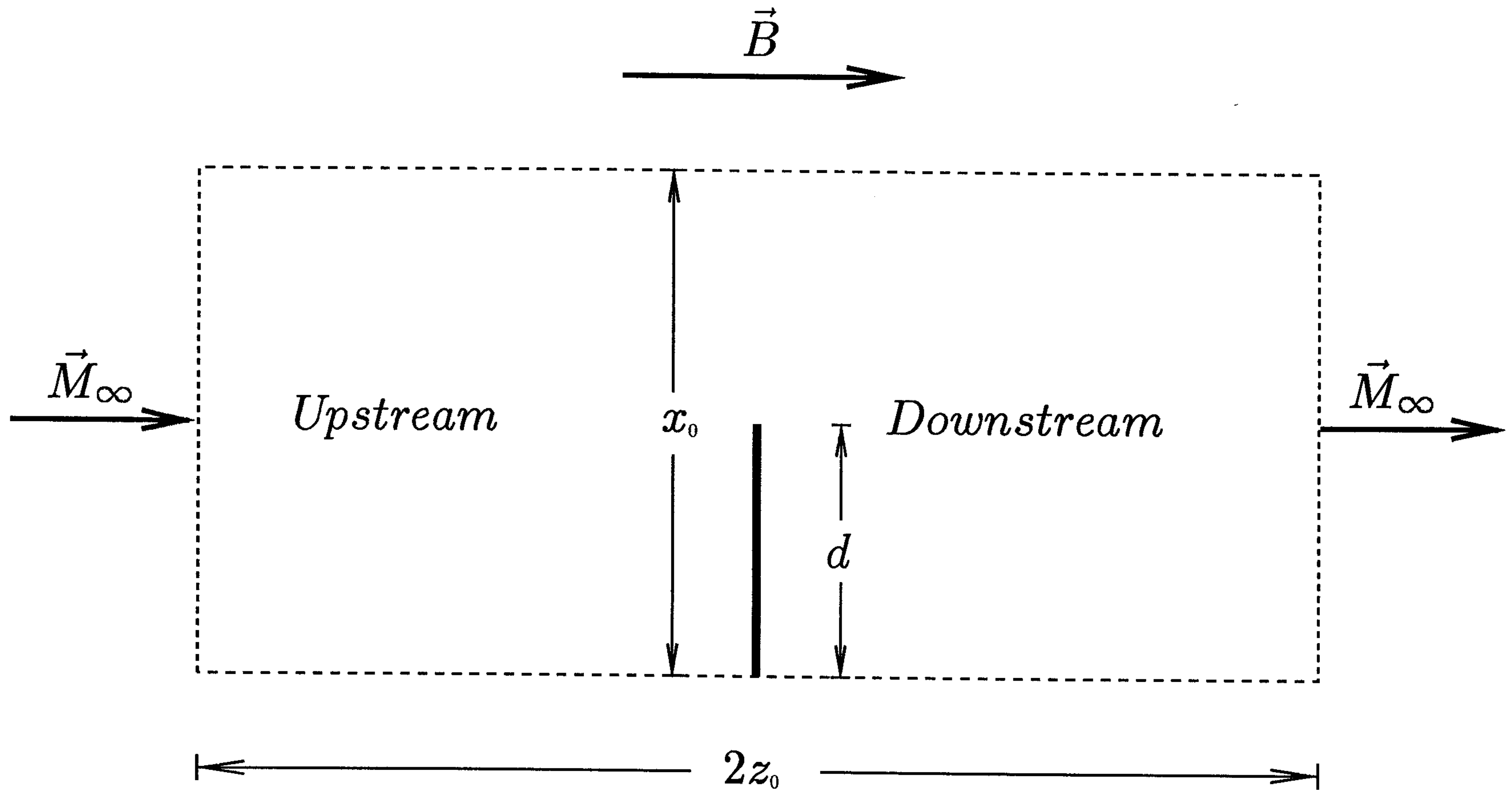

Figure 5.1: Geometry of physical system in the presence of an ambient flow. The thick solid line represents the obstacle with half-width d. The obstacle is located at $z = 0$. The ambient plasma flow is taken to be M_∞ on both the left and right boundaries ($z = \pm z_0$).

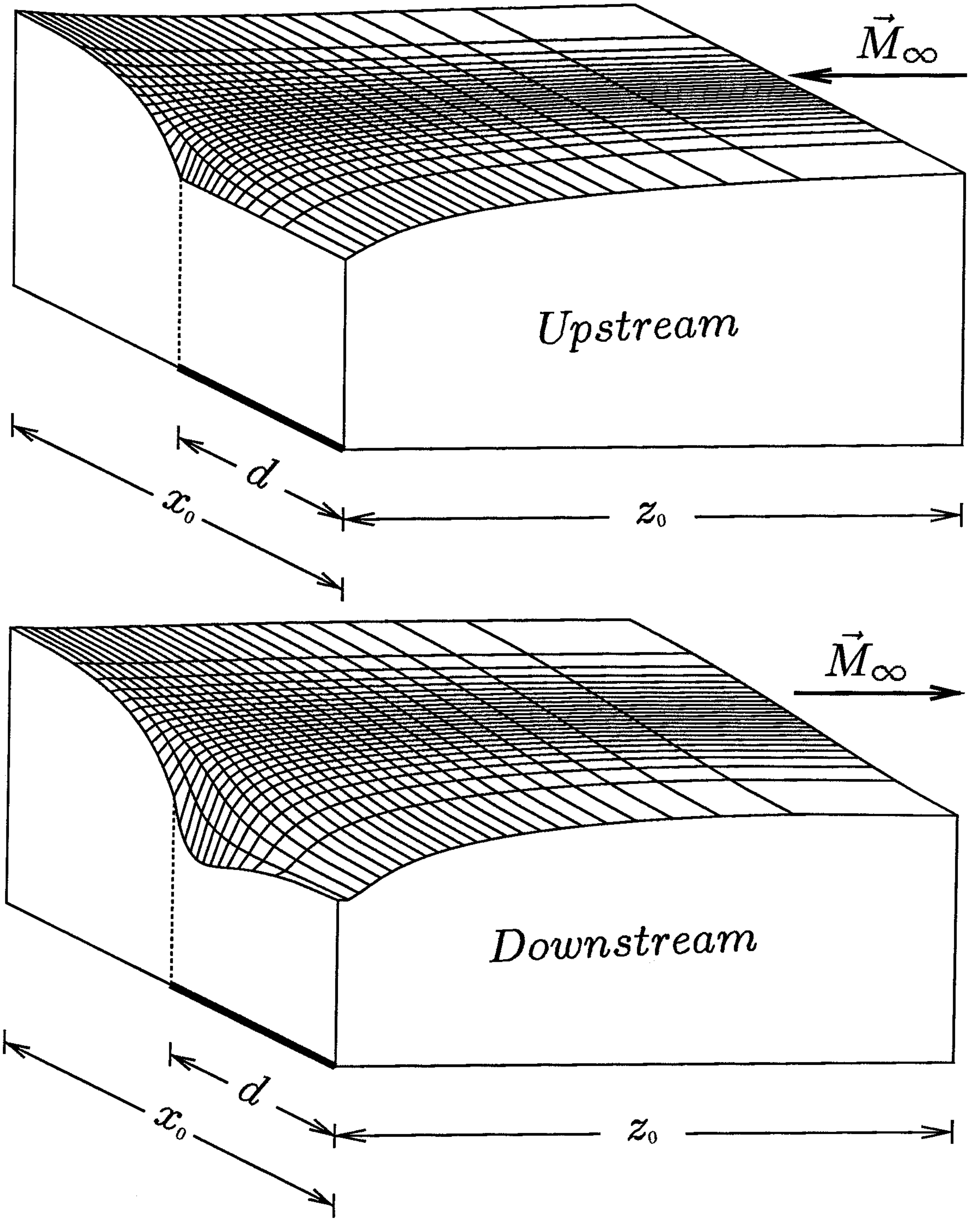

Figure 5.2: $n(x, z)$ obtained from semi-empirical transport equations accounting for anomalous particle transport, ion viscosity, and ion viscous heating in the presence of a subsonic ambient flow. $M_\infty = 0.20$, $D_{\perp t}/D_{\perp c} = 10^4$, $T_{e0}/T_{i\infty} = 1$, $M/m \sim 1837$, $c_{s\infty}/\omega_{ci}d = 10^{-2}$, $x_0 = 2$, and $z_0/L = 2.5$ ($L \equiv c_{s\infty}d^2/D_{\perp t}$). For clarity, the upstream and downstream density profiles are plotted separately.

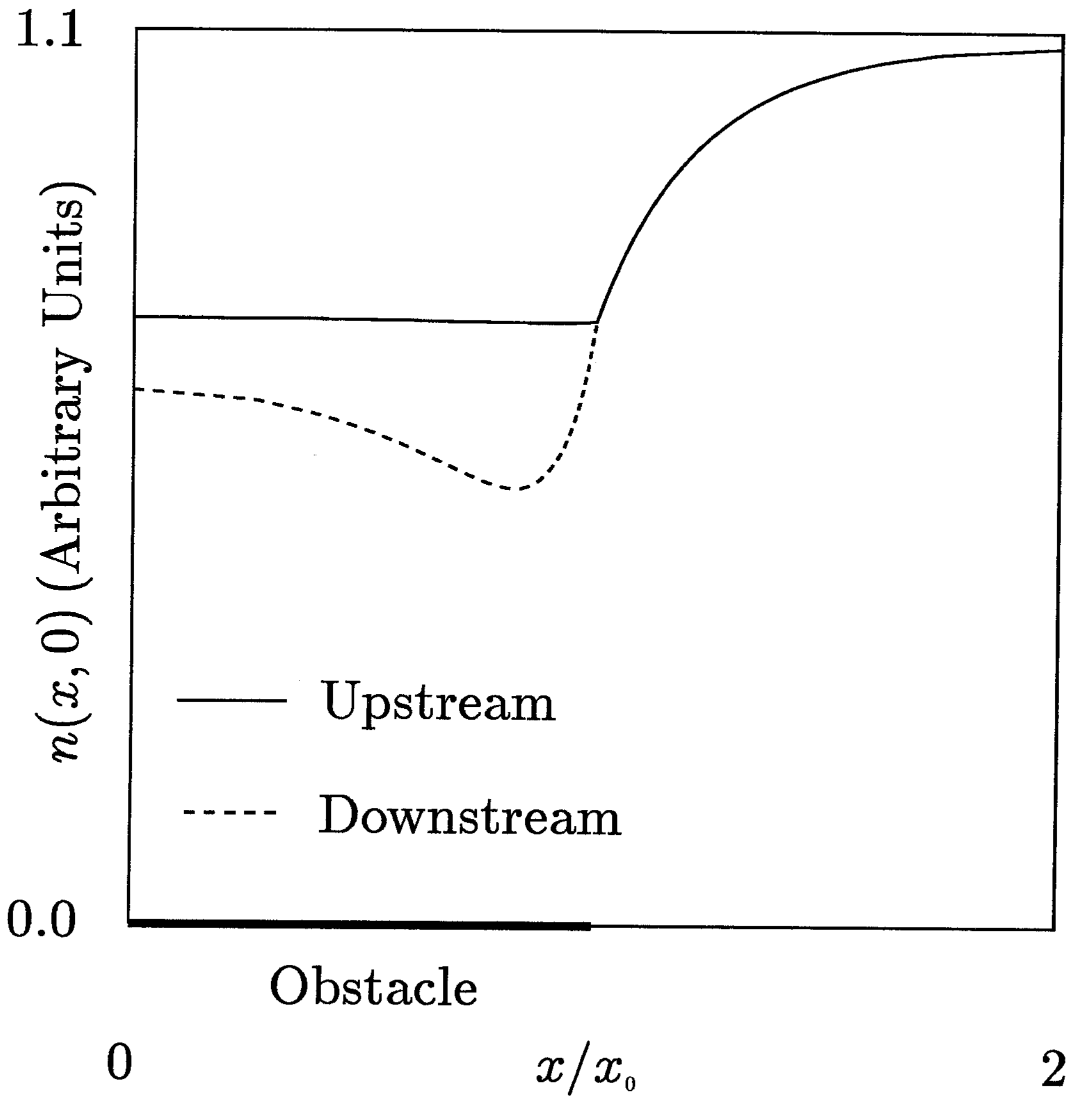

Figure 5.3: 2-D plot of $n(x,0)$ (density profile on upstream and downstream surfaces of obstacle). $n(x,z)$ is obtained from semi-empirical transport equations accounting for anomalous particle transport, ion viscosity, and ion viscous heating in the presence of a subsonic ambient flow. $M_\infty = 0.20$, $D_{\perp t}/D_{\perp c} = 10^4$, $T_{e0}/T_{i\infty} = 1$, $M/m \sim 1837$, $c_{s\infty}/\omega_{ci}d = 10^{-2}$, $x_0 = 2$, and $z_0/L = 2.5$ ($L \equiv c_{s\infty}d^2/D_{\perp t}$). Anomalous transport is assumed to be caused by a randomly fluctuating poloidal electric field.

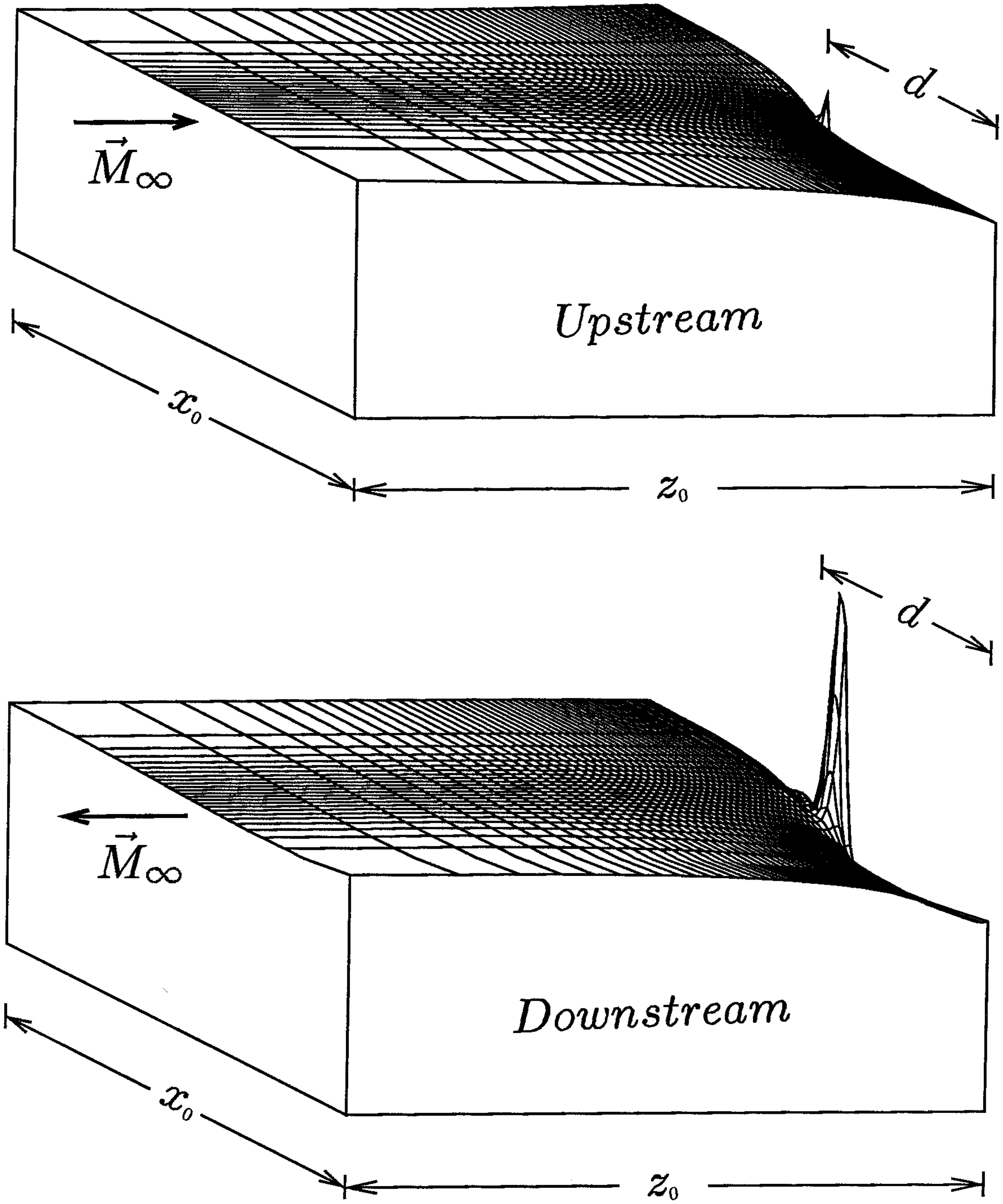

Figure 5.4: $T_i(x,z)$ obtained from semi-empirical transport equations accounting for anomalous particle transport, ion viscosity, and ion viscous heating in the presence of a subsonic ambient flow. $M_\infty = 0.20$, $D_{\perp t}/D_{\perp c} = 10^4$, $T_{e0}/T_{i\infty} = 1$, $M/m \sim 1837$, $c_{s\infty}/\omega_{ci}d = 10^{-2}$, $x_0 = 2$, and $z_0/L = 2.5$ ($L \equiv c_{s\infty}d^2/D_{\perp t}$). For clarity, the upstream and downstream ion temperature profiles are plotted separately.

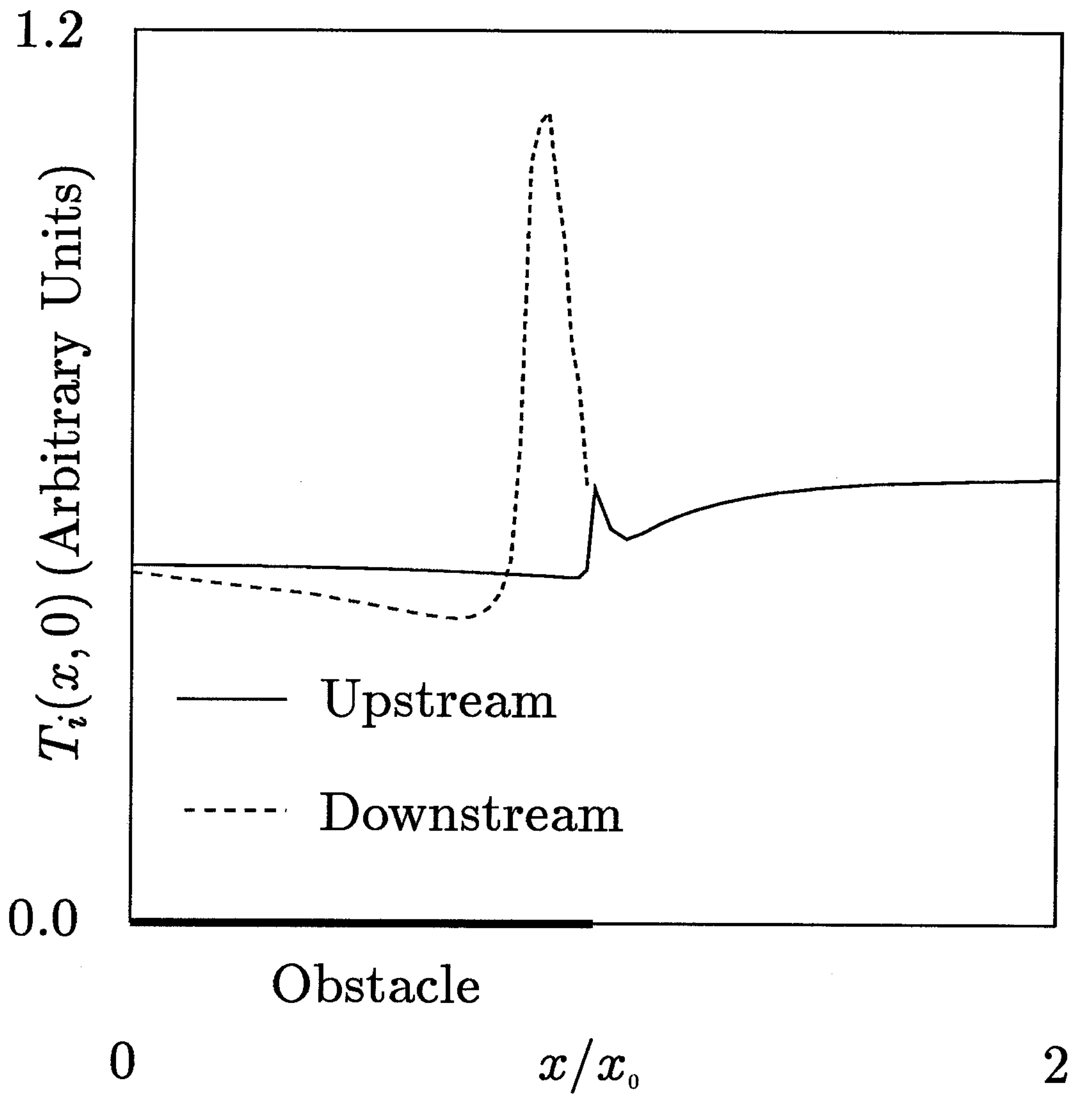

Figure 5.5: 2-D plot of $T_i(x,0)$ (ion temperature profile on upstream and downstream surfaces of obstacle). $T_i(x,z)$ is obtained from semi-empirical transport equations accounting for anomalous particle transport, ion viscosity, and ion viscous heating in the presence of a subsonic ambient flow. $M_\infty = 0.20$, $D_{\perp t}/D_{\perp c} = 10^4$, $T_{e0}/T_{i\infty} = 1$, $M/m \sim 1837$, $c_{s\infty}/\omega_{ci}d = 10^{-2}$, $x_0 = 2$, and $z_0/L = 2.5$ ($L \equiv c_{s\infty}d^2/D_{\perp t}$). Anomalous transport is assumed to be caused by a randomly fluctuating poloidal electric field.

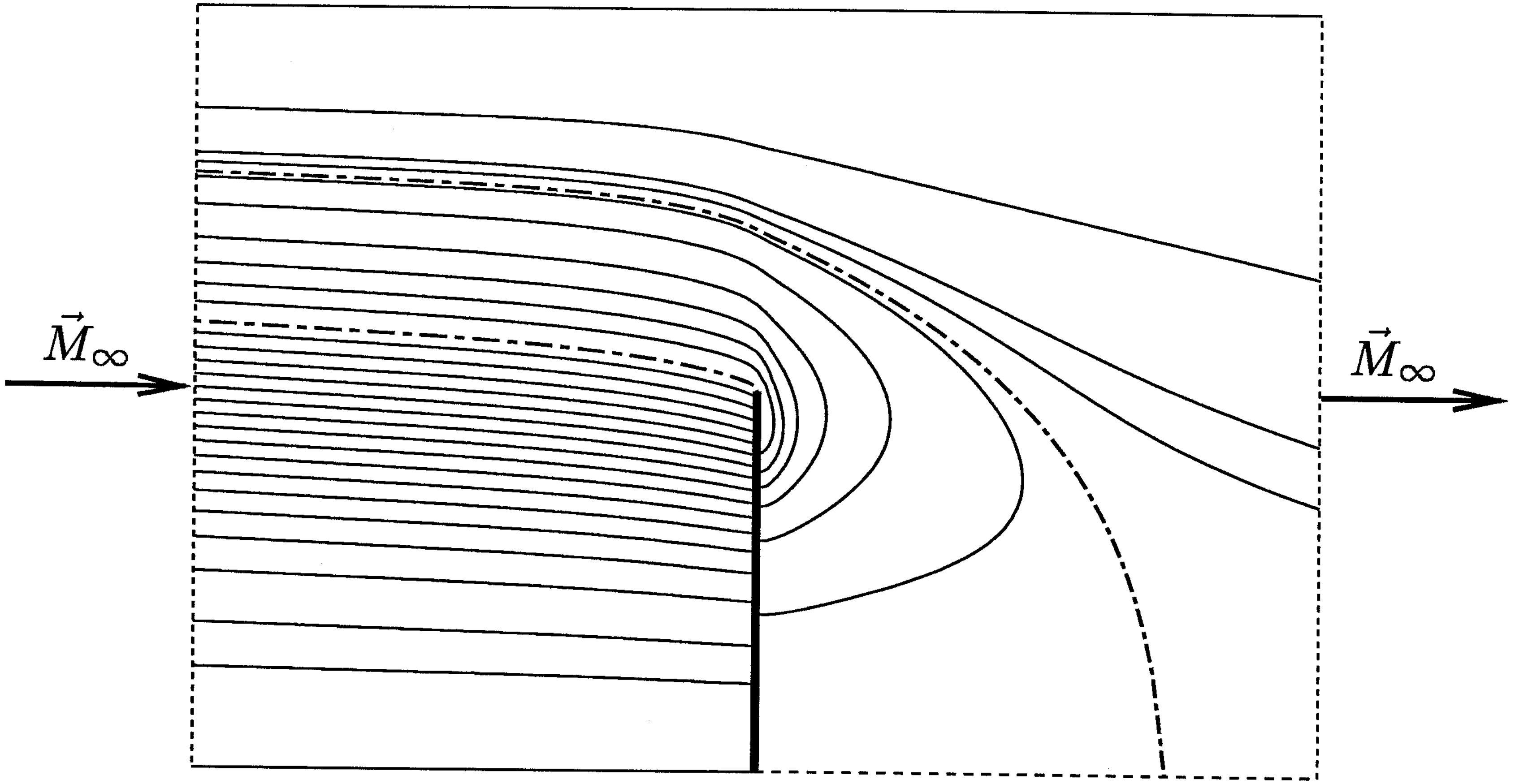

Figure 5.6: Streamlines representing trajectories of ion fluid elements. The plasma response is obtained from semi-empirical transport equations accounting for anomalous particle transport, ion viscosity, and ion viscous heating in the presence of a subsonic ambient flow. $M_\infty = 0.20$, $D_{\perp t}/D_{\perp c} = 10^4$, $T_{e0}/T_{i\infty} = 1$, $M/m \sim 1837$, $c_{s\infty}/\omega_{ci}d = 10^{-2}$, $x_0 = 2$, and $z_0/L = 2.5$ $(L \equiv c_{s\infty}d^2/D_{\perp t})$.

CHAPTER 6

Summary and Conclusions

In this thesis, various aspects of plasma collection by an obstacle were studied in detail. A summary of our primary numerical results and conclusions is given below.

In chapter 3, a number of potentially important physical mechanisms associated with the classical diffusion and collection of plasma particles by a two-dimensional obstacle were considered. Our numerical results suggested that the effects of ion viscosity and viscous heating can be important in the plasma region where the velocity gradient is large, e.g., the region near the obstacle's tip. In fact, the inclusion of ion viscosity and ion viscous heating lead to two unexpected behaviours of the plasma response, which had not been anticipated previously. First, due to ion viscosity, the plasma near the obstacle's tip is denser than the ambient plasma. This result is surprising since the plasma in regions where the collection occurs is expected to be more tenuous than the ambient plasma. Second, due to ion viscous heating, the ion temperature near the obstacle's tip is significantly higher than the ambient ion temperature. This result is also surprising since the ions are expected to cool down as they are accelerated toward the obstacle.

In chapter 4, a semi-empirical model is proposed to account for anomalous transport caused by a randomly fluctuating poloidal electric field. Contrary to that which has been suggested in the literature, our proposed model suggested that in the presence of anomalous transport, it is not physically plausible to postulate that $\eta_\perp/nMD_{\perp t}$, the viscosity/diffusivity, is of the order 1. In fact, our proposed model suggests that $\eta_\perp/nMD_{\perp t} \sim D_{\perp c}/D_{\perp t} \ll 1$ is a more plausible choice. Our numerical results (for a set of plausible plasma parameters) indicated that the ion temperature near the obstacle's tip is up to 85% higher than the ambient ion temperature.

In chapter 5, an extension of the model proposed in chapter 4 was constructed to account for a subsonic ambient plasma flow. This problem is of interest because it has direct applications in the interpretation of Mach probe measurements. Our numerical results suggest that the ions on the upstream side of the obstacle are hotter than those on the downstream side except near the obstacle's tip where the density gradient is largest. There, the ions on the downstream side are hotter than those on the upstream side.

In the course of this thesis, two difficult, yet fundamental, issues have been identified. Because of their complexity, it is likely that these issues cannot be resolved within a reasonable time limit. Consequently, they were left unaddressed. However, it would be interesting to study these fundamental issues in detail. The two unaddressed issues are described below.

First, it has been recognized in chapters 3 and 4 that the obstacle's tip is a special point for the following reason. Below the obstacle, the ion velocity component parallel to the external magnetic field (perpendicular to the obstacle's surface) is taken to be c_s, the ion acoustic speed. This is the Bohm sheath criterion, and is obtained by solving for the one-dimensional collisionless transport equations and requiring that the electrostatic potential be monotonically decreasing with decreasing distance from the obstacle's surface. Since both the Debye shielding distance and the ion Larmor radius are small compared with the width of the obstacle, the one-dimensional Bohm sheath criterion can be applied to the entire surface of the obstacle except for a small region near the tip. Above the obstacle, the ion velocity component parallel to the external magnetic field is, in the absence of an ambient plasma flow, zero due to symmetry. Consequently, the ions appear to make the transition from sonic flow to zero flow in a small scale length. In order to understand this transition, it is perhaps necessary to solve for the two-dimensional plasma-sheath equation self-consistently.

Second, in order to construct a realistic model describing plasma-probe interactions in the SOL (scrape-off layer), it is important, in principle, to include the effect of the containment vessel. Because the vacuum vessel is parallel to the toroidal magnetic field, a magnetic sheath is formed on the surface of the vacuum vessel in addition to the usual electrostatic sheath. Unfortunately, the magnetic sheath is not well understood, and is riddled with numerous problems. Consequently, the effect of the containment vessel was neglected entirely in this thesis.

Obvious and interesting extensions of this thesis are recommended below.

Throughout the course of this thesis, the obstacle is assumed to be insulating. Consequently, the net electric current density is required to vanish at each point on the obstacle's surface. It would be interesting to see the plasma response for an unbiased *conducting* obstacle. For an unbiased conducting obstacle, the net electric current density is not necessarily zero at each point on the obstacle's surface. Instead, the net current density integrated over the entire surface of the obstacle is required to vanish. It would also be interesting to see the result of biasing the conducting obstacle.

In the scrape-off layer, both the electric and the magnetic fields have been observed to be fluctuating. It has been suggested that the electric fluctuation is responsible for anomalous particle transport, and that the magnetic fluctuation is responsible for anomalous energy transport. In this thesis, a semi-empirical model is proposed to account for anomalous transport caused by a randomly fluctuating poloidal electric field. It would be interesting if the same approach is taken to model anomalous transport caused by a randomly fluctuating radial magnetic field.

Appendix A

A One-Dimensional Model of Electrostatic Sheaths with Warm Ions

This appendix contains a simple one-dimensional model of electrostatic sheaths with warm ions. The model presented here is a variation of the one-dimensional model of electrostatic sheaths with cold ions proposed by Chen.[17] Although more rigorous models of electrostatic sheaths with warm ions have been presented in the literature (see, for example, [14–16, 18–20]), our simple model is much easier to understand, and contains the essential physics of sheath formations. An important observation is that all models of electrostatic sheaths suggest that the ions must obtain a speed above some threshold value upon entering the sheath in order for the electrostatic potential to be stable, i.e., monotonically decreasing.

In our model, the plasma is assumed to be collisionless. This is a good assumption if the collisional mean-free-paths are much longer than the thickness of the sheath, i.e,

$$\lambda_{ee} \sim \lambda_{ei} \sim \lambda_{ii} \gg \lambda_D \tag{A.1}$$

where λ_{ee}, λ_{ei}, λ_{ii}, and λ_D are the electron-electron collisional mean-free-path, the electron-ion collisional mean-free-path, the ion-ion collisional mean-free-path, and the Debye length, respectively. Equation (A.1) is satisfied in most tokamak plasmas (see section 3.1). Therefore, our assumption that the plasma is collisionless is justified. The electrons and the ions are also assumed to be isothermal since their self-collisional mean-free-paths are also much longer than the Debye length. Figure A.1 illustrates the geometry of the one-dimensional electrostatic sheath. The ions are assumed to enter the sheath with a speed of v_0. The sheath's thickness is of the order of the Debye length. At the sheath edge ($z = 0$), the electron density and the ion density are assumed to be equal. The equations of motion are written as follows:

$$Mv\frac{dv}{dz} = -e\frac{d\phi}{dz} - \frac{T_{i0}}{n_i}\frac{dn_i}{dz} \tag{A.2}$$

$$0 = e\frac{d\phi}{dz} - \frac{T_{e0}}{n_e} \tag{A.3}$$

$$\frac{d(n_i v)}{dz} = 0 \tag{A.4}$$

$$\frac{d^2\phi}{dz^2} = -\frac{e}{\epsilon_0}(n_i - n_e) \tag{A.5}$$

where M is the ion mass.

By integrating equations (A.2)–(A.4) and rearranging the resulting equations, one obtains:

$$\frac{1}{2}M(v^2 - v_0^2) = -e\phi + T_{i0}\ln\left(\frac{v}{v_0}\right) \tag{A.6}$$

$$n_e = e^{e\phi/T_{e0}} \tag{A.7}$$

$$n_i v = n_0 v_0 \tag{A.8}$$

Near the sheath edge ($z/\lambda_D \ll 1$), we have:

$$\left|\frac{e\phi}{T_{e0}}\right| \ll 1$$

$$\frac{v - v_0}{v_0} \ll 1$$

By linearizing equations (A.6)–(A.8) with respect to the parameters above and rearranging the resulting equations, one obtains:

$$\left.\begin{aligned} n_i &\simeq n_0\left(1 + \frac{e\phi}{Mv_0^2 - T_{i0}}\right) \\ n_e &\simeq n_0\left(1 + \frac{e\phi}{T_{e0}}\right) \end{aligned}\right\} \tag{A.9}$$

where equation (A.9) is valid only for $z/\lambda_D \ll 1$.

Substituting equation (A.9) into equation (A.5), one obtains:

$$\frac{d^2\phi}{dz^2} \simeq \frac{en_0}{\epsilon_0}\frac{e\phi}{T_{e0}}\left(1 - \frac{T_{e0}}{Mv_0^2 - T_i}\right)$$

Since $d\phi/dz$ is taken to be zero at the sheath edge, $d^2\phi/dz^2$ must be negative if ϕ is to decrease with increasing z. Thus, near the sheath edge, both ϕ and $d^2\phi/dz^2$ must be negative. As a result, the Bohm sheath criterion is obtained, i.e.,

$$1 - \frac{T_{e0}}{Mv_0^2 - T_i} > 0$$

Alternatively, the above expression can be written as follows:

$$v_0 > \sqrt{\frac{T_{e0} + T_{i0}}{M}} \qquad (A.10)$$

The most important assumption of our model is that both the electrostatic potential and the electric field are taken to be zero at the sheath edge. However, in order for the ions to acquire a speed of v_0 upon entering the sheath, there must exist a non-zero electric field in the presheath (the transition layer between the main plasma and the sheath region). Therefore, our assumption that both the electrostatic potential and the electric field are zero at the sheath edge is not entirely correct. However, since there are two markedly different scale lengths, the electric field at the sheath edge is much smaller than that within the sheath region, and our assumption is partly justified.

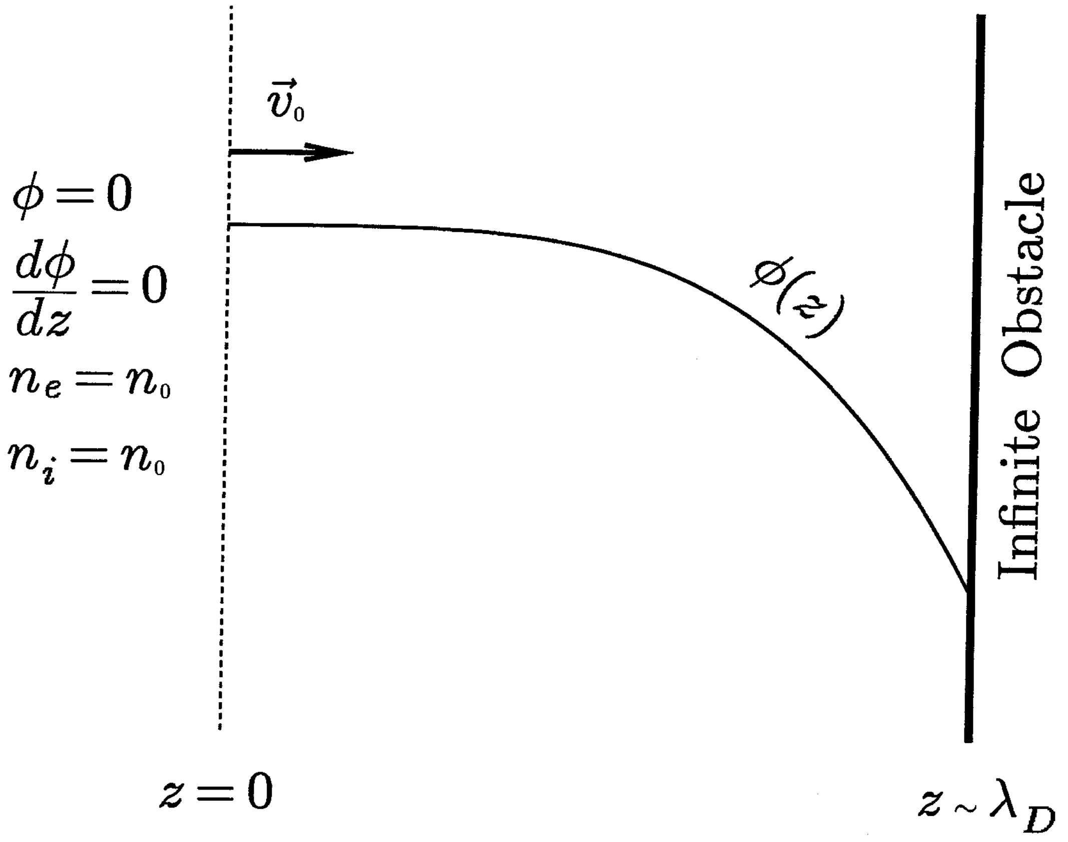

Figure A.1: Geometry of 1-D electrostatic sheaths with stable, monotonically decreasing electrostatic potential. The sheath's thickness is of the order of the Debye shielding distance λ_D. The electrostatic potential ϕ (shown above) and the electric field $-d\phi/dz$ are both taken to be 0 at the sheath edge ($z = 0$) where the plasma is assumed to be quasineutral. The ions enter the sheath with a velocity $\mathbf{v}_0$.

Appendix B

Coordinate Transformations

This appendix contains a detailed description of the coordinate transformations used in solving the two-dimensional transport equations. The parallel gradients are expected to be steepest near the obstacle's surface since this is where the collection of particles, momentum, and energy occurs. The perpendicular gradients are expected to be steepest near the tip of the obstacle. We would like to construct the perpendicular and parallel coordinate transformations in such a manner that the mesh spacing is finest where the gradients are steepest.

B.1 Transformation of z

In the parallel direction, the coordinate transformation is chosen as follows:

$$\Theta(z) = e^{az} \tag{B.1}$$

Using the above coordinate transformation and the basic rules of differentiation, the parallel derivatives are transformed as follows:

$$\left.\begin{aligned} \frac{\partial}{\partial z} &= a\Theta\frac{\partial}{\partial\Theta} \\ \frac{\partial^2}{\partial z^2} &= a^2\left(\Theta^2\frac{\partial^2}{\partial\Theta^2} + \Theta\frac{\partial}{\partial\Theta}\right) \end{aligned}\right\} \tag{B.2}$$

Our task is to find an *optimal* value for the coefficient a. This is achieved by solving the transport equations on a moderately coarse grid with various values of a. Figure B.1 is a plot of $n(x = 0, z)$, the particle density on the bottom boundary, for different values of a. For our particular set of governing equations, we found that there exists a value for a such that $n(x = 0, z)$ corresponding to that value of a is higher than that corresponding to other values of a. This is actually the optimal value of a. The reason is that increasing a reduces the truncation error near the obstacle's surface and at the same time increases the truncation error near the left boundary. The overall truncation error of the solution is the larger of the two truncation errors. For a grid corresponding to uniform spacing in z, the truncation error near the obstacle's surface dominates. In this case, increasing a will improve the solution. The direction in which the curve $n(x = 0, z)$ shifts is the direction toward the optimal solution, e.g., it is the upward direction in our case. However, as a reaches its optimal value, the truncation error near the obstacle's surface is about the same as that near the left boundary. Increasing a further will now cause the truncation error near the left boundary to dominate, and therefore causes the solution to deteriorate. The value of a such that $n(x = 0, z)$ lies above all other curves is therefore the optimal value of a.

B.2 Transformation of x

In our model, x_0 has to be sufficiently large that the plasma is undisturbed far from the obstacle, e.g., the particle density should be approximately uniform on the top periodic boundary. We found that $x_0/d = 2$ meets this requirement. Our coordinate transformation is chosen as follows:

$$\Lambda(x) = \tanh[\, b(x - d)] \tag{B.3}$$

Using the above coordinate transformation and the basic rules of differentiation, the perpendicular derivatives are transformed as follows:

$$\left.\begin{aligned} \frac{\partial}{\partial x} &= b(1 - \Lambda^2)\frac{\partial}{\partial \Lambda} \\ \frac{\partial^2}{\partial x^2} &= b^2(1 - \Lambda^2)\left[(1 - \Lambda^2)\frac{\partial^2}{\partial \Lambda^2} - 2\Lambda\frac{\partial}{\partial \Lambda}\right] \end{aligned}\right\} \tag{B.4}$$

where $0 \leq x \leq 2d$.

As before, we now have to find an algorithm to determine the optimal value for the coefficient b. We have solved the transport equations on a moderately coarse grid for different values of b. The particle density on the right boundary, $n(x, z = z_0)$, is also plotted for several values of b. Unfortunately, these curves do not possess the property discussed in the previous section. Therefore, we have to find a different way to determine the optimal value for b. This is achieved with the following steps. First, we solve the transport equations on a uniform grid (uniform spacing in x) of various sizes: 49×13 (the first and second numbers refer to the number of grid points in the x and z directions, respectively), 97×13, 193×13, and finally 385×13. Figure B.2 is a plot of $n(x, z = z_0)$ for these different grid sizes. We see that as the grid gets finer (in the x-direction), the truncation error becomes smaller. Now, we solve for the transport equations on a grid of 49×13 for different values of b. The optimal value of b is chosen such that $n(x, z = z_0)$ corresponding to this particular value of b is closest to that corresponding to a uniform grid of 385×13. Figure B.3 shows that in this particular case, $b \simeq 2.4$ is the optimal choice.

We can construct a mathematical proof to show that the optimal value for the coefficient b chosen in this manner is independent of the number of grid points used in the z-direction, e.g., we would obtain the same optimal value for b if we used 25 grid points in the z direction instead of 13. Numerical results obtained also confirm this assessment. Because the coordinate transformations in the parallel and perpendicular directions are independent and because our governing equations do not contain any cross-derivatives, e.g., $\partial^2/\partial x \partial z$, we have:

$$n(\Lambda, \Theta, \delta\Lambda, \delta\Theta, b, a) = n(\Lambda, \Theta) + \sum_{k=1}^{\infty} C_k(\Lambda, b)(\delta\Lambda)^k + \sum_{k=1}^{\infty} D_k(\Theta, a)(\delta\Theta)^k$$

The L.H.S. of the above equation is the particle density obtained from the finite-difference approximation of the transport equations. $n(\Lambda, \Theta)$ is the exact solution of the transport equations. The last two terms of the R.H.S. of the above equation are just the truncation errors of the perpendicular and parallel directions, respectively.

The equation above is used to construct the following equation:

$$n(\Lambda,\Theta,\delta\Lambda,\delta\Theta_0,b,a_0)-n(\Lambda,\Theta,\delta\Lambda,\delta\Theta_1,b,a_1)=\sum_{k=1}^{\infty}D_k(\Theta,a_0)(\delta\Theta_0)^k - \sum_{k=1}^{\infty}D_k(\Theta,a_1)(\delta\Theta_1)^k$$

The above equation can be carried one step further to give:

$$\left.\begin{array}{l} n(\Lambda,\Theta,\delta\Lambda_0,\delta\Theta_0,b_0,a_0)- \\ n(\Lambda,\Theta,\delta\Lambda_1,\delta\Theta_0,b_1,a_0) \end{array}\right\} = \left\{\begin{array}{l} n(\Lambda,\Theta,\delta\Lambda_0,\delta\Theta_1,b_0,a_1)- \\ n(\Lambda,\Theta,\delta\Lambda_1,\delta\Theta_1,b_1,a_1) \end{array}\right.$$

In essence, the above equation states that two given finite-difference solutions of the transport equations with different b (grid non-uniformity factor in the x-direction) and a different number of grid intervals in the x-direction will change by exactly the same amount if a (grid non-uniformity factor in the z-direction) and the number of grid intervals in the z-direction are changed accordingly. Figure B.4 is a plot of the particle density on the right boundary with different values of $\delta\Lambda$, $\delta\Theta$, b, and a. It seems to confirm the above assessment. Thus, our method for determining the optimal value for b appears to yield the same result independent of both the number of grid points in the z-direction and a (the grid non-uniformity factor in the z-direction).

B.3 Mesh Discretization

The mesh is uniform in the domain of the transformed coordinates $\Lambda(x)$ and $\Theta(z)$. The spatial derivatives are discretized on this uniform mesh as follows:

$$\left.\begin{aligned} \left(\frac{\partial\Psi}{\partial\Lambda}\right)_{ij} &= \frac{1}{2\delta\Lambda}(\Psi_{i+1,j}-\Psi_{i-1,j}) \\ \left(\frac{\partial\Psi}{\partial\Theta}\right)_{ij} &= \frac{1}{2\delta\Theta}(\Psi_{i,j+1}-\Psi_{i,j-1}) \\ \left(\frac{\partial^2\Psi}{\partial\Lambda^2}\right)_{ij} &= \frac{1}{(\delta\Lambda)^2}(\Psi_{i+1,j}-2\Psi_{ij}+\Psi_{i-1,j}) \\ \left(\frac{\partial^2\Psi}{\partial\Theta^2}\right)_{ij} &= \frac{1}{(\delta\Theta)^2}(\Psi_{i,j+1}-2\Psi_{ij}+\Psi_{i,j-1}) \end{aligned}\right\} \qquad (B.5)$$

where the indices i and j refer to the spatial position in Λ and Θ, respectively. This differencing scheme is second order in both $\delta\Lambda$ and $\delta\Theta$.

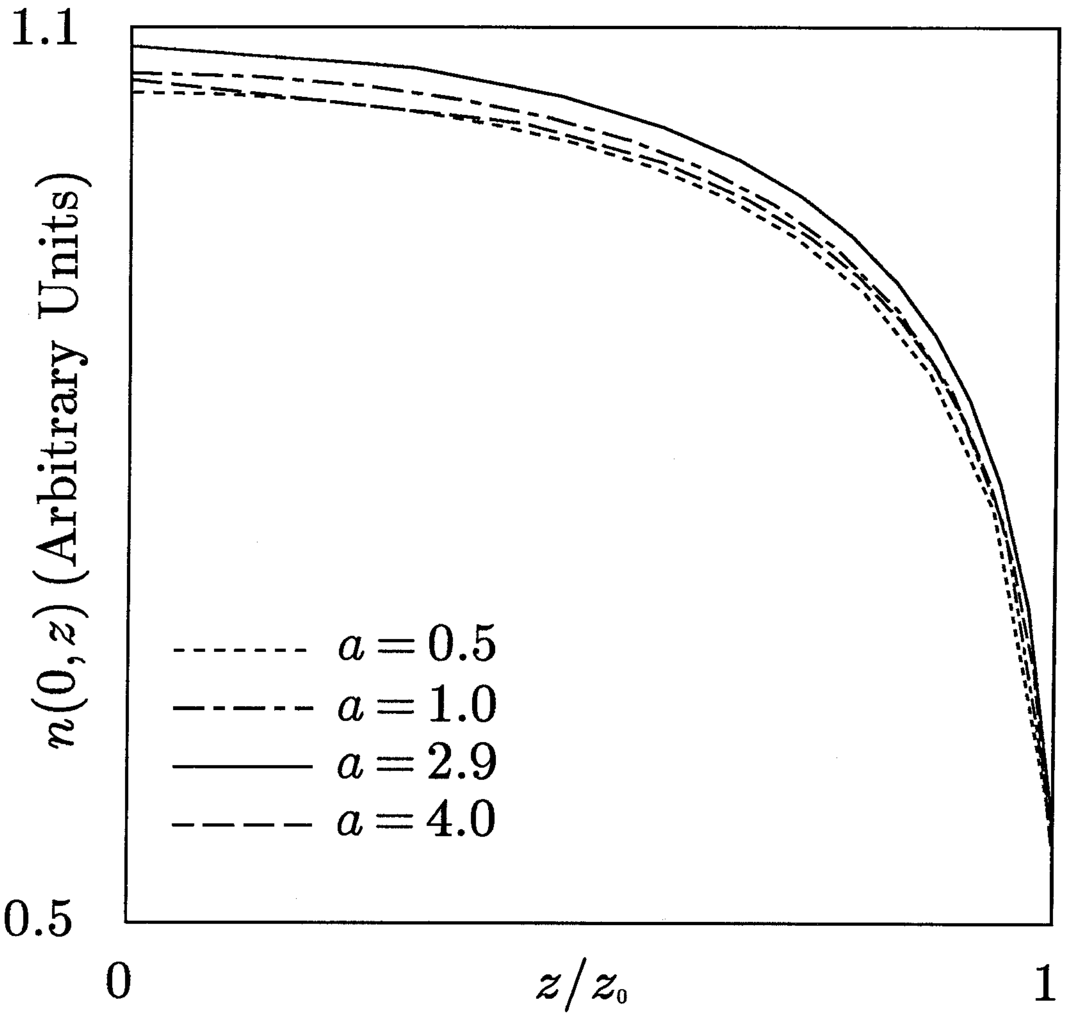

Figure B.1: 2-D plot of $n(x = 0, z)$ (density along bottom boundary) for several values of a, the grid non-uniformity factor in the z-direction. The number of grid intervals (in both the x and z directions) is the same for all of the cases above (12 intervals in the x-direction and 24 intervals in the z-direction). The solid curve corresponds to $a = 2.9$. Any curve corresponding to $a \neq 2.9$ lies below the solid curve, suggesting that $a_{optimal} \simeq 2.9$.

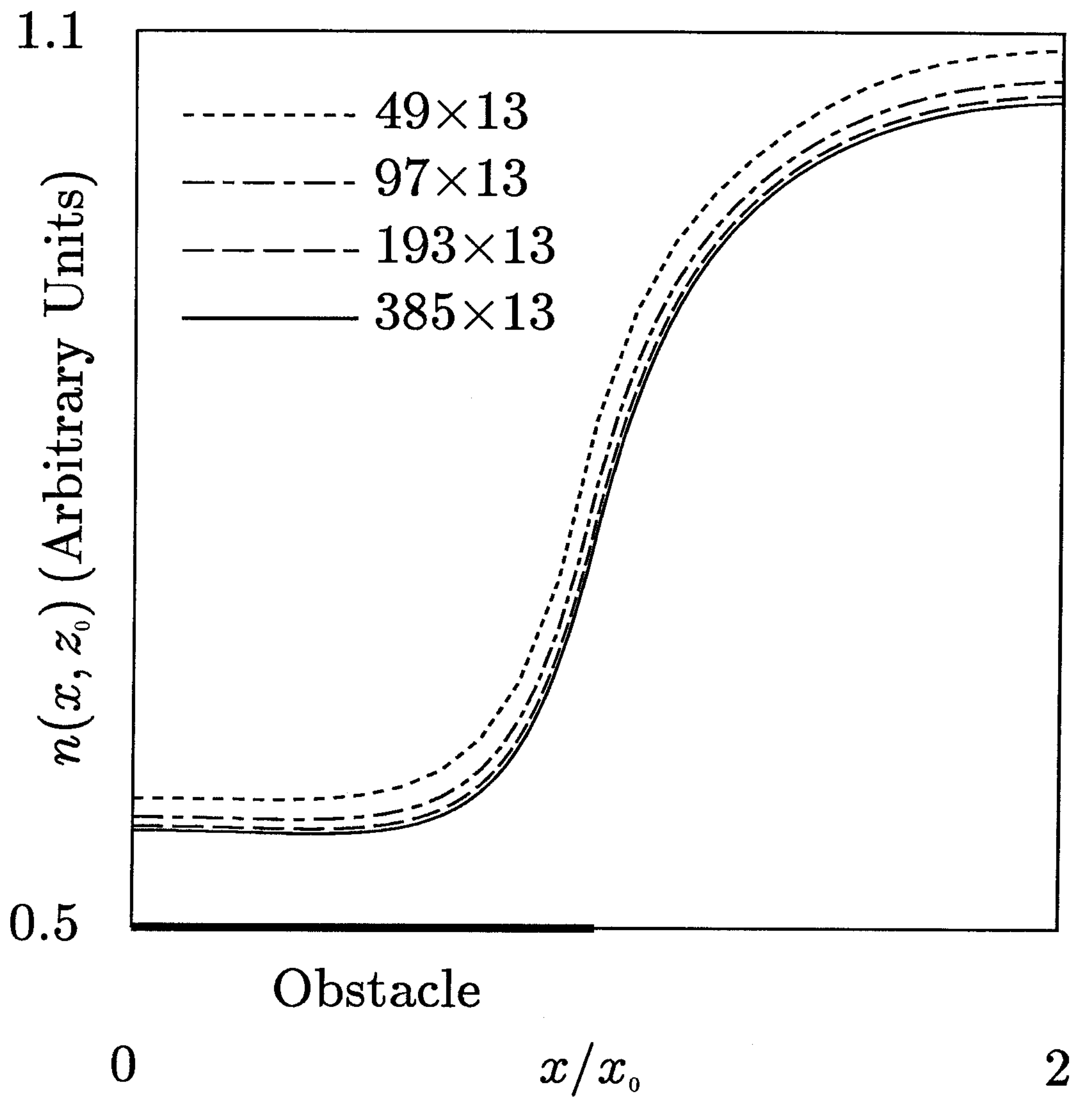

Figure B.2: 2-D plot of $n(x, z_0)$ (density along obstacle's surface) for different grid sizes in the x-direction. The number of grid intervals in the z-direction is the same in all cases (12 intervals in the z-direction). The grid is uniform in the x-direction. Note that as the grid gets finer (in the x-direction), the truncation error is reduced accordingly.

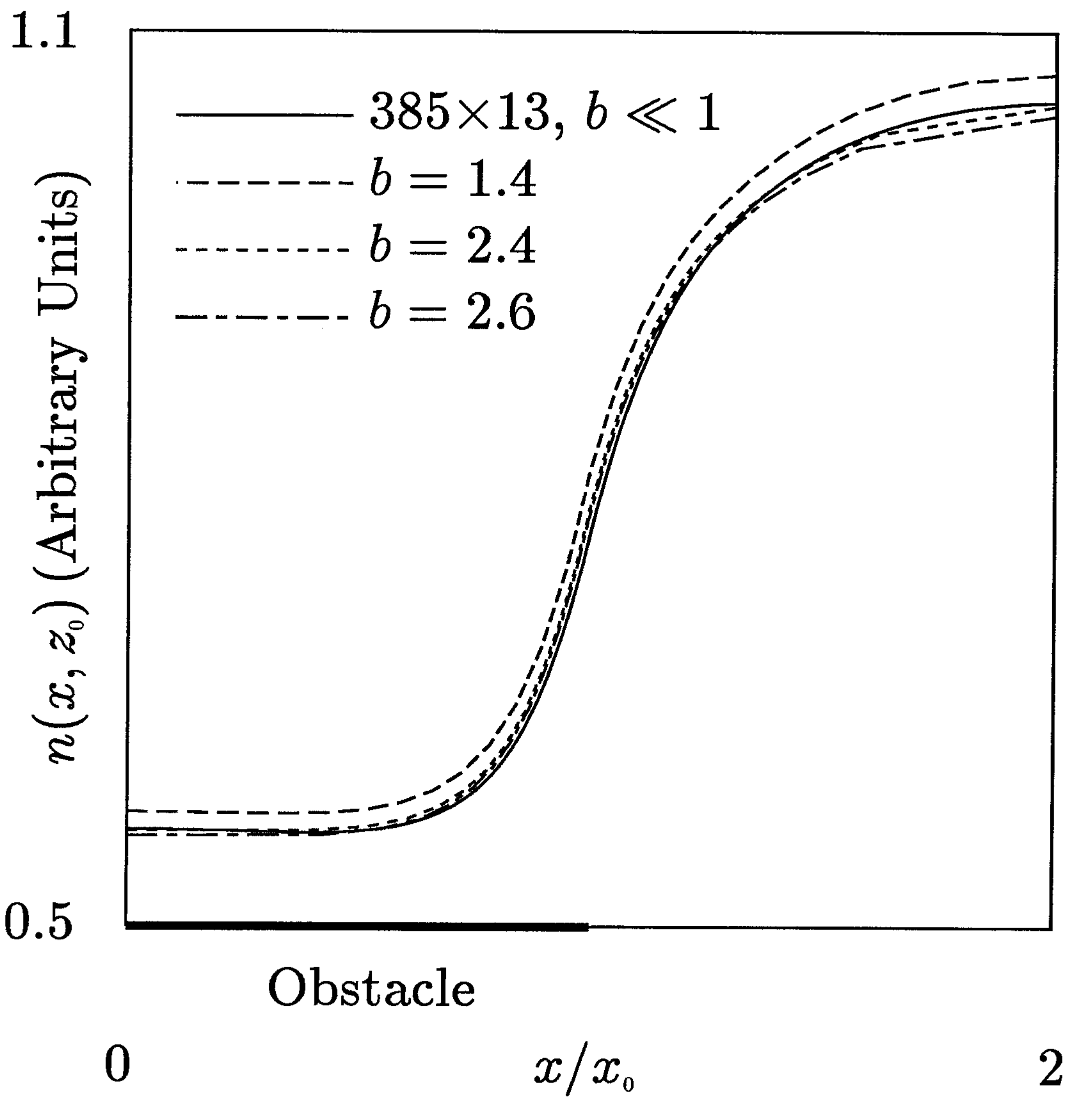

Figure B.3: 2-D plot of $n(x, z_0)$ (density along obstacle's surface) for several values of b, the grid non-uniformity factor in the x-direction. The number of grid intervals in the z-direction is the same for all cases (12 intervals in the z-direction). The solid curve is obtained with 384 uniform grid intervals in the x-direction. Note that the curve corresponding to $b = 2.4$ with 48 grid intervals in the x-direction is closest to the solid curve, suggesting that $b_{optimal} \sim 2.4$.

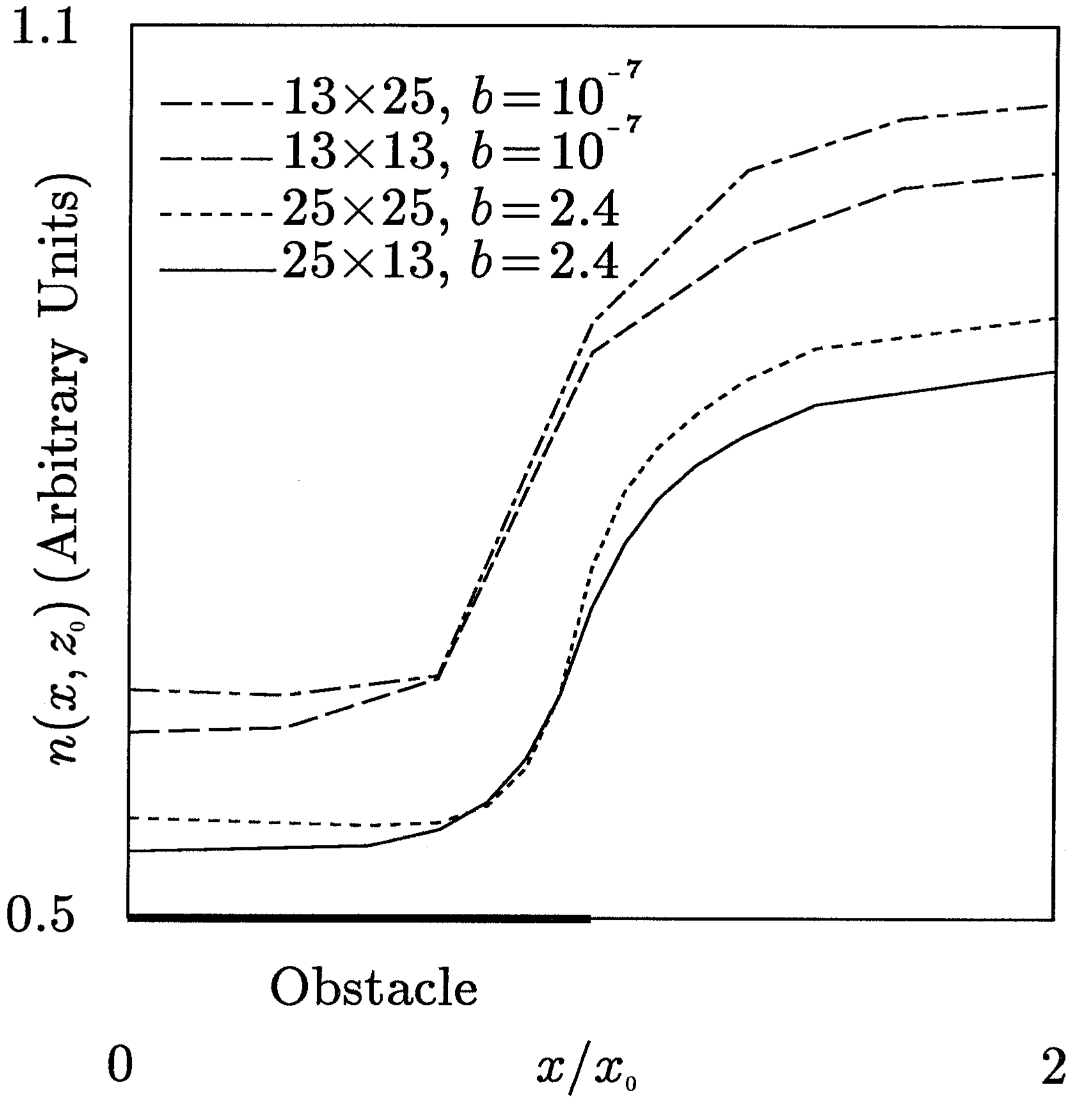

Figure B.4: 2-D plot of $n(x, z_0)$ (density along obstacle's surface) for 4 different grid sizes. It is demonstrated that the choice of $b_{optimal}$ is independent of the grid spacing in the z-direction. From this, one can also infer that the choice of $a_{optimal}$ is independent of the grid spacing in the x-direction.

Appendix C

Plasma Collection by an Obstacle: A 1-D Model

This appendix contains a detailed discussion of a one-dimensional model of the transport equations (3.8)–(3.9). Figure C.1 illustrates the geometry of this model. The obstacles are assumed to be planes extending to infinity in both the x and y directions. This study proves to be useful because the exact solution of the one-dimensional isothermal, inviscid tranport equations is readily available. We can study the general behaviour of the transport equations. We can also compare our numerical solution of the one-dimensional transport equations with the exact solution.

C.1 One-Dimensional Isothermal, Inviscid Transport Equations

In one dimension, the transport equations (3.8)–(3.9) can be written as follows:

$$v\frac{dv}{dz} = -\frac{c_s^2}{n}\frac{dn}{dz} \qquad (C.1)$$

$$\frac{d(nv)}{dz} = S_0 \qquad (C.2)$$

where both v and n are functions of z only. As a reminder, v is taken to be c_s on the obstacle. Equation (C.1) states that in one dimension, the ions free-fall through a scalar potential field.

Integrating the equations above with respect to z, one obtains:

$$\left.\begin{aligned} \frac{1}{2}v^2 &= -c_s^2 \ln\left[\frac{n}{n(0)}\right] \\ nv &= S_0 z \end{aligned}\right\} \qquad (C.3)$$

The equation above can be written as follows:

$$\left.\begin{aligned}\frac{v}{c_s}\exp\left(-\frac{v^2}{2c_s^2}\right)&=e^{-1/2}\frac{z}{z_0}\\ \frac{n}{n(0)}&=\exp\left(-\frac{v^2}{2c_s^2}\right)\\ n(0)&=e^{1/2}\frac{S_0z_0}{c_s}\end{aligned}\right\}\qquad(C.4)$$

Equation (C.4) is the exact solution of the one-dimensional isothermal, inviscid transport equations.

The transport equations (C.1)–(C.2) are suspected to have a singularity at $z = z_0$ for the following reason. At $z = z_0$, v is taken to be c_s by virtue of the Bohm's sheath criterion. Thus, equations (C.1)–(C.2) at $z = z_0$ become:

$$\begin{aligned}\frac{dv}{dz}&=-\frac{c_s}{n}\frac{dn}{dz}\\ n\frac{dv}{dz}+c_s\frac{dn}{dz}&=S_0\end{aligned}$$

If we attempted to substitute the top equation into the bottom one, we would obtain $0 = S_0$, which is known to be wrong.

In fact, we can show that the transport equations (C.1)–(C.2) possess a singular behaviour at $z = z_0$. Substituting equation (C.1) into equation (C.2), one obtains:

$$n\left(1-\frac{v^2}{c_s^2}\right)\frac{dv}{dz}=S_0$$

Substituting equation (C.3) into the equation above, one obtains:

$$\left(1+\frac{v}{c_s}\right)\left(1-\frac{v}{c_s}\right)\frac{dv}{dz}=\frac{v}{z}\qquad(C.5)$$

Consider the following Taylor expansion in the neighbourhood of z_0:

$$\begin{aligned}v(z_0)&=v[z+(z_0-z)]\\ &=v(z)+(z_0-z)\left.\frac{dv}{dz}\right|_z\end{aligned}$$

Since $v(z_0) = c_s$, the equation above becomes:

$$1-\frac{v}{c_s}=(z_0-z)\frac{1}{c_s}\frac{dv}{dz}$$

Substituting the equation above into equation (C.5), one obtains:

$$\lim_{\zeta \to 1} \frac{d(v/c_s)}{dz} = \frac{1}{\sqrt{2}} \lim_{\zeta \to 1} \frac{1}{\sqrt{1-\zeta}} \tag{C.6}$$

where $\zeta = z/z_0$. The equation above describes the singular behaviour of the transport equations (C.1)–(C.2). Although n and v have finite values at the obstacle, their gradients go to infinity there. This is a manifestation of the fact that in our model, the electric field goes to infinity at the obstacle. However, it has been shown by Self[6] that at the sheath edge, the electric field does not really go to infinity. In fact, our model, which assumes that the plasma is quasi-neutral, breaks down at the sheath edge. Thus, as an artifact of our model, the electric field goes to infinity at the obstacle.

C.2 Numerical Method

Since this is a one-dimensional problem, the transport equations (C.1)–(C.2) can be solved efficiently by the Newton-Ralphson method (linearization). Linearizing equations (C.1)–(C.2), one obtains:

$$\xi \frac{dv_0}{dz} + v_0 \frac{d\xi}{dz} - n_1 \frac{c_s^2}{n_0^2} \frac{dn_0}{dz} + \frac{c_s^2}{n_0} \frac{dn_1}{dz} = -v_0 \frac{dv_0}{dz} - \frac{c_s^2}{n_0} \frac{dn_0}{dz} \tag{C.7}$$

$$\xi \frac{dn_0}{dz} + n_0 \frac{d\xi}{dz} + n_1 \frac{dv_0}{dz} + v_0 \frac{dn_1}{dz} = S_0 - n_0 \frac{dv_0}{dz} - v_0 \frac{dn_0}{dz} \tag{C.8}$$

where

$$v = v_0 + \xi$$

$$n = n_0 + n_1$$

We will use the same coordinate transformation as described in Appendix A. At $z = 0$, we require v and dn/dz to vanish. At $z = z_0$, the Bohm's sheath criterion is used to replace the ion momentum equation, and dv/dz and dn/dz are approximated by one-sided finite differences.

C.3 Results

Figure C.2 is a plot of the finite-difference solution of the transport equations (C.1)–(C.2) versus the exact solution. In this case, there are 41 mesh points. Figure C.2 shows that even with only 41 mesh points, there is a good agreement between the finite-difference solution and the exact solution. Figure C.3 is a similar plot with 101 mesh points. The agreement between the finite-difference solution and the exact solution is even better in this case. Both the finite-difference solution and the exact solution of the transport equations (C.1)–(C.2) show that n and v have infinite slopes at the obstacle.

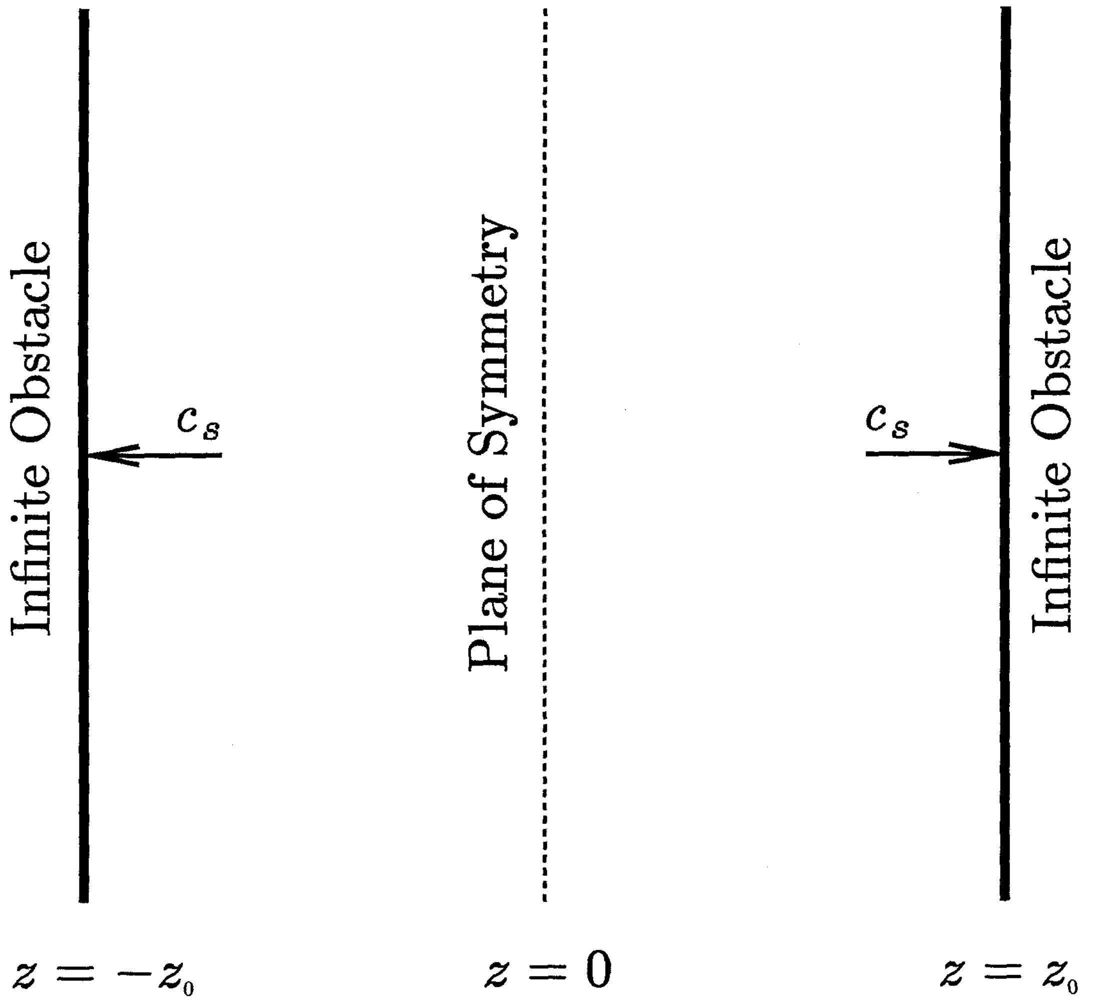

Figure C.1: Geometry of 1-D plasma collection by an obstacle. The ions are assumed to enter the electrostatic sheath at the local ion acoustic speed. The transport process is taken to be inviscid and isothermal.

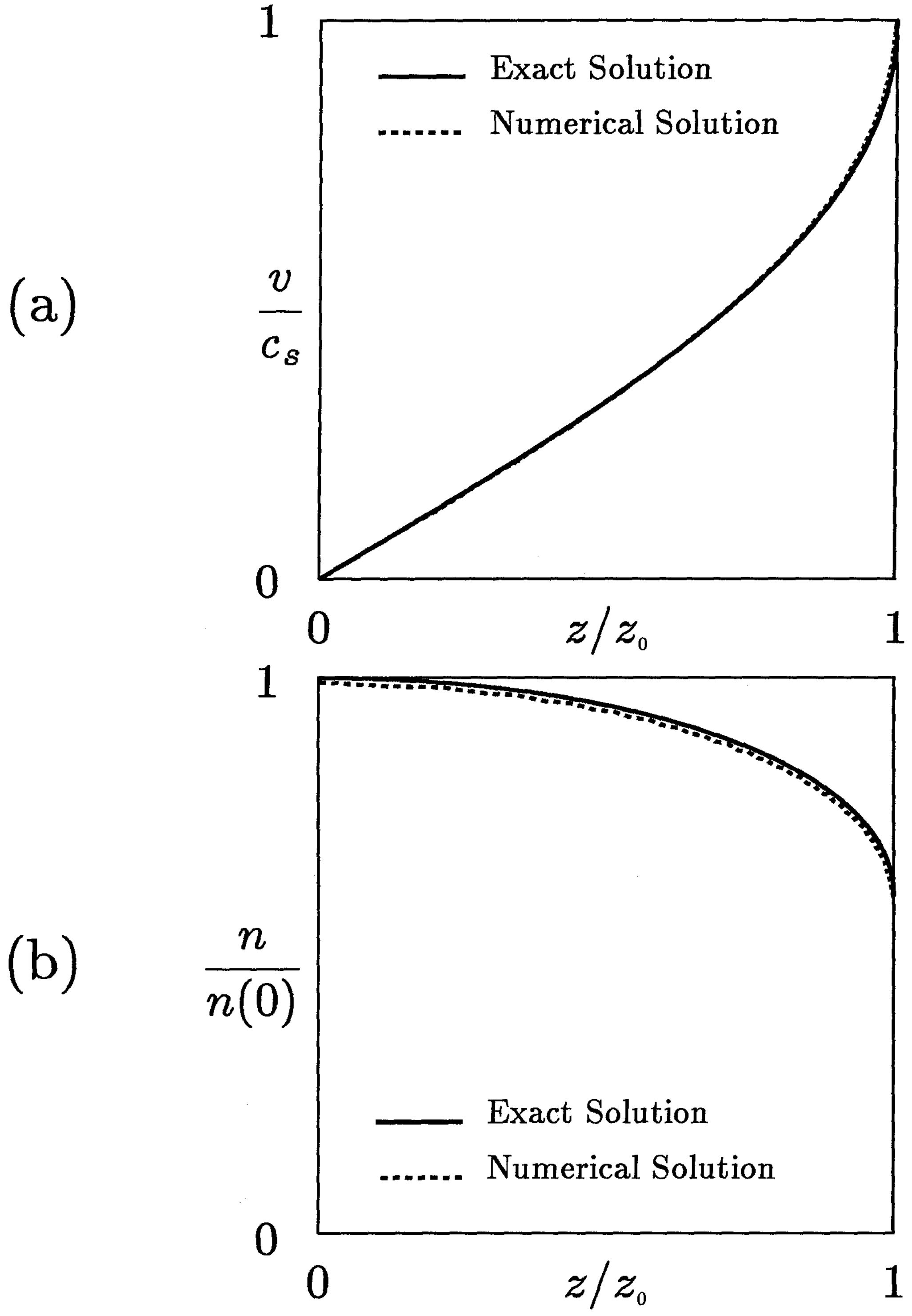

Figure C.2: Comparison between exact solution (both $n(z)$ and $v(z)$) and numerical solution of 1-D isothermal, inviscid transport equations. In this case, the 1-D computational grid has 40 intervals.

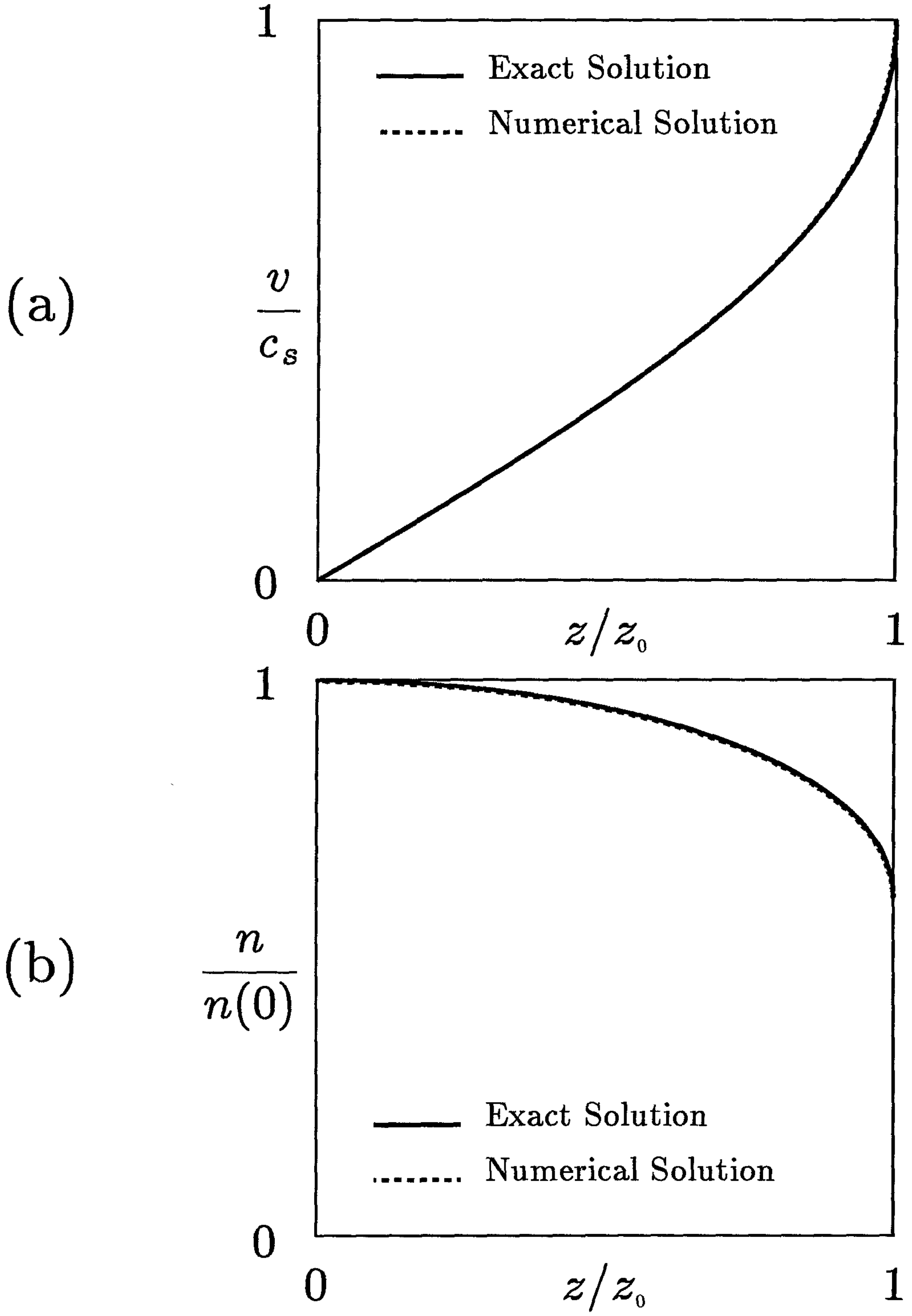

Figure C.3: Comparison between exact solution (both $n(z)$ and $v(z)$) and numerical solution of 1-D isothermal, inviscid transport equations. In this case, the 1-D computational grid has 100 intervals.

Appendix D

Normalization Procedure and Program Listing

This appendix contains a detailed description of the normalization of the macroscopic variables $\mathbf{v}$ (ion fluid velocity), n (particle density), and T_i (ion temperature). A complete listing of the computer code is also included in this appendix.

D.1 Viscid, Non-Isothermal Two-Fluid Equations

When the transport process is assumed to be classical, the two-fluid description of the plasma response can be reduced to equations (3.61)–(3.63). For clarity, these equations are rewritten below:

$$\boldsymbol{\nabla}\cdot(n\mathbf{v}) = S_0 \tag{$D.1$}$$

$$\boldsymbol{\nabla}\cdot(Mn\mathbf{v}\mathbf{v}) = \frac{neB}{1+\alpha^2}(\mathbf{v}_\perp \times \hat{z} - \alpha\mathbf{v}_\perp) - \boldsymbol{\nabla}[n(T_{e0}+T_i)] - \boldsymbol{\nabla}\cdot\boldsymbol{\pi} + S_0 M\mathbf{v} \tag{$D.2$}$$

$$\begin{aligned}\frac{3}{2}n\mathbf{v}\cdot\boldsymbol{\nabla}T_i = &-nT_i\boldsymbol{\nabla}\cdot\mathbf{v} + \frac{\partial}{\partial x}\left(\kappa_\perp\frac{\partial T_i}{\partial x}\right) + \frac{\partial}{\partial z}\left(\kappa_\parallel\frac{\partial T_i}{\partial z}\right)\\ &+\eta_\perp\left[\left(\frac{\partial v_y}{\partial x}\right)^2 + \left(\frac{\partial v_z}{\partial x}\right)^2\right] + S_0 T_{i\infty}\end{aligned} \tag{$D.3$}$$

where

$$\boldsymbol{\nabla}\cdot\boldsymbol{\pi} = -\frac{\partial}{\partial x}\left(\eta_\perp\frac{\partial v_y}{\partial x}\right)\hat{y} - \frac{\partial}{\partial x}\left(\eta_\perp\frac{\partial v_z}{\partial x}\right)\hat{z}$$

Various plasma parameters and transport coefficients are defined as follows:

$$\left.\begin{aligned}
\alpha &= \frac{D_{\perp\infty}\omega_{ci}}{c_{s\infty}^2} \\
c_{s\infty} &= \sqrt{\frac{T_{e0}+T_{i\infty}}{M}} \\
\eta_\perp &= \sqrt{\frac{M}{m}}\, nMD_{\perp\infty}\frac{r^{3/2}}{1+r}\left(\frac{T_i}{T_{i\infty}}\right)^{-1/2} \\
r &= \frac{T_{e0}}{T_{i\infty}} \\
\kappa_{\parallel} &\sim \frac{1}{D_{\perp\infty}}\left(\frac{c_{s\infty}^2}{\omega_{ci}}\right)^2\sqrt{\frac{m}{M}}\,\frac{1}{r^{3/2}(1+r)}\,n\left(\frac{T_i}{T_{i\infty}}\right)^{5/2} \\
\kappa_\perp &\sim \sqrt{\frac{M}{m}}\,D_{\perp\infty}\frac{r^{3/2}}{1+r}\,n\left(\frac{T_i}{T_{i\infty}}\right)^{-1/2}
\end{aligned}\right\} \qquad (D.4)$$

D.2 Normalization Procedure

The ion fluid velocity $\mathbf{v}$ and the ion temperature T_i are normalized to the ion acoustic speed and the ion temperature of the ambient plasma, respectively. The particle density n is not normalized. The spatial coordinates x and z are both normalized to d, the half-width of the obstacle. The resulting normalized variables and coordinates can be written as follows:

$$\tilde{\mathbf{v}} = \mathbf{v}/c_{s\infty}$$

$$\tilde{T}_i = T_i/T_{i\infty}$$

$$\tilde{x} = x/d$$

$$\tilde{z} = z/d$$

The transport equations (D.1)–(D.3) are normalized with respect to the above transformation, and the resulting equations are written below:

$$\tilde{\boldsymbol{\nabla}}\cdot(n\tilde{\mathbf{v}}) = \tilde{S}_0 \qquad (D.5)$$

$$\begin{aligned}
\tilde{\boldsymbol{\nabla}}\cdot(n\tilde{\mathbf{v}}\tilde{\mathbf{v}}) = {}& \frac{(1+r)^{-1/2}}{\tilde{\rho}_i(1+\alpha^2)}\,n(\tilde{\mathbf{v}}_\perp\times\hat{z} - \alpha\tilde{\mathbf{v}}_\perp) - \tilde{\boldsymbol{\nabla}}[n(\delta_1+\delta_2\tilde{T}_i)] \\
& + \frac{\partial}{\partial\tilde{x}}\left(\tilde{\eta}_\perp\frac{\partial\tilde{v}_y}{\partial\tilde{x}}\right)\hat{y} + \frac{\partial}{\partial\tilde{x}}\left(\tilde{\eta}_\perp\frac{\partial\tilde{v}_z}{\partial\tilde{x}}\right)\hat{z} + \tilde{S}_0\tilde{\mathbf{v}} \qquad (D.6)
\end{aligned}$$

$$\frac{3}{2} n\tilde{\mathbf{v}} \cdot \tilde{\boldsymbol{\nabla}}\tilde{T}_i = -n\tilde{T}_i\tilde{\boldsymbol{\nabla}}\cdot\tilde{\mathbf{v}} + \frac{\partial}{\partial\tilde{x}}\left(\tilde{\kappa}_\perp \frac{\partial\tilde{T}_i}{\partial\tilde{x}}\right) + \frac{\partial}{\partial\tilde{z}}\left(\tilde{\kappa}_\parallel \frac{\partial\tilde{T}_i}{\partial\tilde{z}}\right) + \tilde{\eta}_\perp\left[\left(\frac{\partial\tilde{v}_y}{\partial\tilde{x}}\right)^2 + \left(\frac{\partial\tilde{v}_z}{\partial\tilde{x}}\right)^2\right] + \tilde{S}_0 \qquad (D.7)$$

where

$$\left.\begin{aligned}
\delta_1 &= \frac{r}{1+r} \\
\delta_2 &= 1-\delta_1 \\
\tilde{\rho}_i &= \rho_i/d = \frac{1}{\omega_{ci}d}\sqrt{\frac{T_i}{M}} \\
\alpha &= (1+r)^{-1/2}\tilde{D}_{\perp\infty}/\tilde{\rho}_i \\
\tilde{D}_{\perp\infty} &= \frac{D_{\perp\infty}}{c_{s\infty}d} \\
\tilde{\eta}_\perp &= \tilde{\kappa}_\perp = \sqrt{\frac{M}{m}}\,\tilde{D}_{\perp\infty}\frac{r^{3/2}}{1+r}\,n\tilde{T}_i^{-1/2} \\
\tilde{\kappa}_\parallel &\sim \frac{\tilde{\rho}_i^2}{\tilde{D}_{\perp\infty}}\sqrt{\frac{m}{M}}\,r^{-3/2}\,n\tilde{T}_i^{5/2}
\end{aligned}\right\} \qquad (D.8)$$

Equations (D.5)–(D.8) are the dimensionless two-fluid equations describing the viscid, non-isothermal ion motion, provided that the transport process is classical. Given r (the ratio of the electron temperature to the ion temperature far from the obstacle), the ion-to-electron mass ratio, $\tilde{D}_{\perp\infty}$ (the normalized particle diffusion coefficient far from the obstacle), and $\tilde{\rho}_i$ (the ratio of the ion Larmor radius far from the obstacle to the half-width of the obstacle), the plasma response can be obtained by solving equations (D.5)–(D.8).

D.3 Program Listing

A complete listing of our computer code is given below.

```
c*********************************************************************
c*                                                                   *
c*    This program computes the plasma response when the ion motion is *
c*    viscid and non-isothermal.  The electrons are assumed to be     *
c*    inviscid and isothermal.  The transport process is taken to be  *
c*    classical.  A set of 5 coupled non-linear PDE's are solved by   *
c*    the standard method of linearization (Newton-Raphson).  Because *
c*    this method requires much more core memory than our IBM-PC is   *
c*    equiped with, we are forced to utilize to mass storage device as *
c*    the source of "virtual memory."  In order to be able to run a   *
c*    case with a grid of 49 by 193, 4 MB of core memory and 90 MB of *
c*    mass storage are required.                                      *
c*                                                                   *
c*********************************************************************
c
      implicit real*8(a-h,n-z),integer(i-m)
      integer nmax,nmaxml,nb,ndis,npos
      real*8 kperp,kpar
      character*8 crunchr(249,494),crunchrhs(494),crunchdiag(494)
      dimension vx0(49,193),vy0(49,193),vz0(49,193),n0(49,193)
     &,t0(49,193),x(49),z(193),dudz(193),dvdx(49),dvdxsqr(49)
     &,ddvdxdv(49),dudzsqr(193),ddudzdu(193),bandl(249,494)
     &,bandr(249,494),diag(494),rhs(494),sol(47285)
      common /matrx2/ nmax,nmaxml
      common /v0n0/ vx0,vy0,vz0,n0,t0
      common /input1/ aperp,rhoi,x0,z0,imax,jmax,tol0,s,dperp,tau0,kperp
     &,eta,etapar,kpar,imid,qvis
      common /input2/ dzm,x,z,dudz,dudzsqr,ddudzdu,dvdx,dvdxsqr,ddvdxdv
      common /relax/ beta,beta2,del1,del2,optau0
      common /start/ istart,iter
      common /clength/ zpar
      common /error/ errvx0m,errvy0m,errvz0m,errn0m,errt0m,resmax
      common /mesh/ zmeshx
      common /b0/ bandl,bandr
      common /b1/ diag,rhs
      common /b2/ nb,ndis
      equivalence(crunchr,bandr)
      equivalence(crunchrhs,rhs)
      equivalence(crunchdiag,diag)
      call dostim(ihour,imin,isec,ith)
c
c---------------------------------------------------------------------
c
c     Read input parameters from external input data file.
c
      call input
c
c---------------------------------------------------------------------
c
c     Initialized the plasma response (initial guess).
c
      call initial
c
c---------------------------------------------------------------------
c
c     Set up direct access files for virtual memory usage.
c
      maxrecl=8*(nb+2)
      jlim1=68
      jlim2=135
      open(unit=2,file='e:\\tmp\\virtual.dat',status='unknown'
     &,access='direct',form='unformatted',recl=maxrecl)
      open(unit=3,file='d:\\tmp\\virtual.dat',status='unknown'
     &,access='direct',form='unformatted',recl=maxrecl)
```

```
      open(unit=4,file='c:\\tmp\\virtual.dat',status='unknown'
     &,access='direct',form='unformatted',recl=maxrecl)
c
c-----------------------------------------------------------------------
c
c     Keep track of the number of iteration.
c
      iter=0
 1    iter=iter+1
c
c-----------------------------------------------------------------------
c
c     Set up initial relaxation factors.
c
      if (iter.ge.5) then
      beta=1.00000
      beta2=0.00000
      endif
c
c-----------------------------------------------------------------------
c
c     Find maximum density.
c
      n0m=0.
      do 2 i=1,imax
      do 2 j=1,jmax
 2    n0m=dmax1(n0m,dabs(n0(i,j)))
c
c-----------------------------------------------------------------------
c
c     Initialize band matrix.
c
      do 25 i=1,nmax
      diag(i)=1.
      rhs(i)=0.
      do 25 j=1,nb
      bandl(j,i)=0.
 25   bandr(j,i)=0.
c
c-----------------------------------------------------------------------
c
c     Set up the Jacobian matrix of first column of the two-dimensional
c     grid.
c
      do 11 i=1,imax
      ip1=i+1
      im1=i-1
c
c-----------------------------------------------------------------------
c
c     Compute derivatives in the x-direction.
c
      if (i.eq.1) then
      dvx0dx=vx0(2,1)/x(2)
      dvy0dx=vy0(2,1)/x(2)
      dvz0dx=0.
      dn0dx=0.
      dt0dx=0.
      d2vz0dx2=2.*dvdxsqr(1)*(vz0(2,1)-vz0(1,1))
      d2t0dx2=2.*dvdxsqr(1)*(t0(2,1)-t0(1,1))
      else if (i.eq.imax) then
      dvx0dx=-vx0(im1,1)/x(2)
      dvy0dx=-vy0(im1,1)/x(2)
      dvz0dx=0.
```

```
      dn0dx=0.
      dt0dx=0.
      d2vz0dx2=2.*dvdxsqr(i)*(vz0(im1,1)-vz0(i,1))
      d2t0dx2=2.*dvdxsqr(i)*(t0(im1,1)-t0(i,1))
      else
      dvx0dx=dvdx(i)*(vx0(ip1,1)-vx0(im1,1))
      dvy0dx=dvdx(i)*(vy0(ip1,1)-vy0(im1,1))
      dvz0dx=dvdx(i)*(vz0(ip1,1)-vz0(im1,1))
      dn0dx=dvdx(i)*(n0(ip1,1)-n0(im1,1))
      dt0dx=dvdx(i)*(t0(ip1,1)-t0(im1,1))
      d2vy0dx2=dvdxsqr(i)*(vy0(ip1,1)-2.*vy0(i,1)+vy0(im1,1))
     &+ddvdxdv(i)*dvy0dx
      d2vz0dx2=dvdxsqr(i)*(vz0(ip1,1)-2.*vz0(i,1)+vz0(im1,1))
     &+ddvdxdv(i)*dvz0dx
      d2t0dx2=dvdxsqr(i)*(t0(ip1,1)-2.*t0(i,1)+t0(im1,1))
     &+ddvdxdv(i)*dt0dx
      endif
c
c----------------------------------------------------------------------
c
c     Compute derivatives in the z-direction.
c
      dvz0dz=vz0(i,2)/z(2)
      d2t0dz2=2.*dudzsqr(1)*(t0(i,2)-t0(i,1))
c
c----------------------------------------------------------------------
c
      divv0=dvx0dx+dvz0dz
      vdgvx0=vx0(i,1)*dvx0dx
      vdgvy0=vx0(i,1)*dvy0dx
      vdgvz0=vx0(i,1)*dvz0dx
      vdgn0=vx0(i,1)*dn0dx
      vdgt0=vx0(i,1)*dt0dx
      k=5*(i-1)+1
      kp1=k+1
      kp2=k+2
      kp3=k+3
      kp4=k+4
c
c----------------------------------------------------------------------
c
c     Equation for vz1(i,j) has been taken care of since vz(x,z) is
c     equal to zero on this boundary.
c
c----------------------------------------------------------------------
c
      if (i.eq.1) then
c
c----------------------------------------------------------------------
c
c     Equation for vx1(i,j) has been taken care of since vx(x,z) is
c     equal to 0 when x=0.
c
c----------------------------------------------------------------------
c
c     Equation for vy1(i,j) has been taken care of since vy(x,z) is
c     equal to 0 when x=0.
c
c----------------------------------------------------------------------
c
c     Equation for n1(i,j).
c
      diag(kp3)=beta2+beta*divv0
      bandr(2,kp3)=n0(1,1)/x(2)
```

```
      rhs(kp3)=s-n0(1,1)*divv0
c
c-----------------------------------------------------------------------
c
c     Equation for t1(i,j).
c
      bandr(1,kp4)=t0(1,1)/x(2)
      bandr(2,kp4)=-2.*optau0*eta*dvy0dx/(x(2)*dsqrt(t0(1,1)))
      bandl(1,kp4)=s/n0(1,1)**2
      bandr(5,kp4)=-2.*kperp*dvdxsqr(1)/dsqrt(t0(1,1))
      diag(kp4)=beta2+beta*(divv0+2.*(kperp*dvdxsqr(1)/dsqrt(t0(1,1))
     &+kpar*dsqrt(t0(i,1))**5*dudzsqr(1))
     &+0.5*optau0*eta*dvy0dx**2/dsqrt(t0(1,1))**3
     &-2.5*optau0*etapar*dsqrt(t0(1,1))**3*dvz0dz**2
     &+0.5*kperp*d2t0dx2/dsqrt(t0(1,1))**3
     &-2.5*kpar*dsqrt(t0(i,1))**3*d2t0dz2)
      rhs(kp4)=s/n0(1,1)-t0(1,1)*divv0
     &+kperp*d2t0dx2/dsqrt(t0(1,1))+kpar*dsqrt(t0(i,1))**5*d2t0dz2
     &+optau0*(eta*dvy0dx**2/dsqrt(t0(1,1))
     &+etapar*dsqrt(t0(1,1))**5*dvz0dz**2)
c
c-----------------------------------------------------------------------
c
      else if (i.eq.imax) then
c
c-----------------------------------------------------------------------
c
c     Equation for vx1(i,j) has been taken care of since vx(x,z) is
c     equal to 0 when x=0.
c
c-----------------------------------------------------------------------
c
c     Equation for vy1(i,j) has been taken care of since vy(x,z) is
c     equal to 0 when x=0.
c
c-----------------------------------------------------------------------
c
c     Equation for n1(i,j).
c
      diag(kp3)=beta2+beta*divv0
      bandl(8,kp3)=-n0(i,1)/x(2)
      rhs(kp3)=s-n0(i,1)*divv0
c
c-----------------------------------------------------------------------
c
c     Equation for t1(i,j).
c
      bandl(9,kp4)=-t0(i,1)/x(2)
      bandl(8,kp4)=2.*optau0*eta*dvy0dx/(x(2)*dsqrt(t0(i,1)))
      bandl(1,kp4)=s/n0(i,1)**2
      bandl(5,kp4)=-2.*kperp*dvdxsqr(i)/dsqrt(t0(i,1))
      diag(kp4)=beta2+beta*(divv0+2.*(kperp*dvdxsqr(i)/dsqrt(t0(i,1))
     &+kpar*dsqrt(t0(i,1))**5*dudzsqr(1))
     &+0.5*optau0*eta*dvy0dx**2/dsqrt(t0(i,1))**3
     &-2.5*optau0*etapar*dsqrt(t0(i,1))**3*dvz0dz**2
     &+0.5*kperp*d2t0dx2/dsqrt(t0(i,1))**3
     &-2.5*kpar*dsqrt(t0(i,1))**3*d2t0dz2)
      rhs(kp4)=s/n0(i,1)-t0(i,1)*divv0
     &+kperp*d2t0dx2/dsqrt(t0(i,1))+kpar*dsqrt(t0(i,1))**5*d2t0dz2
     &+optau0*(eta*dvy0dx**2/dsqrt(t0(i,1))
     &+etapar*dsqrt(t0(i,1))**5*dvz0dz**2)
c
c-----------------------------------------------------------------------
c
```

```
      else
c
c-----------------------------------------------------------------------
c
c     Equation for vx1(i,j).
c
      bandl(5,k)=-dperp*vx0(i,1)*dvdx(i)
      bandr(5,k)=-bandl(5,k)
      diag(k)=beta2+beta*(1.+dperp*dvx0dx+rhoi*dvy0dx)
      bandl(4,k)=-rhoi*(eta*dvdxsqr(i)/dsqrt(t0(i,1))
     &+(vx0(i,1)-
     &eta*(ddvdxdv(i)+dn0dx/n0(i,1)-0.5*dt0dx/t0(i,1))/dsqrt(t0(i,1)))*
     &dvdx(i))
      bandr(6,k)=-rhoi*(eta*dvdxsqr(i)/dsqrt(t0(i,1))
     &-(vx0(i,1)-
     &eta*(ddvdxdv(i)+dn0dx/n0(i,1)-0.5*dt0dx/t0(i,1))/dsqrt(t0(i,1)))*
     &dvdx(i))
      bandr(1,k)=2.*rhoi*eta*dvdxsqr(i)/dsqrt(t0(i,1))
      bandl(2,k)=(rhoi*eta*dvy0dx/dsqrt(t0(i,1))
     &-dperp*(del1+del2*t0(i,1)))*dvdx(i)/n0(i,1)
      bandr(8,k)=-bandl(2,k)
      bandr(3,k)=(rhoi*eta*dvy0dx/dsqrt(t0(i,1))
     &-dperp*(del1+del2*t0(i,1)))*dn0dx/n0(i,1)**2
      bandl(1,k)=-dperp*del2*dvdx(i)
     &-0.5*rhoi*eta*dvy0dx*dvdx(i)/dsqrt(t0(i,1))**3
      bandr(9,k)=-bandl(1,k)
      bandr(4,k)=dperp*del2*dn0dx/n0(i,1)
     &+0.5*rhoi*(eta/dsqrt(t0(i,1))**3)*
     &(d2vy0dx2+(dn0dx/n0(i,1)-1.5*dt0dx/t0(i,1))*dvy0dx)
      rhs(k)=-vx0(i,1)
     &+rhoi*(eta*(d2vy0dx2+dvy0dx*(dn0dx/n0(i,1)-0.5*dt0dx/t0(i,1)))/
     &dsqrt(t0(i,1))-vdgvy0)
     &-dperp*(del2*dt0dx+(del1+del2*t0(i,1))*dn0dx/n0(i,1)+vdgvx0)
c
c-----------------------------------------------------------------------
c
c     Equation for vy1(i,j).
c
      bandl(6,kp1)=rhoi*vx0(i,1)*dvdx(i)
      bandr(4,kp1)=-bandl(6,k)
      bandl(1,kp1)=-rhoi*dvx0dx+dperp*dvy0dx
      bandl(5,kp1)=-dperp*(eta*dvdxsqr(i)/dsqrt(t0(i,1))
     &+(vx0(i,1)
     &-eta*(ddvdxdv(i)+dn0dx/n0(i,1)-0.5*dt0dx/t0(i,1))/dsqrt(t0(i,1)))*
     &dvdx(i))
      bandr(5,kp1)=-dperp*(eta*dvdxsqr(i)/dsqrt(t0(i,1))
     &-(vx0(i,1)
     &-eta*(ddvdxdv(i)+dn0dx/n0(i,1)-0.5*dt0dx/t0(i,1))/dsqrt(t0(i,1)))*
     &dvdx(i))
      diag(kp1)=beta2+beta*(1.+2.*dperp*eta*dvdxsqr(i)/dsqrt(t0(i,1)))
      bandl(3,kp1)=(rhoi*(del1+del2*t0(i,1))
     &+dperp*eta*dvy0dx/dsqrt(t0(i,1)))*dvdx(i)/n0(i,1)
      bandr(7,kp1)=-bandl(3,kp1)
      bandr(2,kp1)=(rhoi*(del1+del2*t0(i,1))+dperp*eta*dvy0dx/
     &dsqrt(t0(i,1)))*dn0dx/n0(i,1)**2
      bandl(2,kp1)=rhoi*del2*dvdx(i)
     &-0.5*dperp*eta*dvy0dx*dvdx(i)/dsqrt(t0(i,1))**3
      bandr(8,kp1)=-bandl(2,kp1)
      bandr(3,kp1)=-rhoi*del2*dn0dx/n0(i,1)
     &+0.5*dperp*eta*(d2vy0dx2+(dn0dx/n0(i,1)-1.5*dt0dx/t0(i,1))*dvy0dx)
     &/dsqrt(t0(i,1))**3
      rhs(kp1)=-vy0(i,1)
     &+dperp*(eta*(d2vy0dx2+dvy0dx*(dn0dx/n0(i,1)-0.5*dt0dx/t0(i,1)))/
     &dsqrt(t0(i,1))-vdgvy0)
```

```
     &+rhoi*(del2*dt0dx+(del1+del2*t0(i,1))*dn0dx/n0(i,1)+vdgvx0)
c
c-----------------------------------------------------------------------
c
c     Equation for n1(i,j).
c
      bandl(8,kp3)=-n0(i,1)*dvdx(i)
      bandr(2,kp3)=-bandl(8,kp3)
      bandl(3,kp3)=dn0dx
      bandl(5,kp3)=-vx0(i,1)*dvdx(i)
      bandr(5,kp3)=-bandl(5,kp3)
      diag(kp3)=beta2+beta*divv0
      rhs(kp3)=s-n0(i,1)*divv0-vdgn0
c
c-----------------------------------------------------------------------
c
c     Equation for t1(i,j).
c
      bandl(9,kp4)=-t0(i,1)*dvdx(i)
      bandr(1,kp4)=-bandl(9,kp4)
      bandl(4,kp4)=1.5*dt0dx
      bandl(8,kp4)=2.*optau0*eta*dvy0dx*dvdx(i)/dsqrt(t0(i,1))
      bandr(2,kp4)=-bandl(8,kp4)
      bandl(6,kp4)=kperp*dt0dx*dvdx(i)/(n0(i,1)*dsqrt(t0(i,1)))
      bandr(4,kp4)=-bandl(6,kp4)
      bandl(1,kp4)=(s+kperp*dn0dx*dt0dx/dsqrt(t0(i,1)))/n0(i,1)**2
      bandl(5,kp4)=-kperp*dvdxsqr(i)/dsqrt(t0(i,1))
     &+(kperp*(ddvdxdv(i)+dn0dx/n0(i,1)-dt0dx/t0(i,1))/dsqrt(t0(i,1))
     &-1.5*vx0(i,1))*dvdx(i)
      bandr(5,kp4)=-kperp*dvdxsqr(i)/dsqrt(t0(i,1))
     &-(kperp*(ddvdxdv(i)+dn0dx/n0(i,1)-dt0dx/t0(i,1))/dsqrt(t0(i,1))
     &-1.5*vx0(i,1))*dvdx(i)
      diag(kp4)=beta2+beta*(divv0
     &+2.*(kperp*dvdxsqr(i)/dsqrt(t0(i,1))
     &+kpar*dsqrt(t0(i,1))**5*dudzsqr(1))
     &+0.5*optau0*eta*dvy0dx**2/dsqrt(t0(i,1))**3
     &-2.5*optau0*etapar*dsqrt(t0(i,1))**3*dvz0dz**2
     &-0.5*kperp*dt0dx**2/(dsqrt(t0(i,1))*t0(i,1)**2)
     &+0.5*(kperp/dsqrt(t0(i,1))**3)*(d2t0dx2-0.5*dt0dx**2/t0(i,1)
     &+dt0dx*dn0dx/n0(i,1))
     &-2.5*kpar*dsqrt(t0(i,1))**3*d2t0dz2)
      rhs(kp4)=s/n0(i,1)-t0(i,1)*divv0-1.5*vdgt0
     &+optau0*(eta*dvy0dx**2/dsqrt(t0(i,1))
     &+etapar*dsqrt(t0(i,1))**5*dvz0dz**2)
     &+kperp*(d2t0dx2-0.5*dt0dx**2/t0(i,1)+dt0dx*dn0dx/n0(i,1))/
     &dsqrt(t0(i,1))+kpar*dsqrt(t0(i,1))**5*d2t0dz2
c
c-----------------------------------------------------------------------
c
      endif
c
c-----------------------------------------------------------------------
c
      bandr(ndis-1,kp3)=n0(i,1)/z(2)
      bandr(ndis-2,kp4)=(t0(i,1)
     &-2.*optau0*etapar*dsqrt(t0(i,1))**5*dvz0dz)/z(2)
      bandr(ndis,kp4)=-2.*kpar*dsqrt(t0(i,1))**5*dudzsqr(1)
c
c-----------------------------------------------------------------------
c
 11   continue
c
c-----------------------------------------------------------------------
c
```

```
c     Find maximum residue of the first row.
c
      resmax=0.
      do 12 i=1,ndis
 12   resmax=dmax1(resmax,dabs(rhs(i)))
c
c----------------------------------------------------------------------
c
c     Set up the Jacobian matrix for all other columns of the
c     two-dimensional grid except for the last column.
c
      do 30 j=2,jmax-1
      jm1=j-1
      jp1=j+1
      do 35 i=1,imax
      ip1=i+1
      im1=i-1
c
c----------------------------------------------------------------------
c
c     Compute derivatives in the x-direction.
c
      if (i.eq.1) then
      dvx0dx=vx0(2,j)/x(2)
      dvy0dx=vy0(2,j)/x(2)
      dvz0dx=0.
      dn0dx=0.
      dt0dx=0.
      d2vz0dx2=2.*dvdxsqr(1)*(vz0(2,j)-vz0(1,j))
      d2t0dx2=2.*dvdxsqr(1)*(t0(2,j)-t0(1,j))
      else if (i.eq.imax) then
      dvx0dx=-vx0(im1,j)/x(2)
      dvy0dx=-vy0(im1,j)/x(2)
      dvz0dx=0.
      dn0dx=0.
      dt0dx=0.
      d2vz0dx2=2.*dvdxsqr(i)*(vz0(im1,j)-vz0(i,j))
      d2t0dx2=2.*dvdxsqr(i)*(t0(im1,j)-t0(i,j))
      else
      dvx0dx=dvdx(i)*(vx0(ip1,j)-vx0(im1,j))
      dvy0dx=dvdx(i)*(vy0(ip1,j)-vy0(im1,j))
      dvz0dx=dvdx(i)*(vz0(ip1,j)-vz0(im1,j))
      dn0dx=dvdx(i)*(n0(ip1,j)-n0(im1,j))
      dt0dx=dvdx(i)*(t0(ip1,j)-t0(im1,j))
      d2vy0dx2=dvdxsqr(i)*(vy0(ip1,j)-2.*vy0(i,j)+vy0(im1,j))
     &+ddvdxdv(i)*dvy0dx
      d2vz0dx2=dvdxsqr(i)*(vz0(ip1,j)-2.*vz0(i,j)+vz0(im1,j))
     &+ddvdxdv(i)*dvz0dx
      d2t0dx2=dvdxsqr(i)*(t0(ip1,j)-2.*t0(i,j)+t0(im1,j))
     &+ddvdxdv(i)*dt0dx
      endif
c
c----------------------------------------------------------------------
c
c     Compute derivatives in the z-direction.
c
      dvx0dz=dudz(j)*(vx0(i,jp1)-vx0(i,jm1))
      dvy0dz=dudz(j)*(vy0(i,jp1)-vy0(i,jm1))
      dvz0dz=dudz(j)*(vz0(i,jp1)-vz0(i,jm1))
      dn0dz=dudz(j)*(n0(i,jp1)-n0(i,jm1))
      dt0dz=dudz(j)*(t0(i,jp1)-t0(i,jm1))
      d2vz0dz2=dudzsqr(j)*(vz0(i,jp1)-2.*vz0(i,j)+vz0(i,jm1))
     &+ddudzdu(j)*dvz0dz
      d2t0dz2=dudzsqr(j)*(t0(i,jp1)-2.*t0(i,j)+t0(i,jm1))
```

```
     &+ddudzdu(j)*dt0dz
c
c-----------------------------------------------------------------------
c
      vdgvx0=vx0(i,j)*dvx0dx+vz0(i,j)*dvx0dz
      vdgvy0=vx0(i,j)*dvy0dx+vz0(i,j)*dvy0dz
      vdgvz0=vx0(i,j)*dvz0dx+vz0(i,j)*dvz0dz
      divv0=dvx0dx+dvz0dz
      vdgn0=vx0(i,j)*dn0dx+vz0(i,j)*dn0dz
      vdgt0=vx0(i,j)*dt0dx+vz0(i,j)*dt0dz
      k=ndis+5*(i-1)+1
      kp1=k+1
      kp2=k+2
      kp3=k+3
      kp4=k+4
      if (i.eq.1) then
c
c-----------------------------------------------------------------------
c
c     Equation for vx1(i,j) has been taken care of since vx(x,z) is
c     equal to 0 when x=x0.
c
c-----------------------------------------------------------------------
c
c     Equation for vy1(i,j) has been taken care of since vy(x,z) is
c     equal to 0 when x=x0.
c
c-----------------------------------------------------------------------
c
c     Equation for vz1(i,j).
c
      bandr(5,kp2)=-2.*eta*dvdxsqr(1)/dsqrt(t0(1,j))
      diag(kp2)=beta2
     &+beta*(dvz0dz+2.*(eta*dvdxsqr(1)/dsqrt(t0(1,j))
     &+etapar*dudzsqr(j)*dsqrt(t0(1,j))**5))
      bandr(1,kp2)=(etapar*dvz0dz*dsqrt(t0(1,j))**5
     &-del1-del2*t0(1,j))*dn0dz/n0(1,j)**2
      bandr(2,kp2)=del2*dn0dz/n0(1,j)
     &+0.5*eta*d2vz0dx2/dsqrt(t0(1,j))**3
     &-2.5*etapar*dsqrt(t0(1,j))**3*(d2vz0dz2+(dn0dz/n0(1,j)
     &+1.5*dt0dz/t0(1,j))*dvz0dz)
      rhs(kp2)=-(del1+del2*t0(1,j))*dn0dz/n0(1,j)-del2*dt0dz-vdgvz0
     &+eta*d2vz0dx2/dsqrt(t0(1,j))
     &+etapar*dsqrt(t0(1,j))**5*(d2vz0dz2
     &+(dn0dz/n0(1,j)+2.5*dt0dz/t0(1,j))*dvz0dz)
c
c-----------------------------------------------------------------------
c
c     Equation for n1(i,j).
c
      bandr(2,kp3)=n0(1,j)/x(2)
      bandl(1,kp3)=dn0dz
      diag(kp3)=beta2+beta*divv0
      rhs(kp3)=s-n0(1,j)*divv0-vdgn0
c
c-----------------------------------------------------------------------
c
c     Equation for t1(i,j).
c
      bandr(1,kp4)=t0(1,j)/x(2)
      bandr(2,kp4)=-2.*optau0*eta*dvy0dx/(x(2)*dsqrt(t0(1,j)))
      bandl(2,kp4)=1.5*dt0dz
      bandl(1,kp4)=(s+kpar*dsqrt(t0(1,j))**5*dt0dz*dn0dz)/n0(1,j)**2
      bandr(5,kp4)=-2.*kperp*dvdxsqr(1)/dsqrt(t0(1,j))
```

```
       diag(kp4)=beta2+beta*(divv0
     &+2.*(kperp*dvdxsqr(1)/dsqrt(t0(1,j))
     &+kpar*dsqrt(t0(1,j))**5*dudzsqr(j))
     &+0.5*optau0*eta*dvy0dx**2/dsqrt(t0(1,j))**3
     &-2.5*optau0*etapar*dsqrt(t0(1,j))**3*dvz0dz**2
     &+2.5*kpar*dsqrt(t0(1,j))*dt0dz**2
     &+0.5*kperp*d2t0dx2/dsqrt(t0(1,j))**3
     &-2.5*kpar*dsqrt(t0(1,j))**3*(d2t0dz2+2.5*dt0dz**2/t0(1,j)
     &+dt0dz*dn0dz*n0(1,j)))
       rhs(kp4)=s/n0(1,j)-t0(1,j)*divv0-1.5*vdgt0
     &+optau0*(eta*dvy0dx**2/dsqrt(t0(1,j))
     &+etapar*dsqrt(t0(1,j))**5*dvz0dz**2)
     &+kperp*d2t0dx2/dsqrt(t0(1,j))
     &+kpar*dsqrt(t0(1,j))**5*(d2t0dz2+2.5*dt0dz**2/t0(1,j)
     &+dt0dz*dn0dz/n0(1,j))
c
c-----------------------------------------------------------------------
c
      else if (i.eq.imax) then
c
c-----------------------------------------------------------------------
c
c     Equation for vx1(i,j) has been taken care of since vx(x,z) is
c     equal to 0 when x=x0.
c
c-----------------------------------------------------------------------
c
c     Equation for vy1(i,j) has been taken care of since vy(x,z) is
c     equal to 0 when x=x0.
c
c-----------------------------------------------------------------------
c
c     Equation for vz1(i,j).
c
       bandl(5,kp2)=-2.*eta*dvdxsqr(i)/dsqrt(t0(i,j))
       diag(kp2)=beta2
     &+beta*(dvz0dz+2.*(eta*dvdxsqr(i)/dsqrt(t0(i,j))
     &+etapar*dudzsqr(j)*dsqrt(t0(i,j))**5))
       bandr(1,kp2)=(etapar*dvz0dz*dsqrt(t0(i,j))**5
     &-(del1+del2*t0(i,j)))*dn0dz/n0(i,j)**2
       bandr(2,kp2)=del2*dn0dz/n0(i,j)
     &+0.5*eta*d2vz0dx2/dsqrt(t0(i,j))**3
     &-2.5*etapar*dsqrt(t0(i,j))**3*(d2vz0dz2+(dn0dz/n0(i,j)
     &+1.5*dt0dz/t0(i,j))*dvz0dz)
       rhs(kp2)=-(del1+del2*t0(i,j))*dn0dz/n0(i,j)-del2*dt0dz-vdgvz0
     &+eta*d2vz0dx2/dsqrt(t0(i,j))
     &+etapar*dsqrt(t0(i,j))**5*(d2vz0dz2
     &+(dn0dz/n0(i,j)+2.5*dt0dz/t0(i,j))*dvz0dz)
c
c-----------------------------------------------------------------------
c
c     Equation for n1(i,j).
c
      bandl(8,kp3)=-n0(i,j)/x(2)
      bandl(1,kp3)=dn0dz
      diag(kp3)=beta2+beta*divv0
      rhs(kp3)=s-n0(i,j)*divv0-vdgn0
c
c-----------------------------------------------------------------------
c
c     Equation for t1(i,j).
c
      bandl(9,kp4)=-t0(i,j)/x(2)
      bandl(8,kp4)=2.*optau0*eta*dvy0dx/(x(2)*dsqrt(t0(i,j)))
```

```
      bandl(2,kp4)=1.5*dt0dz
      bandl(1,kp4)=(s+kpar*dsqrt(t0(i,j))**5*dt0dz*dn0dz)/n0(i,j)**2
      bandl(5,kp4)=-2.*kperp*dvdxsqr(i)/dsqrt(t0(i,j))
      diag(kp4)=beta2+beta*(divv0
     &+2.*(kperp*dvdxsqr(i)/dsqrt(t0(i,j))
     &+kpar*dsqrt(t0(i,j))**5*dudzsqr(j))
     &+0.5*optau0*eta*dvy0dx**2/dsqrt(t0(i,j))**3
     &-2.5*optau0*etapar*dsqrt(t0(i,j))**3*dvz0dz**2
     &+2.5*kpar*dsqrt(t0(i,j))*dt0dz**2
     &+0.5*kperp*d2t0dx2/dsqrt(t0(i,j))**3
     &-2.5*kpar*dsqrt(t0(i,j))**3*(d2t0dz2+2.5*dt0dz**2/t0(i,j)
     &+dt0dz*dn0dz/n0(i,j)))
      rhs(kp4)=s/n0(i,j)-t0(i,j)*divv0-1.5*vdgt0
     &+optau0*(eta*dvy0dx**2/dsqrt(t0(i,j))
     &+etapar*dsqrt(t0(i,j))**5*dvz0dz**2)
     &+kperp*d2t0dx2/dsqrt(t0(i,j))
     &+kpar*dsqrt(t0(i,j))**5*(d2t0dz2+2.5*dt0dz**2/t0(i,j)
     &+dt0dz*dn0dz/n0(i,j))
c
c-----------------------------------------------------------------------
c
      else
c
c-----------------------------------------------------------------------
c
c     Equation for vx1(i,j).
c
      bandl(5,k)=-dperp*vx0(i,j)*dvdx(i)
      bandr(5,k)=-bandl(5,k)
      diag(k)=beta2+beta*(1.+dperp*dvx0dx+rhoi*dvy0dx)
      bandl(4,k)=-rhoi*(eta*dvdxsqr(i)/dsqrt(t0(i,j))
     &+(vx0(i,j)-
     &eta*(ddvdxdv(i)+dn0dx/n0(i,j)-0.5*dt0dx/t0(i,j))/dsqrt(t0(i,j)))*
     &dvdx(i))
      bandr(6,k)=-rhoi*(eta*dvdxsqr(i)/dsqrt(t0(i,j))
     &-(vx0(i,j)-
     &eta*(ddvdxdv(i)+dn0dx/n0(i,j)-0.5*dt0dx/t0(i,j))/dsqrt(t0(i,j)))*
     &dvdx(i))
      bandr(1,k)=2.*rhoi*eta*dvdxsqr(i)/dsqrt(t0(i,j))
      bandr(2,k)=dperp*dvx0dz+rhoi*dvy0dz
      bandl(2,k)=(rhoi*eta*dvy0dx/dsqrt(t0(i,j))
     &-dperp*(del1+del2*t0(i,j)))*dvdx(i)/n0(i,j)
      bandr(8,k)=-bandl(2,k)
      bandr(3,k)=(rhoi*eta*dvy0dx/dsqrt(t0(i,j))
     &-dperp*(del1+del2*t0(i,j)))*dn0dx/n0(i,j)**2
      bandl(1,k)=-dperp*del2*dvdx(i)
     &-0.5*rhoi*eta*dvy0dx*dvdx(i)/dsqrt(t0(i,j))**3
      bandr(9,k)=-bandl(1,k)
      bandr(4,k)=dperp*del2*dn0dx/n0(i,j)
     &+0.5*rhoi*(eta/dsqrt(t0(i,j))**3)*
     &(d2vy0dx2+(dn0dx/n0(i,j)-1.5*dt0dx/t0(i,j))*dvy0dx)
      rhs(k)=-vx0(i,j)
     &+rhoi*(eta*(d2vy0dx2+dvy0dx*(dn0dx/n0(i,j)-0.5*dt0dx/t0(i,j)))/
     &dsqrt(t0(i,j))-vdgvy0)
     &-dperp*(del2*dt0dx+(del1+del2*t0(i,j))*dn0dx/n0(i,j)+vdgvx0)
      bandl(ndis,k)=-dperp*vz0(i,j)*dudz(j)
      bandr(ndis,k)=-bandl(ndis,k)
      bandl(ndis-1,k)=-rhoi*vz0(i,j)*dudz(j)
      bandr(ndis+1,k)=-bandl(ndis-1,k)
c
c-----------------------------------------------------------------------
c
c     Equation for vy1(i,j).
c
```

```
      bandl(6,kp1)=rhoi*vx0(i,j)*dvdx(i)
      bandr(4,kp1)=-bandl(6,kp1)
      bandl(1,kp1)=-rhoi*dvx0dx+dperp*dvy0dx
      bandl(5,kp1)=-dperp*(eta*dvdxsqr(i)/dsqrt(t0(i,j))
     &+(vx0(i,j)
     &-eta*(ddvdxdv(i)+dn0dx/n0(i,j)-0.5*dt0dx/t0(i,j))/dsqrt(t0(i,j)))*
     &dvdx(i))
      bandr(5,kp1)=-dperp*(eta*dvdxsqr(i)/dsqrt(t0(i,j))
     &-(vx0(i,j)
     &-eta*(ddvdxdv(i)+dn0dx/n0(i,j)-0.5*dt0dx/t0(i,j))/dsqrt(t0(i,j)))*
     &dvdx(i))
      diag(kp1)=beta2+beta*(1.+2.*dperp*eta*dvdxsqr(i)/dsqrt(t0(i,j)))
      bandr(1,kp1)=-rhoi*dvx0dz+dperp*dvy0dz
      bandl(3,kp1)=(rhoi*(del1+del2*t0(i,j))
     &+dperp*eta*dvy0dx/dsqrt(t0(i,j)))*dvdx(i)/n0(i,j)
      bandr(7,kp1)=-bandl(3,kp1)
      bandr(2,kp1)=(rhoi*(del1+del2*t0(i,j))+dperp*eta*dvy0dx/
     &dsqrt(t0(i,j)))*dn0dx/n0(i,j)**2
      bandl(2,kp1)=rhoi*del2*dvdx(i)
     &-0.5*dperp*eta*dvy0dx*dvdx(i)/dsqrt(t0(i,j))**3
      bandr(8,kp1)=-bandl(2,kp1)
      bandr(3,kp1)=-rhoi*del2*dn0dx/n0(i,j)
     &+0.5*dperp*eta*(d2vy0dx2+(dn0dx/n0(i,j)-1.5*dt0dx/t0(i,j))*dvy0dx)
     &/dsqrt(t0(i,j))**3
      rhs(kp1)=-vy0(i,j)
     &+dperp*(eta*(d2vy0dx2+dvy0dx*(dn0dx/n0(i,j)-0.5*dt0dx/t0(i,j)))/
     &dsqrt(t0(i,j))-vdgvy0)
     &+rhoi*(del2*dt0dx+(del1+del2*t0(i,j))*dn0dx/n0(i,j)+vdgvx0)
      bandl(ndis+1,kp1)=rhoi*vz0(i,j)*dudz(j)
      bandr(ndis-1,kp1)=-bandl(ndis+1,kp1)
      bandl(ndis,kp1)=-dperp*vz0(i,j)*dudz(j)
      bandr(ndis,kp1)=-bandl(ndis,kp1)
c
c-----------------------------------------------------------------------
c
c     Equation for vz1(i,j).
c
      bandl(2,kp2)=dvz0dx
      bandl(5,kp2)=-eta*dvdxsqr(i)/dsqrt(t0(i,j))
     &-(vx0(i,j)-eta*(ddvdxdv(i)+dn0dx/n0(i,j)-0.5*dt0dx/t0(i,j))/
     &dsqrt(t0(i,j)))*dvdx(i)
      bandr(5,kp2)=-eta*dvdxsqr(i)/dsqrt(t0(i,j))
     &+(vx0(i,j)-eta*(ddvdxdv(i)+dn0dx/n0(i,j)-0.5*dt0dx/t0(i,j))/
     &dsqrt(t0(i,j)))*dvdx(i)
      diag(kp2)=beta2
     &+beta*(dvz0dz+2.*(eta*dvdxsqr(i)/dsqrt(t0(i,j))
     &+etapar*dudzsqr(j)*dsqrt(t0(i,j))**5))
      bandl(4,kp2)=eta*dvz0dx*dvdx(i)/(n0(i,j)*dsqrt(t0(i,j)))
      bandr(6,kp2)=-bandl(4,kp2)
      bandr(1,kp2)=(eta*dvz0dx*dn0dx/dsqrt(t0(i,j))
     &+(etapar*dvz0dz*dsqrt(t0(i,j))**5
     &-del1-del2*t0(i,j))*dn0dz)/n0(i,j)**2
      bandl(3,kp2)=-0.5*eta*dvz0dx*dvdx(i)/dsqrt(t0(i,j))**3
      bandr(7,kp2)=-bandl(3,kp2)
      bandr(2,kp2)=del2*dn0dz/n0(i,j)
     &+0.5*(eta/dsqrt(t0(i,j))**3)*(d2vz0dx2+(dn0dx/n0(i,j)
     &-1.5*dt0dx/t0(i,j))*dvz0dx)
     &-2.5*etapar*dsqrt(t0(i,j))**3*(d2vz0dz2+(dn0dz/n0(i,j)
     &+1.5*dt0dz/t0(i,j))*dvz0dz)
      rhs(kp2)=-(del1+del2*t0(i,j))*dn0dz/n0(i,j)-del2*dt0dz-vdgvz0
     &+eta*(d2vz0dx2+dvz0dx*(dn0dx/n0(i,j)-0.5*dt0dx/t0(i,j)))/
     &dsqrt(t0(i,j))
     &+etapar*dsqrt(t0(i,j))**5*
     &(d2vz0dz2+dvz0dz*(dn0dz/n0(i,j)+2.5*dt0dz/t0(i,j)))
```

```
c
c-----------------------------------------------------------------------
c
c     Equation for n1(i,j).
c
      bandl(8,kp3)=-n0(i,j)*dvdx(i)
      bandr(2,kp3)=-bandl(8,kp3)
      bandl(3,kp3)=dn0dx
      bandl(1,kp3)=dn0dz
      bandl(5,kp3)=-vx0(i,j)*dvdx(i)
      bandr(5,kp3)=-bandl(5,kp3)
      diag(kp3)=beta2+beta*divv0
      rhs(kp3)=s-n0(i,j)*divv0-vdgn0
c
c-----------------------------------------------------------------------
c
c     Equation for t1(i,j).
c
      bandl(9,kp4)=-t0(i,j)*dvdx(i)
      bandr(1,kp4)=-bandl(9,kp4)
      bandl(4,kp4)=1.5*dt0dx
      bandl(8,kp4)=2.*optau0*eta*dvy0dx*dvdx(i)/dsqrt(t0(i,j))
      bandr(2,kp4)=-bandl(8,kp4)
      bandl(7,kp4)=2.*optau0*eta*dvz0dx*dvdx(i)/dsqrt(t0(i,j))
      bandr(3,kp4)=-bandl(7,kp4)
      bandl(2,kp4)=1.5*dt0dz
      bandl(6,kp4)=kperp*dt0dx*dvdx(i)/(n0(i,j)*dsqrt(t0(i,j)))
      bandr(4,kp4)=-bandl(6,kp4)
      bandl(1,kp4)=(s+kperp*dn0dx*dt0dx/dsqrt(t0(i,j))
     &+kpar*dsqrt(t0(i,j))**5*dn0dz*dt0dz)/n0(i,j)**2
      bandl(5,kp4)=-kperp*dvdxsqr(i)/dsqrt(t0(i,j))
     &+(kperp*(ddvdxdv(i)+dn0dx/n0(i,j)-dt0dx/t0(i,j))/dsqrt(t0(i,j))
     &-1.5*vx0(i,j))*dvdx(i)
      bandr(5,kp4)=-kperp*dvdxsqr(i)/dsqrt(t0(i,j))
     &-(kperp*(ddvdxdv(i)+dn0dx/n0(i,j)-dt0dx/t0(i,j))/dsqrt(t0(i,j))
     &-1.5*vx0(i,j))*dvdx(i)
      diag(kp4)=beta2+beta*(divv0
     &+2.*(kperp*dvdxsqr(i)/dsqrt(t0(i,j))
     &+kpar*dsqrt(t0(i,j))**5*dudzsqr(j))
     &+0.5*optau0*eta*(dvy0dx**2+dvz0dx**2)/dsqrt(t0(i,j))**3
     &-2.5*optau0*etapar*dsqrt(t0(i,j))**3*dvz0dz**2
     &-0.5*kperp*dt0dx**2/(dsqrt(t0(i,j))*t0(i,j)**2)
     &+2.5*kpar*dsqrt(t0(i,j))*dt0dz**2
     &+0.5*kperp*(d2t0dx2-0.5*dt0dx**2/t0(i,j)+dt0dx*dn0dx/n0(i,j))/
     &dsqrt(t0(i,j))**3
     &-2.5*kpar*dsqrt(t0(i,j))**3*(d2t0dz2+2.5*dt0dz**2/t0(i,j)
     &+dt0dz*dn0dz/n0(i,j)))
      rhs(kp4)=s/n0(i,j)-t0(i,j)*divv0-1.5*vdgt0
     &+optau0*(eta*(dvz0dx**2+dvy0dx**2)/dsqrt(t0(i,j))
     &+etapar*dsqrt(t0(i,j))**5*dvz0dz**2)
     &+kperp*(d2t0dx2-0.5*dt0dx**2/t0(i,j)+dt0dx*dn0dx/n0(i,j))/
     &dsqrt(t0(i,j))
     &+kpar*dsqrt(t0(i,j))**5*(d2t0dz2+2.5*dt0dz**2/t0(i,j)
     &+dt0dz*dn0dz/n0(i,j))
c
c-----------------------------------------------------------------------
c
      endif
c
c-----------------------------------------------------------------------
c
c
      bandl(ndis,kp2)=-etapar*dudzsqr(j)*t0(i,j)**2.5
     &-(vz0(i,j)-etapar*t0(i,j)**2.5*
```

```
     &(ddudzdu(j)+dn0dz/n0(i,j)+2.5*dt0dz/t0(i,j)))*dudz(j)
      bandr(ndis,kp2)=-etapar*dudzsqr(j)*t0(i,j)**2.5
     &+(vz0(i,j)-etapar*t0(i,j)**2.5*
     &(ddudzdu(j)+dn0dz/n0(i,j)+2.5*dt0dz/t0(i,j)))*dudz(j)
      bandl(ndis-1,kp2)=(etapar*dvz0dz*t0(i,j)**2.5
     &-del1-del2*t0(i,j))*dudz(j)/n0(i,j)
      bandr(ndis+1,kp2)=-bandl(ndis-1,kp2)
      bandl(ndis-2,kp2)=(2.5*etapar*t0(i,j)**1.5*dvz0dz-del2)*dudz(j)
      bandr(ndis+2,kp2)=-bandl(ndis-2,kp2)
      bandl(ndis+1,kp3)=-n0(i,j)*dudz(j)
      bandr(ndis-1,kp3)=-bandl(ndis+1,kp3)
      bandl(ndis,kp3)=-vz0(i,j)*dudz(j)
      bandr(ndis,kp3)=-bandl(ndis,kp3)
      bandl(ndis+2,kp4)=(2.*optau0*etapar*dsqrt(t0(i,j))**5*dvz0dz
     &-t0(i,j))*dudz(j)
      bandr(ndis-2,kp4)=-bandl(ndis+2,kp4)
      bandl(ndis+1,kp4)=kpar*dsqrt(t0(i,j))**5*dt0dz*dudz(j)/n0(i,j)
      bandr(ndis-1,kp4)=-bandl(ndis+1,kp4)
      bandl(ndis,kp4)=-kpar*dsqrt(t0(i,j))**5*dudzsqr(j)
     &+(kpar*dsqrt(t0(i,j))**5*(ddudzdu(j)
     &+dn0dz/n0(i,j)+5.*dt0dz/t0(i,j))
     &-1.5*vz0(i,j))*dudz(j)
      bandr(ndis,kp4)=-kpar*dsqrt(t0(i,j))**5*dudzsqr(j)
     &-(kpar*dsqrt(t0(i,j))**5*(ddudzdu(j)
     &+dn0dz/n0(i,j)+5.*dt0dz/t0(i,j))
     &-1.5*vz0(i,j))*dudz(j)
c
c-----------------------------------------------------------------------
c
 35   continue
c
c-----------------------------------------------------------------------
c
c     Find maximum residue.
c
      do 36 i=ndis+1,nmax
 36   resmax=dmax1(resmax,dabs(rhs(i)))
c
c-----------------------------------------------------------------------
c
c     Start Gaussian elimination.  Gaussian elimination is done one
c     row at a time.
c
      call gauss
c
c-----------------------------------------------------------------------
c
c     Move that part of the Jacobian matrix that has been eliminated
c     into the virtual storage device.
c
      if (j.le.jlim1) then
      do 40 i=1,ndis
      write(2,rec=(j-2)*ndis+i) crunchdiag(i),(crunchr(ki,i), ki=1,nb)
     &,crunchrhs(i)
 40   continue
      else if (j.le.jlim2) then
      do 45 i=1,ndis
      write(3,rec=(j-jlim1-1)*ndis+i) crunchdiag(i)
     &,(crunchr(ki,i), ki=1,nb),crunchrhs(i)
 45   continue
      else
      do 47 i=1,ndis
      write(4,rec=(j-jlim2-1)*ndis+i) crunchdiag(i)
     &,(crunchr(ki,i), ki=1,nb),crunchrhs(i)
```

```
 47   continue
      endif
c
c---------------------------------------------------------------------
c
c     Reinitialize band matrix.  This band matrix is just a buffer
c     device.
c
      do 50 i=ndis,1,-1
      ipndis=i+ndis
      diag(i)=diag(ipndis)
      diag(ipndis)=1.
      rhs(i)=rhs(ipndis)
      rhs(ipndis)=0.
      do 55 ki=1,i-1
 55   bandl(ki,i)=bandl(ki,ipndis)
      do 50 ki=nb,1,-1
      bandr(ki,i)=bandr(ki,ipndis)
      bandr(ki,ipndis)=0.
 50   bandl(ki,ipndis)=0.
 30   continue
c
c---------------------------------------------------------------------
c
c     Set up Jacobian matrix of the last column of the two-dimensional
c     grid.
c
      do 61 i=1,imax
      ip1=i+1
      im1=i-1
c
c---------------------------------------------------------------------
c
c     Compute derivatives in the z-direction.
c
      if (x(i).lt.1.) then
      dvx0dz=(vx0(i,jmax)-vx0(i,jmax-1))/dzm
      dvy0dz=(vy0(i,jmax)-vy0(i,jmax-1))/dzm
      dvz0dz=(vz0(i,jmax)-vz0(i,jmax-1))/dzm
      dn0dz=(n0(i,jmax)-n0(i,jmax-1))/dzm
      dt0dz=(t0(i,jmax)-t0(i,jmax-1))/dzm
      else
      dvx0dz=0.
      dvy0dz=0.
      dvz0dz=-vz0(i,jmax-1)/dzm
      dn0dz=0.
      dt0dz=0.
      d2t0dz2=2.*dudzsqr(jmax)*(t0(i,jmax-1)-t0(i,jmax))
      endif
c
c---------------------------------------------------------------------
c
c     Compute derivatives in the x-direction.
c
      if (i.eq.1) then
      dvx0dx=vx0(2,jmax)/x(2)
      dvy0dx=vy0(2,jmax)/x(2)
      dvz0dx=0.
      dn0dx=0.
      dt0dx=0.
      d2t0dx2=2.*dvdxsqr(1)*(t0(2,jmax)-t0(1,jmax))
      else if (i.eq.imax) then
      dvx0dx=-vx0(imax-1,jmax)/x(2)
      dvy0dx=-vy0(imax-1,jmax)/x(2)
```

```fortran
      dvz0dx=0.
      dn0dx=0.
      dt0dx=0.
      d2t0dx2=2.*dvdxsqr(imax)*(t0(imax-1,jmax)-t0(imax,jmax))
      else
      dvx0dx=dvdx(i)*(vx0(ip1,jmax)-vx0(im1,jmax))
      dvy0dx=dvdx(i)*(vy0(ip1,jmax)-vy0(im1,jmax))
      dn0dx=dvdx(i)*(n0(ip1,jmax)-n0(im1,jmax))
      dt0dx=dvdx(i)*(t0(ip1,jmax)-t0(im1,jmax))
      dvz0dx=0.5*del2*dt0dx/dsqrt(del1+del2*t0(i,jmax))
      d2vy0dx2=dvdxsqr(i)*(vy0(ip1,jmax)-2.*vy0(i,jmax)+vy0(im1,jmax))
     &+ddvdxdv(i)*dvy0dx
      d2t0dx2=dvdxsqr(i)*(t0(ip1,jmax)-2.*t0(i,jmax)+t0(im1,jmax))
     &+ddvdxdv(i)*dt0dx
      endif
c
c-----------------------------------------------------------------------
c
      divv0=dvx0dx+dvz0dz
      vdgvx0=vx0(i,jmax)*dvx0dx+vz0(i,jmax)*dvx0dz
      vdgvy0=vx0(i,jmax)*dvy0dx+vz0(i,jmax)*dvy0dz
      vdgn0=vx0(i,jmax)*dn0dx+vz0(i,jmax)*dn0dz
      vdgt0=vx0(i,jmax)*dt0dx+vz0(i,jmax)*dt0dz
      k=ndis+5*(i-1)+1
      kp1=k+1
      kp2=k+2
      kp3=k+3
      kp4=k+4
c
c-----------------------------------------------------------------------
c
      if (i.eq.1) then
c
c-----------------------------------------------------------------------
c
c     Equation for vx1(i,j) has been taken care of since vx(x,z) is
c     equal to 0 when x=0.
c
c-----------------------------------------------------------------------
c
c     Equation for vy1(i,j) has been taken care of since vz(x,z) is
c     equal to 0 when x=0.
c
c-----------------------------------------------------------------------
c
c     Equation for vz1(i,j).
c
      diag(kp2)=beta2+beta
      bandr(2,kp2)=-0.5*del2/dsqrt(del1+del2*t0(1,jmax))
      rhs(kp2)=-vz0(1,jmax)+dsqrt(del1+del2*t0(1,jmax))
c
c-----------------------------------------------------------------------
c
c     Equation for n1(i,j).
c
      bandr(2,kp3)=n0(1,jmax)/x(2)
      bandl(1,kp3)=n0(1,jmax)/dzm+dn0dz
      diag(kp3)=beta2+beta*(divv0+vz0(1,jmax)/dzm)
      rhs(kp3)=s-n0(1,jmax)*divv0-vdgn0
      bandl(ndis+1,kp3)=-n0(1,jmax)/dzm
      bandl(ndis,kp3)=-vz0(1,jmax)/dzm
c
c-----------------------------------------------------------------------
c
```

```
c     Equation for t1(i,j).
c
      bandr(1,kp4)=t0(1,jmax)/x(2)
      bandr(2,kp4)=-2.*optau0*eta*dvy0dx/(x(2)*dsqrt(t0(1,jmax)))
      bandl(2,kp4)=(t0(1,jmax)
     &-2.*optau0*etapar*dsqrt(t0(1,jmax))**5*dvz0dz)/dzm+1.5*dt0dz
      bandl(1,kp4)=(s+kperp*dt0dx*dn0dx/dsqrt(t0(1,jmax)))/n0(1,jmax)**2
     &-kpar*dsqrt(t0(1,jmax))**5*(1./dzm-dn0dz/n0(1,jmax))
     &*dt0dz/n0(1,jmax)
      bandr(5,kp4)=-2.*kperp*dvdxsqr(1)/dsqrt(t0(1,jmax))
      diag(kp4)=beta2
     &+beta*(divv0+1.5*vz0(1,jmax)/dzm
     &+2.*kperp*dvdxsqr(1)/dsqrt(t0(1,jmax))
     &-kpar*dsqrt(t0(1,jmax))**5*(dn0dz/n0(1,jmax)+5.*dt0dz/t0(1,jmax))
     &/dzm
     &+0.5*optau0*eta*dvy0dx**2/dsqrt(t0(1,jmax))**3
     &-2.5*optau0*etapar*dsqrt(t0(1,jmax))**3*dvz0dz**2
     &+2.5*kpar*dsqrt(t0(1,jmax))*dt0dz**2
     &+0.5*kperp*d2t0dx2/dsqrt(t0(1,jmax))**3
     &-2.5*kpar*dsqrt(t0(1,jmax))**3*(2.5*dt0dz**2/t0(1,jmax)
     &+dt0dz*dn0dz/n0(1,jmax)))
      rhs(kp4)=s/n0(1,jmax)-t0(1,jmax)*divv0-1.5*vdgt0
     &+kperp*d2t0dx2/dsqrt(t0(1,jmax))
     &+kpar*dsqrt(t0(1,jmax))**5*(2.5*dt0dz**2/t0(1,jmax)
     &+dt0dz*dn0dz/n0(1,jmax))
     &+optau0*(eta*dvy0dx**2/dsqrt(t0(1,jmax))
     &+etapar*dsqrt(t0(1,jmax))**5*dvz0dz**2)
      bandl(ndis+2,kp4)=(2.*optau0*etapar*dsqrt(t0(1,jmax))**5*dvz0dz
     &-t0(1,jmax))/dzm
      bandl(ndis+1,kp4)=kpar*dsqrt(t0(1,jmax))**5*dt0dz/(n0(1,jmax)*dzm)
      bandl(ndis,kp4)=(kpar*(dn0dz/n0(1,jmax)+5.*dt0dz/t0(1,jmax))
     &*dsqrt(t0(1,jmax))**5-1.5*vz0(1,jmax))/dzm
c
c-----------------------------------------------------------------------
c
      else if (i.eq.imax) then
c
c-----------------------------------------------------------------------
c
c     Equation for vx1(i,j) has been taken care of since vx(x,z) is
c     equal to 0 when x=x0.
c
c-----------------------------------------------------------------------
c
c     Equation for vy1(i,j) has been taken care of since vy(x,z) is
c     equal to 0 when x=x0.
c
c-----------------------------------------------------------------------
c
c     Equation for vz1(i,j) has been taken care of since vz(x,z) is
c     equal to 0 when x/d > 1.
c
c-----------------------------------------------------------------------
c
c     Equation for n1(i,j).
c
      bandl(8,kp3)=-n0(i,jmax)/x(2)
      diag(kp3)=beta2+beta*divv0
      rhs(kp3)=s-n0(i,jmax)*divv0
      bandl(ndis+1,kp3)=-n0(i,jmax)/dzm
c
c-----------------------------------------------------------------------
c
c     Equation for t1(i,j).
```

```
c
      bandl(9,kp4)=-t0(i,jmax)/x(2)
      bandl(8,kp4)=2.*optau0*eta*dvy0dx/(x(2)*dsqrt(t0(i,jmax)))
      bandl(1,kp4)=(s+kperp*dt0dx*dn0dx/dsqrt(t0(i,jmax)))/n0(i,jmax)**2
      bandl(5,kp4)=-2.*kperp*dvdxsqr(i)/dsqrt(t0(i,jmax))
      diag(kp4)=beta2
     &+beta*(divv0
     &+2.*(kperp*dvdxsqr(i)/dsqrt(t0(i,jmax))
     &+kpar*dsqrt(t0(i,jmax))**5*dudzsqr(jmax))
     &+0.5*optau0*eta*dvy0dx**2/dsqrt(t0(i,jmax))**3
     &-2.5*optau0*etapar*dsqrt(t0(i,jmax))**3*dvz0dz**2
     &+0.5*kperp*d2t0dx2/dsqrt(t0(i,jmax))**3
     &-2.5*kpar*dsqrt(t0(i,jmax))**3*d2t0dz2)
      rhs(kp4)=s/n0(i,jmax)-t0(i,jmax)*divv0
     &+kperp*d2t0dx2/dsqrt(t0(i,jmax))+kpar*dsqrt(t0(i,jmax))**5*d2t0dz2
     &+optau0*(eta*dvy0dx**2/dsqrt(t0(i,jmax))
     &+etapar*dsqrt(t0(i,jmax))**5*dvz0dz**2)
      bandl(ndis+2,kp4)=(2.*optau0*etapar*dsqrt(t0(i,jmax))**5*dvz0dz
     &-t0(i,jmax))/dzm
      bandl(ndis,kp4)=-2.*kpar*dsqrt(t0(i,jmax))**5*dudzsqr(jmax)
c
c-----------------------------------------------------------------------
c
      else
c
c-----------------------------------------------------------------------
c
      if (x(i).lt.1.) then
c
c-----------------------------------------------------------------------
c
c     Equation for vx1(i,j).
c
      bandl(5,k)=-dperp*vx0(i,jmax)*dvdx(i)
      bandr(5,k)=-bandl(5,k)
      diag(k)=beta2+beta*(1.+dperp*(vz0(i,jmax)/dzm+dvx0dx)+rhoi*dvy0dx)
      bandl(4,k)=-rhoi*(eta*dvdxsqr(i)/dsqrt(t0(i,jmax))
     &+(vx0(i,jmax)-
     &eta*(ddvdxdv(i)+dn0dx/n0(i,jmax)
     &-0.5*dt0dx/t0(i,jmax))/dsqrt(t0(i,jmax)))*dvdx(i))
      bandr(6,k)=-rhoi*(eta*dvdxsqr(i)/dsqrt(t0(i,jmax))
     &-(vx0(i,jmax)-
     &eta*(ddvdxdv(i)+dn0dx/n0(i,jmax)
     &-0.5*dt0dx/t0(i,jmax))/dsqrt(t0(i,jmax)))*dvdx(i))
      bandr(1,k)=rhoi*(2.*eta*dvdxsqr(i)/dsqrt(t0(i,jmax))
     &+vz0(i,jmax)/dzm)
      bandr(2,k)=dperp*dvx0dz+rhoi*dvy0dz
      bandl(2,k)=(rhoi*eta*dvy0dx/dsqrt(t0(i,jmax))
     &-dperp*(del1+del2*t0(i,jmax)))*dvdx(i)/n0(i,jmax)
      bandr(8,k)=-bandl(2,k)
      bandr(3,k)=(rhoi*eta*dvy0dx/dsqrt(t0(i,jmax))
     &-dperp*(del1+del2*t0(i,jmax)))*dn0dx/n0(i,jmax)**2
      bandl(1,k)=-dperp*del2*dvdx(i)
     &-0.5*rhoi*eta*dvy0dx*dvdx(i)/dsqrt(t0(i,jmax))**3
      bandr(9,k)=-bandl(1,k)
      bandr(4,k)=dperp*del2*dn0dx/n0(i,jmax)
     &+0.5*rhoi*(eta/dsqrt(t0(i,jmax))**3)*
     &(d2vy0dx2+(dn0dx/n0(i,jmax)-1.5*dt0dx/t0(i,jmax))*dvy0dx)
      rhs(k)=-vx0(i,jmax)
     &+rhoi*(eta*(d2vy0dx2+dvy0dx*(dn0dx/n0(i,jmax)-0.5*dt0dx/t0(i,jmax)
     &))/dsqrt(t0(i,jmax))-vdgvy0)
     &-dperp*(del2*dt0dx+(del1+del2*t0(i,jmax))*dn0dx/n0(i,jmax)+vdgvx0)
      bandl(ndis,k)=-dperp*vz0(i,jmax)/dzm
      bandl(ndis-1,k)=-rhoi*vz0(i,jmax)/dzm
```

```
c
c-----------------------------------------------------------------------
c
c     Equation for vy1(i,j).
c
      bandl(6,kp1)=rhoi*vx0(i,jmax)*dvdx(i)
      bandr(4,kp1)=-bandl(6,kp1)
      bandl(1,kp1)=-rhoi*(vz0(i,jmax)/dzm+dvx0dx)+dperp*dvy0dx
      bandl(5,kp1)=-dperp*(eta*dvdxsqr(i)/dsqrt(t0(i,jmax))
     &+(vx0(i,jmax)
     &-eta*(ddvdxdv(i)+dn0dx/n0(i,jmax)-0.5*dt0dx/t0(i,jmax))/
     &dsqrt(t0(i,jmax)))*dvdx(i))
      bandr(5,kp1)=-dperp*(eta*dvdxsqr(i)/dsqrt(t0(i,jmax))
     &-(vx0(i,jmax)
     &-eta*(ddvdxdv(i)+dn0dx/n0(i,jmax)-0.5*dt0dx/t0(i,jmax))/
     &dsqrt(t0(i,jmax)))*dvdx(i))
      diag(kp1)=beta2+beta*(1.+dperp*(
     &2.*eta*dvdxsqr(i)/dsqrt(t0(i,jmax))+vz0(i,jmax)/dzm))
      bandr(1,kp1)=-rhoi*dvx0dz+dperp*dvy0dz
      bandl(3,kp1)=(rhoi*(del1+del2*t0(i,jmax))
     &+dperp*eta*dvy0dx/dsqrt(t0(i,jmax)))*dvdx(i)/n0(i,jmax)
      bandr(7,kp1)=-bandl(3,kp1)
      bandr(2,kp1)=(rhoi*(del1+del2*t0(i,jmax))+dperp*eta*dvy0dx/
     &dsqrt(t0(i,jmax)))*dn0dx/n0(i,jmax)**2
      bandl(2,kp1)=rhoi*del2*dvdx(i)
     &-0.5*dperp*eta*dvy0dx*dvdx(i)/dsqrt(t0(i,jmax))**3
      bandr(8,kp1)=-bandl(2,kp1)
      bandr(3,kp1)=-rhoi*del2*dn0dx/n0(i,jmax)
     &+0.5*dperp*eta*(d2vy0dx2+(dn0dx/n0(i,jmax)
     &-1.5*dt0dx/t0(i,jmax))*dvy0dx)
     &/dsqrt(t0(i,jmax))**3
      rhs(kp1)=-vy0(i,jmax)
     &+dperp*(eta*(d2vy0dx2+dvy0dx*(dn0dx/n0(i,jmax)
     &-0.5*dt0dx/t0(i,jmax)))/
     &dsqrt(t0(i,jmax))-vdgvy0)
     &+rhoi*(del2*dt0dx+(del1+del2*t0(i,jmax))*dn0dx/n0(i,jmax)+vdgvx0)
      bandl(ndis+1,kp1)=rhoi*vz0(i,jmax)/dzm
      bandl(ndis,kp1)=-dperp*vz0(i,jmax)/dzm
c
c-----------------------------------------------------------------------
c
c     Equation for vz1(i,j).  On this part of the boundary ( x/d < 1 ),
c     the Bohm's sheath criterion is imposed.
c
      diag(kp2)=beta2+beta
      bandr(2,kp2)=-0.5*del2/dsqrt(del1+del2*t0(i,jmax))
      rhs(kp2)=-vz0(i,jmax)+dsqrt(del1+del2*t0(i,jmax))
c
c-----------------------------------------------------------------------
c
c     Equation for n1(i,j).
c
      bandl(8,kp3)=-n0(i,jmax)*dvdx(i)
      bandr(2,kp3)=-bandl(8,kp3)
      bandl(3,kp3)=dn0dx
      bandl(1,kp3)=n0(i,jmax)/dzm+dn0dz
      bandl(5,kp3)=-vx0(i,jmax)*dvdx(i)
      bandr(5,kp3)=-bandl(5,kp3)
      diag(kp3)=beta2+beta*(divv0+vz0(i,jmax)/dzm)
      rhs(kp3)=s-n0(i,jmax)*divv0-vdgn0
      bandl(ndis+1,kp3)=-n0(i,jmax)/dzm
      bandl(ndis,kp3)=-vz0(i,jmax)/dzm
c
c-----------------------------------------------------------------------
```

```
c
c     Equation for t1(i,j).
c
      bandl(9,kp4)=-t0(i,jmax)*dvdx(i)
      bandr(1,kp4)=-bandl(9,kp4)
      bandl(4,kp4)=1.5*dt0dx
      bandl(8,kp4)=2.*optau0*eta*dvy0dx*dvdx(i)/dsqrt(t0(i,jmax))
      bandr(2,kp4)=-bandl(8,kp4)
      bandl(2,kp4)=(t0(i,jmax)
     &-2.*optau0*etapar*dsqrt(t0(i,jmax))**5*dvz0dz)/dzm+1.5*dt0dz
      bandl(6,kp4)=kperp*dt0dx*dvdx(i)/(n0(i,jmax)*dsqrt(t0(i,jmax)))
      bandr(4,kp4)=-bandl(6,kp4)
      bandl(1,kp4)=(s+kperp*dt0dx*dn0dx/dsqrt(t0(i,jmax))
     &+kpar*dsqrt(t0(i,jmax))**5*dt0dz*dn0dz)/n0(i,jmax)**2
     &-kpar*dsqrt(t0(i,jmax))**5*dt0dz/(n0(i,jmax)*dzm)
      bandl(5,kp4)=-kperp*dvdxsqr(i)/dsqrt(t0(i,jmax))
     &-(1.5*vx0(i,jmax)
     &-optau0*del2*eta*dvz0dx/dsqrt(t0(i,jmax)*(del1+del2*t0(i,jmax)))
     &-kperp*(ddvdxdv(i)+dn0dx/n0(i,jmax)-dt0dx/t0(i,jmax))/
     &dsqrt(t0(i,jmax)))*dvdx(i)
      bandr(5,kp4)=-kperp*dvdxsqr(i)/dsqrt(t0(i,jmax))
     &+(1.5*vx0(i,jmax)
     &-optau0*del2*eta*dvz0dx/dsqrt(t0(i,jmax)*(del1+del2*t0(i,jmax)))
     &-kperp*(ddvdxdv(i)+dn0dx/n0(i,jmax)-dt0dx/t0(i,jmax))/
     &dsqrt(t0(i,jmax)))*dvdx(i)
      diag(kp4)=beta2
     &+beta*(divv0-(kpar*dsqrt(t0(i,jmax))**5*
     &(dn0dz/n0(i,jmax)+5.*dt0dz/t0(i,jmax))-1.5*vz0(i,jmax))/dzm
     &+2.*kperp*dvdxsqr(i)/dsqrt(t0(i,jmax))
     &+0.5*optau0*eta*(dvy0dx**2+dvz0dx**2)/dsqrt(t0(i,jmax))**3
     &-2.5*optau0*etapar*dsqrt(t0(i,jmax))**3*dvz0dz**2
     &-0.5*kperp*dt0dx**2/(dsqrt(t0(i,jmax))*t0(i,jmax)**2)
     &+2.5*kpar*dsqrt(t0(i,jmax))*dt0dz**2
     &+0.5*kperp*(d2t0dx2-0.5*dt0dx**2/t0(i,jmax)+dt0dx*dn0dx/n0(i,jmax)
     &)/dsqrt(t0(i,jmax))**3
     &-2.5*kpar*dsqrt(t0(i,jmax))**3*(2.5*dt0dz**2/t0(i,jmax)
     &+dt0dz*dn0dz/n0(i,jmax))
     &+0.5*optau0*del2**2*eta*dvz0dx*dt0dx/
     &(dsqrt(t0(i,jmax)*(del1+del2*t0(i,jmax)))*(del1+del2*t0(i,jmax))))
      rhs(kp4)=s/n0(i,jmax)-t0(i,jmax)*divv0-1.5*vdgt0
     &+optau0*(eta*(dvz0dx**2+dvy0dx**2)/dsqrt(t0(i,jmax))
     &+etapar*dsqrt(t0(i,jmax))**5*dvz0dz**2)
     &+kperp*(d2t0dx2-0.5*dt0dx**2/t0(i,jmax)+dt0dx*dn0dx/n0(i,jmax))
     &/dsqrt(t0(i,jmax))
     &+kpar*dsqrt(t0(i,jmax))**5*(2.5*dt0dz**2/t0(i,jmax)
     &+dt0dz*dn0dz/n0(i,jmax))
      bandl(ndis+2,kp4)=(2.*optau0*etapar*dsqrt(t0(i,jmax))**5*dvz0dz
     &-t0(i,jmax))/dzm
      bandl(ndis+1,kp4)=kpar*dsqrt(t0(i,jmax))**5*dt0dz/(n0(i,jmax)*dzm)
      bandl(ndis,kp4)=(kpar*dsqrt(t0(i,jmax))**5*(dn0dz/n0(i,jmax)
     &+5.*dt0dz/t0(i,jmax))-1.5*vz0(i,jmax))/dzm
c
c-----------------------------------------------------------------------
c
      else
c
c-----------------------------------------------------------------------
c
c     Equation for vx1(i,j).
c
      bandl(5,k)=-dperp*vx0(i,jmax)*dvdx(i)
      bandr(5,k)=-bandl(5,k)
      diag(k)=beta2+beta*(1.+dperp*dvx0dx+rhoi*dvy0dx)
      bandl(4,k)=-rhoi*(eta*dvdxsqr(i)/dsqrt(t0(i,jmax))
```

```
     &+(vx0(i,jmax)-
     &eta*(ddvdxdv(i)+dn0dx/n0(i,jmax)-0.5*dt0dx/t0(i,jmax))
     &/dsqrt(t0(i,jmax)))*dvdx(i))
      bandr(6,k)=-rhoi*(eta*dvdxsqr(i)/dsqrt(t0(i,jmax))
     &-(vx0(i,jmax)-
     &eta*(ddvdxdv(i)+dn0dx/n0(i,jmax)-0.5*dt0dx/t0(i,jmax))
     &/dsqrt(t0(i,jmax)))*dvdx(i))
      bandr(1,k)=2.*rhoi*eta*dvdxsqr(i)/dsqrt(t0(i,jmax))
      bandl(2,k)=(rhoi*eta*dvy0dx/dsqrt(t0(i,jmax))
     &-dperp*(del1+del2*t0(i,jmax)))*dvdx(i)/n0(i,jmax)
      bandr(8,k)=-bandl(2,k)
      bandr(3,k)=(rhoi*eta*dvy0dx/dsqrt(t0(i,jmax))
     &-dperp*(del1+del2*t0(i,jmax)))*dn0dx/n0(i,jmax)**2
      bandl(1,k)=-dperp*del2*dvdx(i)
     &-0.5*rhoi*eta*dvy0dx*dvdx(i)/dsqrt(t0(i,jmax))**3
      bandr(9,k)=-bandl(1,k)
      bandr(4,k)=dperp*del2*dn0dx/n0(i,jmax)
     &+0.5*rhoi*(eta/dsqrt(t0(i,jmax))**3)*
     &(d2vy0dx2+(dn0dx/n0(i,jmax)-1.5*dt0dx/t0(i,jmax))*dvy0dx)
      rhs(k)=-vx0(i,jmax)
     &+rhoi*(eta*(d2vy0dx2+dvy0dx*(dn0dx/n0(i,jmax)-0.5*dt0dx/t0(i,jmax)
     &))/dsqrt(t0(i,jmax))-vdgvy0)
     &-dperp*(del2*dt0dx+(del1+del2*t0(i,jmax))*dn0dx/n0(i,jmax)+vdgvx0)
c
c-----------------------------------------------------------------------
c
c     Equation for vy1(i,j).
c
      bandl(6,kp1)=rhoi*vx0(i,jmax)*dvdx(i)
      bandr(4,kp1)=-bandl(6,kp1)
      bandl(1,kp1)=-rhoi*dvx0dx+dperp*dvy0dx
      bandl(5,kp1)=-dperp*(eta*dvdxsqr(i)/dsqrt(t0(i,jmax))
     &+(vx0(i,jmax)
     &-eta*(ddvdxdv(i)+dn0dx/n0(i,jmax)-0.5*dt0dx/t0(i,jmax))
     &/dsqrt(t0(i,jmax)))*dvdx(i))
      bandr(5,kp1)=-dperp*(eta*dvdxsqr(i)/dsqrt(t0(i,jmax))
     &-(vx0(i,jmax)
     &-eta*(ddvdxdv(i)+dn0dx/n0(i,jmax)-0.5*dt0dx/t0(i,jmax))
     &/dsqrt(t0(i,jmax)))*dvdx(i))
      diag(kp1)=beta2+beta*(1.+2.*dperp*eta*dvdxsqr(i)
     &/dsqrt(t0(i,jmax)))
      bandl(3,kp1)=(rhoi*(del1+del2*t0(i,jmax))
     &+dperp*eta*dvy0dx/dsqrt(t0(i,jmax)))*dvdx(i)/n0(i,jmax)
      bandr(7,kp1)=-bandl(3,kp1)
      bandr(2,kp1)=(rhoi*(del1+del2*t0(i,jmax))+dperp*eta*dvy0dx/
     &dsqrt(t0(i,jmax)))*dn0dx/n0(i,jmax)**2
      bandl(2,kp1)=rhoi*del2*dvdx(i)
     &-0.5*dperp*eta*dvy0dx*dvdx(i)/dsqrt(t0(i,jmax))**3
      bandr(8,kp1)=-bandl(2,kp1)
      bandr(3,kp1)=-rhoi*del2*dn0dx/n0(i,jmax)
     &+0.5*dperp*eta*(d2vy0dx2+(dn0dx/n0(i,jmax)-1.5*dt0dx/t0(i,jmax))*
     &dvy0dx)
     &/dsqrt(t0(i,jmax))**3
      rhs(kp1)=-vy0(i,jmax)
     &+dperp*(eta*(d2vy0dx2+dvy0dx*(dn0dx/n0(i,jmax)
     &-0.5*dt0dx/t0(i,jmax)))/dsqrt(t0(i,jmax))-vdgvy0)
     &+rhoi*(del2*dt0dx+(del1+del2*t0(i,jmax))*dn0dx/n0(i,jmax)+vdgvx0)
c
c-----------------------------------------------------------------------
c
c     Equation for vz1(i,j) has been taken care of since vz(x,z) is
c     equal to 0 when x/d > 1.
c
c-----------------------------------------------------------------------
```

```
c
c     Equation for n1(i,j).
c
      bandl(8,kp3)=-n0(i,jmax)*dvdx(i)
      bandr(2,kp3)=-bandl(8,kp3)
      bandl(3,kp3)=dn0dx
      bandl(5,kp3)=-vx0(i,jmax)*dvdx(i)
      bandr(5,kp3)=-bandl(5,kp3)
      diag(kp3)=beta2+beta*divv0
      rhs(kp3)=s-n0(i,jmax)*divv0-vdgn0
      bandl(ndis+1,kp3)=-n0(i,jmax)/dzm
c
c-----------------------------------------------------------------------
c
c     Equation for t1(i,j).
c
      bandl(9,kp4)=-t0(i,jmax)*dvdx(i)
      bandr(1,kp4)=-bandl(9,kp4)
      bandl(4,kp4)=1.5*dt0dx
      bandl(8,kp4)=2.*optau0*eta*dvy0dx*dvdx(i)/dsqrt(t0(i,jmax))
      bandr(2,kp4)=-bandl(8,kp4)
      bandl(6,kp4)=kperp*dt0dx*dvdx(i)/(n0(i,jmax)*dsqrt(t0(i,jmax)))
      bandr(4,kp4)=-bandl(6,kp4)
      bandl(1,kp4)=(s+kperp*dt0dx*dn0dx/dsqrt(t0(i,jmax)))/n0(i,jmax)**2
      bandl(5,kp4)=-kperp*dvdxsqr(i)/dsqrt(t0(i,jmax))
     &-(1.5*vx0(i,jmax)
     &-kperp*(ddvdxdv(i)+dn0dx/n0(i,jmax)-dt0dx/t0(i,jmax))/
     &dsqrt(t0(i,jmax)))*dvdx(i)
      bandr(5,kp4)=-kperp*dvdxsqr(i)/dsqrt(t0(i,jmax))
     &+(1.5*vx0(i,jmax)
     &-kperp*(ddvdxdv(i)+dn0dx/n0(i,jmax)-dt0dx/t0(i,jmax))/
     &dsqrt(t0(i,jmax)))*dvdx(i)
      diag(kp4)=beta2
     &+beta*(divv0
     &+2.*(kperp*dvdxsqr(i)/dsqrt(t0(i,jmax))
     &+kpar*dsqrt(t0(i,jmax))**5*dudzsqr(jmax))
     &+0.5*optau0*eta*dvy0dx**2/dsqrt(t0(i,jmax))**3
     &-2.5*optau0*etapar*dsqrt(t0(i,jmax))**3*dvz0dz**2
     &-0.5*kperp*dt0dx**2/(dsqrt(t0(i,jmax))*t0(i,jmax)**2)
     &+0.5*kperp*(d2t0dx2-0.5*dt0dx**2/t0(i,jmax)+dt0dx*dn0dx/n0(i,jmax)
     &)/dsqrt(t0(i,jmax))**3
     &-2.5*kpar*dsqrt(t0(i,jmax))**3*d2t0dz2)
      rhs(kp4)=s/n0(i,jmax)-t0(i,jmax)*divv0-1.5*vdgt0
     &+optau0*(eta*dvy0dx**2/dsqrt(t0(i,jmax))
     &+etapar*dsqrt(t0(i,jmax))**5*dvz0dz**2)
     &+kperp*(d2t0dx2-0.5*dt0dx**2/t0(i,jmax)+dt0dx*dn0dx/n0(i,jmax))
     &/dsqrt(t0(i,jmax))+kpar*dsqrt(t0(i,jmax))**5*d2t0dz2
      bandl(ndis+2,kp4)=(2.*optau0*etapar*dsqrt(t0(i,jmax))**5*dvz0dz
     &-t0(i,jmax))/dzm
      bandl(ndis,kp4)=-2.*kpar*dsqrt(t0(i,jmax))**5*dudzsqr(jmax)
c
c-----------------------------------------------------------------------
c
c     Include heat generated by viscosity at the tip of the obstacle
c     with the following statements.
c
      if (i.eq.imid) then
      rhs(kp4)=rhs(kp4)+qvis
      diag(kp4)=diag(kp4)-beta2+beta2/rhoi
      endif
c
c-----------------------------------------------------------------------
c
      endif
```

```
c
c-----------------------------------------------------------------------
c
      endif
c
c-----------------------------------------------------------------------
c
 61   continue
c
c-----------------------------------------------------------------------
c
c     Find maximum residue of the last row.
c
      do 62 i=ndis+1,nmax
 62   resmax=dmax1(resmax,dabs(rhs(i)))
c
c-----------------------------------------------------------------------
c
c     Solve for the last two rows of the two-dimensional grid.
c
      call eband
c
c-----------------------------------------------------------------------
c
c     start backward substitution
c
      do 80 j=jmax-1,2,-1
      do 90 i=ndis,1,-1
      ipndis=i+ndis
      sol(j*ndis+i)=rhs(ipndis)
 90   rhs(ipndis)=rhs(i)
      if (j.le.jlim1) then
      do 100 i=1,ndis
      read(2,rec=(j-2)*ndis+i) crunchdiag(i),(crunchr(ki,i), ki=1,nb)
     &,crunchrhs(i)
 100  continue
      else if (j.le.jlim2) then
      do 105 i=1,ndis
      read(3,rec=(j-jlim1-1)*ndis+i) crunchdiag(i)
     &,(crunchr(ki,i), ki=1,nb),crunchrhs(i)
 105  continue
      else
      do 107 i=1,ndis
      read(4,rec=(j-jlim2-1)*ndis+i) crunchdiag(i)
     &,(crunchr(ki,i), ki=1,nb),crunchrhs(i)
 107  continue
      endif
      do 110 i=ndis,1,-1
      dummy=rhs(i)
      do 120 ki=1,nb
      temp=-bandr(ki,i)
 120  if (temp.ne.0.) dummy=dummy+temp*rhs(ki+i)
 110  rhs(i)=dummy/diag(i)
 80   continue
      do 130 i=1,nmax
 130  sol(i)=rhs(i)
c
c-----------------------------------------------------------------------
c
c     Update the variables and compute the maximum corrections.
c
      errvx0m=0.
      errvy0m=0.
      errvz0m=0.
```

```
      errn0m=0.
      errt0m=0.
      do 250 j=1,jmax
      npos=5*(j-1)*imax
      do 250 i=1,imax
      k=npos+5*(i-1)+1
      temp00=sol(k)
      temp01=sol(k+1)
      temp02=sol(k+2)
      temp03=sol(k+3)
      temp04=sol(k+4)
      errvx0m=dmax1(errvx0m,dabs(temp00))
      errvy0m=dmax1(errvy0m,dabs(temp01))
      errvz0m=dmax1(errvz0m,dabs(temp02))
      errn0m=dmax1(errn0m,dabs(temp03))
      errt0m=dmax1(errt0m,dabs(temp04))
      vx0(i,j)=vx0(i,j)+temp00
      vy0(i,j)=vy0(i,j)+temp01
      vz0(i,j)=vz0(i,j)+temp02
      n0(i,j)=n0(i,j)+temp03
 250  t0(i,j)=t0(i,j)+temp04
c
c-----------------------------------------------------------------------
c
c     Write result to output data file after every iteration.
c
      call output
      write(*,'(i4,3g20.10)') iter,errn0m,n0m,resmax
c
c-----------------------------------------------------------------------
c
c     Check to see if convergence is reached.
c
      if (errn0m.ge.tol0*n0m) goto 1
c
c-----------------------------------------------------------------------
c
c     Close virtual memory access.
c
      close(unit=2)
      close(unit=3)
      close(unit=4)
c
c-----------------------------------------------------------------------
c
      do 1210 i=imax,1,-1
      vz0(i,1)=0.
 1210 if (x(i).ge.1.) vz0(i,jmax)=0.
      do 1300 j=jmax,1,-1
      vx0(1,j)=0.
      vy0(1,j)=0.
      vx0(imax,j)=0.
 1300 vy0(imax,j)=0.
c
c-----------------------------------------------------------------------
c
c     Write final result to output data file.
c
      call output
c
c-----------------------------------------------------------------------
c
c     Compute time elapsed.
c
```

```
      call dostim(ihour1,imin1,isec1,ith1)
      total=3600.*dble(ihour1-ihour)+60.*dble(imin1-imin)
     &+dble(isec1-isec)+dble(ith1-ith)/100.
      write(*,*) 'total time in seconds =',total
c
c-----------------------------------------------------------------------
c
      stop
      end
c
c-----------------------------------------------------------------------
c
      subroutine input
      implicit real*8(a-h,o-z),integer(i-n)
      real*8 kperp,kpar,lambda
      dimension x(49),z(193),dudz(193),dvdx(49),dvdxsqr(49),ddvdxdv(49)
     &,dudzsqr(193),ddudzdu(193)
      common /matrx2/ nmax,nmaxml
      common /input1/ aperp,rhoi,x0,z0,imax,jmax,tol0,s,dperp,tau0,kperp
     &,eta,etapar,kpar,imid,qvis
      common /input2/ dzm,x,z,dudz,dudzsqr,ddudzdu,dvdx,dvdxsqr,ddvdxdv
      common /relax/ beta,beta2,del1,del2,optau0
      common /start/ istart,iter
      common /mesh/ zmeshx
      common /b2/ nb,ndis
      open(unit=1,file='in.dat',status='old')
      read(1,*) aperp,rhoi,tau0,eta,kperp,lambda
      read(1,*) x0,z0
      read(1,*) imax,jmax
      read(1,*) tol0
      read(1,*) s
      read(1,*) beta,beta2
      read(1,*) istart
      read(1,*) zmeshx
      close(unit=1)
      imid=(imax-1)/2+1
      s=s/z0
      dperp=aperp*rhoi
      ndis=5*imax
      nmax=2*ndis
      nmaxml=nmax-1
      nb=5*(imax+1)-1
      optau0=1.+tau0
      del1=tau0/optau0
      del2=1.-del1
      etapar=rhoi**2/(dperp*eta*optau0*dsqrt(tau0)**3)
      eta=dperp*eta*dsqrt(tau0)**3/optau0
      kperp=eta
      kpar=etapar
c
c-----------------------------------------------------------------------
c
c     Set up coordinate arrays and coordinate transfomation.
c
      dv=2.*((dexp(2.*zmeshx)-1.)/(dexp(2.*zmeshx)+1.))/dble(imax-1)
      tdv=2.*dv
      dvsqr=dv**2
      imid=(imax-1)/2+1
      v=0.
      do 10 i=imid,imax
      x(i)=1.+0.5*dlog((1.+v)/(1.-v))/zmeshx
      dummy=zmeshx*(1.-v**2)
      dvdx(i)=dummy/tdv
      dvdxsqr(i)=dummy**2/dvsqr
```

```
      ddvdxdv(i)=-2.*zmeshx*v
 10   v=v+dv
      do 15 i=1,imid-1
      x(i)=2.-x(2*imid-i)
      dvdx(i)=dvdx(2*imid-i)
      dvdxsqr(i)=dvdxsqr(2*imid-i)
 15   ddvdxdv(i)=-ddvdxdv(2*imid-i)
      dvdxsqr(1)=1./x(2)**2
      dvdxsqr(imax)=dvdxsqr(1)
c
c-----------------------------------------------------------------------
c
      du=-1./dble(jmax-1)
      dusqr=du**2
      tdu=2.*du
      do 20 j=1,jmax-1
      u=1.+du*dble(j-1)
      dummy=-0.5/(z0*u)
      dudz(j)=dummy/tdu
      dudzsqr(j)=dummy**2/dusqr
      z(j)=z0*(1.-u**2)
 20   ddudzdu(j)=-dummy/u
      z(jmax)=z0
      dzm=z0-z(jmax-1)
      dudz(jmax)=1./dzm
      dudzsqr(jmax)=1./dzm**2
      dudzsqr(1)=1./z(2)**2
c
c-----------------------------------------------------------------------
c
      qvis=0.5*eta*dsqrt(optau0)**3/(lambda*(x(imid+1)-1.))
      return
      end
c
c-----------------------------------------------------------------------
c
      subroutine initial
      implicit real*8(a-h,n-z),integer(i-m)
      real*8 kperp,kpar
      dimension vx0(49,193),vy0(49,193),vz0(49,193),n0(49,193)
     &,t0(49,193),x(49),z(193),dudz(193),dvdx(49),dvdxsqr(49)
     &,ddvdxdv(49),dudzsqr(193),ddudzdu(193)
      common /v0n0/ vx0,vy0,vz0,n0,t0
      common /input1/ aperp,rhoi,x0,z0,imax,jmax,tol0,s,dperp,tau0,kperp
     &,eta,etapar,kpar,imid,qvis
      common /input2/ dzm,x,z,dudz,dudzsqr,ddudzdu,dvdx,dvdxsqr,ddvdxdv
      common /start/ istart,iter
      if (istart.eq.0) then
      do 10 i=1,imax
      do 20 j=1,jmax
      vx0(i,j)=0.
      vy0(i,j)=0.
      vz0(i,j)=0.
      n0(i,j)=1.
 20   t0(i,j)=1.0
 10   if (x(i).lt.1.) vz0(i,jmax)=1.
      else
      open(unit=1,file='g.dat',status='old')
      do 30 k=1,26
 30   read(1,*)
      do 40 i=1,imax
      do 40 j=1,jmax
 40   read(1,*) vx0(i,j),vy0(i,j),vz0(i,j),n0(i,j),t0(i,j)
      close(unit=1)
```

```
      endif
      return
      end
c
c-----------------------------------------------------------------------
c
      subroutine length
      implicit real*8(a-h,n-z),integer(i-m)
      real*8 kperp,kpar
      dimension vx0(49,193),vy0(49,193),vz0(49,193),n0(49,193)
     &,t0(49,193),x(49),z(193),dudz(193),dvdx(49),dvdxsqr(49)
     &,ddvdxdv(49),dudzsqr(193),ddudzdu(193)
      common /v0n0/ vx0,vy0,vz0,n0,t0
      common /input2/ dzm,x,z,dudz,dudzsqr,ddudzdu,dvdx,dvdxsqr,ddvdxdv
      common /clength/ zpar
      common /input1/ aperp,rhoi,x0,z0,imax,jmax,tol0,s,dperp,tau0,kperp
     &,eta,etapar,kpar,imid,qvis
      test=0.5*(n0(1,1)+n0(1,jmax))
      do 10 j=jmax,3,-2
      if ((n0(1,j).le.test).and.(n0(1,j-2).ge.test))
     &zpar=z(jmax)-z(j)+(z(j)-z(j-2))*(test-n0(1,j))
     &/(n0(1,j-2)-n0(1,j))
 10   continue
      return
      end
c
c-----------------------------------------------------------------------
c
      subroutine output
      implicit real*8(a-h,n-z),integer(i-m)
      real*8 kperp,kpar
      dimension vx0(49,193),vy0(49,193),vz0(49,193),n0(49,193)
     &,t0(49,193),x(49),z(193),dudz(193),dvdx(49),dvdxsqr(49)
     &,ddvdxdv(49),dudzsqr(193),ddudzdu(193)
      common /v0n0/ vx0,vy0,vz0,n0,t0
      common /input1/ aperp,rhoi,x0,z0,imax,jmax,tol0,s,dperp,tau0,kperp
     &,eta,etapar,kpar,imid,qvis
      common /input2/ dzm,x,z,dudz,dudzsqr,ddudzdu,dvdx,dvdxsqr,ddvdxdv
      common /relax/ beta,beta2,del1,del2,optau0
      common /start/ istart,iter
      common /clength/ zpar
      common /error/ errvx0m,errvy0m,errvz0m,errn0m,errt0m,resmax
      common /mesh/ zmeshx
c
c-----------------------------------------------------------------------
c
c      compute collection length
c
       call length
c
c-----------------------------------------------------------------------
c
      open(unit=1,file='out.dat',status='unknown')
      write(1,*) ' parallel particle collection length  = ', zpar
      write(1,*) ' x0                                 = ', x0
      write(1,*) ' z0                                 = ', z0
      write(1,*) ' imax                               = ', imax
      write(1,*) ' jmax                               = ', jmax
      write(1,*) ' mesh non-uniformity factor ( x )   = ', zmeshx
      write(1,*) ' alpha_perp                         = ', aperp
      write(1,*) ' rho_i                              = ', rhoi
      write(1,*) ' perpendicular diffusion coeficcient  = ', dperp
      write(1,*) ' perpendicular viscosity/diffusivity  = ', eta/dperp
      write(1,*) ' perpendicular kappa/viscosity        = ', kperp/eta
```

```
      write(1,*) ' parallel kappa/perpendicular kappa   = ', kpar/kperp
      write(1,*) ' T_e/T_i                              = ', tau0
      write(1,*) ' particle source (s_p)                = ', s
      write(1,*) ' maximum error on vx                  = ', errvx0m
      write(1,*) ' maximum error on vy                  = ', errvy0m
      write(1,*) ' maximum error on vz                  = ', errvz0m
      write(1,*) ' maximum error on n                   = ', errn0m
      write(1,*) ' maximum error on T                   = ', errt0m
      write(1,*) ' maximum residue                      = ', resmax
      write(1,*) ' number of iterations                 = ', iter
      write(1,*) ' convergence criteria                 = ', tol0
      write(1,*) ' under relaxation factor #1 ( beta )  = ', beta
      write(1,*) ' under relaxation factor #2 ( beta2 ) = ', beta2
      write(1,*) ' '
      write(1,*) ' '
      do 10 i=1,imax
      do 10 j=1,jmax
 10   write(1,*) vx0(i,j),vy0(i,j),vz0(i,j),n0(i,j),t0(i,j)
      close(unit=1)
      return
      end
c
c-----------------------------------------------------------------------
c
      subroutine gauss
      implicit real*8(a-h,o-z),integer(i-n)
      dimension bandl(249,494),bandr(249,494),diag(494),rhs(494)
      common /b0/ bandl,bandr
      common /b1/ diag,rhs
      common /b2/ nb,ndis
      do 10 i=1,ndis
      do 10 j=1,nb
      ipj=i+j
      temp=-bandl(j,ipj)/diag(i)
      if (temp.eq.0.) goto 10
      diag(ipj)=diag(ipj)+temp*bandr(j,i)
      rhs(ipj)=rhs(ipj)+temp*rhs(i)
      do 20 k=1,j-1
 20   bandl(k,ipj)=bandl(k,ipj)+temp*bandr(j-k,i)
      do 30 k=1,nb-j
 30   bandr(k,ipj)=bandr(k,ipj)+temp*bandr(j+k,i)
 10   continue
      return
      end
c
c-----------------------------------------------------------------------
c
      subroutine eband
      implicit real*8(a-h,o-z),integer(i-n)
      dimension bandl(249,494),bandr(249,494),diag(494),rhs(494)
      common /b0/ bandl,bandr
      common /b1/ diag,rhs
      common /b2/ nb,ndis
      common /matrx2/ n,nl1
c
c-----------------------------------------------------------------------
c
c     forward elimination
c
      do 100 i=1,nl1
      jmax=n-i
      if (jmax.gt.nb) jmax=nb
      do 90 j=1,jmax
      jr=j+i
```

```
      jp1=j+1
      jl1=j-1
      if (bandl(j,jr).eq.0.) go to 90
      temp=-bandl(j,jr)/diag(i)
      diag(jr)=diag(jr)+temp*bandr(j,i)
      rhs(jr)=rhs(jr)+temp*rhs(i)
      do 50 k=jp1,jmax
      kcol=k-j
      bandr(kcol,jr)=bandr(kcol,jr)+temp*bandr(k,i)
 50   continue
      do 60 k=1,jl1
      kcol=j-k
      bandl(kcol,jr)=bandl(kcol,jr)+temp*bandr(k,i)
 60   continue
 90   continue
 100  continue
c
c-----------------------------------------------------------------------
c
c     backward substitution
c
      rhs(n)=rhs(n)/diag(n)
      do 200 ii=1,nl1
      i=n-ii
      jmax=ii
      if (jmax.gt.nb) jmax=nb
      temp=rhs(i)
      do 150 j=1,jmax
      temp=temp-bandr(j,i)*rhs(i+j)
 150  continue
 200  rhs(i)=temp/diag(i)
c
c-----------------------------------------------------------------------
c
      return
      end
```

REFERENCES

[1] S. J. Zweben and R. W. Gould, Nucl. Fusion **25**, 171 (1985).

[2] P. C. Stangeby and G. M. McCracken and S. K. Erents and G. Matthews, J. Vac. Sci. Technol. A **2**, 702 (1984).

[3] J. Allen and P. J. Harbour, J. Nucl. Mater. **145-147**, 264 (1987).

[4] B. LaBombard and B. Lipschultz, Rev. Sci. Instrum. **57**, 2415 (1986).

[5] U. Samm and P. Bogen and H. A. Claassen and H. Gerhauser and H. Hartwig and E. Hintz and K. Höthker and Y. T. Lie and A. Pospieszczyk and G. G. Ross, J. Nucl. Mater. **145-147**, 206 (1987).

[6] K. McCormick and Z. A. Pietrzyk and H. Murmann and M. Lenoci and the ASDEX Team, J. Nucl. Mater. **145-147**, 215 (1987).

[7] G. F. Matthews and P. C. Stangeby and P. Sewell, J. Nucl. Mater. **145-147**, 220 (1987).

[8] J. Allen and P. J. Harbour, J. Nucl. Mater. **145-147**, 264 (1987).

[9] P. C. Stangeby, Phys. Fluids **27**, 2699 (1984).

[10] I. H. Hutchinson, Phys. Fluids **30**, 3777 (1987).

[11] P. C. Stangeby, J. Phys. D: Appl. Phys. **18**, 1547 (1984).

[12] P. C. Stangeby, Phys. Fluids **28**, 644 (1984).

[13] P. C. Stangeby, Phys. Fluids **27**, 2699 (1984).

[14] D. Bohm, in *The Characteristics of Electrical Discharges in Magnetic Fields*, edited by A. Guthrie and R. K. Wakerling (McGraw-Hill, New York, 1949), Chap. 3.

[15] E. R. Harrison and W. B. Thompson, Proc. Phys. Soc. **74**, 145 (1959).

[16] S. A. Self, Phys. Fluids **6**, 1762 (1963).

[17] F. F. Chen, in *Plasma Diagnostic Techniques*, edited by R. H. Huddlestone and S. L. Leonard (Academic Press, New York, 1965), Chap. 4.

[18] P. C. Stangeby and J. E. Allen, J. Phys. A **3**, 304 (1970).

[19] J. E. Allen, J. Phys. D **9**, 2331 (1976).

[20] R. C. Bissell and P. C. Johnson, Phys. Fluids **30**, 779 (1986).

[21] B. J. Braams and C. E. Singer, Fusion Technology **9**, 320 (1986).

[22] L. Spitzer, *Physics of Fully Ionized Gases* (Interscience Publishers, 1962).

[23] S. I. Braginskii, *Reviews of Plasma Physics*, edited by M. A. Leontovich (Consultants Bureau, New York, 1965), Vol. 1, p. 205.

[24] G. Schmidt, *Physics of High Temperature Plasmas* (Academic Press, New York, 1979).

[25] P. C. Stangeby, J. Phys. D **18**, 1547 (1985).

[26] J. H. Ferziger, *Numerical Methods for Engineering Application* (John Wiley & Sons, 1981).

[27] J. Stoer and R. Bulirsch, *Introduction to Numerical Analysis*, translated by R. Bartels, W. Gautschi, and C. Witzgall (Springer-Verlag, New York, 1980).

[28] G. Dahlquist and Å. Björck, *Numerical Methods*, translated by N. Anderson (Prentice-Hall, New Jersey, 1974).

[29] B. B. Kadomtsev, *Plasma Turbulence*, translated by L. C. Ronson, translation edited by M. G. Rusbridge (Academic Press, New York, 1965).

[30] P. C. Liewer, Nucl. Fusion **25**, 543 (1985).

[31] S. J. Zweben and P. C. Liewer and R. W. Gould, J. Nucl. Mater. **111&112**, 39 (1982).

[32] P. C. Liewer and J. M. McChesney and S. J. Zweben and R. W. Gould, Phys. Fluids **29**, 309 (1986).

[33] H. Lin and R. D. Bengtson and Ch. P. Ritz, Phys. Fluids B **1**, 2027 (1989).

[34] P. J. Harbour and G. Proudfoot, J. Nucl. Mater. **121**, 222 (1984).

[35] P. C. Stangeby, Phys. Fluids **31**, 2726 (1988).

[36] I. H. Hutchinson, Phys. Fluids **31**, 2728(1988).